DISS. ETH NO. 19981

THE MARINE BIOGEOCHEMICAL CYCLE OF SILICON: INSIGHTS FROM SILICON STABLE ISOTOPES

A dissertation submitted to

ETH ZURICH

for the degree of

Doctor of Sciences

presented by

GREGORY FRIEDRICH DE SOUZA

dipl. natw. ETH

born 30.04.1981

citizen of

Sempach and Ettiswil LU

accepted on the recommendation of

Prof. Dr. Bernard Bourdon, examiner

Dr. Ben C. Reynolds, co-examiner

Prof. Dr. Nicolas Gruber, co-examiner

Prof. Dr. Gideon Henderson, co-examiner

2011

...the sea is not a pattern, it is a struggle.

– Colm Tóibín in *The Empty Family*

Contents

Summary III

Zusammenfassung V

1 Introduction 1

1.1 Oceanic nutrient cycles . . . 2

1.2 The marine Si cycle . . . 10

1.3 Silicon isotope geochemistry . . . 15

1.4 Aims of this thesis . . . 20

2 Methods 23

2.1 Preconcentration of Si from seawater . . . 23

2.2 Chromatographic purification of Si . . . 25

2.3 Mass spectrometry . . . 26

2.4 Method evaluation . . . 28

3 Isotope fractionation in the sea: what should we expect? 33

3.1 Introduction . . . 34

3.2 The Rayleigh equation: conditions and limitations . . . 37

3.3 A simple spatial framework . . . 38

3.4 Implications . . . 40

4 The basin-scale Atlantic δ^{30}Si distribution 43

4.1 Introduction . . . 44

4.2 Methods . . . 45

4.3 Results . . . 49

4.4 Discussion . . . 50

4.5 Global δ^{30}Si distribution: Perspectives . . . 61

4.6 Summary and Conclusions 64

5 Controls on δ^{30}Si in the Atlantic thermocline 65

5.1 Introduction 66
5.2 Methods 69
5.3 Results 70
5.4 Discussion 72
5.5 Summary and Conclusions 78

6 The South Pacific δ^{30}Si distribution 81

6.1 Introduction 81
6.2 Sampling and hydrographic description 82
6.3 Results 90
6.4 Discussion 93
6.5 Conclusions 102

7 Concluding remarks 107

7.1 Summary 107
7.2 Synthesis 109

A Supplementary Information 113

A.1 Appendix to Chapter 3 113
A.2 Appendix to Chapter 4 117
A.3 Appendix to Chapter 5 125
A.4 Appendix to Chapter 6 128

References 131

Summary

The ocean owes much of its ability to regulate the CO_2 content of Earth's atmosphere to the activity of photosynthesising microorganisms in its sunlit surface, which take up CO_2 and export it to the deep sea in the form of organic matter. Much of this export of carbon is accomplished by diatoms, siliceous algae that have a vital requirement for silicon (Si). Diatoms tend to flourish in dynamic regions of the ocean that play a key role in controlling the exchange of CO_2 between the ocean and the atmosphere, with the result that the cycles of Si and carbon in the ocean are closely linked. In this thesis, I investigate the marine Si cycle by analysing the stable isotope composition of Si dissolved in seawater, expressed as δ^{30}Si. The uptake of dissolved Si by diatoms in the surface ocean is associated with the fractionation of Si isotopes, such that biological activity, which drives the cycling of Si in the sea, produces an isotopic signal that may be used to trace the pathways and processes by which Si is cycled within the ocean.

I begin by using simple models to illustrate some fundamental characteristics of stable isotope systems in the sea. This discussion highlights the pitfalls associated with the use of non-dimensional models to interpret data that possess spatial structure, and suggests mechanisms that can be expected to exert control on the oceanic δ^{30}Si distribution. Specifically, I show that physical transport processes must play an important role in producing the gradients observed in δ^{30}Si values, as well as other stable isotope tracers, in the subsurface ocean.

In the second part of this thesis, I present δ^{30}Si data from the deep Atlantic Ocean over a latitudinal range from Denmark Strait (64° N) to Drake Passage (56° S). In Atlantic deepwaters, δ^{30}Si values exhibit a pronounced and systematic meridional gradient, ranging from low δ^{30}Si values in the South Atlantic to high values in the subpolar North Atlantic. Through analysis of the Atlantic δ^{30}Si systematics, I show that this meridional gradient documents the quasi-conservative mixing of Si between the two sources of deepwater in the Atlantic Ocean, North Atlantic Deep Water (NADW) and Antarctic Bottom Water (AABW). This strong mixing control on the δ^{30}Si distribution implies that the dissolution of diatom opal sinking through the Atlantic water column contributes negligibly to the Si inventory of Atlantic deepwaters. In addition, the documented quasi-conservativity also necessitates that pro-

cesses such as boundary exchange, which have been suggested to be large sources of Si to the ocean, do not add significant amounts of Si to the deep Atlantic Ocean.

Considering the Si mass balance of the North Atlantic in the context of the meridional overturning circulation (MOC), I argue that the high δ^{30}Si value of NADW reflects the transport of high δ^{30}Si values into the North Atlantic by thermocline- and intermediate-level watermasses in the upper return path of the MOC. Since these watermasses, Subantarctic Mode Water (SAMW) and Antarctic Intermediate Water (AAIW), are formed at high southern latitudes, this inference implies that the meridional Atlantic δ^{30}Si gradient ultimately owes its origin to diatom Si uptake and export in the surface Southern Ocean, which fractionates Si isotopes between the upper and lower limbs of the MOC.

The third part of this thesis presents a detailed analysis of the δ^{30}Si distribution in the thermocline of the Atlantic Ocean. Elevated values of δ^{30}Si are not restricted to the surface ocean, where they are produced by biological activity, but extend to significant depths within the thermocline. Building upon the fundamental arguments regarding oceanic stable isotope systematics introduced earlier, I show that this observation documents that a significant proportion of Si in the upper Atlantic Ocean is transported into the interior in its dissolved form, i.e. as a preformed component. In the context of theories of thermocline ventilation and nutrient supply, I suggest a mechanism by which the observed subsurface δ^{30}Si gradient may be produced.

The final dataset presented in this thesis is from the eastern South Pacific Ocean, which is an important location for the formation of SAMW and AAIW. By analysing the δ^{30}Si distribution from the Antarctic Zone of the Southern Ocean (62° S) to the tropical Pacific (12° S), I trace the introduction of high δ^{30}Si values into the ocean interior by these watermasses. I show that high-latitude winter mixed layers partially preserve the high δ^{30}Si values created in the summer by diatom growth, as a result of efficient export of diatom opal past the depth of deep winter convection. These high winter mixed layer δ^{30}Si values are subducted into the interior during the formation of SAMW and AAIW, and are conserved as the watermasses transit the South Pacific to the subtropics.

Unlike the deep Atlantic Ocean, the deep Pacific Ocean shows no significant variation in δ^{30}Si values, which remain indistinguishable from those in the deep Southern Ocean. Whilst uncertainties stemming from contradictory literature data in the North Pacific Ocean hinder firm conclusions, the southern and equatorial Pacific δ^{30}Si distribution appears to indicate that deepwater δ^{30}Si values are not strongly altered by the dissolution of opal along their deep circulation path. This implies that deepwater δ^{30}Si values vary little in the absence of the introduction of a preformed δ^{30}Si signal, such as in the North Atlantic Ocean.

The data presented in this thesis thus bear witness to the strength of δ^{30}Si as a tracer of the transport and cycling of Si in the sea, and provide a coherent view of oceanic Si biogeochemistry that emphasises the importance of the Southern Ocean for the marine Si cycle.

Zusammenfassung

Der regulierende Einfluss des Ozeans auf den atmosphärischen CO_2-Gehalt ist zu einem grossen Teil dem oberflächennahen Wachstum von photosynthetisierenden Mikroorganismen zu verdanken, die CO_2 aufnehmen und in Form von organischem Material in die Tiefsee exportieren. Ein Grossteil dieses Kohlenstoffexports wird von Diatomeen bewerkstelligt – kieselige Algen, die für den Bau ihrer Opalschalen auf Silizium (Si) angewiesen sind. Diatomeen gedeihen in dynamischen Ozeanregionen die für den Austausch von CO_2 zwischen Ozean und Atmosphäre massgeblich sind. Die marinen Kreisläufe von Si und Kohlenstoff sind daher eng verbunden. In dieser Doktorarbeit untersuche ich den marinen biogeochemischen Kreislauf von Si mittels der Isotopenzusammensetzung von im Meerwasser gelöstem Silizium (δ^{30}Si). Die Aufnahme von gelöstem Si durch Diatomeen führt zu einer Si-Isotopenfraktionierung. Biologische Aktivität im Oberflächenozean produziert daher ein isotopisches Signal im Meerwasser, das zur Studie des Si-Kreislaufs eingesetzt werden kann.

Zu Beginn dieser Arbeit mache ich einige grundsätzlichen Überlegungen zur Systematik von stabilen Isotopen im Ozean, die ich anhand von einfachen Modellen illustriere. Diese Diskussion zeigt die Probleme auf, die durch die Anwendung von nichtdimensionalen Modellen auf Daten mit räumlicher Stuktur auftreten, und identifiziert Mechanismen, welche die marine δ^{30}Si-Verteilung massgeblich beeinflussen können. Speziell weise ich darauf hin, dass physikalische Transportprozesse einen wesentlichen Beitrag zur Erzeugung der beobachteten Variation von δ^{30}Si-Werten im Ozeaninnern leisten müssen.

Im zweiten Teil dieser Arbeit präsentiere ich δ^{30}Si-Daten aus dem tiefen Atlantischen Ozean von Dänemarkstrasse (64°N) bis Drakestrasse (56° S). Die δ^{30}Si-Werte in atlantischen Tiefenwässern weisen einen klaren und systematischen meridionalen Gradienten auf, von tiefen δ^{30}Si-Werten im Südatlantik zu hohen Werten im subpolaren Nordatlantik. Eine Analyse der atlantischen δ^{30}Si-Systematik zeigt, dass dieser Gradient das quasi-konservative Mischen von Si aus Nordatlantischem Tiefenwasser (NADW) und Antarktischem Bodenwasser (AABW) dokumentiert. Das konservative Verhalten von Silizium im tiefen Atlantik belegt, dass die Auflösung von sinkendem Opal vernachlässigbar wenig zum Si-Inventar der atlantischen Tiefenwässer beiträgt. Zudem weist es darauf hin,

dass der Austausch von Stoffen an den Ozeanrändern keine signifikante Quelle von Si im tiefen Ozean darstellt.

Eine Betrachtung der Si-Massenbilanz des Nordatlantiks im Kontext der meridionalen Umwälzzirkulation (MOC) deutet darauf hin, dass der hohe δ^{30}Si-Wert von NADW einen hohen δ^{30}Si-Wert in den Thermoklinen- und Zwischenwässern des oberen MOC-Astes widerspiegelt, die Si in den Nordatlantik zuführen. Da diese Wassermassen – Subantarktisches Modewasser (SAMW) und Antarktisches Zwischenwasser (AAIW) – in hohen südlichen Breiten gebildet werden, kann der hohe δ^{30}Si-Wert des Nordatlantiks letzendlich durch die Aufnahme und den Export von Si durch Diatomeen im Südlichen Ozean erklärt werden, welche Si-Isotopen zwischen dem oberen und unteren Ast der MOC fraktioneren.

Der dritte Teil dieser Arbeit beinhaltet eine detaillierte Analyse der Si-Isotopenverteilung in der atlantischen Thermokline. Erhöhte δ^{30}Si-Werte werden nicht nur in der euphotischen Zone beobachtet, wo sie durch biologische Si-Aufnahme erzeugt werden, sondern erstrecken sich auch bis in signifikante Tiefen in die Thermokline. Aufbauend auf die vorangegangenen Überlegungen zur marinen Isotopensystematik dokumentiert diese Beobachtung einen signifikanten Anteil an *preformed* (in gelöster Form in die Thermokline transportiertem) Silizium im oberflächennahen Si-Inventar. Unter Berücksichtigung von Theorien zur Ventilation und Nährstoffversorgung der Thermokline stelle ich einen Mechanismus zur Erzeugung der beobachteten δ^{30}Si-Verteilung vor.

Im letzten Teil der Arbeit präsentiere ich einen δ^{30}Si-Datensatz aus dem östlichen Südpazifik, der eine wichtige Quelle von SAMW und AAIW darstellt. Durch die Analyse der δ^{30}Si-Verteilung von der antarktischen Zone des Südlichen Ozean bis in den tropischen Pazifik verfolge ich die Erzeugung der hohen δ^{30}Si-Werte dieser Wassermassen, sowie ihr Einbringen in das Thermoklineninnere. Die hohen δ^{30}Si-Werte, die während des australen Sommers im Oberflächenwasser der hohen südlichen Breiten produziert werden, bleiben in den Wintermischungsschichten teilweise erhalten. Dies ist eine Folge des effizienten Opalexports in Tiefen, die der jährlichen Konvektion nicht zugänglich sind. Die hohen δ^{30}Si-Werte der Wintermischungsschichten werden während der Subduktion von SAMW und AAIW in das Thermoklineninnere eingebracht; diese bleiben während des Transports dieser Wassermassen bis in die Subtropen erhalten.

Im Gegensatz zum tiefen Atlantik weist der tiefe Pazifik keine signifikante δ^{30}Si-Variabilität auf. Obwohl widersprüchliche Literaturdaten aus dem Nordpazifik verlässliche Rückschlüsse erschweren, deutet die δ^{30}Si-Verteilung im Süd- und Äquatorialpazifik darauf hin, dass die δ^{30}Si-Werte von Tiefenwässern nur minim durch die Auflösung von sinkendem Opal verändert werden. Dies impliziert, dass eine signifikante Variation von δ^{30}Si-Werten im Tiefenwasser das Einbringen eines *preformed* δ^{30}Si-Signals wie im Nordatlantik voraussetzt.

Chapter 1

Introduction

Energy from the Sun is harnessed by photosynthetic phytoplankton – free-floating microscopic algae and other simple microorganisms – in the ocean's sunlit surface, enabling them to produce their organic tissues from carbon dioxide (CO_2) dissolved in seawater. This production of fixed carbon, termed oceanic primary productivity, forms the nutritional basis for almost all oceanic life, whilst the associated oxygen production supports aerobic life over the entire surface of the planet. Furthermore, the ecosystem supported by primary productivity in the surface ocean produces a sinking flux of organic matter into the deep ocean, a biologically-driven "pump" of carbon (Volk and Hoffert, 1985) that plays a vital role in determining that 98% of the CO_2 in the ocean–atmosphere system resides within the ocean. Due to the greenhouse properties of CO_2, this strong partitioning of the exogenic carbon inventory has important consequences for Earth's radiative balance, and thus global climate: it is estimated that the partial pressure of CO_2 (pCO_2) in Earth's atmosphere would be about 60% higher in the absence of this pump (Sarmiento and Toggweiler, 1984).

Phytoplankton have obligatory requirements for certain elements – macro- and micronutrients – in order to photosynthesise, and thus the magnitude and distribution of oceanic primary productivity is dependent on the distribution of dissolved nutrients within the accessible near-surface ocean (Falkowski et al., 1998). These distributions are, in turn, the result of the interaction between the ocean's circulation, which transports dissolved nutrients through the global ocean, and biogeochemical processes, which remove nutrients from the surface ocean and export them to the deep. The global oceanic cycles of nutrients and carbon are thus controlled by a complex series of interacting processes, the unravelling of which is necessary to understand how the ocean modulates atmospheric pCO_2 (Ito and Follows, 2005), how it has reacted to changes in external forcing in the past (Sigman et al., 2010), and how it is likely to do so in the face of the current anthropogenic climate perturbation (Sarmiento et al., 2004b). This thesis employs the tools of isotope geochemistry to investigate the oceanic cycle of silicon (Si), a nutrient that is particularly relevant for the oceanic carbon (C) cycle. The pathways and processes by which Si is cycled through the ocean are elucidated through the analysis of the stable isotope composition of silicic acid, its dissolved form in seawater.

1.1 Oceanic nutrient cycles

The oceanic distributions of dissolved nutrients can be understood as a dynamic equilibrium between the creation of spatial concentration gradients due to biological activity, and their erosion by ocean mixing processes (Gruber and Sarmiento, 2002). The importance of the dynamics of the ocean system in maintaining this balance is illustrated by the fact that, in the absence of replenishment from the deep, biological export of particulate matter would deplete the upper ocean of nutrients within approximately 50 years[1]. Conversely, without biological drawdown, ocean models indicate that the surface ocean nutrient distribution would begin to resemble that of the underlying thermocline within a decade (Sarmiento and Gruber, 2006). Thus, global oceanic nutrient distributions reflect a steady state in which the downward export of particulate organic matter is balanced by an upward flux of dissolved nutrients. Where and how dissolved nutrients are returned to the near-surface ocean depends on the mechanisms and pathways by which dense, nutrient-rich deepwaters are brought towards the surface in the ocean's meridional overturning circulation (MOC; Fig. 1.1). Thus, the replenishment of nutrients in the near-surface – one side of the balance that cycles nutrients through the ocean – is strongly dependent upon the nature of the physical circulation. This necessitates that the biogeochemical cycling of nutrients in the ocean be viewed in the context of its circulation, and thus conceptual models of ocean biogeochemistry have evolved with changing physical oceanographic paradigms. In the following, I provide a brief history of this evolution, which also allows the introduction of key concepts that will be referred to throughout this thesis.

1.1.1 Classical paradigms of ocean circulation and biogeochemical cycling

A major feature of the ocean's structure is its permanent thermocline, a region of enhanced vertical temperature, salinity and density gradients that extends across the upper 1 km of the ocean at mid- to low latitudes (Locarnini et al., 2010). Robinson and Stommel (1959) presented a theory of the oceanic thermocline that interpreted it as the result of a vertical diffusive–advective balance between warm surface waters and cold waters of the abyss. Following this theory, the classical ocean circulation models of Stommel (1958) and Stommel and Arons (1960) assumed that while dense water is added to the deep ocean at localised deepwater formation regions in the North Atlantic and Southern Ocean, it is removed through a uniformly-distributed upwelling across the thermocline. This

---

[1] assuming, following Palter et al. (2010), a thermocline phosphate inventory of 150 Tmol and an export flux of 3 Tmol/yr.

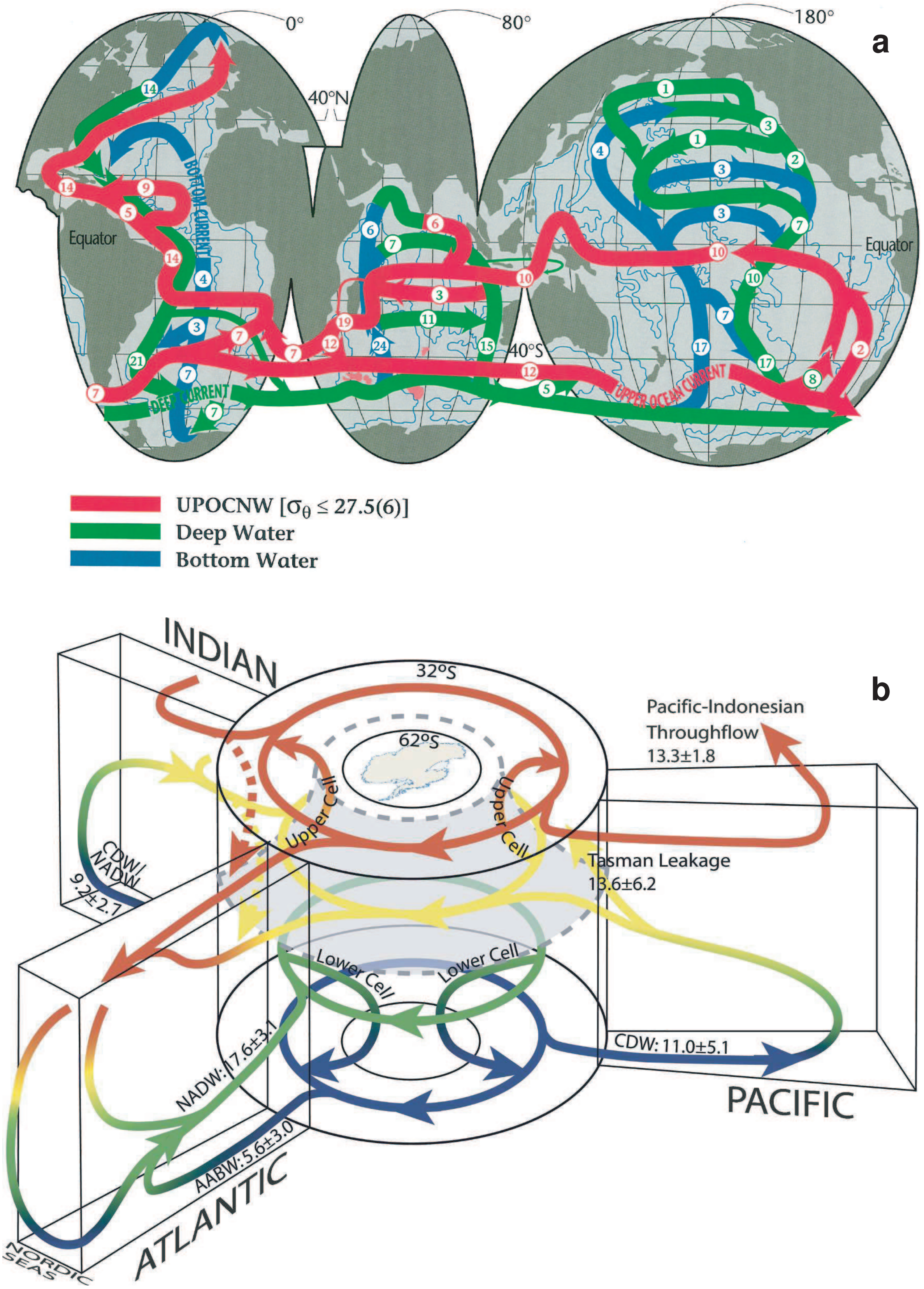
a
0°
80°
180°
40°N
Equator
Equator
40°S
BOTTOM CURRENT
DEEP CURRENT
UPPER OCEAN CURRENT
UPOCNW [$\sigma_\theta \leq 27.5(6)$]
Deep Water
Bottom Water
b
INDIAN
32°S
62°S
Pacific-Indonesian Throughflow
13.3±1.8
Upper Cell
Upper Cell
Tasman Leakage
13.6±6.2
CDW/NADW
9.2±2.1
Lower Cell
Lower Cell
NADW: 17.6±3.1
AABW: 5.6±3.0
CDW: 11.0±5.1
PACIFIC
ATLANTIC
NORDIC SEAS

Figure 1.1: Two schematic representations of the meridional overturning circulation by (a) Schmitz (1996a) and (b) Lumpkin and Speer (2007). In panel *b*, colours correspond to neutral density (γ^n) ranges: red, $\gamma^n < 27.0$; yellow, $\gamma^n = 27.0$–27.6; green, $\gamma^n = 27.6$–28.15; blue, $\gamma^n > 28.15$. These correspond to upper, intermediate, deep and bottom waters respectively.

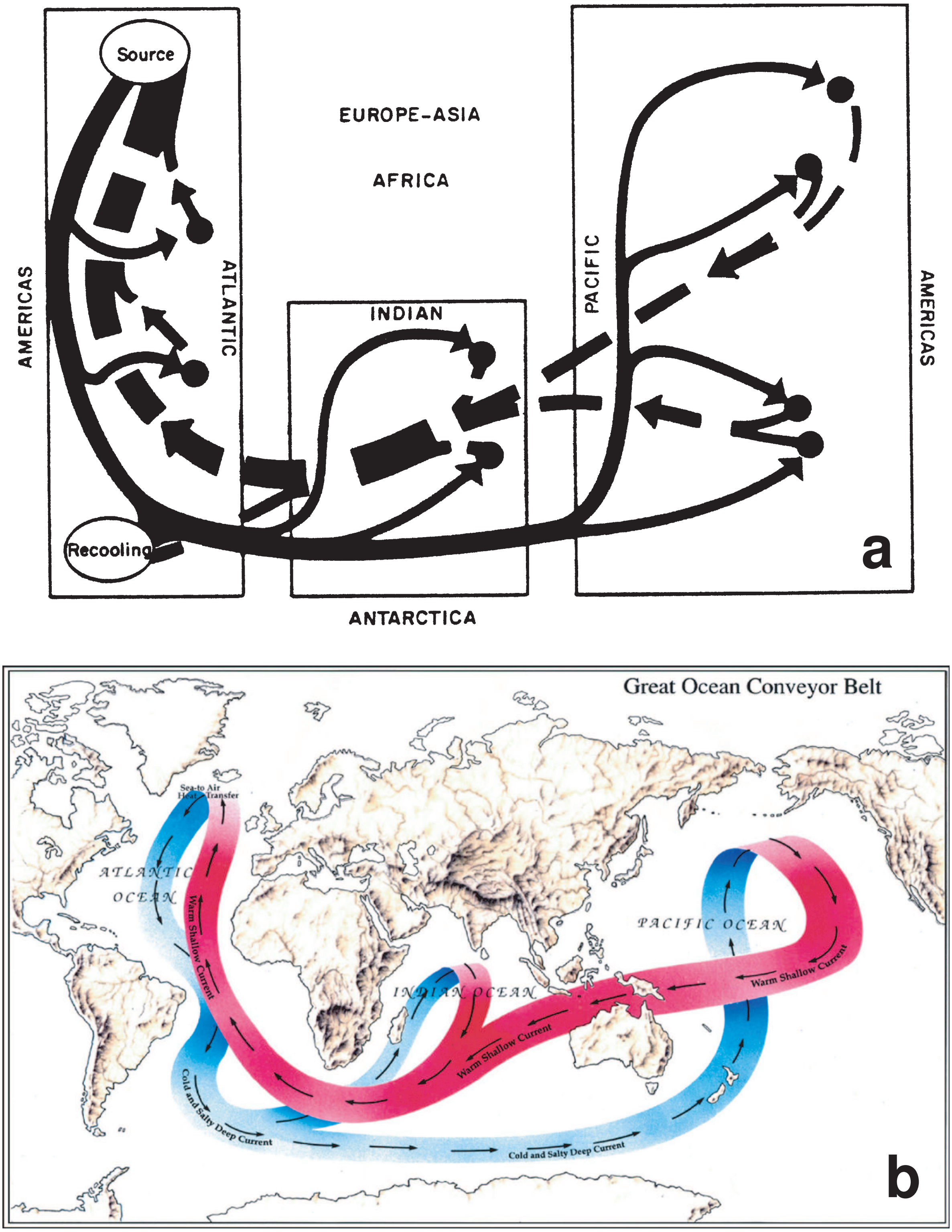
Source
EUROPE-ASIA
AFRICA
AMERICAS
ATLANTIC
INDIAN
PACIFIC
AMERICAS
Recooling
a
ANTARCTICA
Great Ocean Conveyor Belt
Sea-to Air Heat Transfer
ATLANTIC OCEAN
Warm Shallow Current
INDIAN OCEAN
PACIFIC OCEAN
Warm Shallow Current
Warm Shallow Current
Cold and Salty Deep Current
Cold and Salty Deep Current
b

Figure 1.2: Two representations of the Global Ocean Conveyor. From (a) Broecker and Peng (1982) and (b) Broecker (1987, by Joe Le Monnier, *Natural History Magazine*).

physical model thus implies a widespread communication between the deep and the near-surface ocean, such that surface primary productivity can be supported by a nutrient transfer directed vertically everywhere in the ocean, with nutrients being supplied by the diffusive–advective balance of upwelling and turbulent mixing that maintains the oceanic thermocline. This concept is an important component of the "Global Ocean Conveyor Belt" (GOCB; Broecker and Peng, 1982; Broecker, 1987, 1991). The GOCB, represented schematically in Figs. 1.2 and 1.3a, is a conceptual model that aims to explain the fact that oceanic deepwaters become increasingly nutrient-rich from the North Atlantic to the North Pacific Ocean. In accordance with Stommel and Arons (1960), this model assumes that some of the deepwater formed in the North Atlantic is continually lost to upwelling along the deep circulation path. However, since upwelled waters are exposed to biological activity at the surface, their nutrients are stripped out and re-exported to depth along their surface transit to the North Atlantic. This constant export flux of nutrients, together with the directed transport towards the North Pacific, progressively enriches deepwaters in nutrients (Fig. 1.3a). The GOCB paradigm thus interprets deep interbasin nutrient gradients as a dynamic equilibrium between the advective transport of nutrient-poor North Atlantic waters towards the North Pacific and a lateral diffusive mixing flux that, due to the concentration gradient, is directed towards the North Atlantic (Broecker and Peng, 1982). The explanatory potential of this simple concept, together with the powerful image of the conveyor belt (Fig. 1.2b), resulted in it becoming the dominant paradigm in ocean biogeochemistry for almost three decades. However, the GOCB relegates a vital feature of the abyssal ocean to a minor role: the formation of Antarctic Bottom Water (AABW) in the Southern Ocean is conceptualised simply as a "recooling" (Fig. 1.2a) of North Atlantic Deep Water (NADW), even though this water mass possesses very different biogeochemical properties to that of NADW, such that its spreading in the abyssal ocean strongly influences biogeochemical tracer fields at depth (Broecker, 1974, 1979; Broecker et al., 1985, 1991). More fundamentally, numerous observations were at odds with the uniform upwelling envisaged by Stommel and Arons (1960), and thus with the physical basis for the GOCB. Worthington (1977) highlighted the fact that the Si-depleted upper waters leaving the Pacific for the North Atlantic (Fig. 1.2) could not be fed by the upwelling of Si-rich Pacific deepwaters unless vast amounts of opal sediment were deposited in the Pacific, contrary to observations. In addition, a diffusive thermocline *sensu* Robinson and Stommel (1959) requires strong turbulent mixing across density surfaces in the thermocline, i.e. a large value of diapycnal diffusivity κ_v. Tracer studies began to indicate that there was little observational support for strong diapycnal mixing: Rooth and Östlund (1972) drew upon the distribution of tritium in the subtropical North Atlantic thermocline to argue that diapycnal mixing is minor compared to lateral exchange processes associated with the formation of thermocline watermasses (see also Fine et al., 1981), a concept suggested by Welander (1959) that was formalised by the ventilated thermocline theory of Luyten et al. (1983). In the early

1990s, additional observational support for low diapycnal mixing in the open ocean thermocline came from deliberate conservative tracer release experiments (e.g. Ledwell et al., 1993, 1998; Law et al., 2001) and direct measurements of ocean microstructure (e.g. Toole et al., 1994; Polzin et al., 1995). These studies demonstrated that, contrary to the assumption of Stommel and Arons (1960), turbulent diapycnal mixing in the open ocean thermocline is an order of magnitude too small to support the observed magnitude of dense-to-light water transformation associated with the MOC. Thus, an alternative means of dense-to-light water transformation must exist.

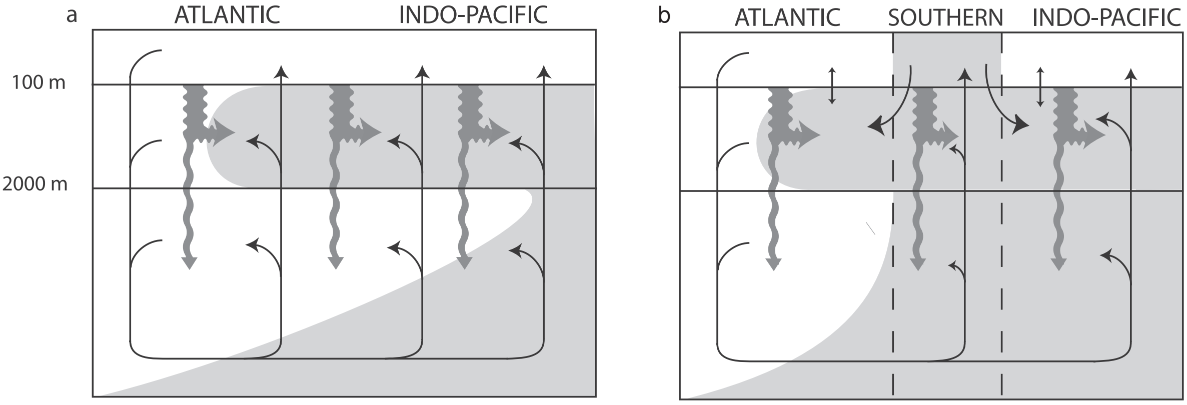

Figure 1.3: Conceptual models of the controls on oceanic nutrient distributions from Sarmiento et al. (2007). Panel *a* is a representation of Broecker and Peng's (1982) GOCB, while panel *b* represents the model presented by Sarmiento et al. (2004a, 2007). See text for details.

1.1.2 Southern Ocean winds and a new biogeochemical paradigm

An alternative mechanism of upwelling ocean deepwaters was provided by Toggweiler and Samuels (1993a; 1993b), based on their analysis of the Pacific radiocarbon (Δ^{14}C) distribution. They showed that numerical ocean models of the time, which upwelled deepwaters into the low-latitude thermocline, produced a Δ^{14}C distribution that is inconsistent with observations. The most realistic Δ^{14}C distribution was produced by a model configuration where Pacific deepwaters were returned to the Southern Ocean at mid-depth, rather than upwelling to the surface. Toggweiler and Samuels (1993a; 1993b) proposed that most deepwater upwelling occurs in the Southern Ocean, driven ultimately by the divergent Ekman transport produced by the strong westerly winds that encircle Antarctica. This view was later summarised in a schematic diagram by Toggweiler et al. (2006), shown in Fig. 1.4. The waters upwelled to the surface are transported to the north and south in the surface Southern Ocean by Ekman transport. In the far south, the upwelled waters experience buoyancy loss along the Antarctic shelf and sink to ultimately form Antarctic Bottom Water. The upwelled waters that

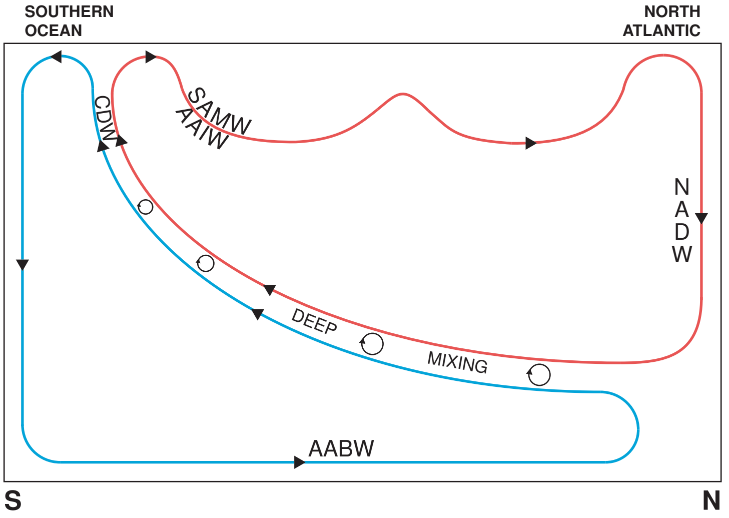

Figure 1.4: Toggweiler et al.'s (2006) cartoon representation of the ocean circulation, separated into two "loops" that upwell to the surface in the Southern Ocean.

are transported northward gain heat and freshwater, which decreases their density, such that, when subducted, they enter the interior as intermediate or mode waters, as illustrated in Figure 1.4.

As can be drawn from Fig. 1.4, this mechanism of deepwater upwelling implies a radically different transport of dissolved nutrients through the ocean from that envisaged by Broecker and Peng (1982). In such a regime, nutrients in the oceanic thermocline are not replenished directly from the deep ocean, but are rather heaved upwards in the Southern Ocean and supplied to the thermocline via a more circuitous route through the surface Southern Ocean, where they are exposed to biological activity. This route means that biological utilisation of nutrients in the surface Southern Ocean plays an important role in determining the supply of nutrients to the rest of the surface ocean, with consequences for the magnitude of primary productivity that can be supported, as well as its ecological composition. Sarmiento et al. (2004a) provided strong support for this mode of nutrient transport by analysing the oceanic distribution of a novel tracer, Si*, which they defined as the difference between the concentrations of silicon, Si, and nitrate, NO_3, in a water parcel[2]. Sarmiento et al. (2004a) showed that the unique negative Si* signature of Subantarctic Mode Water (SAMW, Fig. 1.4), which documents a deficit in Si relative to NO_3, is transmitted to the oceanic thermocline everywhere except in the North Pacific. Sarmiento et al. (2007) argued that this is due to the exceptionally high opal production in the Southern Ocean, which shunts Si (and, to a smaller degree, other macronutrients) from the surface to the deep Southern Ocean (i.e. from the red to the blue loops of Fig. 1.4), thereby trapping Si within the Southern Ocean. Their conceptual model, which emphasises the importance of localised upwelling in the Southern Ocean (and, to some extent, in the North Pacific) is able to

---

[2] i.e., $Si^* = Si - NO_3$.

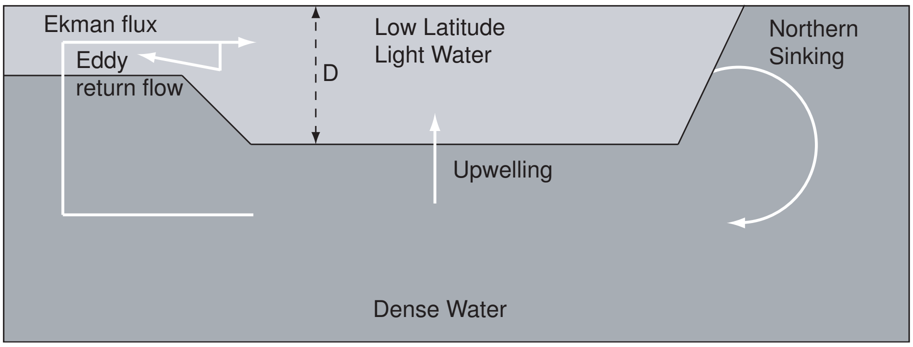

Figure 1.5: A representation of the key features of the analytical model of Gnanadesikan (1999b). *D* is the depth of the oceanic pycnocline that separates light upper ocean waters from dense abyssal waters. See text for details.

explain the observed subtle variations in the relative enrichment of Si and NO_3 in the deep ocean from the simple relationship expected based on the Global Ocean Conveyor Belt paradigm (Fig. 1.3a Broecker and Peng, 1982).

1.1.3 The ocean's dynamic balance: a simple model

The discussion above has described two contrasting conceptual models of how nutrients are transported through the ocean. These two models differ because the physical paradigms they are based upon assume different driving mechanisms of the MOC: the classical model of Broecker and Peng (1982) relies largely on uniform upwelling of deepwaters to the surface produced by downward diapycnal mixing of heat, whilst the revised model of Sarmiento et al. (2004a, 2007) restricts deep upwelling largely to the Southern Ocean, where it is directly driven by winds. In actual fact, considering the energy required to drive the overturning circulation, it appears likely that both wind-driven upwelling and diapycnal mixing contribute to the MOC (Wunsch and Ferrari, 2004; Kuhlbrodt et al., 2007). Thus, in order to understand how the ocean circulation transport nutrients, supports biological activity in the surface, and interacts with it to produce the observed biogeochemical tracer fields, we require a framework that considers both these driving mechanisms. Such a framework is supplied by the simple analytical model of Gnanadesikan (1999b).

As shown in Fig. 1.5, Gnanadesikan's (1999b) model interprets the depth *D* of the oceanic pycnocline, which separates the light waters of the upper ocean from the dense waters of the deep, as a function of a few key processes within the ocean: the formation of deepwaters in the North Atlantic, the wind-driven upwelling of deepwaters and their northward Ekman transport in the Southern Ocean, the southward eddy-induced advection of light waters, and low-latitude deepwater upwelling. Waters that sink in the North Atlantic can return to the surface by the two pathways discussed in Sections 1.1.1 and 1.1.2 (Fig. 1.5). Firstly, diapycnal mixing within the thermocline results in a downward heat flux, which lightens the dense waters and produces an upwelling flux through the thermocline (i.e. following Robinson and Stommel (1959)). Secondly, the wind stress acting on the surface Southern Ocean produces a surface Ekman transport divergence that drives the upwelling of deepwaters, which are converted to lighter waters at the surface (i.e., following Toggweiler and Samuels (1993b)). Gnanadesikan (1999b) showed that the partitioning of deepwater upwelling between these two pathways depends on the importance of both diapycnal mixing and the advective ("bolus") effects of eddies, represented by the diapycnal and isopycnal eddy diffusivities κ_v and A_I respectively. When κ_v and A_I are negligible, both low-latitude upwelling and the eddy return flow are minimal (Fig. 1.5), such that deep upwelling is driven by the Ekman transport in the surface Southern Ocean, as proposed by Toggweiler and Samuels (1993b; 1995; 1998). If, on the other hand, A_I is large enough that the southward advective eddy transport in the Southern Ocean compensates the northward Ekman transport, most upwelling of deepwater takes place at low latitudes (Stommel, 1958; Stommel and Arons, 1960). This simultaneously requires a large κ_v in the pycnocline, in order to maintain the observed depth of the oceanic pycnocline in the face of a large upwelling flux.

This simple model thus makes an important point: the pathways by which dissolved nutrients in dense waters of the deep ocean return to the surface ocean to support primary productivity depend on the vigourousness of turbulent mixing across and along density surfaces (κ_v and A_I). There is no consensus on the relevant values of these parameters for the real ocean (Holloway, 1986; Olbers and Wenzel, 1989; Ledwell et al., 1998; Munk and Wunsch, 1998; Toggweiler and Samuels, 1998), which results in uncertainties in the main pathways of the MOC and associated nutrient transport. As mentioned in Section 1.1.1, tracer release experiments and microstructure measurements find low values of κ_v ($\mathcal{O}(10^{-5}$ m^2/s)) in the pelagic thermocline, a value that is small enough to require significant wind-driven upwelling in the Southern Ocean. However, Munk and Wunsch (1998) argue on the basis of the abyssal stratification that basin-average diapycnal diffusivities are considerably larger ($\mathcal{O}(10^{-4}$ m^2/s)) due to strong boundary mixing (e.g. Polzin et al., 1997). Low values of diapycnal diffusivity are supported both by model sensitivity studies constrained by observations of export production and biogeochemical tracer distributions (Gnanadesikan and Toggweiler, 1999; Gnanadesikan et al., 2002, 2004; Schmittner et al., 2009), and by observations of the thermocline Δ^{14}C distribution (Toggweiler et al., 1991), whilst the distribution of the biogeochemical tracer Si* provides strong support for a Southern Ocean source of nutrients to the thermocline (Sarmiento et al., 2004a). However, other syntheses of observational hydrographic data (Talley et al., 2003; Talley, 2008) would appear to support a diapycnal diffusivity of $\mathcal{O}(10^{-4}$ m^2/s). A recent modelling study took into account the uncertainty in upwelling pathways implied by these various studies (Palter et al., 2010), and estimated that nutrients supplied from the Southern Ocean via SAMW support anywhere between 33% and 75% of low-latitude primary productivity.

To sum up, whilst considerable recent advances have been made and novel ideas have been proposed within the last decade that have provided a new view of the cycling of nutrients within the ocean, significant uncertainties regarding the pathways of oceanic nutrient transport remain that are intimately linked to our incomplete understanding of the dynamics of the meridional overturning circulation.

Table 1.1: Fluxes associated with the marine Si cycle, as presented by Tréguer et al. (1995).

Flux source	**Tmol Si yr^{-1}**
Inputs	
Riverine	5.0±1.1
Aeolian	0.5±0.5
Seafloor weathering	0.4±0.3
Hydrothermal	0.2±0.1
Total inputs	6.1±2.0
Outputs	
Coastal	1.2±0.7
Abyssal	5.9±1.1
Total outputs	7.1±1.8
Biological fluxes	
Opal production	240±40
Opal export	120±20
Ratio internal cycling:inputs	23–53

1.2 The marine Si cycle

The discussion in Section 1.1 has focused on large-scale interrelationships that apply to all dissolved nutrients, but also highlighted the fact that Si behaves differently from other oceanic macronutrients (Section 1.1.2). In the following, I briefly introduce the marine Si cycle and, without attempting an exhaustive review of the literature, discuss some key features of its marine cycle that lead to its singular behaviour and coupling to the carbon cycle in the ocean.

1.2.1 Fundamentals

The global ocean contains about 10^{17} moles of dissolved Si in the form of monomeric orthsilicic acid ($Si(OH)_4$; Iler, 1979; Stumm and Morgan, 1981), corresponding to an average concentration of 71 µM (Tréguer et al., 1995). Inputs of Si to the ocean, which are primarily riverine (see Table 1.1), contribute about 6×10^{12} mol Si per year, yielding a residence time of Si in the ocean of about 15,000 years (Tréguer et al., 1995; DeMaster, 2002, 2009). In the absence of biological cycling, Si concentrations would thus be essentially constant throughout the ocean, varying only with seawater salinity. In fact, they range from <1 µM in the low-latitude surface to >170 µM in the mid-depth North

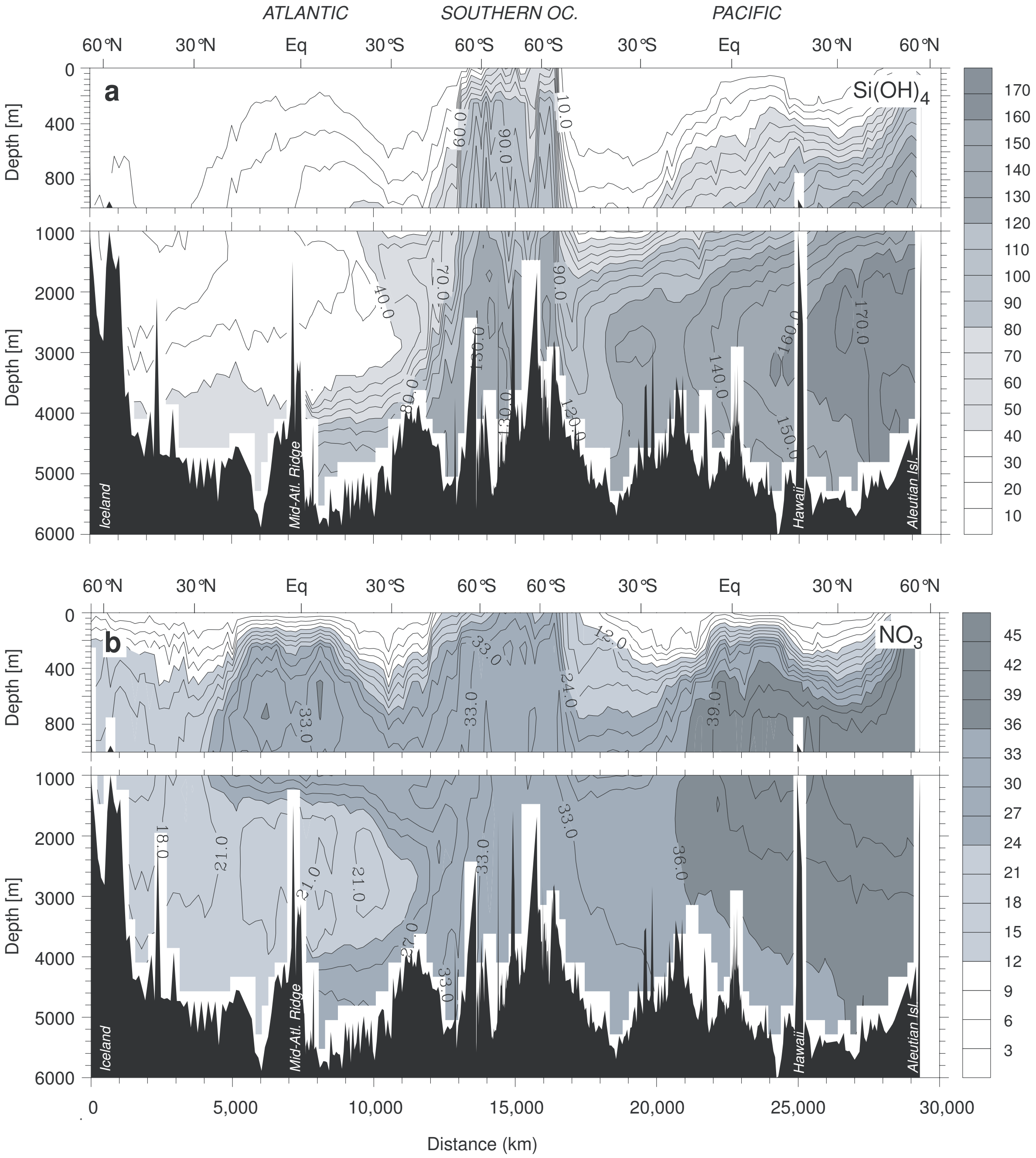

Figure 1.6: Global depth sections of (*a*) Si concentration and (*b*) NO_3 concentration. The sections begin in the North Atlantic on the left, reach the Southern Ocean in the centre, and continue towards the North Pacific on the right. Silicon concentrations display sharp lateral gradients around the Southern Ocean, and are low in the upper 1 km of the water column, increasing only slowly with depth, unlike NO_3 concentrations. Marked similarities also exist between the two distributions, such as the low-nutrient tongue of North Atlantic Deep Water extending southwards from the North Atlantic at around 3000 m depth, and the higher nutrients extending northwards at intermediate Atlantic depths, associated with Antarctic Intermediate Water. From Sarmiento and Gruber (2006), using data from the CLIVAR and Carbon Hydrographic Data Office (`http://cchdo.ucsd.edu/`).

Pacific (Garcia et al., 2010b), as is to be expected for an element that is cycled vigorously through the ocean[3] (Section 1.1.2). The biogenic flux of particulate Si out of the surface ocean is estimated to be 120×10^{12} mol/yr (Nelson et al., 1995; Tréguer et al., 1995), such that the fluxes associated with the biological cycling of Si within the ocean are 20 times larger than the fluxes of Si into the ocean. Figure 1.6a shows the distribution of dissolved Si in the ocean in a section from the North Atlantic, through the Southern Ocean, to the North Pacific. A comparison with the NO_3 distribution in Fig. 1.6b reveals both similarities and clear differences, highlighting the fact that Si does not behave identically to other macronutrients. The two distributions are most similar at the large scale, exhibiting a tongue of low concentrations extending throughout the mid-depth deep Atlantic, a shoaling of isolines in the Southern Ocean, and a mid-depth maximum in the deep Pacific. These are features that are controlled by the circulation processes discussed in Section 1.1 (see also Levitus et al., 1993). However, in other aspects the distributions are remarkably different: unlike the rapid increase of NO_3 with depth away from the surface, Si concentrations remain relatively low throughout the upper 1 km of the water column, except in the equatorial and northern Pacific. Conversely, Si concentrations show a much sharper lateral gradient around the Southern Ocean, especially within the upper ocean, but also extending to depth. There is, in fact, a general enhancement in the lateral or interbasin concentration gradient of Si relative to NO_3 in the deep ocean: Si concentrations increase around 6.5 times more strongly than NO_3 concentrations between the North Atlantic and the North Pacific, with a significant local Si maximum in the Southern Ocean. Thus while the similarities between the two nutrient distributions can be related to the large-scale circulation, the observed differences must have their ultimate origin in biogeochemical processes that differentiate between Si and other nutrients. These are discussed in the following.

1.2.2 The relationship between diatom ecology and Si and C biogeochemistry

In the ocean, Si is utilised almost exclusively[4] by a single group of photosynthetic phytoplankton, diatoms (Bacillariophyceae), which take up silicic acid to form their opaline cell walls, called frustules (Del Amo and Brzezinski, 1999). The metabolic and morphological response of diatoms to environmental stress factors results in increased silicification, such that diatoms that are stressed – e.g. by grazing pressure, low light or paucity of micronutrients such as iron – have higher ratios of Si to organic tissue (e.g. Brzezinski, 1985; Takeda, 1998; Claquin et al., 2002; Marchetti and Harrison, 2007; Pondaven et al., 2007; Marchetti and Cassar, 2009).

---

[3] These concentrations additionally show that the ocean is strongly undersaturated with respect to opal over its entire depth, given an opal solubility of 900–1500 µM (Sarmiento and Gruber, 2006).

[4] Silicon is also utilised by other planktonic organisms such as dinoflagellates and radiolaria, and by benthic organisms, such as siliceous sponges. However, these can be neglected to first order, due to the dominant influence of diatom uptake and export on oceanic Si fluxes (Nelson et al., 1995; Tréguer et al., 1995; Ragueneau et al., 2000; DeMaster, 2009).

The ecological strategy of diatoms plays an important role in determining their importance for oceanic carbon export and for the oceanic distribution of Si. In nutrient-replete conditions, diatoms have a strong competitive advantage and tend to dominate the phytoplankton assemblage (Ragueneau et al., 2000, and references therein). This is likely the combined result of the reduced energetic requirement of producing their silica frustules compared to an organic cell wall (Raven, 1983), reduced grazing mortality due to their relatively large cell size and the protection afforded by their frustule (Smetacek, 1999; Pondaven et al., 2007), and their ability to rapidly take up and store nutrients within their cell vacuoles, depriving competing organisms of nutrients while allowing their own rapid growth (Raven, 1983; Falkowski et al., 2003). Diatoms thus tend to flourish in dynamic physical settings that provide turbulent pulses of nutrients (Margalef, 1978; Tozzi et al., 2004; Armbrust, 2009), whilst their large cell size (and thus low surface area to volume ratio) is a disadvantage in nutrient-depleted waters. Thus, nutrient-replete biomes such as coastal upwelling zones and regions of upwelling in the open ocean, such as the Southern Ocean, select for diatoms (Follows et al., 2007; Dutkiewicz et al., 2009). In such regions, diatom populations follow strongly seasonal bloom–dump patterns, with rapid growth followed by population collapse, aggregation and sinking once the bloom has depleted surface nutrients (e.g. Smetacek, 1985).

This combination of the restriction of diatoms to regions of strong upward water flux and their tendency to sink rapidly out of the surface upon death results in a “trapping” of dissolved Si within regions of upwelling such as the Southern Ocean[5] (Fig. 1.6). It is also an important factor in determining the important role that diatoms play in the soft-tissue pump of carbon to the deep sea (Smetacek, 1999; Dugdale and Wilkerson, 2001; Dunne et al., 2005; Jin et al., 2006), although the relationship between diatom production and carbon export is not simple. In his review of the oceanic export efficiency of carbon, Buesseler (1998) found that efficient carbon export from the surface ocean is associated with blooms formed by diatom-dominated ecosystems. This is consistent with the suggestions by Dugdale et al. (1995) and Dugdale and Wilkerson (1998) that new and export production are regulated by the supply of Si that supports diatom production in the equatorial Pacific.

Ragueneau et al. (2000) documented that although Si:C ratios of export vary considerably between ocean regions, a systematic correlation exists between the export fluxes of Si and C within ocean regions, with a systematic increase in Si:C ratios from the Si-poor Atlantic to the Si-rich Southern Ocean and North Pacific (Fig. 1.7). This led them to suggest an extension of the hypothesis of Dugdale et al. (1995) to the entire ocean, i.e. that the supply of Si regulates C export via its control on diatom production. Similarly to Goldman (1988), Buesseler (1998) and Smetacek et al. (2004), they suggested that, amongst other factors, the nature of the food web structure associated with diatom-dominated

---

[5] In the Southern Ocean, this effect is amplified by the fact that diatoms are heavily silicified due iron- and light-limitiation (e.g. Chisholm and Morel, 1991).

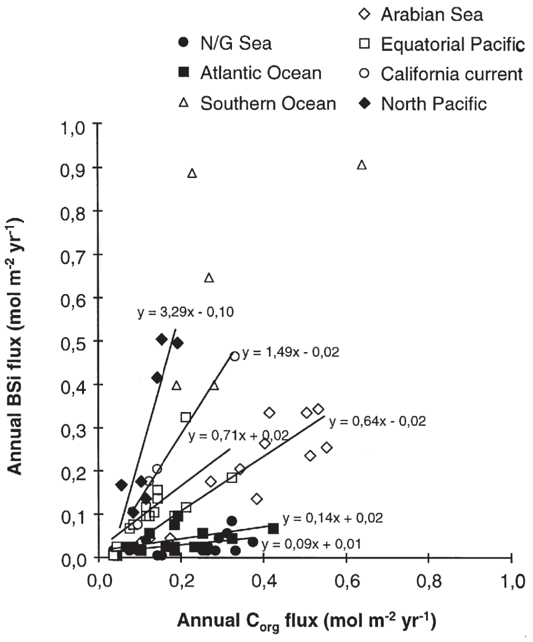

Figure 1.7: Relationship between Si and C export fluxes in a wide range of ocean regions. Note the low Si:C ratios of export in the Atlantic Ocean, and high ratios in the Southern Ocean and North Pacific. From Ragueneau et al. (2000).

ecosystems may play a significant role in governing this connection. As exported particulate matter sinks, its Si:C ratio increases in the mesopelagic (Ragueneau et al., 2002), producing a decoupling between Si and C that is possibly related to the mesopelagic foodweb that feeds on sinking organic matter (Ragueneau et al., 2006). This decoupling of Si and C appears to be at least partially counteracted by the tendency of diatoms to form rapidly-sinking aggregates that efficiently transport opal and organic matter to depth (Ragueneau et al., 2006; Loucaides et al., 2011).

Thus, the above brief discussion highlights the fact that the singularity of the marine Si cycle, and its coupling to that of carbon, is at least partially the result of the peculiarities of the ecological specialisation of diatoms: their opportunistic bloom–dump behaviour (Smetacek, 1985; Buesseler, 1998; Ragueneau et al., 2006), their tendency to form aggregates that sink rapidly through the water column (Alldredge and Gotschalk, 1989; Nelson et al., 1995), their biomineralisation response to grazing (Pondaven et al., 2007) and growth-rate limitation (Martin-Jézéquel et al., 2000, and references therein), and their large cell size, which favours their packaging within the rapidly sinking-faecal pellets of larger heterotrophs (Ragueneau et al., 2000). This strong export tendency (Dugdale et al.'s (1995) "silicate pump") combines with the physical circulation processes discussed in Section 1.1 to produce the observed oceanic Si distribution; in this thesis, I attempt to tease apart these two influences by examining the stable isotope composition of dissolved Si in the sea.

1.3 Silicon isotope geochemistry

Silicon, a tetravalent metalloid with atomic number 14, is the second-most abundant element in Earth's crust after oxygen. It possesses three stable, non-radiogenic isotopes with nominal atomic masses 28, 29 and 30. These isotopes are present in terrestrial materials in the approximate abundances 92.2%, 4.7% and 3.1% respectively (Rosman and Taylor, 1998).

The differences in isotope mass result in systematic differences in their behaviour during chemical reactions and certain physical processes[6] (Bigeleisen and Mayer, 1947; Urey, 1947; Bigeleisen, 1949a; Bigeleisen, 1955, reviewed in Young et al., 2002), a process commonly known as mass-dependent isotope fractionation. Such isotope fractionation may be the result of mass-dependent differences in the vibrational energy of bonds formed by the isotopes of an element (equilibrium isotope fractionation) or be due to differences in their rates of reaction (kinetic isotope fractionation). The mass-dependent isotope fractionation associated with a chemical reaction $A \rightleftharpoons B$ or $A \rightarrow B$ can be characterised by its fractionation factor α, defined as $\alpha = R_B/R_A$, where R_A and R_B are the isotope ratios in the phase A and B, respectively. Since fractionation factors are generally numbers very close to unity, they are often expressed as the isotope effect ε (in ‰), given by the approximate relationships $\varepsilon \approx 1000 \ln \alpha$ or $\varepsilon \approx (\alpha - 1) \times 1000$.

Due to mass-dependent fractionation processes, the isotope composition of Si varies in different materials on Earth (Reynolds and Verhoogen, 1953; Douthitt, 1982; Ding et al., 1996; De La Rocha et al., 1997, 2000; Opfergelt et al., 2008; Georg et al., 2009) as well as in the Solar System (Epstein and Taylor, 1970; Georg et al., 2007; Fitoussi et al., 2009; Armytage et al., 2011). These variations are usually expressed in the delta notation as δ^{30}Si, which is the deviation of the ^{30}Si/^{28}Si ratio in a material from that of the standard reference material NBS28 (NIST RM8546), expressed in parts per thousand:

$$\delta^{30}\text{Si (in ‰)} = \left(\frac{\left(\frac{^{30}\text{Si}}{^{28}\text{Si}}\right)_{\text{sample}}}{\left(\frac{^{30}\text{Si}}{^{28}\text{Si}}\right)_{\text{NBS 28}}} - 1 \right) \times 1000$$

As can be drawn from this definition, a positive δ^{30}Si value indicates that a given material is enriched in the higher-mass isotopes relative to the reference, whilst negative δ^{30}Si values indicate a depletion. The δ^{30}Si value of the Bulk Silicate Earth is estimated to be -0.29 ± 0.08‰ (Fitoussi et al., 2009; Savage et al., 2010). Terrestrial δ^{30}Si values in nature range from about -6‰ to +3‰ (Fig. 1.8), with the lowest values observed in silcretes (Basile-Doelsch et al., 2005) and the highest in dissolved Si in rivers and surface ocean waters (Ding et al., 2004; Reynolds et al., 2006a).

---

[6] such as diffusion (Criss, 1999).

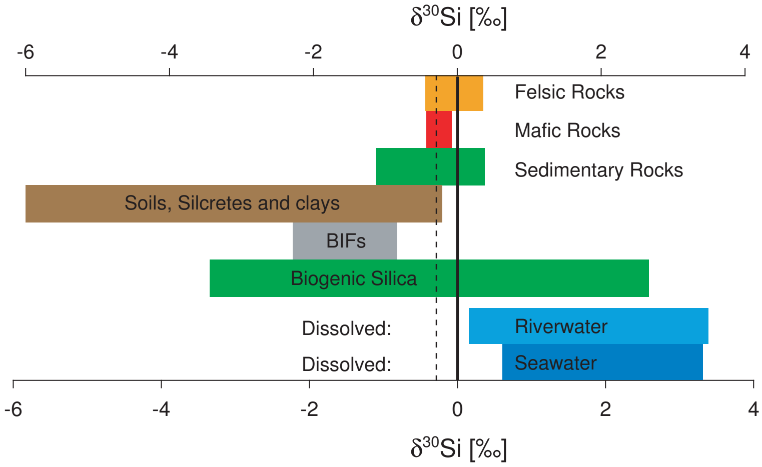

Figure 1.8: A summary figure indicating the observed range of δ^{30}Si values in terrestrial materials (from Reynolds, 2011).

1.3.1 Oceanic Si isotope systematics

In this section, I introduce the processes relevant to the marine Si cycle that produce mass-dependent Si isotope fractionation, and summarise observations of δ^{30}Si values of seawater and key sources of Si to the sea published in the literature up to the commencement of this thesis in 2007.

Fractionating processes

There are three processes that are known to fractionate Si isotopes in the ocean. The uptake of Si by diatoms during the formation of their frustules is associated with an isotope effect ε of approximately -1.1‰ (De La Rocha et al., 1997; Milligan et al., 2004; Varela et al., 2004), such that diatom frustules possess a lower δ^{30}Si value than the seawater they grow in. Based on the absence of a detectable dependence on temperature (12° C–22° C; De La Rocha et al., 2000) and growth rate (Milligan et al., 2004), it has been suggested that this is the result of a kinetic isotope effect related to transport of silicon across the cell membrane (Milligan et al., 2004). The isotope effect associated with the dissolution of diatom frustules in seawater has been estimated at -0.55‰ independent of temperature (3° C–22° C) and dissolution rate (Demarest et al., 2009), whilst Si uptake and spicule formation by benthic siliceous sponges is associated with a large and variable isotope effect of up to -4‰ (De La Rocha, 2003; Wille et al., 2010). Of these three processes, it is the fractionation of Si isotopes during Si uptake by diatoms that is the most important control on seawater δ^{30}Si values, as the following brief history of δ^{30}Si observations will show.

Observations of seawater δ^{30}Si

The discovery that the fractionation of Si isotopes by diatoms appears to be independent of both species and temperature (De La Rocha et al., 1997) awakened hopes that the record of δ^{30}Si values in diatom opal sediment could be used to reconstruct the past nutrient state of the surface ocean (De La Rocha et al., 1998, cf. Altabet and François, 1994). Refining the use of this sedimentary geochemical record required a better understanding of the Si isotope system in the oceans. Towards this goal, De La Rocha et al. (2000) attempted to characterise the δ^{30}Si values of Si sources to the ocean, as well as the δ^{30}Si distribution within the ocean. They analysed Si isotope compositions of a number of major & minor rivers as well as hydrothermal fluids from the East Pacific Rise, and published the first seawater δ^{30}Si data from a number of sites in the global ocean (Fig. 1.9). De La Rocha et al.'s (2000) riverine data indicated that dissolved Si in rivers possesses a higher δ^{30}Si value (+0.4‰ to +1.2‰, averaging +0.8 ± 0.3‰)[7] than igneous silicate materials (-0.3‰), the ultimate source of riverine Si. Hydrothermal fluids ($n = 2$), however, are similar to igneous silicates (-0.2‰ to -0.4‰). On the basis of this data and the source partitioning of Tréguer et al. (1995), De La Rocha et al. (2000) estimated a δ^{30}Si value for Si input to the ocean of +0.6‰.

The seawater δ^{30}Si analyses of De La Rocha et al. (2000) were restricted to waters with Si concentrations, [Si], above 10 µM, which excludes most near-surface and surface waters. Nonetheless, they were able to show that seawater δ^{30}Si values increase towards the surface, up to values of +1.7‰ in the euphotic zone of the Californian coastal upwelling. They attributed this increase to Si isotope fractionation by diatoms, which preferentially incorporate the light isotopes of Si into their frustules and export this low δ^{30}Si signature to depth, leaving seawater enriched in the heavier isotopes. In addition, De La Rocha et al. (2000) were able to show that δ^{30}Si values in deep seawater decrease from values of about +1.3‰ in the North Atlantic to about +0.9‰ in the North Pacific, which they interpreted to be related to the cumulative effect of opal dissolution along the "ocean conveyor" (Broecker, 1987).

Strong support for a major control of diatom Si uptake on seawater δ^{30}Si values came from Varela et al. (2004), who studied the latitudinal variation of δ^{30}Si values in the surface Southern Ocean (70°S to 50°S along 170°W; Fig 1.9). They showed that the strong [Si] gradients across Southern Ocean fronts, associated with the enhanced drawdown of Si by heavily silicified diatoms (Brzezinski et al., 2003), are associated with significant gradients in the δ^{30}Si value of dissolved Si. Values of δ^{30}Si increased systematically with decrease in [Si], from +1.6‰ south of the Southern ACC Front to +3.1‰ just south of the Antarctic Polar Front. The δ^{30}Si systematics of these surface waters, together with analyses of simultaneously sampled biogenic silica, confirmed that natural diatom assemblages

---

[7] Georg et al. (2006a) arrived at a similar average δ^{30}Si value of +0.8±0.2‰ ($1\sigma_{SD}$) for four rivers in the Swiss Alps, although Ding et al. (2004) found δ^{30}Si values as high as +3.4‰ in the Chang Jiang.

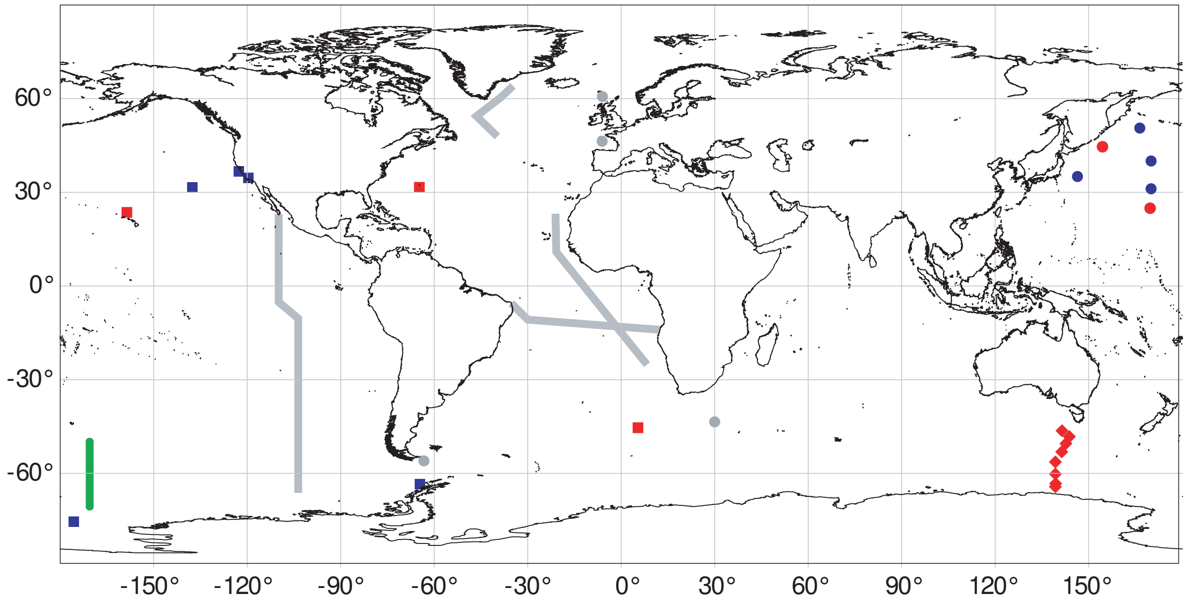

Figure 1.9: Distribution of published seawater δ^{30}Si data in 2007, along with schematic representations (grey lines and dots) of the cruise tracks and stations from which samples were obtained for this thesis. Published data are from De La Rocha et al. (2000, squares), Varela et al. (2004, green line), Cardinal et al. (2005, diamonds) and Reynolds et al. (2006a, circles) and are colour-coded according to whether samples were collected over the entire water column (red), the mesopelagic (blue) or the surface (green).

fractionate Si isotopes to a similar degree to that observed in the laboratory (De La Rocha et al., 1997).

Following the development of multicollector ICP-MS methods for δ^{30}Si analysis (De La Rocha, 2002; Cardinal et al., 2003) and the inclusion of a preconcentration step for low-[Si] samples (Cardinal et al., 2005), the first complete water column δ^{30}Si profiles (including surface-water samples with [Si] as low as 2 µM) were published by Cardinal et al. (2005), from a transect in the Southern Ocean south of Australia (65°S to 47°S at ~140°E; Fig 1.9). They showed that the deep Southern Ocean has an essentially invariant δ^{30}Si value of +1.2‰. As observed by Varela et al. (2004), Cardinal et al. (2005) documented an increase in surface δ^{30}Si values towards the north, but observed additional complexity in the Subantarctic Zone, which exhibited lower δ^{30}Si values at lower [Si] than further south. In addition, they documented a meridional δ^{30}Si gradient in the upper subsurface ocean, with higher δ^{30}Si values towards the north that they attributed to seasonal interaction with the mixed layer and the influence of opal dissolution.

Reynolds et al. (2006a) presented full depth profiles from the subarctic and subtropical North Pacific (150°–170°E; Fig 1.9). They found low δ^{30}Si values of around +0.6‰ similar to those documented by De La Rocha et al. (2000), associated with the very high Si concentrations of North Pacific Deep Water, and slightly higher values of +1.1‰ in more southerly abyssal waters of Southern Ocean origin. This value of +1.1‰ is identical within error to the constant value of +1.2‰ found by Cardinal et al. (2005) in the deep Southern Ocean. Reynolds et al. (2006a) thus argued that deepwater δ^{30}Si variability in the deep Pacific Ocean is controlled by large-scale water mass mixing of waters from the North Pacific with those of Southern Ocean origin.

These pioneering contributions have thus established that seawater δ^{30}Si values are variable and strongly controlled by isotope fractionation during diatom Si utilisation in the euphotic zone. The isotope effect of this utilisation in the field has been estimated, using simple models, to be similar to that observed in the laboratory. Furthermore, these studies have revealed that the deep ocean exhibits interbasin differences in δ^{30}Si, a finding that contrasts with the homogeneity of the stable nitrogen isotope composition of deep ocean nitrate, δ^{15}N–NO_3. Although the oceanic δ^{15}N–NO_3 system is more complex than that of δ^{30}Si (Sigman et al., 2009b), the two systems have some clear similarities, such as the production of an elevated δ-value in the euphotic zone by biological utilisation. More fundamentally, the fact that both elements are drawn down to low values over most of the surface ocean (Garcia et al., 2010b) places a strong mass-balance constraint on the isotopic composition of the particulate material exported from the surface[8], such that this flux should have little potential to influence the isotopic composition of the dissolved pool in deepwaters. In this context, little deepwater variability is expected for both isotope systems. Indeed, a global circulation model study that traced the fractionation of Si isotopes in the ocean (Wischmeyer et al., 2003) produced little interbasin deepwater δ^{30}Si variability (<0.05‰).

Thus, the unexpected presence of an interbasin deepwater gradient in δ^{30}Si indicates an incomplete understanding of the controls on the oceanic δ^{30}Si distribution. Identification of the origin of such large-scale variability, which represents a fundamental, unique feature of the δ^{30}Si tracer field, should provide key insights into the processes and pathways by which Si is cycled in the ocean. Furthermore, a better understanding of the controls on seawater δ^{30}Si is a vital prerequiste for the robust interpretation of diatom opal δ^{30}Si palæorecords, since these may record a conflated signal of changes in both the source of Si as well as the degree of Si utilisation. However, the early studies of the marine δ^{30}Si distribution were unable to provide a coherent picture of the origin of seawater δ^{30}Si variation at the global scale, with the interbasin δ^{30}Si gradient being variously ascribed to opal dissolution along the circulation path of deepwaters (De La Rocha et al., 2000) or the mixing of watermasses of different origins (Reynolds et al., 2006a). This thesis aims to improve our understanding of the relative importance of these processes, as detailed below.

---

[8] although this constraint is partially relaxed for δ^{15}N–NO_3 where N_2 fixation takes place.

1.4 Aims of this thesis

1.4.1 Strategic aims

The geographical distribution of seawater δ^{30}Si data published before the commencement of this thesis, shown in Figure 1.9, highlights the limited spatial coverage of the time. The Atlantic Ocean, typically the most thoroughly sampled ocean basin, was essentially unsampled. Thus, an important aim of this thesis was to expand the seawater δ^{30}Si database by sampling ocean regions that were severely underrepresented in the extant database. The distribution of expeditions from which samples were collected for this thesis (marked in Fig. 1.9) illustrates this strategy. Naturally, expanding the observational database is not an end in itself, but serves the purpose of enabling us to better characterise the oceanic δ^{30}Si distribution. An important feature of this distribution is the interbasin δ^{30}Si gradient in the ocean's deepwaters (see Section 1.3.1). Deepwater δ^{30}Si variability is small compared to the large δ^{30}Si variations in the upper ocean, which predicated the second important aim of this thesis: to produce high-precision δ^{30}Si data that would enable a robust characterisation of the δ^{30}Si distribution even in the deep – in other words, a strong focus on quality before quantity.

1.4.2 Scientific aims

The introduction to this thesis has highlighted the relevance of the marine Si cycle to the ocean's biological pump, which sequesters atmospheric CO_2 in the deep sea. It has also presented some key questions regarding the cycling of Si and other nutrients in the sea that remain inadequately answered, limiting our predictive power of the ocean's response to changed boundary conditions in the future (e.g. Schmittner et al., 2009) and the mechanisms by which it has altered atmospheric CO_2 levels in the past (e.g. Sigman et al., 2010). The distributions of dissolved biogeochemical tracers harbour vital information on ocean biogeochemistry that can be used to resolve such ambiguities (e.g. Najjar et al., 2007), especially since, by their inherently integrative nature, they compensate for the strong undersampling of the ocean that results from its vast size.

The discussion in Section 1.3.1 has shown that the δ^{30}Si value of Si in seawater traces the cycling of Si in the sea, and that its large-scale distribution exhibits unexpected features that must reflect a fundamental, and possibly underappreciated, characteristic of oceanic Si biogeochemistry. The oceanic δ^{30}Si distribution may thus deliver us a new, more detailed view of the oceanic biogeochemical cycle of Si, by providing an additional, direct and element-specific constraint on the processes and pathways that cycle Si in the ocean. Thus, this thesis aims to provide a better understanding of the dominant controls on the oceanic δ^{30}Si distribution, with a view to providing new insights into the transport and cycling of Si within the ocean. Specifically, I hope to address the following questions:

How do biological isotope fractionation and the physical circulation interact to produce the observed δ^{30}Si distribution? What does this reveal about the primary pathways of Si transport and the nature of Si cycling in the sea?

1.4.3 Outline

What follows is arranged in six chapters. Chapter 2 provides a brief overview of the sample preparation and analytical methods used to produce the δ^{30}Si data, along with an evaluation of the performance of these methods. In Chapter 3, I show that consideration of the nature of biogeochemical cycling, and the physical setting in which biological isotope fractionation takes place in the ocean, precludes the use of non-dimensional isotope distillation models to interpret marine stable isotope distributions. Chapter 4 deals with the δ^{30}Si distribution in the deep Atlantic Ocean from Denmark Strait (64° N) to Drake Passage (56° S), which documents a coherent meridional δ^{30}Si gradient related to the quasi-conservative mixing of Si from the two sources of deepwater to the Atlantic Ocean, North Atlantic Deep Water (NADW) and Antarctic Bottom Water (AABW). I show that this deep meridional δ^{30}Si gradient most likely owes its origin to the export of a high δ^{30}Si signature from the Southern Ocean in Antarctic Intermediate Water (AAIW) and Subantarctic Mode Water (SAMW). Chapter 5 is devoted to the distribution of δ^{30}Si values in the ventilated Atlantic thermocline; I relate the vertical gradient in thermocline δ^{30}Si values, observed to extend to potential densities of $\sigma_\theta = 27$, to the preformed component of Si, transported into the interior during the subduction of the water masses that ventilate the thermocline. In Chapter 6, I present δ^{30}Si data from the eastern South Pacific Ocean, which is a key location for the formation of AAIW and SAMW. I exploit the broad latitudinal sampling range, from the Antarctic Zone of the Southern Ocean to the equatorial Pacific, to trace how high δ^{30}Si values in the surface Southern Ocean are incorporated into AAIW and SAMW and exported to the low-latitude thermocline. Finally, Chapter 7 provides a brief synthesis of the data presented in this thesis, which allows the distillation of some fundamental insights regarding the controls on seawater δ^{30}Si values and the biogeochemical cycle of Si in the sea.

Chapter 2

Methods

The concentration of silicon in seawater, [Si], varies by more than two orders of magnitude (from <1 µM to ~180 µM), while the salt content of seawater varies only minimally around an average of ~0.5 M (primarily Na^+, Mg^{2+}, Cl^- and SO_4^{2-}). The resulting matrix-to-analyte mole ratios of 4×10^3 to 5×10^5 represent an analytical hurdle that must be overcome before Si isotope compositions can be measured by multicollector inductively-coupled plasma mass spectrometry (MC-ICPMS), which requires highly pure solutions of the analyte (Albarède and Beard, 2004). Here, this separation of Si from sea salt is achieved by a combination of two procedures: preconcentration of Si from seawater by adsorption to a precipitate, and chromatographic separation using a cation-exchange resin, following procedures developed previously at ETH Zurich (Georg et al., 2006b; Reynolds et al., 2006a). Some modifications were made to the existing procedures in order to best adapt them to the sample set on which this thesis is based: the diverse nature of the seawater samples included in a large-scale survey necessitates that the preconcentration procedure can assure reproducibly near-quantitative Si yields from both highly nutrient-depleted and nutrient-enriched seawater samples. In addition, in the interest of efficiency, an improvement in the sample throughput of the chromatographic separation is advantageous.

2.1 Preconcentration of Si from seawater

Reynolds et al. (2006a) applied a modification of the MAGIC (MAGnesium-Induced Coprecipitation) method of Karl and Tien (1992) to preconcentrate Si from seawater. This method relies on the adsorption of Si onto the surface of a brucite ($Mg(OH)_2$) precipitate. The formation of this precipitate is induced by the addition of a base (NaOH) to seawater, resulting in the spontaneous precipitation of seawater Mg as brucite above pH ~9.7. Subsequent centrifuging of the sample allows easy separation of silicon (in the precipitate) from a large proportion of the salt matrix (in the supernatant).

However, in contrast to phosphorus, for which the method was originally developed, the adsorption of silicon after a single coprecipitation step is not quantitative, with some 6–7% of Si remaining in the supernatant. This is undesirable, since the adsorption of silicon onto brucite is accompanied by isotope fractionation, such that non-quantitative yields will result in a systematic error in measured δ^{30}Si values. Reynolds et al. (2006a) solved this problem by using a two-step precipitation procedure to achieve quasi-quantitative yields of $>$97%. Based on this encouraging result, I attempted to improve Si yields to $\sim$100% and achieve this level of Si yield for all seawater sample types. This was accomplished by a systematic study of the behaviour of Si during the coprecipitation procedure. It was observed that the yield of the coprecipitation procedure is dependent on:

- **Seawater Si concentration**: The yield of the single-step precipitation decreases with increasing seawater [Si], from 95% at 30 µM to 90% at 100 µM.
- **Reaction time**: The silicon yield for a given base addition increases during agitation of the sample for $\sim$1 hr after formation of the precipitate (from 88% to 93% for a nutrient-rich seawater). For highly nutrient-rich samples, long reaction/settling times of $\sim$1 day were observed to further improve the yield.
- **Amount of Mg precipitated**: High Si yields (98–99%) are achievable in a short time with the single-step procedure if a large amount (40–60%) of seawater Mg is precipitated.

An optimum coprecipitation procedure is one that provides reproducible and high Si yields while concurrently minimising the associated Mg matrix. The two-step precipitation procedure was found to eliminate the dependency of Si yield on seawater [Si] and increase the overall yield of the procedure. When 10% of seawater Mg was precipitated in each of the two precipitation steps and long reaction/settling times ($\sim$1 day) were implemented, the procedure provided yields generally in excess of 99% independent of seawater type. This method is highly suitable for water samples with [Si] above $\sim$13 µM, but for more depleted samples the Mg:Si ratio becomes unacceptably high ($\gg$800). For seawaters with low [Si], I thus followed Reynolds et al. (2006a) in duplicating the preconcentration step: I used my improved-yield procedure to scavenge Si from a large volume of Si-poor seawater onto $Mg(OH)_2$, then dissolved this precipitate and added it to a small volume of the original (unprocessed) seawater sample, producing a high-Si (and high-Mg) seawater. Samples thus enriched have [Si] $>$13 µM and can be processed identically to other Si-rich samples. Use of this repeated precipitation necessitates very high Si yields, since two scavenging steps (and thus two possible fractionation steps) are implemented. Tests of the procedure, in which the same sample was subjected to the preconcentration procedures for both Si-rich and Si-poor samples, show that the $\sim$99% yields in each step are high enough to prevent any significant systematic error in measured δ^{30}Si values, as documented by a difference of 0.04$\pm$0.10‰ (propagated $2\sigma_{SEM}$, n = 12) in measured δ^{30}Si values.

At the end of the preconcentration procedure, the $Mg(OH)_2$ precipitate is dissolved in a small amount of 6 M HCl and the solution diluted with ultrapure water to 64 µM Si for further chromatographic separation of Si. At this point, the solutions contain 3–53 mM Mg as their main matrix. The matrix-to-analyte ratio has thus been reduced 100- to 600-fold during the preconcentration procedure, which allows the use of relatively small chromatographic columns for the subsequent purification of Si.

2.2 Chromatographic purification of Si

Georg et al. (2006b) developed an innovative chromatographic method for the purification of Si solutions. Recognising that Si in mildly acidic solutions is present as uncharged orthosilicic acid (H_4SiO_4), they used a cation-exchange chromatographic medium (AG50W–X12, Bio-Rad Laboratories, USA) to separate the cationic matrix, which binds to the medium at low acid strength, from Si, which does not interact with the medium as long as it remains in its uncharged orthosilicic acid form. The lack of interaction between Si and the resin results in very rapid and well-defined Si elution from the chromatographic column, and reduces the potential for isotope fractionation associated with binding to and/or release from the exchange sites, thus assuring both quantitative yields (given suitable loading conditions; Fitoussi et al., 2009) and rapid sample processing. A disadvantage of this method is that it does not separate Si from the uncharged and anionic matrix, which similarly does not interact with the resin. It is thus to be expected that seawater samples processed in this way will contain chloride and sulphate from residual seawater in the precipitate pellet after centrifugation, as well as seawater phosphate, which is also quantitatively scavenged by the Si preconcentration procedure (Karl and Tien, 1992). As detailed in Section 2.4, the seawater contribution of Cl^- and SO_4^{2-} is minimal, whilst matrix- and standard-addition tests have shown that the mass-spectrometric procedure is insensitive to the presence of these anionic components, such that the chromatographic method of Georg et al. (2006b) can be applied for the purification of Si from my preconcentrated seawater samples. Given the low cation load of the sample solutions ($\leq$110 µeq per ml), it was considered feasible to use a chromatographic medium with a lower retention capacity (and thus higher flow rate) than the 12% crosslinkage resin used by Georg et al. (2006b). The 8% crosslinkage cation-exchange medium AG50W–X8 (Bio-Rad Laboratories, USA) has a retention capacity of 1.7 meq/ml wet resin, such that a 1 ml resin bed should provide sufficient retention of the $\leq$0.11 meq cations present in 1 ml of the sample solution. Tests of this medium against AG50W–X12 used by Georg et al. (2006b) showed that this is indeed the case; levels of cation matrix in the purified Si solutions were negligible, independent of the medium used, while Si yields remained quantitative. Since use of AG50W–X8 reduces the time required for chromatography by about 25%, it was used for the purification of Si from all samples reported in this thesis. A detailed schematic of the chromatographic procedure is given in Table 2.1.

Table 2.1: Scheme for chromatographic purification of Si from preconcentrated seawater samples. Chromatography was carried out in polypropylene BioSpin columns with a polyethylene bed support, filled with 1 ml of pre-cleaned AG50W–X8 chromatographic medium.

Step	Volume	Concentration	Reagent
Clean	Fill	3 M	HCl
	Fill	6 M	HCl
	0.3 ml	conc.	HNO_3
	Fill	6 M	HCl
	Fill	3 M	HCl
	Fill	6 M	HCl
	Fill	3 M	HCl
Rinse	Fill		mQe
	(...continue until elute pH ≈ 7)		
Load	1 ml		sample
Elute &	1 ml		mQe
collect	1 ml		mQe

2.3 Mass spectrometry

2.3.1 Analytical protocol

Multicollector inductively-couple plasma mass-spectrometric (MC-ICPMS) analysis of all three isotopes of silicon (^{28}Si, ^{29}Si, ^{30}Si) requires high mass resolution in order to fully resolve polyatomic interferences, especially that of $^{14}N^{16}O^+$ on $^{30}Si^+$. The double-focussing high-resolution MC-ICPMS *NuPlasma 1700* (Nu Instruments, UK) is capable of the required mass resolution ($\sim$1800) while maintaining peak flatness, such that it is possible to resolve all major polyatomic interferences ($^{12}C^{16}O^+$, $^{14}N^{14}N^+$, $^{14}N^{14}N^{1}H^+$ and $^{14}N^{16}O^+$) from the three Si^+ ion beams, as shown in Fig. 2.1. The measured ^{29}Si/^{28}Si ratios are used to verify mass-dependency (i.e. complete resolution of all interferences), but will not be reported in this thesis.

The sample is taken up by a 6mm PFA nebuliser and introduced into the plasma via the Nu Instruments DSN-100 desolvating unit. Silicon isotope composition is measured in static mode using a standard–sample bracketing protocol (Albarède and Beard, 2004) and reported as deviation from the standard reference material NBS28 in standard delta notation as δ^{30}Si:

$$\delta^{30}\text{Si (in ‰)} = \left(\frac{\left(\frac{^{30}\text{Si}}{^{28}\text{Si}}\right)_{\text{sample}}}{\left(\frac{^{30}\text{Si}}{^{28}\text{Si}}\right)_{\text{NBS 28}}} - 1 \right) \times 1000$$

In the protocol used here, one sample analysis is represented by five measurements (36×5 sec integrations each) of a sample, each of which is bracketed by the primary standard NBS28. Each analysis thus requires $\sim$1 hr of instrument time and consumes $\sim$ 30 nmoles of Si, although I typically chromatographically purify 64 nmoles Si per sample.

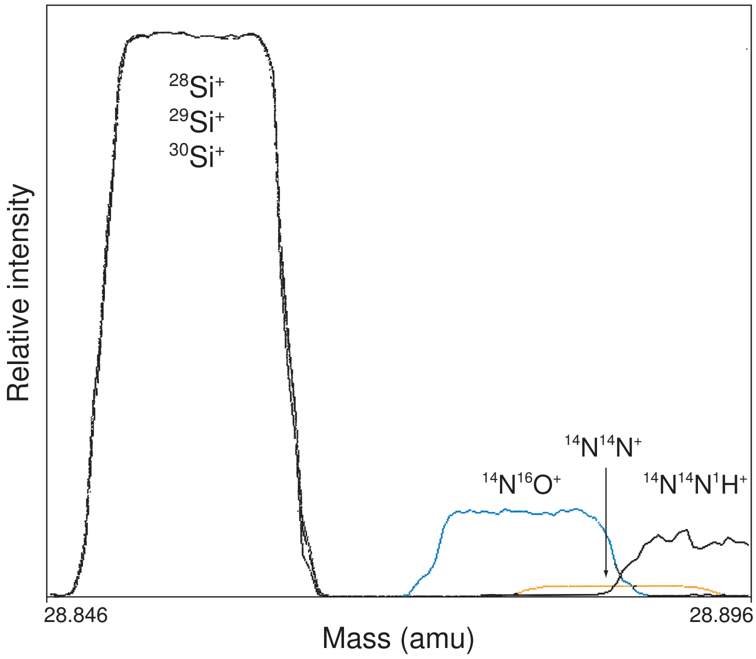

Figure 2.1: An instrumental mass scan illustrating that the polyatomic interferences are clearly resolved from the three Si^+ beams.

2.3.2 Error statistics

The secondary isotopic standard Diatomite (Brzezinski et al., 2006; Reynolds et al., 2007) is analysed repeatedly during each batch of sample analyses as a control on analysis accuracy. The resulting large number of analyses (∼300 over >3yr) allows estimation of the long-term analytical reproducibility from the variance of the values obtained from these analyses. As shown in Fig. 2.2, the measured values are normally-distributed with a mean of +1.22‰ and a standard deviation of ±0.06 ‰. The long-term analytical reproducibility is thus ±0.12‰ ($2\sigma_{SD}$), similar to the reproducibility of ±0.14‰ reported by Reynolds et al. (2006b) using the same method and on the same mass spectrometer. This reproducibility is similar to that reported by Brzezinski et al. (2006) using gas-source mass spectrometry (±0.14‰; $2\sigma_{SD}$), and compares favourably with the precision achieved by most other laboratories as estimated in the laboratory intercomparison of Reynolds et al. (2007, their Table 2).

In general, errors on seawater δ^{30}Si values in this thesis are reported as twice the standard error of the mean ($2\sigma_{SEM}$) of multiple analyses, at least two of which are from separate analytical sessions. Exceptions are samples that could only be analysed a single time, either due to their low Si content or because of time constraints. In these cases, errors on the datapoints are reported as the external reproducibility ($2\sigma_{SD}$). Each analysis is, as noted in Section 2.3.1, the mean of five bracketed measurements of the sample, such that each analysis can be viewed as a group of 9 values. In this

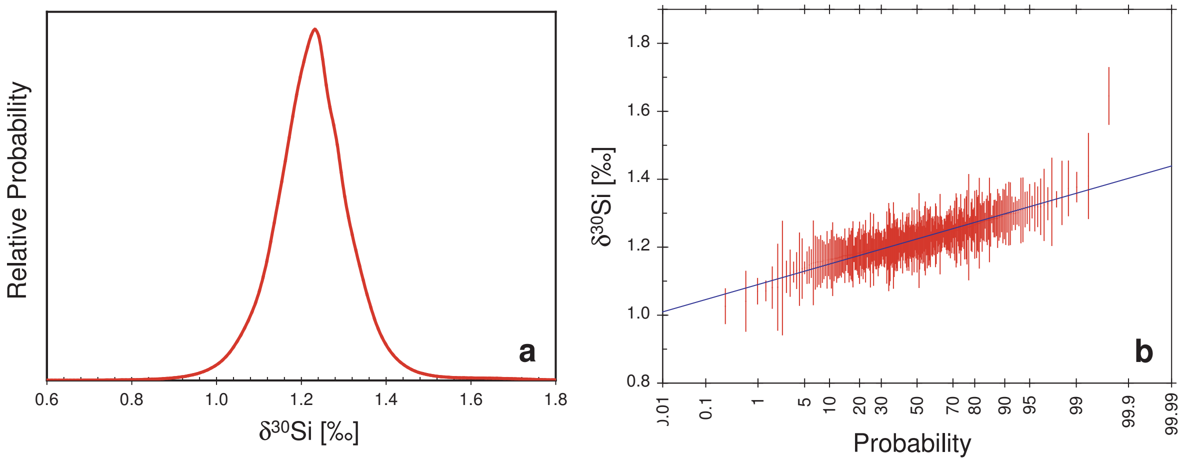

Figure 2.2: External reproducibility of the standard–sampling bracketing protocol, represented by ∼300 analyses of the secondary standard Diatomite. Panel *a* shows the probability density function of measured δ^{30}Si values, with a mean of +1.22±0.12‰($2\sigma_{SD}$). Panel *b* is a probability diagram that allows evaluation of conformance to normal distribution. All δ^{30}Si analyses but one plot along a linear array, indicating that they sample from a single normal distribution, which is strong evidence that the observed standard deviation of ±0.06‰ characterises long-term external reproducibility of the analytical protocol. Plots were created using *Isoplot* (K. R. Ludwig, Berkeley Geochronological Center).

case of a set of data groups with equal group sizes, the estimate of the standard error of the mean simplifies from its general form:

$$\widehat{SE}(\overline{y}) = \sqrt{\frac{\sum_{i=1}^{k} n_i^2}{N^2}\widehat{\sigma}_b^2 + \frac{\widehat{\sigma}_w^2}{N}}$$

to the usual expression for the standard error of the set of group averages:

$$\widehat{SE}(\overline{y}) = \sqrt{\frac{\sum_{i=1}^{k}(\overline{y}_i - \overline{y})^2}{k(k-1)}}$$

where $\widehat{SE}(\overline{y})$ is the estimate of the standard error on the mean value $\overline{y}$, k is the number of groups, n_i is the number of observations in each group, N is the total number of observations and $\widehat{\sigma}_w^2$ and $\widehat{\sigma}_b^2$ are estimates of the within-group and between-group variances, respectively.

2.4 Method evaluation

2.4.1 Reagents

All acids used for $Mg(OH)_2$ precipitate dissolution and cation chromatography were purified either by sub-boiling distillation in PFA elbows or using the PicoTrace distillation system (PicoTrace GmbH, Germany). The intensity of the $^{28}Si^{+}$ beam in the MC-ICPMS for chromatography blank samples was indistinguishable from that for ≥18.2 MΩcm water and is negligible. Reagent-grade sodium hydroxide (Merck KGaA, Germany) exhibited a detectable Si blank (corresponding to 1 ppm Si in the solid) during photospectrometry (Hach Lange GmbH, Germany), and thus semiconductor-grade NaOH (Sigma-Aldrich, USA) with an undetectable Si blank (<10 ppb Si in the solid) was used for precipitation of all samples included in this thesis. The maximum Si blank that could be associated with NaOH addition is thus a negligible ~0.003% of sample Si.

2.4.2 Anion matrix effects

The fact that the cation exchange procedure does not separate the sample's anionic matrix from Si is a potential source of concern for the mass-spectrometric analysis of $\delta^{30}Si$. The principal anionic matrix of seawater consists of Cl^{-} and SO_4^{2-}, while the MAGIC co-precipitation procedure also quantatively scavenges PO_4^{3-} from seawater, such that the Si:P mole ratio in the final solution should be essentially identical to that of seawater, in which this ratio ranges from 0.02 to 0.2. It is thus vital to assess the presence and magnitude of any influence this anionic matrix might have on the accuracy of the $\delta^{30}Si$ analyses.

Most of the Cl^{-} and SO_4^{2-} matrix from seawater is removed along with the supernatant solution after centrifugal separation of the $Mg(OH)_2$ precipitate and adsorbed Si. Any seawater Cl^{-} and SO_4^{2-} that remains in the sample is from residual seawater in the sample tube after removal of the supernatant, for example within the precipitate porosity. The magnitude of this contribution was assessed by ICP-OES analysis of seawater samples after pre-concentration of Si, which indicated that the samples contained only about 3–4 µmoles of SO_4^{2-}, equivalent to only ~100 µl of residual seawater. The same samples contain 300–400 µmoles of Cl^{-}, most of which (~210 µmoles) is contributed by HCl used for dissolution of the precipitate. The influence of these anions on the measurement of $\delta^{30}Si$ was assessed by adding primary and secondary standards to either a silicon-free artificial seawater prepared in-house ($[Cl^{-}]$ = 490 mM, $[SO_4^{2-}]$ = 25 mM), or natural seawater samples from which Si had been stripped using $Mg(OH)_2$, and processing these as normal seawater samples. This approach gave values of $\delta^{30}Si_{NBS+SW} = +0.03 \pm 0.09‰$ ($2\sigma_{SEM}$, $n = 6$) and $\delta^{30}Si_{DIATOMITE+SW} = +1.24 \pm 0.05‰$ ($2\sigma_{SEM}$, $n = 10$). These values are identical within error to the expected values of 0‰ and +1.22‰ for the undoped NBS28 and Diatomite respectively, indicating that no significant matrix effects are related to the Cl^{-} and SO_4^{2-} matrix of my seawater samples. However, these tests cannot assess the influence of the PO_4^{3-} matrix, since no PO_4^{3-}-bearing salt was added to the artificial seawater and PO_4^{3-} had been stripped along with Si from the natural seawater samples used. I did not perform specific PO_4^{3-}-doping tests, but rather performed standard addition tests as detailed below.

2.4.3 Testing accuracy by standard addition

I verified the accuracy of the seawater δ^{30}Si analyses using the standard addition method applied to standard-sample bracketing isotopic analyses by Tipper et al. (2008). Briefly, a pure standard of known isotopic composition is added to a sample at different standard:sample ratios, the resulting mixtures chromatographically purified and subsequently analysed by standard-sample bracketing. If the analyses are accurate, i.e. no analytical artefacts are associated with any subtle differences between the matrices of the sample and the bracketing standard, the isotopic compositions of the standard-sample mixtures should vary linearly with the proportion of standard in the mixture, f_{STD}, from the value of the standard (at $f_{\mathrm{STD}} = 1$) to the value of the sample ($f_{\mathrm{STD}} = 0$).

In the standard addition tests, I utilised the standard IRMM-018, since its δ^{30}Si value of –1.61‰ (Reynolds et al., 2007) produces a significant δ^{30}Si change even at low f_{STD} values. Figure 2.3 shows the results of two such standard addition tests. The standard-sample mixtures show a clear and strong linear variation with f_{STD} (MSWD of 0.83 and 0.84), with excellent agreement of the measured δ^{30}Si values of both the pure standard and the pure sample with those predicted by linear regression of the standard-sample mixtures. These results thus clearly document that my chromatographic and mass spectrometric procedure produces accurate and precise δ^{30}Si data.

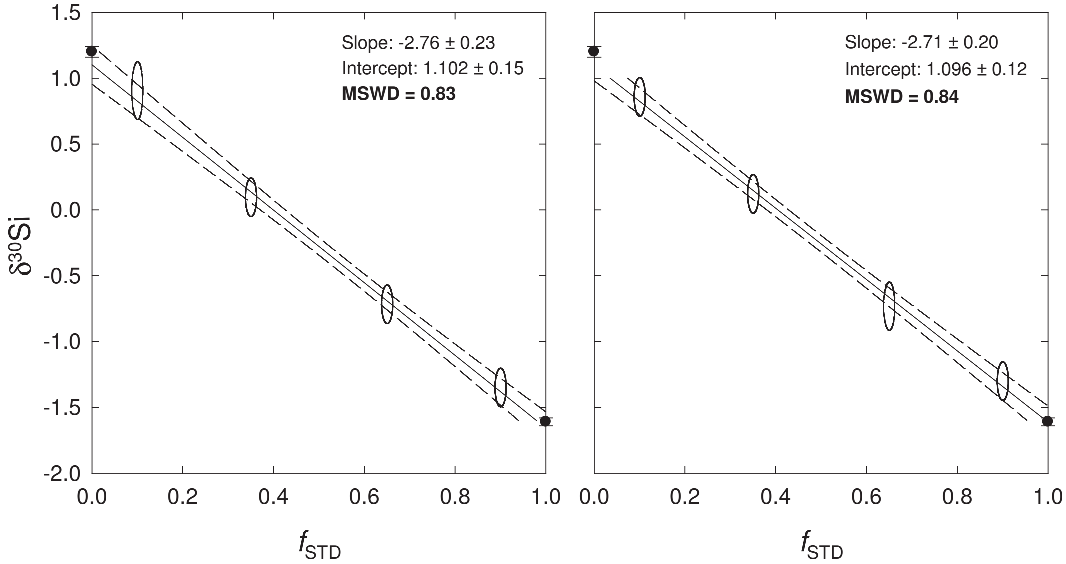

Figure 2.3: Plots showing the linear variation of δ^{30}Si values of standard-sample mixtures with the fraction of standard in the mixture, f_{STD}. Filled circles at the extremes of the x-axis represent the pure sample and standard (at x = 0 and x = 1 respectively). Linear regressions utilise only mixture data and are calculated in *Isoplot* (K. R. Ludwig, Berkeley Geochronological Center) using the algorithm of York (1968). MSWD values less than unity would seem to indicate that the errors on the datapoints (external $2\sigma_{\mathrm{SD}}$) are slightly overestimated.

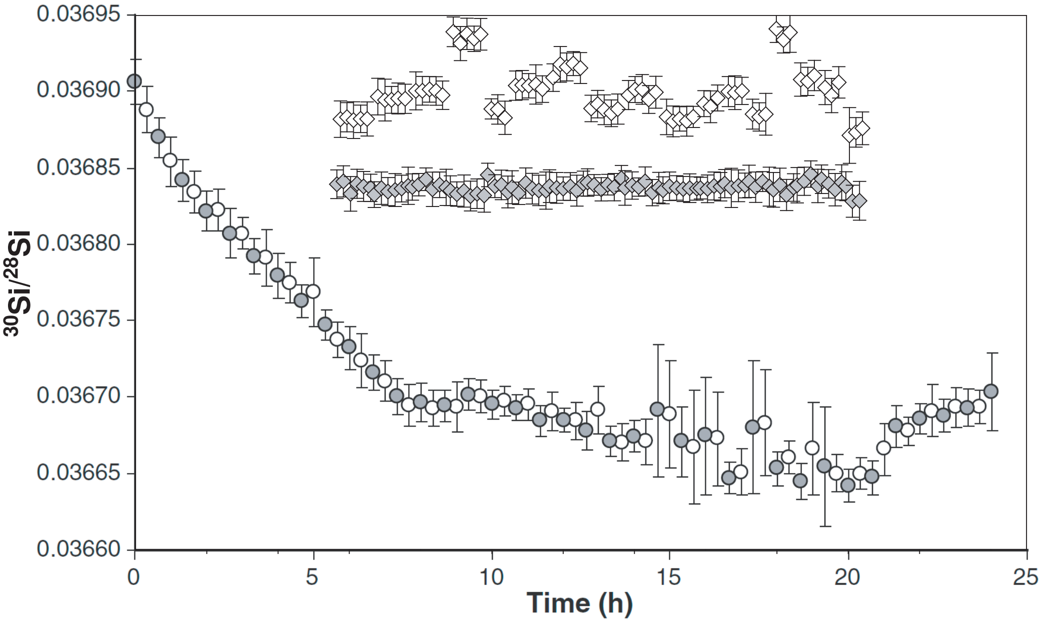

Figure 2.4: A comparison of raw $^{30}Si/^{28}Si$ ratios measured in our laboratory (diamonds) and by Zambardi and Poitrasson (2011) (circles), modified from their Figure 2a (grey symbols represent the bracketing standard, white symbols represent samples). The contrasting stability of instrumental mass bias is apparent. Error bars are internal $2\sigma_{SD}$ (diamonds) or not specified (circles).

2.4.4 A comparison to external normalisation protocols

A number of laboratories analysing Si stable isotopes by MC-ICPMS utilise an external normalisation protocol that relies on the addition of magnesium (Mg) to the purified Si solution, following which instrumental mass bias variations are corrected for by normalising measured Si isotope ratios using the mass bias estimated from Mg isotope ratios (e.g. Cardinal et al., 2003; Engström et al., 2006; Zambardi and Poitrasson, 2011). These studies, almost exclusively performed on the ThermoFinnigan *Neptune*, typically highlight the necessity for external Mg normalisation in order to conduct precise and accurate Si isotope analyses. I have shown above that the standard-sample bracketing protocol in use in our laboratory is capable of producing accurate and precise δ^{30}Si data. A reason for this apparent discrepancy in the necessity for external normalisation is suggested by a comparison of the instrumental mass bias variations observed in our laboratory with a time series of measured Si isotope ratios published by Zambardi and Poitrasson (2011). As Fig. 2.4 shows, instrumental conditions in our laboratory are vastly more stable, in terms of mass bias, than those documented in the data of Zambardi and Poitrasson (2011). This might be due to a number of factors. It is possible that mass bias variability of the *NuPlasma 1700* is instrinsically smaller than that of the *Neptune*, or that our sample introduction system provides more stable conditions at the interface. However, Van den

Boorn et al. (2006) did achieve a similar order of external precision using a *Neptune* MC-ICPMS without external normalisation, which would argue against a fundamental difference between instruments or desolvating nebuliser systems. Another possibility is the care taken in maximising the stability of the conditions at the interface. The use of a dedicated desolvating nebuliser system for silicon isotope measurements has proven useful in improving stability and minimising instrumental Si background. Additionally, no isotopic analyses are carried out in our laboratory during the first ∼12 hours of an analytical session, in order to allow conditions at the front end of the instrument to stabilise, with fine-focusing of the ion beams being performed only after this time period. This precaution, which is a luxury that might not be available to researchers in a full economic costing environment, ensures that during a typical session, mass bias variability is minimal, i.e. considerably less than 1‰ in δ^{30}Si over 12 hours, as opposed to the ∼5.5‰ drift observed over 8 hours in the data of Zambardi and Poitrasson (2011) (Fig. 2.4).

Chapter 3

Isotope fractionation in the sea: what should we expect?*

Abstract

The stable isotopic compositions of elements dissolved in seawater are a valuable source of information on elemental cycling within the ocean, since by their integrative nature they provide a synoptic view of ocean biogeochemistry. However, oceanic stable isotope distributions are often interpreted using overly simplistic models, notably the Rayleigh equation (Rayleigh, 1902), which ignores critical complexities of the system as well as the spatial separation of biogeochemical processes in the ocean. Here we utilise simple models to illustrate the necessity of accounting for these factors in order to correctly interpret the observed oceanic stable isotope tracer fields. We use a simple advection-diffusion-reaction model to examine the processes determining oceanic stable isotope distributions in the upper ocean, where the strongest vertical isotopic gradients are observed. The model demonstrates that these subsurface gradients owe their existence to physical processes that introduce the isotopic signal of biological uptake into the subsurface. This schematic physical-biological framework thus not only allows a more accurate interpretation of novel stable isotope distributions, but also emphasises the importance of the physical circulation in controlling the distribution of biogeochemically cycled elements in the upper ocean.

---

*a version of this chapter will be submitted to *Nature Geoscience* as: G. F. de Souza and B. C. Reynolds, *What controls stable isotope distributions in the sea?*

3.1 Introduction

Whilst the study of the stable isotopic composition of dissolved components of seawater has a long history (Miyake and Wada, 1967), the past decade has seen a surge of interest in the development and application of novel stable isotope tracers in the sea (Bermin et al., 2006; Ripperger et al., 2007; Lacan et al., 2008). This renewed interest has been driven both by the recognition of the importance of transition metals in modulating oceanic productivity (Martin, 1990) and by significant analytical developments in the field of isotope geochemistry. Furthermore, the growing realisation of the complexity of oceanic trace element distributions (e.g. Measures et al., 2008; Boyd and Ellwood, 2010) makes stable isotope data a welcome additional element-specific constraint on the processes that cycle elements in the ocean. These developments have culminated in the international GEOTRACES programme to sample the global ocean for analysis of trace elements and their isotopes over the coming decade (SCORWorkingGroup, 2007), with the hope of setting the stage for a paradigm shift in our understanding of ocean biogeochemistry. At the threshold to this new era, it seems appropriate to critically review our expectations for the behaviour of stable isotope systems in the sea.

In the case of elements that are cycled within the oceans by biogeochemical processes, the most pronounced variations in stable isotope composition are generally caused by isotopic discrimination during uptake by photosynthesising biota in the sunlit surface ocean, the euphotic zone (e.g. Sigman et al., 1999; De La Rocha et al., 2000; John et al., 2007; Ripperger et al., 2007). It is thus in the near-surface ocean that the strongest gradients in the stable isotopic composition of dissolved elements are observed (e.g. Sigman et al., 1999; De La Rocha et al., 2000; Reynolds et al., 2006a; Ripperger et al., 2007), associated with gradients in their concentration. These isotopic gradients are commonly (Altabet et al., 1999; De La Rocha et al., 2000; Altabet, 2001; Ripperger et al., 2007; Lacan et al., 2008) analysed and interpreted using the Rayleigh distillation equation (Rayleigh, 1902, see caption of Fig. 3.1). The Rayleigh equation has a tradition of application in the field of stable isotope geochemistry, and has been applied with success in the oceanic setting to describe changes in the nitrogen isotopic composition of surface ocean nitrate (δ^{15}N–NO_3; Sigman et al., 1999). Possibly as a consequence of this, the expectation that the stable isotope systematics of dissolved elements in the global ocean can be described by a “Rayleigh-like” system is now implicitly or explicitly voiced in numerous publications (e.g. Wischmeyer et al., 2003; Ripperger et al., 2007). However, we argue that the complexities of elemental cycling, together with the spatially heterogeneous distribution of biogeochemically relevant processes in the ocean, violate the fundamental assumptions of the Rayleigh equation, and that in order to correctly interpret the effects of biogeochemical cycling on stable isotope distributions, the oceans’ spatial dimension must be taken into account, as we do in a simple one-dimensional advection-diffusion-reaction (1-D ADR) model.

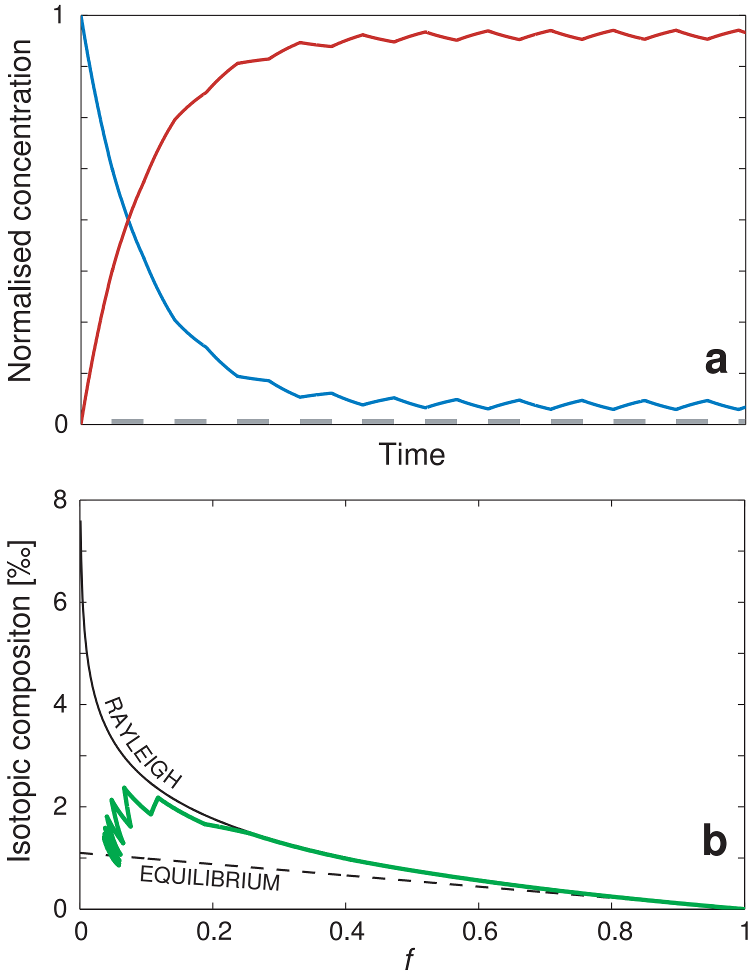

Figure 3.1: Behaviour of a closed system with periodic back-reaction. *a*, Time evolution of the reactant (blue) and product (red) pools of an element that is isotopically fractionated during formation of the product. The chemically closed system tends towards equilibrium but is periodically disturbed by intervals of back-reaction of the product to the reactant (grey bars along the x-axis), with no associated isotope fractionation, leading to minor saw-tooth undulations in reactant and product concentrations; *b*, Evolution of the isotopic composition of the reactant (green line) as permil deviation of the isotope ratio from a constant value, plotted against its normalised concentration $f = C(t)/C(0)$. The solid black curve represents the isotopic composition of the reactant predicted by the Rayleigh equation $R/R_0 = f^{\alpha-1}$, where R is the ratio of two stable isotopes of a reactant, R_0 is its initial isotopic ratio, f is the proportion of reactant still available for reaction, and α is the isotopic fractionation factor associated with the reaction. The dashed line represents the isotopic composition of the reactant predicted by a model that assumes equilibrium conditions. Although the forward reaction is sufficiently dominant that the system draws down the reactant to low concentrations ($f < 0.1$), the isotopic composition of the reactant evolves to markedly less extreme values in this closed system with back-reaction than predicted for an irreversible reaction by the Rayleigh equation. All isotopic compositions are calculated using $\alpha = 0.9989$ (see Appendix A.1.1).

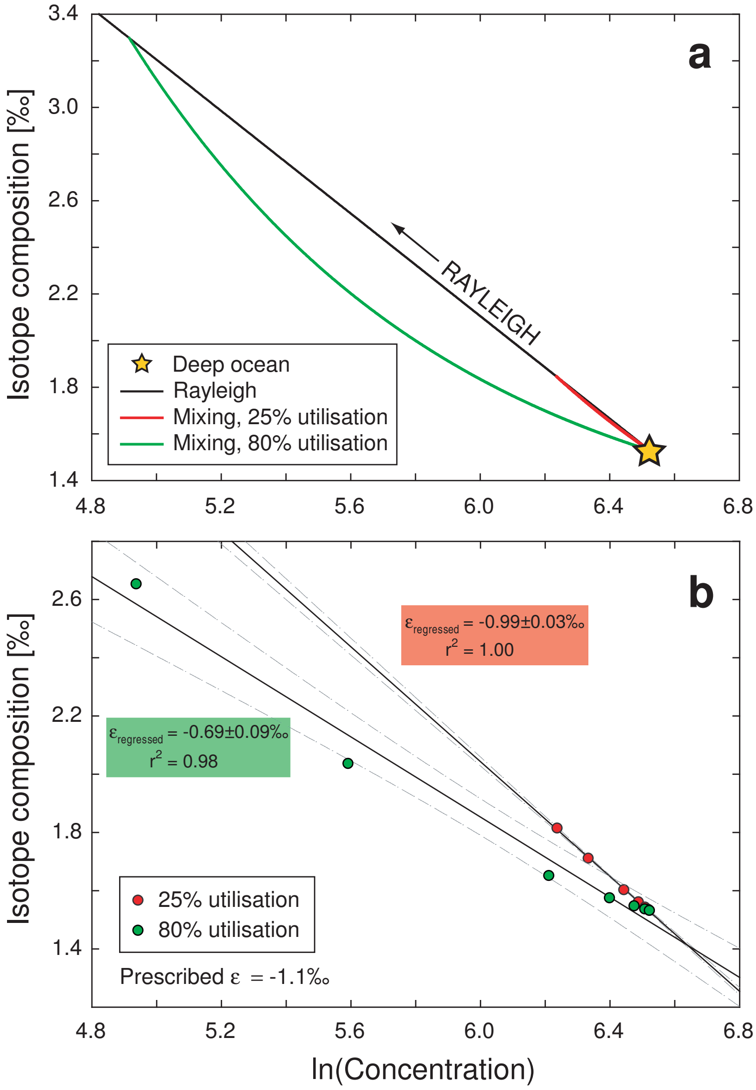

Figure 3.2: The effect of ocean heterogeneity on stable isotope systematics. *a*, Consider a hypothetical, initially homogeneous two-box ocean (Appendix A.1.2) in which the concentration of an element in the surface box is set by the concentration in the deep box. If the element is consumed irreversibly in the surface box, its isotopic composition evolves according to the Rayleigh equation, i.e. along the solid black line. When water from this surface box subsequently mixes with water from the deep, the resulting water mass will have characteristics determined by a binary mixing array (coloured lines). The deviation from the Rayleigh curve depends strongly on the degree to which the element is stripped from the surface box (red vs. green line). After Sigman et al. (1999). *b*, The same behaviour is shown in the spatially-resolved 1–D ADR model (see text). Gridpoints at 50 m depth intervals have been chosen to simulate typical near-surface sampling density for stable isotope analyses. At low utilisation (25%; f = 0.75), the water column is well approximated by the logarithmic relationship predicted by the Rayleigh equation, with the regression yielding an estimated isotope effect, $\varepsilon_{\text{regressed}}$, almost identical ($-0.99 \pm 0.03$‰; $2\sigma_{\text{SE}}$) to that prescribed in the model (-1.1‰). However, at relatively high utilisation (80%; f = 0.2), physical mixing processes result in significant deviation from Rayleigh-like systematics, such that $\varepsilon_{\text{regressed}}$ is significantly lower (-0.69 ± 0.09‰; $2\sigma_{\text{SE}}$) than the prescribed model value. Note that the linear correlation coefficient remains very high, an argument often presented as support for the suitability of applying the Rayleigh equation (the value of 0.98 also applies to a regression through all model grid points). ε is defined as $(\alpha - 1) \times 1000$ in units of permil.

3.2 The Rayleigh equation: conditions and limitations

Three principal conditions must be fulfilled for a fractionating process to be described by the Rayleigh equation, only one of which is commonly explicitly acknowledged in oceanographic studies of stable isotope tracers. This is the condition that the system is chemically closed, such that no replenishment of the reactant can occur. This closed-system condition is frequently taken into account (e.g. Sigman et al., 1999; Varela et al., 2004), for example by applying the Rayleigh equation to the surface mixed layer only in settings where it is sufficiently isolated from subsurface waters by density stratification. Most workers, however, neglect the fact that the Rayleigh equation also requires that the fractionating process is irreversible, since any back-reaction similarly constitutes a replenishment of the reactant. This irreversibility condition, which has been referred to in discussions of kinetic isotope fractionation for over half a century (Bigeleisen, 1949b; Buchanan et al., 1953; Kendall and Doctor, 2003), is highly relevant to oceanic stable isotope systems, since any recycling of an element within the zone of active biological uptake will fundamentally alter the isotopic evolution of the dissolved pool. We illustrate this using a numerical model of isotope fractionation (Appendix A.1.1): when the product of a fractionating reaction is periodically allowed to back-react, the stable isotopic composition of the dissolved pool is strongly affected (Fig. 3.1). At the low concentrations typical for biogeochemically cycled elements in the surface ocean, the Rayleigh equation predicts a markedly different stable isotope composition of the dissolved pool compared to the model with periodic back-reaction, in which the isotopic signal of biological utilisation is strongly dampened. Thus, for elements that adsorb to and desorb from particles, or are recycled within the euphotic zone due to remineralisation of organic matter (e.g. transition metals incorporated into metalloenzymes) or hard parts (e.g. silicon), application of the Rayleigh equation will result in erroneously low estimates of the isotope effect associated with biological uptake. The significance of this complexity has apparently been overlooked while adopting the methods used to interpret oceanic δ^{15}N–NO$_3$, for which it is not relevant: although significant *nitrogen* recycling takes place within the euphotic zone, the conversion to *nitrate* – i.e. the reaction that leads to replenishment of the reactant – occurs primarily, albeit not exclusively, at depth (Ward, 2008).

A further central characteristic of the Rayleigh model that is commonly ignored is its essentially non-dimensional nature. Since the equation describes the evolution of the isotopic composition of a single pool of reactant, it requires chemical homogeneity within the system. If only a portion of a dissolved pool reacts, as is the case in the ocean (i.e. at its surface), a fractionation signal is only produced in this pool. The system-wide isotopic distribution is then determined by the interaction between fractionated and unfractionated pools, e.g. during mixing. This is illustrated by a two-box model (Fig. 3.2a), which represents the spatial heterogeneity of biological activity in the ocean in the simplest possible form. Significant deviations from Rayleigh behaviour result from the interaction of the surface ocean with the subsurface when strong vertical concentration gradients exist, as is the case for biogeochemically cycled elements over most of the ocean. This simple model result clearly indicates that it is erroneous to expect (Wischmeyer et al., 2003) the global ocean to behave as a “Rayleigh-like” system.

3.3 A simple spatial framework

The physical separation of biogeochemically relevant processes thus requires that oceanic stable isotope distributions be interpreted in an appropriate spatial framework. This is especially true in the near-surface ocean, where the strongest gradients in concentration and stable isotope composition are observed (Sigman et al., 1999; Reynolds et al., 2006a; Ripperger et al., 2007). Thus, in order to interpret these strong isotopic gradients, we require an alternate model that captures the most important features of the near-surface ocean. One-dimensional advection–diffusion–reaction (1-D ADR) models fulfil this requirement well (Appendix A.1.3). A vertical ADR model applied to the near-surface ocean correctly describes the system insofar as the elements necessary for biological production are provided from below by physical transport processes, and are returned to depth by particulate export. Of course, this 1-D model process only schematically represents what is in actuality a complex three-dimensional recycling pathway (Jenkins and Doney, 2003; Williams and Follows, 2003). Nonetheless, analysis of the systematics of this simple model affords insights into the mechanisms that exert control on stable isotope distributions in the upper ocean, as we show below.

Figure 3.3 illustrates the result of coupling an advective-diffusive transport scheme (Appendix A.1.3) to the non-dimensional isotope fractionation model used to produce Fig. 3.1. The simplicity of the model’s equilibrium solutions allows us to assess the role played by individual processes in determining the near-surface isotopic distribution. Within the euphotic zone, where active biological uptake and isotope fractionation take place, the stable isotope composition of the dissolved pool is determined by the equilibrium between supply by the physical circulation and particulate export to the deeper water column. Importantly, however, the extent of an isotopic gradient in the subsurface water column is strongly controlled by the model’s vertical diffusivity (Fig. 3.3b). The isotopic signal produced by biological uptake in the euphotic zone is increasingly propagated into the subsurface as diffusivity increases (Fig. 3.3c). This feature follows directly from the nature of the ADR model, but nonetheless provides a vital insight: where a gradient in the concentration of a biogeochemically cycled element in the upper ocean is accompanied by an isotopic gradient towards the value of the euphotic zone (Altabet et al., 1999; Sigman et al., 2000; De La Rocha et al., 2000; Altabet, 2001;

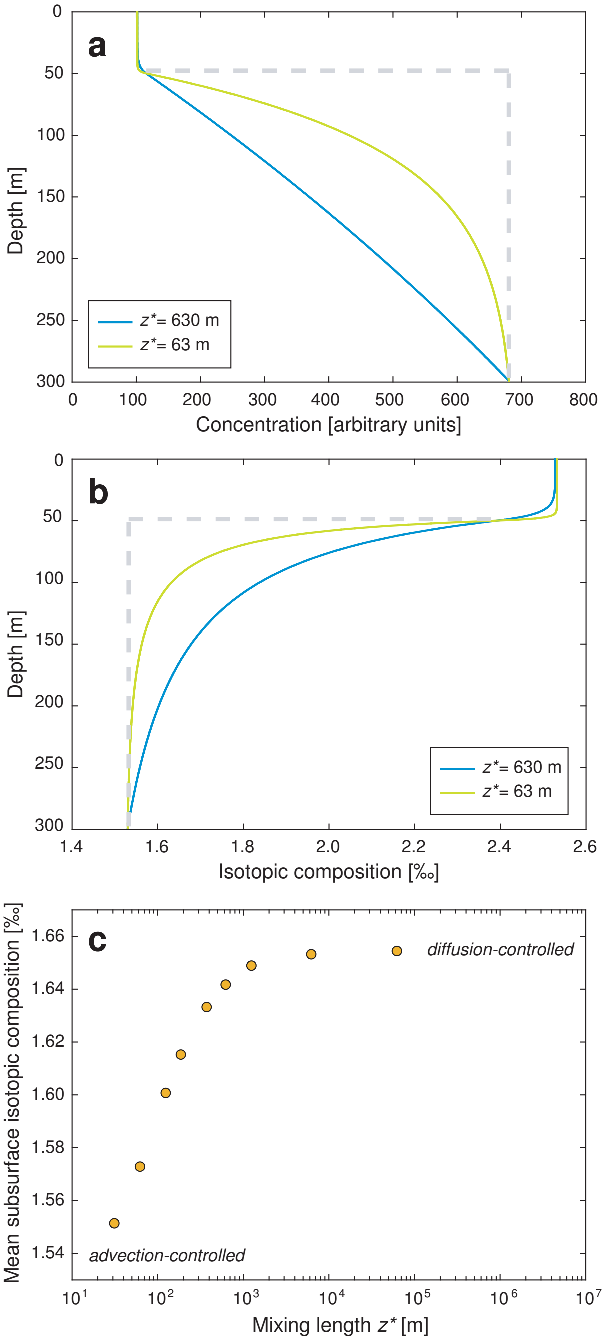

Figure 3.3: Results of the vertical advection–diffusion–reaction model. Depth profiles of (a) concentration and (b) isotopic composition of a dissolved element for two values of mixing length ($z* = \kappa_z/w$), a measure of the strength of diffusive mixing relative to advection (κ_z and w respectively; see also Appendix A.1.3). The dashed grey lines schematically represent the end-member case of zero diffusivity; *c*, Variation of the concentration-weighted mean isotopic composition below the zone of active uptake with mixing length. The increase in weighted mean isotopic composition is due to deepening of the isotopic gradient with increasing diffusive mixing, as also illustrated in panel *b*.

Reynolds et al., 2006a; Ripperger et al., 2007) both these gradients must be primarily the result of an oceanic process equivalent to the model's diffusivity parameter; i.e. mixing. Vertical turbulent mixing across the density gradient in the upper ocean is not sufficiently vigorous (Ledwell et al., 1993) to produce such gradients at the scale of the main thermocline, such that the observed distributions may be produced by boundary mixing (Munk and Wunsch, 1998), or by horizontal mixing where the density surfaces of the ocean's thermocline impinge upon its surface (Wunsch and Ferrari, 2004, see also Chapter 5). Irrespective of the exact mechanism, it is clear that the observed subsurface isotopic gradients must be produced by the physical transport, into the subsurface, of water parcels that have experienced active uptake. This inference is substantiated by mass balance considerations (Appendix A.1.4), which indicate that the remineralisation of sinking particles cannot produce an isotopic gradient of the correct sign.

3.4 Implications

Given the strong physical control on the upper ocean isotopic distribution, it is not surprising that the Rayleigh equation consistently underestimates the isotope effect of biological uptake when applied to water column data (Fig. 3.2b; Altabet et al., 1999; Altabet, 2001), since it attributes concentration and isotopic composition variations with depth to utilisation, not physical processes. More fundamentally, however, the fact that the isotopic signature of utilisation is observed within the subsurface upper ocean for a number of biologically cycled elements (Chapter 4; Sigman et al., 2000; Ripperger et al., 2007) bears witness to the importance of the physical circulation in determining the upper ocean distribution of these elements. Specifically, the presence of such a utilisation signature in the isotopic composition of an element in the subsurface implies that a significant proportion of its upper ocean inventory is 'preformed', i.e. advected into the subsurface by the physical circulation, rather than being added by remineralisation of sinking particles. This inference is consistent with an emerging view of the transport of biogeochemical tracers in the ocean: it is becoming increasingly clear that waters of Southern Ocean origin are a dominant source of macronutrients in the low-latitude thermocline (Sarmiento et al., 2004a; Palter et al., 2010), a three-dimensional conception of nutrient transport by the large-scale ocean circulation that explains numerous previously puzzling features of ocean biogeochemistry (Gruber and Sarmiento, 2002). Provided that they are not rapidly scavenged out of the water column, the large-scale circulation will similarly introduce other biogeochemically cycled trace elements into the upper ocean, making them accessible for supply to biota in the sunlit surface ocean and associated isotope fractionation. Conceptual models of oceanic stable isotope systematics must take this dynamic setting into account, by paying heed to (a) the effects of ocean circulation, which can be considered to set the 'background' isotopic distribution of biogeochemically cycled elements in the upper ocean, and (b) the vertical balance of elemental supply and export, which may modify this distribution both through elemental cycling and additional effects such as isotope fractionation during remineralisation. This same conceptual framework may also be applied to understanding the oceanic distribution of elemental ratios (e.g. Elderfield and Rickaby, 2000). As the GEOTRACES programme begins to ease data limitation in the modern ocean, such a conceptual physical-biological framework will provide the foundation for a broader-based understanding of the interaction between biological utilisation and the physical circulation in determining stable isotope distributions in the sea.

Chapter 4

The basin-scale Atlantic δ^{30}Si distribution*

Abstract

The fractionation of silicon (Si) stable isotopes by biological activity in the surface ocean makes the stable isotope composition of silicon (δ^{30}Si) dissolved in seawater a sensitive tracer of the oceanic biogeochemical Si cycle. We present a high-precision dataset that characterizes the δ^{30}Si distribution in the deep Atlantic Ocean from Denmark Strait to Drake Passage, documenting strong meridional and smaller, but resolvable, vertical δ^{30}Si gradients. We show that these gradients are related to the two sources of deep and bottom waters in the Atlantic Ocean: waters of North Atlantic and Nordic origin carry a high δ^{30}Si signature of $\geq$+1.7‰ into the deep Atlantic, whilst Antarctic Bottom Water transports Si with a low δ^{30}Si value of around +1.2‰. The deep Atlantic δ^{30}Si distribution is thus governed by the quasi-conservative mixing of Si from these two isotopically distinct sources. This disparity in Si isotope composition between the North Atlantic and Southern Ocean is in marked contrast to the homogeneity of the stable nitrogen isotope composition of deep ocean nitrate (δ^{15}N-NO$_3$). We infer that the meridional δ^{30}Si gradient derives from the transport of the high δ^{30}Si signature of Southern Ocean intermediate/mode waters into the North Atlantic by the upper return path of the meridional overturning circulation (MOC). The basin-scale deep Atlantic δ^{30}Si gradient thus owes its existence to the interaction of the physical circulation with biological nutrient uptake at high southern latitudes, which fractionates Si isotopes between the abyssal and intermediate/mode waters formed in the Southern Ocean.

---

[*] submitted to *Global Biogeochemical Cycles* as G. F. de Souza, B. C. Reynolds, J. Rickli, M. Frank, M. Saito, L. J. A. Gerringa and B. Bourdon: “Southern Ocean control of silicon stable isotope distribution in the deep Atlantic Ocean”. Orthography follows American rules, as required by the journal.

4.1 Introduction

The oceanic biogeochemical cycle of silicon (Si) is tied to that of carbon by the important role played by diatoms – siliceous phytoplankton – in global new production (Smetacek, 1999; Ragueneau et al., 2000, and references therein). Diatoms additionally tend to dominate the phytoplankton community in dynamic upwelling regions (Margalef, 1978; Jin et al., 2006; Dutkiewicz et al., 2009) such as the Southern Ocean, which play an important role in the oceanic control of atmospheric pCO_2 (Marinov et al., 2006; Gruber et al., 2009). Silicon fluxes associated with diatom productivity and export are so large that they dominantly control the Si cycle in the sea (Tréguer et al., 1995; DeMaster, 2009). Since diatoms preferentially incorporate the lighter isotopes of Si into their opaline frustules (De La Rocha et al., 1997), diatom uptake of Si in the sunlit surface ocean alters the stable isotope composition of dissolved Si in seawater (expressed as δ^{30}Si; see Section 4.2.2). As a result of this, seawater δ^{30}Si values trace biogeochemical processes affecting Si, and thus constraining the mechanisms that govern the oceanic δ^{30}Si distribution allows direct inference of the pathways and processes by which Si is cycled within the ocean. This is particularly interesting in the context of an emerging paradigm of oceanic nutrient cycling (Gruber and Sarmiento, 2002; Sarmiento et al., 2004a, 2007; Palter et al., 2010) that stresses the importance of lateral transport processes, modulated by biology in the Southern Ocean, in determining global oceanic nutrient distributions, and thus ultimately oceanic primary productivity (Sarmiento et al., 2004a). In addition, a better knowledge of the processes that control the modern δ^{30}Si distribution will allow more robust interpretations of diatom opal δ^{30}Si records from deep-sea sediment cores (e.g. De La Rocha et al., 1998; Beucher et al., 2007; Pichevin et al., 2009), improving our understanding of how diatom productivity may have affected atmospheric pCO_2 over glacial–interglacial cycles (Brzezinski et al., 2002; Matsumoto et al., 2002; Crosta et al., 2007). Together, these two complementary issues provide strong motivation to study the modern oceanic δ^{30}Si distribution, particularly in the Atlantic Ocean.

The Atlantic is the best studied of the major ocean basins. Ever since the first description of its deep hydrography (Thomson, 1878), both the physical and chemical oceanography of the Atlantic Ocean have been the subject of intense study, such that much is known about Atlantic circulation (e.g. Wüst, 1935; Reid, 1989; Tsuchiya, 1989; Peterson and Stramma, 1991; Schmitz and McCartney, 1993; Dickson and Brown, 1994; Reid, 1994; Schmitz, 1996b; Larqué et al., 1997; Jenkins, 1998; Stramma and England, 1999; Stramma and Schott, 1999; Sloyan and Rintoul, 2001a; Lumpkin and Speer, 2003) as well as the distribution of biogeochemical tracers (e.g. Broecker et al., 1980; Broecker and Takahashi, 1980; Kawase and Sarmiento, 1985, 1986; Broecker et al., 1991; Tsuchiya et al., 1992, 1994; Sarmiento et al., 2007). This well-founded understanding of the system, combined with the fact that the deep Atlantic exhibits strong meridional contrasts in physical and chemical tracers, makes the Atlantic Ocean ideally suited to constraining processes determining the behavior of a relatively novel isotopic tracer such as seawater δ^{30}Si.

In-depth studies of seawater δ^{30}Si (Varela et al., 2004; Cardinal et al., 2005; Reynolds et al., 2006a; Beucher et al., 2008) have thus far focused on high-nutrient, low-chlorophyll (HNLC) regions that are the key areas for ocean–climate interaction and overlie opal-rich sediments. The Atlantic Ocean has been somewhat neglected, most likely due to its modest contribution to biological Si cycling in the modern ocean, reflected by a very low opal export flux for its area (6% of global export; Sarmiento et al., 2007). However, the fact that the primary formation regions of the deep and bottom waters that fill the global ocean are situated at its northern and southern end (Warren, 1981) makes the Atlantic highly relevant to the global oceanic Si cycle. Furthermore, as it contains the world's youngest and least Si-rich deepwaters (0–300 yr ventilation ages; Matsumoto, 2007), a firm handle on the δ^{30}Si distribution in the deep Atlantic is crucial to better resolve an interesting feature of the oceanic δ^{30}Si distribution: it appears that the North Atlantic and North Pacific have distinct deepwater δ^{30}Si values, which would contrast the homogeneity of the stable nitrogen isotopic composition of deep oceanic nitrate, δ^{15}N-NO$_3$. However, the Atlantic end of this interbasin gradient is represented by only three depth profiles near Bermuda (De La Rocha et al., 2000). This poor spatial resolution hinders a robust analysis of the mechanisms leading to the observed distribution, and modeling studies have delivered conflicting results in this regard (Wischmeyer et al., 2003; Reynolds, 2009).

In order to characterize the δ^{30}Si systematics of the Atlantic Ocean, we have analyzed a suite of Atlantic seawater samples from Denmark Strait to Drake Passage. Chapter 5 discusses the δ^{30}Si distribution in the main thermocline, whilst this chapter focuses on the Atlantic δ^{30}Si distribution below 2000 m water depth. We show that the deep Atlantic exhibits a strong meridional δ^{30}Si gradient, which we relate to the interaction of the global meridional overturning circulation (MOC) with biological Si cycling processes at high southern latitudes, thereby providing evidence for the importance of a Southern Ocean source of nutrients to the low-latitude thermocline. Furthermore, we show that the distribution of seawater δ^{30}Si values robustly confirms earlier interpretations of quasi-conservative behavior of Si at depth in the Atlantic Ocean.

4.2 Methods

4.2.1 Sample collection

A total of 84 seawater samples from the Atlantic Ocean and adjacent basins are included in this study (Fig. 4.1, Table 4.1). These include 25 samples originally collected for analysis of neodymium and hafnium isotopic composition (Rickli et al., 2009) at 6 stations in the eastern Atlantic Ocean during

Table 4.1: Location of expeditions and stations from which samples were collected for this study. See also Fig. 4.1.

Cruise	Region	Station No.	Location	Latitude	Longitude
64PE318	North Atlantic	7	Faroe–Shetland Channel	60°6’ N	5°48’ W
64PE319	North Atlantic	2	Irminger Basin	64° N	34°15’ W
		3	Irminger Basin	62°21’ N	36° W
		5	Irminger Basin	60 °26’ N	37°55’ W
		8	Labrador Sea	54°4’ N	45°50’ W
		11	Newfoundland Basin	47°48’ N	39°24’ W
ANT XXIII/1	Eastern Atlantic	PS 69/3	Bay of Biscay	46°25’ N	5°55’ W
	(subtropical and tropical)	PS 69/6	Bay of Biscay	45°45’ N	5°32’ W
		PS 69/11	Canary/Cape Verde Basin	22°30’ N	20°30’ W
		PS 69/14	Cape Verde Basin	10°37’ N	20°8’ W
		PS 69/18	Guinea Basin/Chain Fracture Zone	0°42’ S	11°16’ W
		PS 69/21	Angola Basin	11°52’ S	2°31’ W
		PS 69/26	Cape Basin	25° S	8°17’ E
KN 192–5	Tropical Atlantic	3	Brazil Basin	11°30’ S	25° W
	(eastern and western)	13	Angola Basin	13°29’ S	0° W
ANT XXIII/3	South Atlantic	PS 69/140	Drake Passage	56°26’ S	63°18’ W
		PS 69/224	Drake Passage	56°56’ S	62°21’ W

expedition ANT XXIII/1 of R/V *Polarstern* (October–November 2005). Two detailed depth profiles (17 samples each) from the tropical Brazil and Angola Basins were collected during expedition KN192-5 of R/V *Knorr* (November–December 2007). A further 23 samples were collected at 6 stations along GEOTRACES section GA02 in the northeastern and northwestern Atlantic, during expeditions 64PE318 and 64PE319 of R/V *Pelagia* (April–May 2010). In addition, two samples from Drake Passage (R/V *Polarstern* expedition ANT XXIII/3) were procured. All samples were filtered onboard using 0.45 µm nitrocellulose (*Polarstern*), 0.45 µm polycarbonate (*Knorr*) or 0.2 µm cellulose acetate (*Pelagia*) filters. Samples from *Polarstern* expeditions were acidified onboard with 0.1% v/v distilled 9.5 M HCl (Rickli et al., 2009), while samples from expeditions KN192-5, 64PE318 and 64PE319 were acidified with 0.1% v/v distilled 6 M HCl in the laboratory at least 12 hr before preconcentration of Si.

4.2.2 Sample preconcentration and analysis

We typically process 64 nmoles (1.8 µg) of Si for each mass-spectrometric analysis of Si stable isotope composition. Prior to the chromatographic separation of Si from sea salt, Si is preconcentrated by coprecipitation with brucite using a method modified from Karl and Tien (1992). This preconcentration decreases the associated salt cation and anion matrix by more than two orders of magnitude, permitting the use of small ion exchange columns. Our two-step precipitation procedure (similar to that used by Reynolds et al. (2006a)) achieves Si yields generally in excess of 99% (and always $>$97.5%): in a first step, $\sim$10% of seawater Mg is precipitated as $Mg(OH)_2$ by adding $\sim$1% v/v of 1 M NaOH solution (semiconductor grade; Sigma-Aldrich) to the pH-neutralised seawater sample. This solution is shaken for 1 hr and allowed to react and settle for 24 hr before being centrifuged. The second precipitation step is carried out by further addition of 1 M NaOH to precipitate $\sim$10% of the

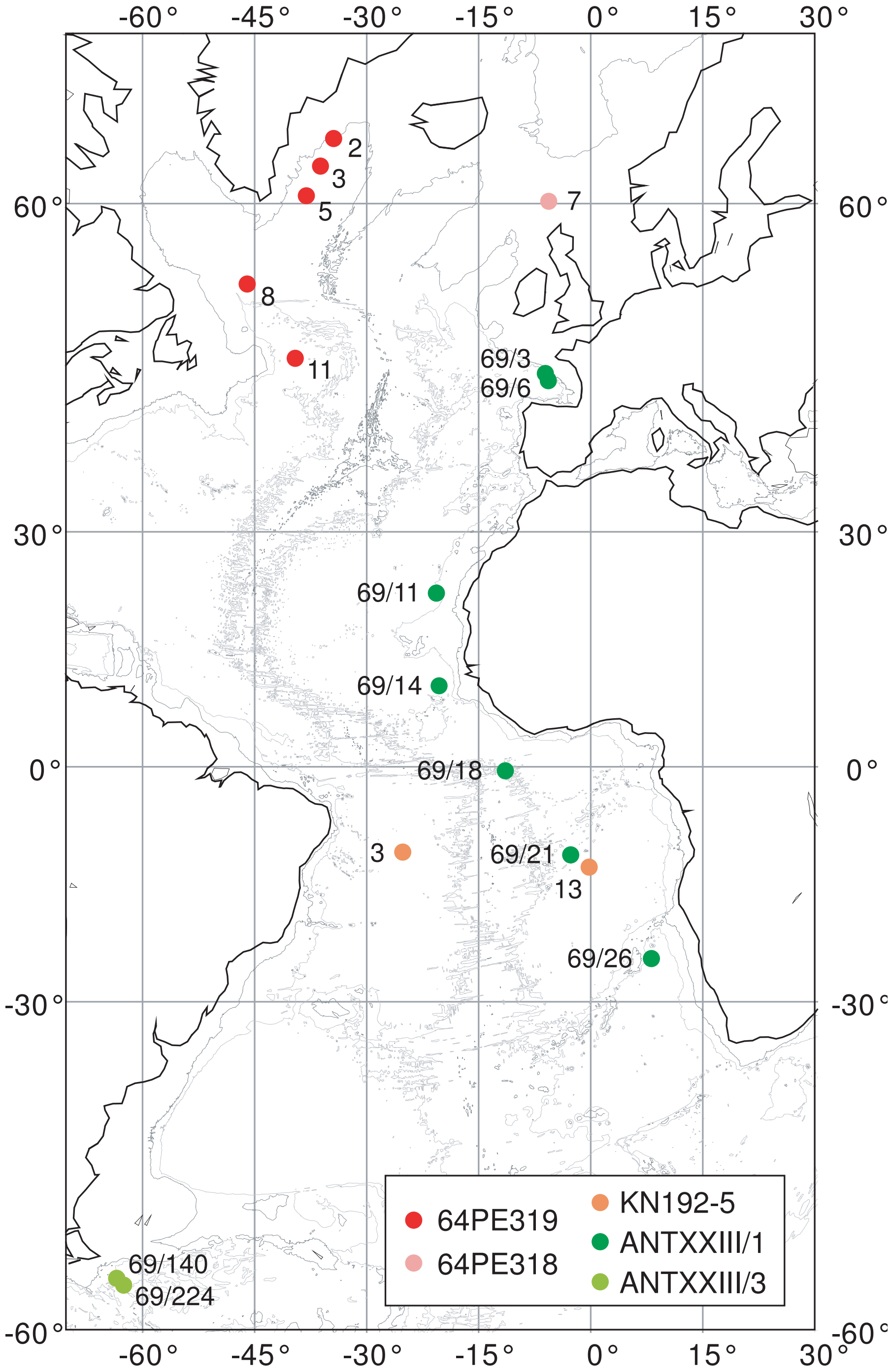
-60°
-45°
-30°
-15°
0°
15°
30°
60°
30°
0°
-30°
-60°
2
3
5
7
8
11
69/3
69/6
69/11
69/14
69/18
3
69/21
13
69/26
69/140
69/224
64PE319
64PE318
KN192-5
ANTXXIII/1
ANTXXIII/3

Figure 4.1: Map of the Atlantic Ocean illustrating locations from which samples for this study were collected. Depth contours are shown at 2000 m (dark gray) and 4000 m (light gray). Numbers represent cruise station designations. See also Table 4.1.

remaining sample Mg, followed by shaking for 1 hr, settling for at least 24 hr and centrifuging. The supernatant is removed and the yield of the coprecipitation determined by photospectrometric analysis of supernatant Si concentration using the molybdate blue method (Strickland and Parsons, 1968). The precipitate is then dissolved in a small volume of 6 M HCl and diluted with ultrapure water ($>$18.2 MΩcm) to 64 µM (1.8 ppm) Si, at which point it contains $\leq$53 mM Mg (i.e. $\leq$0.11 meq Mg/ml) as its main cationic matrix at a pH of 2–3. One milliliter of this solution is passed through a cation-exchange column with a retention capacity of 1.7 meq (1 ml AG50W-X8; BioRad Laboratories) to separate uncharged H_4SiO_4 from the cationic matrix. The uncharged and anionic matrix, which consists primarily of Cl^-, SO_4^{2-} and PO_4^{3-}, is not removed by this method, such that the final solution contains $\sim$1.5 mM Cl^- (mainly from HCl), $\sim$1 µM seawater SO_4^{2-}, and a PO_4^{3-} concentration that depends on the seawater P:Si ratio (which ranges from $\sim$0.02–0.2). Phosphate, sulphate and chloride doping tests have shown that the presence of these anions does not result in analytical artifacts; in fact, the insensitivity of our analytical setup to the presence of SO_4^{2-} has been previously documented by Georg et al. (2006b), a finding that contrasts with the matrix effects observed by van den Boorn et al. (2009) using a different analytical system, perhaps due to the different sample introduction systems used. We verified the accuracy of our seawater δ^{30}Si analyses using the standard addition method applied to isotopic analyses by Tipper et al. (2008, see Section 2.4.3).

The purified Si solution is analyzed for Si stable isotope composition using a high-resolution multicollector inductively-coupled plasma mass spectrometer (MC-ICPMS *NuPlasma 1700*; Nu Instruments, UK) in static mode by standard–sample bracketing, with one δ^{30}Si analysis consisting of 5 bracketed measurements (36 × 5 s integrations each) of the sample. Detailed descriptions of the chromatographic separation and mass-spectrometric methods used are given by Georg et al. (2006b).

Silicon stable isotope composition is reported as the permil deviation from the standard reference material NBS28, δ^{30}Si, which is defined as:

$$\delta^{30}\mathrm{Si} = \left(\frac{\left(\frac{^{30}\mathrm{Si}}{^{28}\mathrm{Si}}\right)_{\mathrm{sample}}}{\left(\frac{^{30}\mathrm{Si}}{^{28}\mathrm{Si}}\right)_{\mathrm{NBS\,28}}} - 1 \right) \times 1000 \ \ [‰]$$

The long-term external reproducibility of our δ^{30}Si analyses is ±0.12‰ ($2\sigma_{SD}$), as estimated from the variance of $>$300 analyses of the secondary isotopic standard Diatomite (Brzezinski et al., 2006) over $>$3 yr. The average δ^{30}Si value of Diatomite measured over this period is +1.22±0.01‰ ($2\sigma_{SEM}$), consistent with the inter-laboratory comparison study of Reynolds et al. (2007). Except in the case of near-surface samples with low amounts of Si, reported sample δ^{30}Si values are the mean of at least 3, and up to 11, complete replicate analyses in at least 2 separate analytical sessions. External errors on the seawater data, reported as 2 standard errors of the mean ($2\sigma_{SEM}$), are usually ±0.07‰

or better (see Table 4.2).

In the following, the notations Si, [Si] and δ^{30}Si will refer to *dissolved* silicon (i.e. silicic acid), its concentration, and its stable isotope composition respectively.

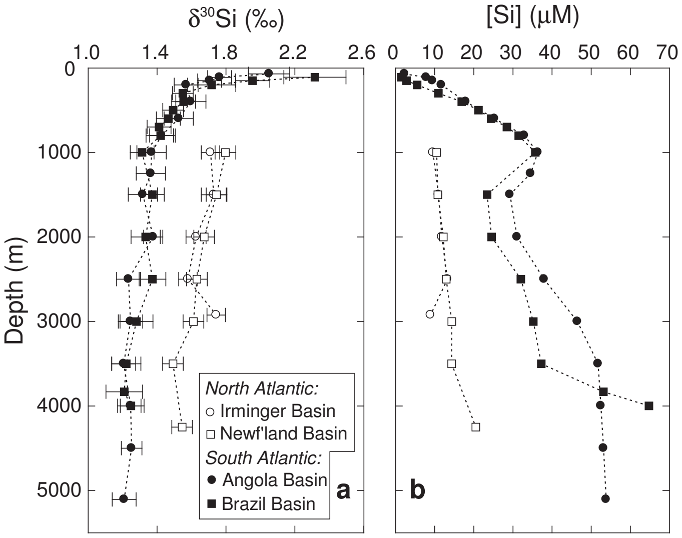

Figure 4.2: Depth profiles of (a) δ^{30}Si values and (b) Si concentrations. The western North Atlantic (Irminger and Newfoundland Basins; 64PE319 Stas 5 and 11) is offset towards higher δ^{30}Si values and lower [Si] than the South Atlantic (Brazil and Angola Basins; KN192-5 Stas 3 and 13). Note the increase in δ^{30}Si at the base of the water column in the Irminger Basin, associated with the lower [Si] of Denmark Strait Overflow Water. See Appendix A.2.1 for δ^{30}Si and [Si] depth profiles from all stations included in this study.

4.3 Results

Depth profiles of δ^{30}Si (see examples in Fig. 4.2a) show the typical increase in δ^{30}Si values towards the surface that is expected from the preferential uptake of lighter Si isotopes by diatoms in the surface ocean . Values of δ^{30}Si range from approximately +1.2‰ in bottom waters to almost +3‰ in the surface mixed layer (Table 4.2; all depth profile diagrams are provided in Appendix A.2.1). The gradient towards higher δ^{30}Si values is largest in the upper ocean, above the salinity minimum at $\sim$1000 m associated with Antarctic Intermediate Water (AAIW) in the South Atlantic. Below this, δ^{30}Si gradients are much smaller, but δ^{30}Si values generally continue to decrease with depth, with the exception of the northernmost North Atlantic (Irminger Basin; 64PE319 Stas 3 and 5), where δ^{30}Si values increase slightly with depth near the very bottom of the water column (Fig. 4.2b), associated with stronger gradients in temperature and [Si] (Table 4.2). Furthermore, the entire water column exhibits a clear difference in δ^{30}Si values between the North and South Atlantic (Fig. 4.2). At temperate northern latitudes around 45°N, the western Atlantic (64PE319 Sta 11) exhibits lower [Si] and higher δ^{30}Si values than the eastern Atlantic (ANTXXIII/1 Stas 3 and 6; Table 4.2).

A remarkably strong coherence in the δ^{30}Si systematics of the entire sampled Atlantic is illustrated by the relationship between concentration and isotopic composition of Si. Graphs of δ^{30}Si values versus [Si] (Fig. 4.3a) and its reciprocal, 1/[Si] (Fig. 4.3b) reveal that samples from all regions exhibit the same relationship between these parameters, even when their δ^{30}Si depth profiles exhibit clear differences. In Fig. 4.3b, the existence of two linear arrays with different slopes is apparent. These arrays intersect at a δ^{30}Si value of +1.55–1.6‰ and 1/[Si] of 0.09–0.06, corresponding to a potential density σ_θ of 26.75–27.00 (water depth 300–400 m), i.e. in the range of densities of Subantarctic Mode Water (SAMW) in the Atlantic (Larqué et al., 1997; Sallée et al., 2010).

In the following discussion, we describe and discuss the deep Atlantic δ^{30}Si distribution below 2000 m water depth (Section 4.4.1), and draw upon the δ^{30}Si signature of the intermediate and upper Atlantic to explain its ultimate origin (Sections 4.4.2, 4.4.3 and 4.4.4) in the context of the MOC.

4.4 Discussion

4.4.1 Quasi-conservativity of Si

It is a striking feature of the deep Atlantic δ^{30}Si distribution that the North Atlantic water column exhibits consistently higher δ^{30}Si values than the South Atlantic (Fig. 4.2, Table 4.2). In a plot of δ^{30}Si values against the reciprocal of Si concentration, 1/[Si], this meridional gradient is expressed as a linear array for water samples below 2000 m (Fig. 4.3d). The existence of such a linear relationship is indicative of conservative mixing between two distinct reservoirs, or endmembers (see e.g. Albarède, 1996, for a derivation). The deep Atlantic δ^{30}Si systematics thus strongly suggests that the distribution of Si in the deep Atlantic is controlled by binary mixing, with no significant sources or sinks. This would imply that Si is quasi-conservative in the deep Atlantic, which might intuitively seem unlikely for a biologically cycled nutrient. As we show below, however, it can be demonstrated that this is indeed the case in the deep Atlantic Ocean.

Broecker et al. (1991), and more recently Sarmiento et al. (2007), have shown that while the effect of opal dissolution on deep Atlantic [Si] can be resolved by careful analysis, this effect is of minor importance (<5% contribution) in controlling deep [Si]. Similarly, in their analysis of GEOSECS nutrient data, Anderson and Sarmiento (1994) find that "the remineralization signal in the deep Atlantic is practically non-existent". In the case of Si, this is partially due to the low Atlantic opal productivity (Sarmiento et al., 2007), but the leading-order control is the order-of-magnitude disparity in [Si] between the two water masses filling the deep Atlantic, i.e. North Atlantic Deep Water (NADW, [Si] $<$20 µM) and Antarctic Bottom Water (AABW, [Si] $\sim$120 µM). This pronounced [Si] contrast means

Table 4.2: Hydrographic parameters, nutrient concentrations, δ^{30}Si values and parameters related to the endmember contribution calculation for all samples. *n* refers to the number of complete replicate analyses of δ^{30}Si. ^{a} Entries with brackets are North Atlantic samples with PO_4^* values below 0.76 µmol/kg that were corrected to this value (see Appendix A.2.2). Corresponding $\Delta\delta^{30}Si_{msr-mix}$ values are also given in brackets. Data continues in Table 4.3 on following page.

Cruise & Station	**Depth**	θ	***S***	σ_θ	**[PO$_4$]**	**[NO$_3$]**	**[Si]**	δ^{30}**Si**	**2**σ_{SEM}	***n***	**PO$_4^{*a}$**	$\Delta\delta^{30}$**Si**$_{mix}{}^{a}$
	m	℃	psu	kg/m^3	µM	µM	µM	‰	external		µmol/kg	‰
64PE318 Sta 7	250	9.21	35.405	27.40	0.76	11.7	4.5	1.85	0.08	2	-	-
	600	2.40	34.980	27.92	0.93	13.8	6.6	1.78	0.07	3	-	-
	1000	–0.69	34.908	28.07	1.04	15.1	11.0	1.69	0.06	9	-	-
64PE319 Sta 2	2207	1.26	34.897	27.94	0.89	13.3	6.8	1.86	0.07	3	0.72 (0.76)	-0.49 (0.16)
64PE319 Sta 3	800	3.84	34.937	27.74	1.11	17.1	9.8	1.78	0.07	3	-	-
	1000	3.65	34.925	27.79	1.11	17.1	11.0	1.76	0.07	3	-	-
	1500	3.49	34.918	27.82	1.10	17.1	11.5	1.66	0.06	4	-	-
	2000	3.05	34.914	27.88	0.96	14.6	8.9	1.64	0.06	4	0.77	0.04
	2690	1.27	34.896	27.94	0.92	14.0	8.2	1.69	0.07	3	0.75 (0.76)	-0.09 (-0.01)
64PE319 Sta 5	1000	3.55	34.969	27.74	1.11	16.9	9.6	1.71	0.05	5	-	-
	1500	3.44	34.925	27.78	1.13	17.1	11.0	1.73	0.07	4	-	-
	2000	3.08	34.920	27.82	1.12	17.0	11.8	1.63	0.06	5	0.78	0.06
	2500	2.68	34.914	27.86	1.11	16.6	13.3	1.58	0.05	6	0.78	0.00
	2924	1.23	34.898	27.93	0.96	14.2	8.9	1.74	0.05	5	0.77	0.11
64PE319 Sta 8	1000	3.48	34.982	27.73	1.11	17.0	9.4	1.79	0.06	4	-	-
	3424	2.02	34.896	27.89	1.10	16.5	16.8	1.58	0.08	4	0.78	0.01
64PE319 Sta 11	1000	4.60	36.362	27.70	1.14	17.6	10.5	1.80	0.06	4	-	-
	1500	3.80	36.318	27.75	1.16	17.5	10.8	1.75	0.06	4	-	-
	2000	3.41	36.318	27.78	1.16	17.8	12.2	1.67	0.06	4	-	-
	2500	3.05	35.844	27.81	1.14	17.4	13.0	1.63	0.06	4	0.76	-0.04
	3000	2.74	35.583	27.85	1.13	17.1	14.4	1.61	0.06	4	0.76	-0.09
	3500	2.34	35.584	27.88	1.14	17.2	14.3	1.49	0.06	4	0.76	-0.18
	4250	1.89	35.583	27.90	1.15	17.1	20.5	1.55	0.06	4	0.80	0.02
ANT XXIII/1 Sta 69/3	991	9.86	35.790	27.59	1.1	16.02	9.6	1.58	0.05	7	-	-
	2000	3.86	35.033	27.83	1.3	18.54	20.6	1.45	0.05	8	0.76	-0.28
ANT XXIII/1 Sta 69/6	200	11.66	35.623	27.14	0.5	8.21	2.6	2.11	0.19	1	-	-
	455	10.87	35.580	27.25	0.7	10.99	4.4	1.55	0.07	3	-	-
	3000	2.54	34.937	27.88	1.5	20.02	36.8	1.29	0.05	5	0.88	-0.05
	4621	2.09	34.897	27.88	1.6	21.28	46.1	1.29	0.06	7	0.95	-0.01
ANT XXIII/1 Sta 69/11	100	18.12	36.309	26.25	1.1	15.93	3.8	1.95	0.07	3	-	-
	200	15.64	36.012	26.61	1.2	19.27	5.4	1.70	0.08	2	-	-
	943	6.79	35.036	27.48	2.1	30.34	21.9	1.46	0.06	4	-	-
	2500	3.02	34.972	27.86	1.5	21.96	32.4	1.38	0.05	5	0.86	0.01
	4106	2.01	34.889	27.88	1.6	22.67	49.0	1.30	0.05	5	0.99	0.02
ANT XXIII/1 Sta 69/14	40	28.47	35.592	22.69	0.0	0.00	0.9	2.89	0.18	1	-	-
	100	15.82	35.587	26.24	1.7	25.09	7.3	1.79	0.12	3	-	-
	200	13.08	35.318	26.62	1.7	25.54	9.3	1.63	0.07	6	-	-

Table 4.3: Data continued from previous page.

Cruise & Station	**Depth** m	θ ℃	***S*** psu	σ_θ kg/m^3	**[PO$_4$]** µM	**[NO$_3$]** µM	**[Si]** µM	δ^{30}**Si** ‰	**2σ_{SEM}** external	***n***	**PO$_4^{*a}$** µmol/kg	$\Delta\delta^{30}$**Si**$_{mix}$^{a} ‰
ANT XXIII/1 Sta 69/18	100	15.37	35.612	26.36	1.0	13.50	5.0	1.73	0.07	3	-	-
	200	14.01	35.414	26.51	1.4	19.39	7.3	1.70	0.07	6	-	-
	500	7.31	34.640	27.09	2.3	32.95	20.5	1.54	0.04	8	-	-
ANT XXIII/1 Sta 69/21	100	17.14	35.918	26.19	1.3	18.27	5.2	1.88	0.06	4	-	-
	200	11.32	35.089	26.79	2.0	29.94	11.5	1.59	0.08	9	-	-
	800	4.79	34.505	27.31	2.8	38.92	32.8	1.43	0.04	8	-	-
	4500	1.96	34.876	27.88	1.6	23.43	52.5	1.28	0.04	8	0.98	-0.01
ANT XXIII/1 Sta 69/26	770	4.96	34.428	27.23	2.5	35.28	29.5	1.51	0.06	8	-	-
	2024	3.06	34.877	27.78	1.7	24.88	36.6	1.38	0.06	8	0.88	0.03
	3500	2.00	34.853	27.85	1.8	25.34	60.3	1.28	0.07	5	0.96	-0.02
	4766	0.74	34.730	27.85	2.3	31.58	109.9	1.20	0.04	11	1.29	-0.02
KN192-5 Sta 3	109	20.93	36.454	25.62	0.6	5.38	1.5	2.32	0.18	1	-	-
	150	16.65	35.840	26.24	0.8	9.68	2.8	1.95	0.10	1	-	-
	200	13.14	35.271	26.57	1.1	16.99	5.5	1.72	0.14	1	-	-
	300	10.10	34.891	26.85	1.7	25.48	10.9	1.55	0.06	4	-	-
	399	7.71	34.656	27.05	2.1	31.55	16.9	1.55	0.07	3	-	-
	499	6.52	34.553	27.13	2.2	33.45	21.2	1.49	0.06	4	-	-
	599	5.51	34.475	27.20	2.2	34.73	24.4	1.47	0.07	3	-	-
	699	4.99	34.472	27.26	2.4	35.75	28.5	1.41	0.07	3	-	-
	800	4.54	34.472	27.31	2.4	35.72	31.5	1.42	0.08	2	-	-
	999	3.94	34.574	27.45	2.3	33.47	35.7	1.31	0.07	3	-	-
	1499	3.82	34.907	27.73	1.6	24.05	23.4	1.37	0.07	3	-	-
	2000	3.17	34.942	27.82	1.4	20.92	24.5	1.33	0.08	2	0.86	-0.03
	2499	2.70	34.919	27.85	1.5	21.59	32.0	1.37	0.08	4	0.89	0.05
	3000	2.46	34.910	27.86	1.5	21.65	35.2	1.28	0.10	4	0.92	-0.02
	3500	2.19	34.894	27.87	1.5	21.25	37.2	1.22	0.08	2	0.91	-0.11
	3832	1.71	34.846	27.87	1.6	23.49	53.1	1.21	0.11	2	1.01	-0.07
	3999	1.38	34.812	27.87	1.7	25.05	64.8	1.25	0.08	5	1.09	-0.01
KN192-5 Sta 13	70	19.80	36.372	25.86	0.8	9.91	2.3	2.05	0.12	1	-	-
	110	14.65	35.530	26.46	1.8	28.06	7.8	1.76	0.07	3	-	-
	150	12.87	35.264	26.62	1.9	30.57	9.4	1.71	0.07	3	-	-
	200	11.67	35.124	26.75	2.1	33.26	11.7	1.57	0.07	3	-	-
	399	8.48	34.771	27.02	2.4	38.54	17.9	1.60	0.09	7	-	-
	600	6.01	34.553	27.20	2.6	40.96	25.3	1.53	0.08	2	-	-
	799	4.59	34.496	27.32	2.6	37.87	32.9	1.43	0.07	3	-	-
	999	3.97	34.572	27.45	2.4	35.11	36.4	1.37	0.08	2	-	-
	1249	3.73	34.737	27.60	2.1	31.00	34.5	1.36	0.08	2	-	-
	1499	3.62	34.860	27.71	1.8	26.67	29.2	1.32	0.08	2	-	-
	1999	3.14	34.915	27.80	1.6	23.58	31.1	1.38	0.06	11	0.90	0.05
	2499	2.67	34.905	27.84	1.6	23.49	38.0	1.23	0.07	3	0.88	-0.11
	3000	2.31	34.890	27.86	1.6	23.96	46.5	1.25	0.07	7	0.92	-0.06
	3500	2.10	34.883	27.87	1.6	24.11	51.8	1.21	0.07	3	0.91	-0.13
	3999	2.00	34.878	27.87	1.6	23.99	52.5	1.25	0.06	4	0.93	-0.08
	4499	1.96	34.874	27.87	1.6	24.09	53.2	1.25	0.06	4	0.94	-0.06
	5106	1.93	34.871	27.87	1.6	23.98	53.8	1.21	0.07	3	0.94	-0.10
ANT XXIII/3 Sta 69/140	3600	0.65	34.711	27.84	1.8	31.95	121.7	1.21	0.06	4	-	-
ANT XXIII/3 Sta 69/224	1250	2.16	34.643	27.67	2.5	34.22	87.8	1.23	0.05	7	-	-

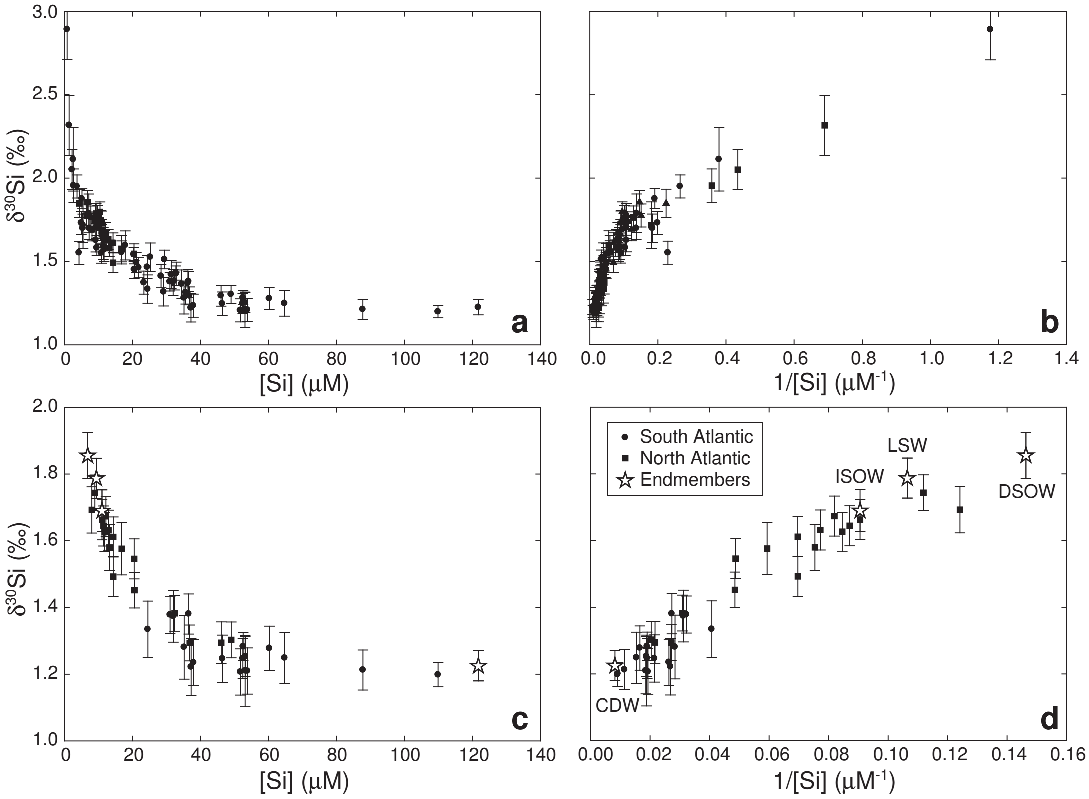

Figure 4.3: Silicon isotope systematics of the Atlantic Ocean, plotted as δ^{30}Si vs. [Si] (left panels) and as mixing diagrams of δ^{30}Si vs.1/[Si] (right panels). Panels *a* and *b* include all samples, while *c* and *d* focus on the water column below 2000 m. A clear and coherent relationship between δ^{30}Si and [Si] or 1/[Si] is seen in all panels. The mixing diagram in panel *b* exhibits two linear relationships between δ^{30}Si and 1/[Si], intersecting at δ^{30}Si values of +1.55–1.6‰. Panel *d* focuses on the Si isotope systematics of the deep Atlantic below 2000 m, emphasizing the tightness of the linear relationship at depth. Stars in *c* and *d* represent the deep water mass endmembers of Southern Ocean and North Atlantic origin (CDW: Circumpolar Deep Water, ISOW: Iceland-Scotland Overflow Water, LSW: Labrador Sea Water, DSOW: Denmark Strait Overflow Water). Note that the water mass labeled as ISOW for clarity would more correctly be named Faroe-Shetland Overflow Water, which is a dominant component of ISOW (Dickson and Brown, 1994).

that admixture of Si-rich AABW to Si-poor NADW leads to large [Si] changes, such that mixing of these two water masses exerts by far the strongest control on variations in Atlantic [Si] below a water depth of around 2000 m. Silicon concentrations are thus closely correlated with conservative and quasi-conservative tracers of water mass mixing such as salinity (Holfort and Siedler, 2001) and PO_4^* (Broecker et al., 1991, see also Appendix A.2.2) in the deep Atlantic, with the exception of a few local anomalies (e.g. van Bennekom and Berger, 1984).

The influence of the contrasting northern and southern water masses on the deep Atlantic δ^{30}Si systematics is apparent in Fig. 4.3d. Low δ^{30}Si values are associated with the high Si concentrations of AABW, whilst the highest δ^{30}Si values are observed for the precursors of NADW, i.e. the dense Si-poor overflows from the Nordic seas (Denmark Strait Overflow Water and Iceland-Scotland Overflow

Water, DSOW and ISOW) as well as Labrador Sea Water (LSW) (Dickson and Brown, 1994). These northern and southern sources of deepwater thus represent the two isotopic endmembers inferred above to be controlling the Atlantic δ^{30}Si distribution. By calculating the deviation of measured δ^{30}Si values from those expected from pure mixing of these endmembers, we can quantify the degree of conservativity of Si. Following Gruber (1998), we utilize the quasi-conservative tracer PO_4^* (Broecker et al., 1991) to independently calculate the contribution of North Atlantic waters f_{NA} to each sample (see Appendix A.2.2 for details). The δ^{30}Si value expected from pure binary mixing, $\delta^{30}Si_{mix}$, is then:

$$\delta^{30}Si_{mix} = \frac{f_{NA}\delta^{30}Si_{NA}[Si]_{NA} + (1 - f_{NA})\delta^{30}Si_{SO}[Si]_{SO}}{f_{NA}[Si]_{NA} + (1 - f_{NA})[Si]_{SO}}$$

where *NA* and *SO* refer to the North Atlantic and Southern Ocean components respectively, and $\delta^{30}Si_i$ and $[Si]_i$ are the isotopic composition and concentration of Si in the component *i*. The deviation of the measured value from this value is given by $\Delta\delta^{30}Si_{msr-mix}$, defined as:

$$\Delta\delta^{30}Si_{msr-mix} = \delta^{30}Si_{measured} - \delta^{30}Si_{mix}$$

Values of $\Delta\delta^{30}Si_{msr-mix}$ for the deep Atlantic are, with some notable exceptions, generally smaller than the associated uncertainties (Fig. 4.4b; Appendix A.2.2). This close correspondence of measured and calculated δ^{30}Si values demonstrates that Si is predominantly quasi-conservative in the deep Atlantic. The sample most strongly offset from the 1:1 line in Fig. 4.4a is a sample from the Bay of Biscay, whose chemistry (PO_4^*, δ^{30}Si, or both) is influenced by Mediterranean Overflow Water (Gruber, 1998). There is a slight tendency of measured δ^{30}Si values in the South Atlantic to be marginally lower than calculated values (Fig. 4.4). These offsets are associated with samples from the deep Angola basin, where seawater neodymium isotope compositions appear to be affected by the Congo Fan (Rickli et al., 2009). The observed slight δ^{30}Si deviations from pure mixing might thus indicate that Si release from the Congo Fan (van Bennekom and Berger, 1984; Warren and Speer, 1991; Ragueneau et al., 2009) plays a minor role in modulating deep δ^{30}Si values here.

The strongest control on the deep Atlantic δ^{30}Si distribution is the physical circulation: Antarctic Bottom Water advects a low δ^{30}Si value of around +1.2‰ into the Atlantic from the south, while high δ^{30}Si values of +1.7‰ to +1.85‰ are introduced into the North Atlantic by the NADW-precursors. Mixing between these water masses results in the observed small δ^{30}Si gradients with depth in the water column of individual stations, but also in the large-scale meridional δ^{30}Si gradient. The propagation of the high δ^{30}Si signal from the North Atlantic also traces the path of deepwater circulation: as noted in Section 4.3, the mid-latitude western Atlantic water column, which is strongly influenced by the deep western boundary current transporting NADW southwards, displays both lower [Si] and higher δ^{30}Si

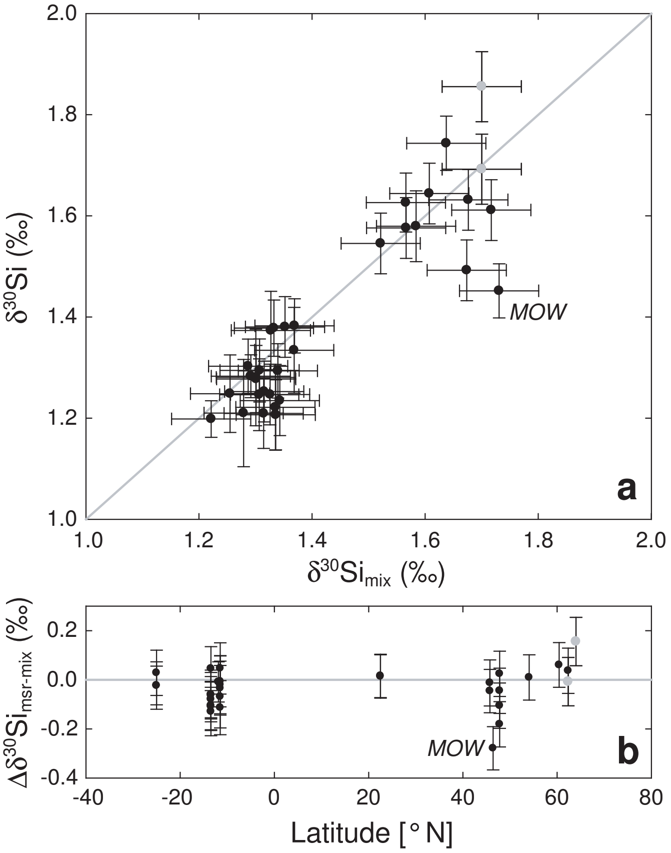

Figure 4.4: Quantifying the degree of conservativity of δ^{30}Si for samples below 2000 m. (a) A cross-plot of measured δ^{30}Si values with $\delta^{30}Si_{mix}$ values based on endmember contribution calculations (see Appendix A.2.2) shows good correspondence between the two values. Note that the sample affected by Mediterranean Outflow Water (MOW) lies most strongly away from the 1:1 line. (b) The latitudinal distribution of the deviation of measured δ^{30}Si values from those expected from mixing ($\Delta\delta^{30}Si_{msr-mix}$; see text) for the same samples, emphasizing that binary mixing explains deep δ^{30}Si values over the entire latitudinal range, with most sample plotting within error of $\Delta\delta^{30}Si_{msr-mix}$ = 0. Errors are propagated from δ^{30}Si and $\delta^{30}Si_{mix}$ values. Samples whose PO_4^* values were corrected to the North Atlantic endmember value of 0.76 µmol/kg (see Appendix A.2.2) are indicated as gray datapoints in both panels.

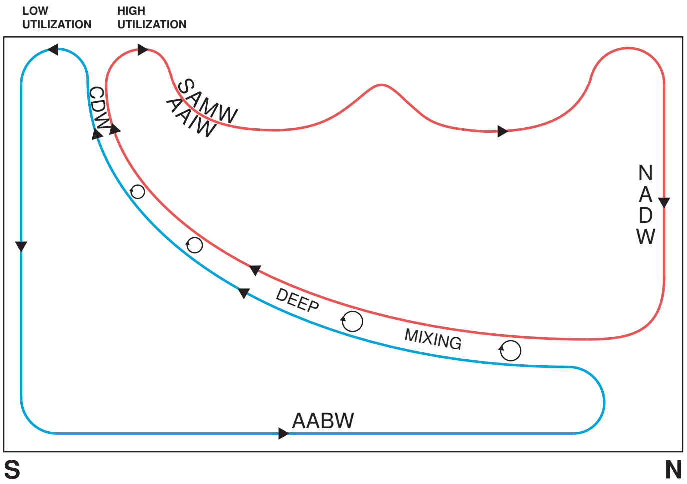

Figure 4.5: A cartoon illustration of large-scale features of the meridional overturning circulation, modified from Toggweiler et al. (2006).

values than the eastern Atlantic at the same latitude (Supplementary Figure A.2, Table 4.2).

By documenting the quasi-conservativity of Si and emphasizing the dominant influence of circulation on the δ^{30}Si distribution, our data robustly confirm minimal influence of opal dissolution on the Si distribution in the Atlantic (Broecker et al., 1991; Sarmiento et al., 2007), and indicate that processes such as boundary exchange, which has been suggested to result in a significant flux of Si into the global ocean (Jeandel et al., 2009), do not play a significant role in controlling the Si budget in the deep Atlantic.

4.4.2 Origin of δ^{30}Si signatures

The distinct δ^{30}Si signatures of North Atlantic and Southern Ocean waters are at odds with their homogeneity in δ^{15}N-NO_3 (e.g. Sigman et al., 2009a). Such a difference between these two broadly comparable nutrient isotope systems is surprising, and must reflect a dissimilarity in the oceanic cycles of Si and N. In the following, we first elucidate how the North Atlantic and Southern Ocean water masses obtain their distinct δ^{30}Si signatures, and the implications that this has for the oceanic Si cycle. Comparison with the δ^{15}N-NO_3 system allows us to suggest a reason for the difference between oceanic δ^{30}Si and δ^{15}N-NO_3 distributions.

Toggweiler et al. (2006) introduced a cartoon representation of the ocean circulation that provides an illustrative schematic framework for the following arguments (see also Gordon, 1991; Schmitz, 1996b,a). They separate the meridional overturning circulation (MOC) into two domains, or “loops”, as shown in Fig. 4.5: a southern loop dominated by AABW, and a northern loop dominated by NADW, fed by northward flow through the thermocline. These two domains interact to form Circumpolar Deep

Water (CDW) that upwells in the Southern Ocean, feeding both circulation loops. The prolonged exposure of the northern loop to biological activity at the surface leads to a strong depletion in nutrients. Below, we explain the origin of deepwater δ^{30}Si values in the context of this schematic, beginning with the southern loop.

Antarctic Bottom Water forms in the high latitudes of the Southern Ocean, primarily in the Weddell Sea (Weiss et al., 1979; Orsi et al., 1999), through a series of interactions of surface waters with shelf waters densified by brine rejection (Foster and Carmack, 1976; Huhn et al., 2008). Due to a combination of high upwelling rates and micronutrient- and light-limitation of plankton growth (e.g. Chisholm and Morel, 1991), these waters all contain high levels of macronutrients. The waters brought to the surface Antarctic by upwelling of CDW thus experience little Si depletion before they sink and are incorporated into AABW (Fig. 4.5), such that their nutrient properties remain similar to those of the upwelling CDW. Furthermore, the sinking waters entrain significant volumes of surrounding water as they traverse the slope, and experience strong mixing in the region of the Antarctic Circumpolar Current, such that they exit the Southern Ocean containing a considerable admixture of CDW (e.g. Mantyla and Reid, 1983). Considering this formation process, it is unsurprising that the δ^{30}Si value of AABW is indistinguishable from that of CDW at about +1.2‰ (this study and Cardinal et al., 2005), a value that in turn must reflect the balance of silicon inputs to and outputs from the Southern Ocean.

The North Atlantic water masses that contribute to NADW (i.e. DSOW, ISOW and LSW), on the other hand, are formed by the buoyancy loss of surface waters from lower latitudes that are transported into the high-latitude North Atlantic by the Gulf Stream/North Atlantic Current (e.g. Hansen and Østerhus, 2000; McCartney and Mauritzen, 2001; Brambilla et al., 2008), as represented by the northern loop of Fig. 4.5. Deep convection in the subpolar North Atlantic leads to the formation of Subpolar Mode Water, including its densest type, Labrador Sea Water (McCartney and Talley, 1982; Brambilla et al., 2008). Similarly, the Nordic overflows DSOW and ISOW are fed by light-to-dense conversions of waters of shallow North Atlantic origin in the Norwegian Sea (Mauritzen, 1996a,b; Hansen and Østerhus, 2000; Isachsen et al., 2007; Eldevik et al., 2009). In both of these cases, the surface waters that experience buoyancy loss have very low [Si] (Garcia et al., 2010b), such that, although they may have elevated δ^{30}Si values as a result of biological uptake of Si, they have limited potential to influence the δ^{30}Si value of a water mass formed by deep convection. This is because the Si budget – and thus δ^{30}Si signature – of the homogenized watermass formed by convection is strongly weighted ($\sim$95%) towards the entrained subsurface waters. In the case of both LSW and the Nordic overflows, these subsurface waters possess North Atlantic characteristics (McCartney and Talley, 1982; McCartney and Mauritzen, 2001). Thus, in order to trace the cause of the high δ^{30}Si value of NADW, we must understand what controls the Si budget, and thus δ^{30}Si value, of the North Atlantic subsurface.

4.4.3 Influence of the large-scale circulation

The northern loop of Fig. 4.5 indicates that the deep export of NADW from the North Atlantic is compensated by northward flow of waters in the upper ocean. This feature is supported by numerous observational constraints and inverse models (Schmitz and McCartney, 1993; Schmitz, 1995, 1996b; Ganachaud and Wunsch, 2000; Sloyan and Rintoul, 2001b,a; Lumpkin and Speer, 2003, 2007). The flow of upper Atlantic waters into the North Atlantic is associated with a northward transport of nutrients in the subsurface (e.g. Rintoul and Wunsch, 1991) that strongly influences the North Atlantic nutrient budget; indeed, the advective nutrient transport associated with the MOC is vital in maintaining North Atlantic nutrient stocks in the long term (Williams et al., 2006; Palter and Lozier, 2008). Such a dominant term in the nutrient mass balance should be a strong control on the δ^{30}Si value of the North Atlantic subsurface. Below, we estimate a δ^{30}Si value for this input.

Since the magnitude of diapycnal mixing in the main thermocline is small (Ledwell et al., 1993; Toggweiler and Samuels, 1993b; Toole et al., 1994; Schmittner et al., 2009), it is likely that the nutrients transported by the northward flow in the Atlantic thermocline are dominantly sourced from the waters that introduce nutrients into the thermocline in the south, i.e. SAMW and AAIW (Tsuchiya, 1989; Schmitz and McCartney, 1993; Sarmiento et al., 2004a; Williams et al., 2006; Palter and Lozier, 2008; Moore et al., 2009; Palter et al., 2010). The importance of a southern source of nutrients to the thermocline is also indicated by the δ^{30}Si systematics, in which the intersect between the upper- and deeper-ocean δ^{30}Si–1/[Si] relationships occurs at potential densities corresponding to these water masses. The intermediate cross-equatorial transport into the North Atlantic takes place in the σ_θ interval 26.8–27.2 (Schmitz, 1995, and references therein), which closely corresponds to the density range of SAMW and AAIW in the South Atlantic (σ_θ = 26.8–27.3; Larqué et al. (1997); Sallée et al. (2010)). The corresponding samples in our South Atlantic dataset have δ^{30}Si values ranging from +1.45‰ to +1.6‰, with an average of +1.5‰ when weighted by [Si] in the water mass. The NADW complex being transported southwards at 45°N has a concentration-weighted average only slightly higher than this (+1.6‰). In the context of the large-scale circulation represented by Fig. 4.5, this similarity suggests that the 0.4‰ offset in δ^{30}Si values between NADW and AABW is largely the result of the δ^{30}Si difference between the water masses of Southern Ocean origin, i.e. between AABW and SAMW/AAIW.

We investigate this possibility using an 8-box model based on the 7-box models of Toggweiler (1999) and Reynolds (2009) (see Appendix A.2.3). As illustrated in Fig. 4.6a, the circulation simulated by this model bears a close resemblance to the schematic view of Fig. 4.5. In its standard configuration, the model reproduces the observed deep δ^{30}Si gradient (Fig. 4.6b), which Reynolds (2009) has shown to be a robust feature of such models. In order to identify the ultimate source of this gradient, a simple

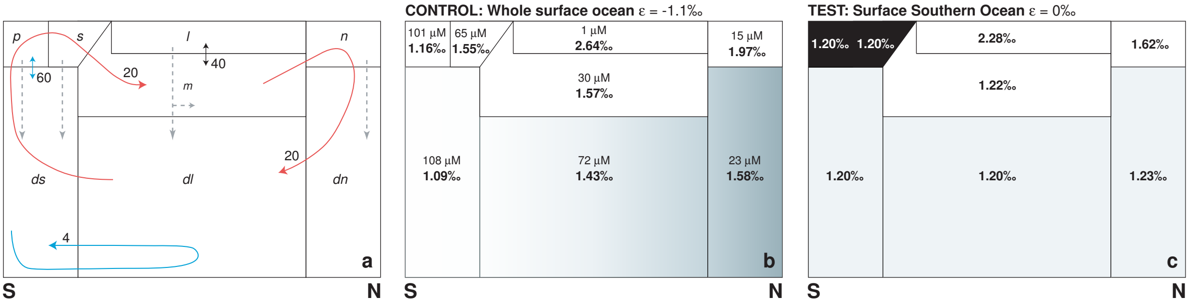

Figure 4.6: Results of the 8-box model. Panel *a* shows the model architecture, modified from Toggweiler (1999), with water fluxes in Sv (solid lines) and particulate export (dashed gray arrows). Boxes are *p*: southern polar surface, *s*: subantarctic surface, *l*: low-latitude surface, *n*: northern high-latitude surface, *m* thermocline and intermediate, *ds*: deep southern, *dl*: deep low-latitude, *dn*: deep northern box. Panels *b* and *c* show model results with isotope fractionation during utilization (represented by the isotope effect ε) prescribed (b) throughout the surface ocean and (c) everywhere in the surface ocean *except* the surface Southern Ocean boxes (filled). It can be seen that the North Atlantic–Southern Ocean δ^{30}Si gradient produced by the control model *b* disappears in the test case *c*. Modeled Si concentrations are identical for both model runs.

test is performed: by “switching off” isotope fractionation during utilization in the surface Southern Ocean, the model is prevented from creating an isotopic difference between intermediate and deep Southern Ocean waters. This approach has the advantage of leaving the elemental distribution of Si unaffected, which considerably simplifies the interpretation of model results. In this test configuration (Fig. 4.6c), the δ^{30}Si value of the North Atlantic is essentially identical to that of the deep Southern Ocean, despite isotope fractionation in the low- and high northern latitude surface ocean and a deep [Si]-gradient identical to that of the standard configuration. The presence of a deep δ^{30}Si gradient in the model is thus dependent upon the introduction of a high-δ^{30}Si signal into intermediate waters from the surface Southern Ocean. This model result thus supports the inference, based on knowledge of the large-scale circulation and the similarity between SAMW/AAIW and NADW δ^{30}Si values, that the transport of Si with a high δ^{30}Si value into the North Atlantic by the upper return path of the MOC must play an important role in producing the δ^{30}Si difference between NADW and AABW. Silicon uptake and isotope fractionation by diatoms in the surface Southern Ocean thus effectively fractionate Si isotopes between the two MOC loops of Fig. 4.5, producing a Si biogeochemical divide analogous to that for carbon (Marinov et al., 2006).

4.4.4 Si and N cycles

If the contrast in the δ^{30}Si signatures of NADW and AABW is due in large part to a δ^{30}Si difference between shallow and deep Southern Ocean waters, we should address (a) what in turn causes this difference, and (b) why this process does not result in a similar contrast in δ^{15}N-NO_3. A comparison of δ^{30}Si and δ^{15}N-NO_3 data in the Southern Ocean is highly instructive in this regard (Fig. 4.7; Sigman et al., 2000; Cardinal et al., 2005; DiFiore et al., 2006).

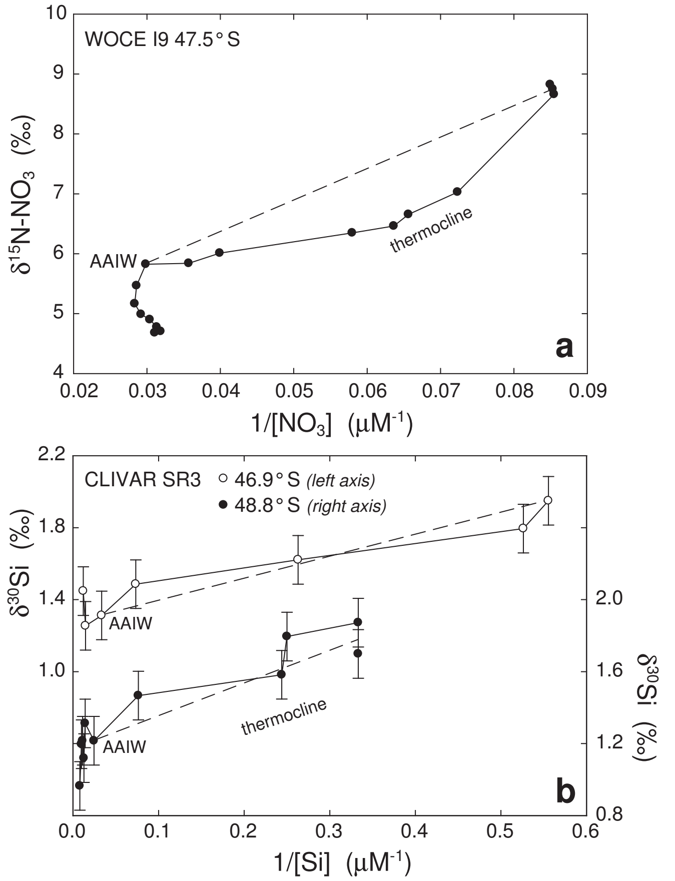

Figure 4.7: Data from station depth profiles (bottom to surface) plotted in mixing space to illustrate relationships between (a) δ^{15}N-NO$_3$ (Sigman et al., 2000) and (b) δ^{30}Si values (Cardinal et al., 2005) of water masses in the Subantarctic Southern Ocean. Whilst δ^{15}N-NO$_3$ values in the Subantarctic thermocline are too low to be explained by mixing in the local water column (dashed line in *a*), δ^{30}Si values are consistent with such a mixing origin (dashed lines in *b*). Silicon isotope data are converted from δ^{29}Si using the conversion factor of 1.96 (Reynolds et al., 2006b). Nitrate concentrations were converted to µM using a constant σ_θ of 27 as in Sigman et al. (2000).

Sigman et al. (2000) found that δ^{15}N-NO$_3$ values in the Subantarctic thermocline were too low to be explained by mixing in the Subantarctic alone (Fig. 4.7a), and hypothesized that this feature might be due to the influence of subtropical waters whose isotopic composition has been affected either by nitrogen fixation or by mixing with very N-depleted low-latitude surface waters. The same mixing calculation for the δ^{30}Si data of Cardinal et al. (2005) reveals that, unlike δ^{15}N-NO$_3$, δ^{30}Si values in the Subantarctic thermocline are consistent with mixing between Antarctic and Subantarctic waters (Fig. 4.7b), as also concluded by Fripiat (2010). Figure 4.8 clearly illustrates the relationship between the salinity minimum of AAIW in the Subantarctic subsurface and elevated δ^{30}Si values there (Fig. 4.8b), an association that is not observed to the same extent for δ^{15}N-NO$_3$ (Fig. 4.8a). Considering that mixing with low-nutrient subtropical surface waters should affect both δ^{30}Si and δ^{15}N-NO$_3$ values in the Subantarctic thermocline to a similar degree, we suggest that the lower-than-expected δ^{15}N-NO$_3$ of the Subantarctic thermocline (Fig. 4.7a) results rather from the influence of low-latitude nitrogen fixation.

This suggests a cause for the difference between the oceanic δ^{30}Si and δ^{15}N-NO$_3$ distribution at the basin scale: SAMW/AAIW δ^{15}N-NO$_3$ values are depressed even at high latitudes due to the influence of regions of nitrogen fixation, a signal that is reinforced by “downstream” nitrogen fixation at low northern latitudes (Knapp et al., 2008) that further reduces the δ^{15}N-NO$_3$ of the Atlantic thermocline. No such complexity influences the Si isotope system, such that southern mode and intermediate waters (a) form with a higher δ^{30}Si value than the deep Southern Ocean and (b) can impart this high value to the entire Atlantic thermocline. The MOC-driven nutrient transport into the North Atlantic – the northern loop of Fig. 4.5 – is thus significantly different in δ^{30}Si, but not in δ^{15}N-NO$_3$, from the deep Southern Ocean. The δ^{30}Si and δ^{15}N-NO$_3$ signatures of NADW thus ultimately reflect processes related to the interaction of biology and the physical circulation in the Southern Ocean (nutrient utilization, water mass subduction) and the global low-latitude upper ocean (nitrogen fixation, thermocline ventilation, MOC closure).

4.5 Global δ^{30}Si distribution: Perspectives

Although the focus of this paper is the biogeochemistry of Si in the Atlantic Ocean, it would be amiss not to at least briefly discuss this first comprehensive Atlantic δ^{30}Si dataset in the global context. In their “first look” at seawater δ^{30}Si values, De La Rocha et al. (2000) argued for a diatom dissolution flux into deepwaters with, on average, a lower δ^{30}Si value than seawater. Beucher et al. (2008), in contrast, utilized a compilation of Southern Ocean and Pacific data to argue for a δ^{30}Si value of the dissolution flux that is higher than that of deepwaters. This study has highlighted the important role, also recognized by De La Rocha et al. (2000), that physical processes – i.e. deepwater formation

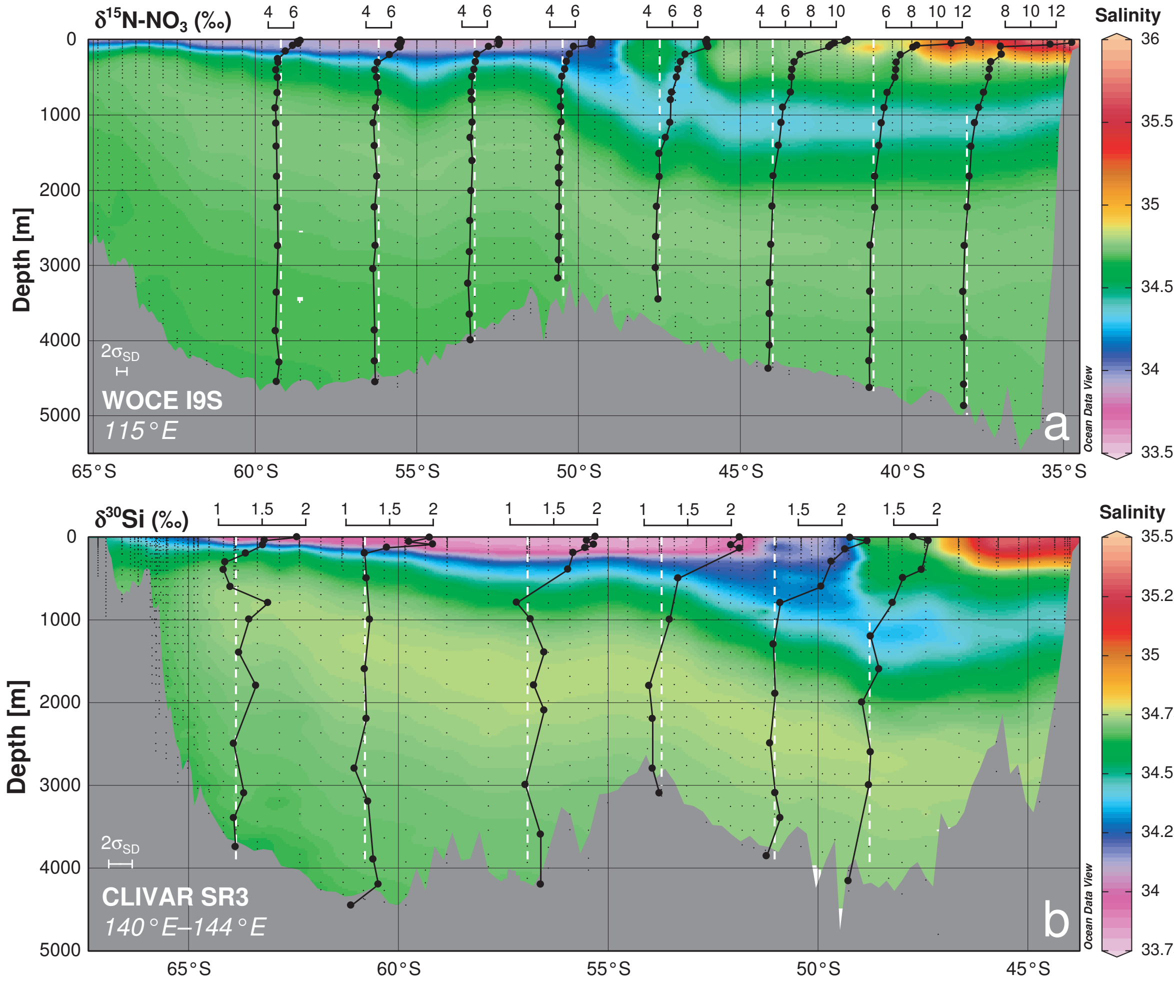

Figure 4.8: Relationship between water masses and nutrient isotope composition in the Southern Ocean south of Australia. The salinity color map indicates the presence of AAIW in the subsurface as a salinity minimum north of ∼50°S. Superimposed on this are depth profiles of (a) δ^{15}N-NO$_3$ values (Sigman et al., 2000) and (b) δ^{30}Si values (Cardinal et al., 2005). The δ^{30}Si data show a clear relationship of elevated values in the Subantarctic subsurface associated with the salinity minimum, whilst δ^{15}N-NO$_3$ values remain relatively low throughout the Subantartic subsurface, with large isotopic gradients remaining restricted to the uppermost water column as in the Antarctic (see also DiFiore et al., 2006). The dashed line in each depth profile marks the sampling position and indicates the isotope composition of the mean deep ocean (panel *a*, δ^{15}N-NO$_3$ = 5‰) or the deep Southern Ocean (panel *b*, δ^{30}Si = 1.2‰). Silicon isotope data are converted from δ^{29}Si as in Fig. 4.7. Salinity color maps were created with ODV (Schlitzer, 2009) using data from the eWOCE (Schlitzer, 2000) and CCHDO (http://cchdo.ucsd.edu/) databases.

and nutrient transport by the ocean circulation – play in setting deep ocean δ^{30}Si values. We would thus argue that global deepwater δ^{30}Si gradients cannot be interpreted quite as simply as either of these previous contributions has done. Rather, interpretation of the oceanic δ^{30}Si distribution must consider the influence of both biological cycling and ocean circulation – that is, the *remineralized* and *preformed* contributions to the observed δ^{30}Si distribution.

Such analyses may be performed in the quantitative framework of global circulation models (GCMs), provided that these models conform to the observational constraint of a strong deepwater δ^{30}Si gradient, which is not the case for the only published GCM study (Wischmeyer et al., 2003). Reynolds (2009) did reproduce this gradient with box models, but could not adequately explain the disagreement with GCM results. In fact, several plausible reasons do exist for the inability of Wischmeyer et al.'s (2003) model to produce deepwater δ^{30}Si gradients. An evaluation of the ventilation behavior of 13 ocean models (Dutay et al., 2002) has demonstrated that the physical model employed by Wischmeyer et al. (2003) strongly underestimates the ventilation of intermediate waters, which our analysis would indicate are vital for the production of a large-scale deepwater δ^{30}Si gradient. The poor intermediate water ventilation in Wischmeyer et al.'s (2003) model might be due to its representation of lateral mixing (Maier-Reimer et al., 1993), which does not parametrize the advection of density and tracers by mesoscale eddies (Gent and McWilliams, 1990). This eddy-induced transport plays an important role in the subduction of water masses in the Southern Ocean (Marshall, 1997), and its correct parametrization has been shown to improve GCM representation of the oceanic Si cycle (Gnanadesikan, 1999a; Gnanadesikan and Toggweiler, 1999). Additionally, models lacking the Gent-McWilliams parametrization tend to overestimate the Si export flux from the Southern Ocean (Gnanadesikan, 1999a; Dunne et al., 2007), which is perhaps why the coupled biological-physical model of Wischmeyer et al. (2003) displays its strongest deviation from observational [Si] data in the surface Southern Ocean, suggesting that Si cycling in this region is inaccurately captured. Furthermore, the physical model in Wischmeyer et al.'s (2003) study employed an upwind tracer advection scheme (Maier-Reimer et al., 1993) that results in large numerical diffusion (e.g. Gerya, 2010). This implicit strong mixing might inhibit large isotopic gradients at depth, as well as diluting any high-δ^{30}Si signal in intermediate waters by strong vertical mixing with the deep. It is thus possible that the combination of these dynamical and biogeochemical weaknesses prevented Wischmeyer et al.'s (2003) model from forming southern intermediate and mode waters with the correct biogeochemical properties, such that it did not accurately represent the northward MOC-driven nutrient transport. Future modeling efforts should focus on reproducing the large-scale, first-order observational constraints that we have documented here.

4.6 Summary and Conclusions

Our high-precision δ^{30}Si dataset for the Atlantic Ocean demonstrates the strength of seawater δ^{30}Si as a tracer of the biogeochemical cycling of Si in the sea. The stable isotope composition of dissolved silicon traces mixing between water masses of North Atlantic and Southern Ocean origin, which implies that Si has no significant sources or sinks at depth in the Atlantic Ocean. The contrasting δ^{30}Si values of the North Atlantic and the deep Southern Ocean are, in turn, most likely the result of the fractionation signature introduced into the thermocline by the interaction of biological Si uptake with mode- and intermediate-water mass formation at high southern latitudes. Biological activity in the surface Southern Ocean thus imparts distinct δ^{30}Si values to the two “loops” of *Toggweiler et al.*’s (2006) MOC representation, with the large-scale interaction of these loops producing the basin-scale Atlantic δ^{30}Si distribution.

The Si isotope data presented here thus provide strong evidence for a regime of nutrient transport in the ocean that is closely coupled to lateral transports related to the meridional overturning circulation. In combination with our box-modeling approach, the δ^{30}Si data robustly and independently corroborate previous inferences (Sarmiento et al., 2004a) of the importance of the Southern Ocean’s biogeochemical divide (Marinov et al., 2006) in determining global oceanic nutrient distributions, and thus the distribution and magnitude of oceanic primary productivity. Furthermore, the pathways of large-scale tracer transport in the ocean are directly relevant to the fundamental mechanisms driving the MOC (Gnanadesikan, 1999b). The insights provided by seawater δ^{30}Si data thus reach far beyond the oceanic Si cycle and touch upon fundamental questions in modern oceanography.

Chapter 5

Controls on δ^{30}Si in the Atlantic thermocline*

Abstract

The distribution of nutrients within the global low-latitude thermocline regulates the magnitude and distribution of oceanic primary productivity, with implications for marine food webs and ocean– atmosphere CO_2 exchange. We present a high-precision dataset of the stable isotope composition (δ^{30}Si) of dissolved silicon (Si) in the thermocline of the Atlantic Ocean that provides new insights into the processes governing the thermocline distribution of Si. Although depth profiles of δ^{30}Si values vary with location, the entire sampled thermocline exhibits a single, coherent δ^{30}Si–[Si] relationship. The Atlantic δ^{30}Si systematics reveals the presence of two biogeochemical regimes of Si cycling, separated by lower-thermocline waters of Southern Ocean origin. The pivotal role of these water masses bears witness to their importance as a source of Si to the Atlantic thermocline. Within the thermocline, high δ^{30}Si values are not restricted to the euphotic zone where fractionation of Si isotopes by diatom productivity takes place, but extend significantly into the subsurface. The presence at depth of elevated δ^{30}Si values, which trace Si that has been previously fractionated at the surface, documents that a significant proportion of the Atlantic Si inventory is preformed, i.e. transported into the interior by the circulation. Thermocline ventilation and the associated mixing processes are thus instrumental in determining the thermocline δ^{30}Si distribution by introducing the signal of biological Si utilisation into the interior. This emphasizes the importance of physical ventilation processes, and their interaction with biological nutrient drawdown over the surface ocean, in determining the thermocline distribution of Si.

---

*A version of this chapter will be submitted to *Global Biogeochemical Cycles* as G. F. de Souza, B. C. Reynolds, and B. Bourdon: “Strong physical control on the silicon stable isotope distribution in the oceanic thermocline”.

5.1 Introduction

The supply of nutrients from the shallow subsurface ocean supports marine primary productivity in the ocean's sunlit surface layer, the euphotic zone. The food web that is supported by this photosynthetic production of fixed carbon produces organic matter that sinks through the oceanic water column. Some of this organic matter escapes degradation in the shallow subsurface – both in the seasonal thermocline accessible to wintertime entrainment, and in the main thermocline below it – and exports nutrients and carbon to the deep sea, where they are sequestered for tens to hundreds of years. Thus, in order for primary productivity to be maintained on multiannual timescales (Williams and Follows, 2003), the shallow subsurface nutrient inventory must be replenished by a flux of dissolved nutrients from the deep ocean into the main thermocline, and from there to the seasonal thermocline, which interacts with the euphotic zone over the annual cycle.

In the classical view, this nutrient transfer is directed vertically everywhere in the ocean, with nutrients being supplied from below by upwelling and/or turbulent mixing *across* density surfaces. However, numerous observations (e.g. Rooth and Östlund, 1972; Toole et al., 1994; Ledwell et al., 1998) indicate that such diapycnal mixing is inhibited by the strong density gradient of the open ocean thermocline, requiring that both the replenishment of thermocline nutrients and their distribution within the thermocline be re-interpreted in the context of a thermocline that mixes primarily *along* density surfaces, i.e. a thermocline that is to a large degree isopycnal, or adiabatic (Iselin, 1939; Stommel, 1979; Luyten et al., 1983), with diapycnal mixing restricted to a few suitable locations (Munk and Wunsch, 1998; Naveira Garabato et al., 2004). Williams and Follows (1998) were the first to emphasize the importance of lateral, wind-driven processes in transferring nutrients from the main thermocline to the euphotic zone at the scale of the subtropical gyre, whilst Sarmiento et al. (2004a) demonstrated the near-global importance of mode waters formed at high southern latitudes for the transfer of nutrients from the deep ocean to the base of the main thermocline.

Since the distribution of nutrients in the thermocline determines the distribution (Palter et al., 2005), magnitude (Sarmiento et al., 2004a) and ecological assemblage (Egge and Asknes, 1992; Cermeño et al., 2008) of low-latitude primary productivity, a more complete understanding of the processes responsible for the observed nutrient tracer fields will improve our understanding of the ultimate controls on primary productivity, allowing better assessments of how ocean productivity may change in the future (Sarmiento et al., 2004b; Cermeño et al., 2008) and why it has changed in the past (Brzezinski et al., 2002; Kohfeld et al., 2005; Galbraith et al., 2008).

The export of organic matter to the deep ocean is strongly driven by diatoms (Buesseler, 1998), siliceous phytoplankton with an opportunistic ecological strategy (Margalef, 1978) that results in their forming large blooms in times of sufficient nutrient availability, followed by population collapse and

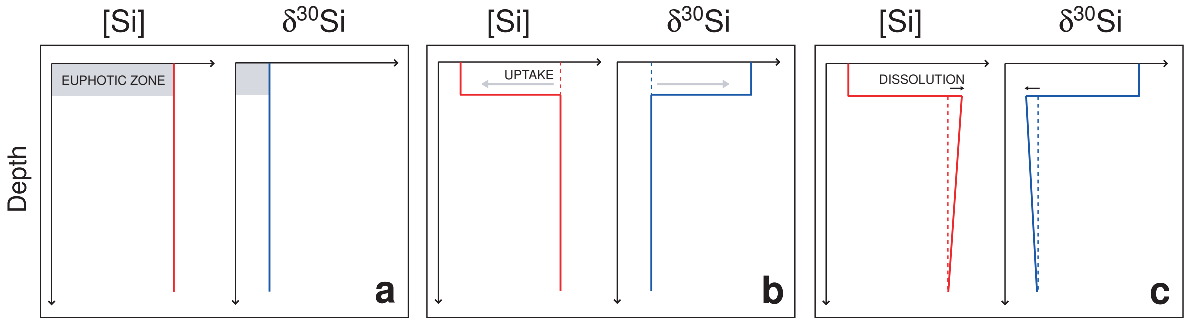

Figure 5.1: A one-dimensional schematic indicating the effect of biological cycling on oceanic δ^{30}Si values. Consider an initially homogeneous water column (panel *a*; gray band marks the euphotic zone); diatom utilization of Si in the euphotic zone (panel *b*) will result in a decrease in [Si] and corresponding increase in δ^{30}Si value of the euphotic zone, since diatoms preferentially incorporate the lighter isotopes of Si. The subsequent export and dissolution (panel *c*) of this diatom opal with low δ^{30}Si value (with or without accompanying isotope fractionation) will lead to decrease in δ^{30}Si values in the subsurface. The panels of the schematic may be viewed as snapshots of a stagnant water column or equilibria of a purely advective (upwelling) scheme and follow from simple isotopic mass balance. Whilst the exact shape of the gradient produced by dissolution in panel *c* depends on the assumed depth evolution of the opal dissolution flux, mass balance demands that dissolution lower the δ^{30}Si value of the subsurface, such that it cannot produce a δ^{30}Si gradient towards the δ^{30}Si value of the euphotic zone.

sinking once nutrients are depleted. This boom–bust behavior makes diatom productivity and export the most important mechanism for the cycling of silicon (Si) within the ocean (Tréguer et al., 1995; DeMaster, 2009) and strongly couples the marine cycles of carbon and Si (Smetacek, 1999; Dugdale and Wilkerson, 2001). The stable Si isotope composition of silicic acid in seawater (expressed as δ^{30}Si; see Section 5.2.2) is an excellent tracer of this cycling, since the uptake of silicic acid by diatoms in the euphotic zone is associated with Si isotope fractionation (De La Rocha et al., 1997): diatoms preferentially incorporate the lighter isotopes of Si into their opaline frustules, such that a dissolved Si pool that has been partially utilized by diatoms in the euphotic zone is enriched in its heavier isotopes, and hence bears a high δ^{30}Si value (e.g. Cardinal et al., 2005). The dissolution of diatom opal, on the other hand, tends to lower seawater δ^{30}Si values, an effect that might be amplified by Si isotope fractionation during opal dissolution (Demarest et al., 2009). Seawater δ^{30}Si values may thus be applied to infer the processes that are are dominantly responsible for the observed oceanic Si distribution, and pathways by which oceanic Si transport takes place.

In this contribution, we focus on the δ^{30}Si distribution in the main thermocline, where the strongest δ^{30}Si depth gradients are seen (Reynolds et al., 2006a; Beucher et al., 2008, 2011). Thus far, the origin of these gradients has not been discussed in detail. This is surprising, since it is not obvious how they are produced: as illustrated by the one-dimensional (1D) schematic of Fig. 5.1, the biological cycling processes discussed above cannot produce the observed higher δ^{30}Si values in the subsurface water column. Some other processes must thus introduce high δ^{30}Si values, produced in the euphotic zone, into the subsurface. We utilize our Atlantic thermocline δ^{30}Si data, which represent the first comprehensive δ^{30}Si dataset from the subducted thermocline, to elucidate the processes by which the subsurface gradients in δ^{30}Si are produced. We show that the Atlantic δ^{30}Si systematics documents a decoupling of thermocline Si cycling from the deep ocean, which provides evidence for the importance of Southern Ocean sources of nutrients to the thermocline and minimal influence of low-latitude deepwater upwelling. By considering the magnitudes of the relevant processes and their timescales, we show that the vertical δ^{30}Si gradient within the thermocline must be related to the preformed component of Si, which is transported into the thermocline during water mass subduction. In the conceptual framework of ventilated thermocline theory (Luyten et al., 1983), we elucidate the processes by which this preformed δ^{30}Si gradient may come about, and discuss the processes that lead to the coherent δ^{30}Si systematics of the Central Waters of the Atlantic thermocline. This analysis provides insights into the complex series of physical–biological interactions that controls the distribution of Si within the ventilated thermocline.

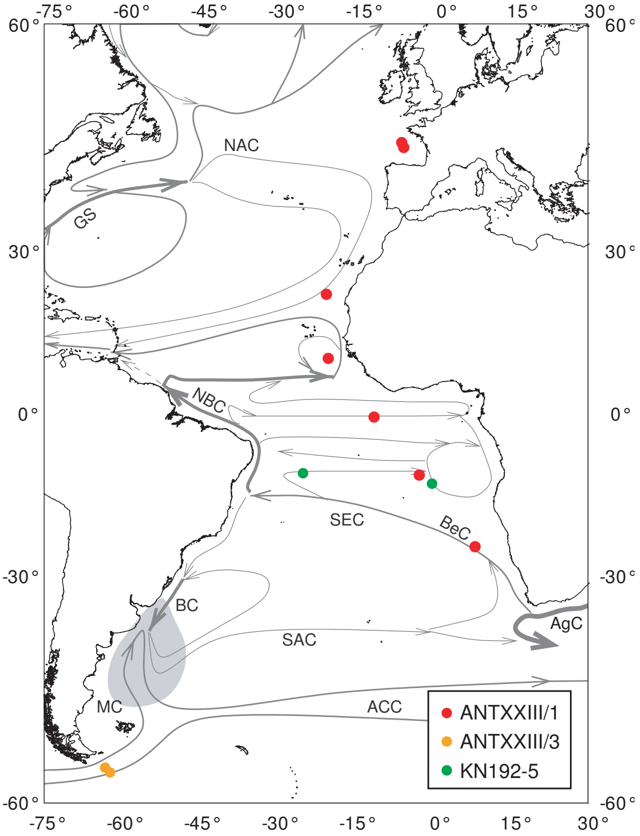

Figure 5.2: Locations from which samples were procured for this study, with schematic representation of upper ocean currents from Stramma et al. (2001). See also Table 4.1. The Brazil–Malvinas Confluence is indicated by gray shading. ACC: Antarctic Circumpolar Current; MC: Malvinas Current; AgC: Agulhas Current; SAC: South Atlantic Current; BC: Brazil Current; BeC: Benguela Current; SEC: South Equatorial Current; NBC: North Brazil Current; GS: Gulf Stream; NAC: North Atlantic Current.

5.2 Methods

5.2.1 Sample Collection

Our sampling of the Atlantic thermocline can be viewed as a combination of two strategies: six stations cover a wide latitudinal range of the eastern Atlantic at relatively low depth resolution, while two stations in the eastern and western Atlantic are sampled at high depth resolution ($\leq$ 100 m in the thermocline). This combination allows both a broad overview of the Atlantic thermocline distribution, as well as a more detailed analysis of selected depth profiles.

A total of 61 seawater samples from the Atlantic Ocean and adjacent basins, previously introduced in Chapter 4, are included in this study, although our discussion will focus primarily on 30 samples with potential density $\sigma_\theta \leq 27.3$. Twenty-nine samples were collected at 6 stations from the Bay of Biscay to the Cape Basin in the eastern Atlantic Ocean, during expedition ANT XXIII/1 of R/V *Polarstern* (Rickli et al. (2009); October–November 2005; see Fig. 5.2 and Table 4.1 for all station locations). Two detailed profiles (17 samples each) from the tropical Brazil and Angola Basins were collected during expedition KN192-5 of R/V *Knorr* (November–December 2007). In addition, two samples from Drake Passage (R/V *Polarstern* expedition ANT XXIII/3) were procured. All samples were filtered onboard using either 0.45 µm nitrocellulose (*Polarstern*) or 0.45 µm polycarbonate (*Knorr*) filters. Samples from the *Polarstern* expeditions were acidified onboard with 0.1% v/v distilled 9.5 M HCl (Rickli et al., 2009), while samples from expeditions KN192-5 were acidified with 0.1% v/v distilled 6 M HCl in the laboratory at least 12 hr before preconcentration.

5.2.2 Sample Preconcentration and Analysis

A detailed description of sample processing and isotopic analysis is given in Chapter 4. Briefly, Si is pre-concentrated from seawater samples by co-precipitation with brucite, following a method modified from Karl and Tien (1992). After this preconcentration step, cation exchange chromatography (AG50W-X8; BioRad Laboratories) is employed to separate uncharged H_4SiO_4 from the cationic matrix. The stable isotopic composition of Si is subsequently measured on a high-resolution MC-ICPMS (*NuPlasma 1700*; Nu Instruments, UK) using a standard–sample bracketing protocol. Silicon stable isotope composition is reported as the deviation from the standard reference material NBS28, δ^{30}Si, expressed in permil:

$$\delta^{30}\text{Si (in ‰)} = \left(\frac{\left(\frac{^{30}\text{Si}}{^{28}\text{Si}}\right)_{\text{sample}}}{\left(\frac{^{30}\text{Si}}{^{28}\text{Si}}\right)_{\text{NBS 28}}} - 1 \right) \times 1000$$

The long-term external reproducibility of our δ^{30}Si analyses is $\pm$0.12‰ ($2\sigma_{SD}$), as estimated from the variance of $>$300 measurements of the secondary isotopic standard Diatomite (Brzezinski et al., 2006; Reynolds et al., 2007) over $>$3 yr. The average δ^{30}Si value of Diatomite measured over this period is +1.22$\pm$0.01‰ ($2\sigma_{SEM}$), which is consistent with the inter-laboratory comparison study of Reynolds et al. (2007). Except in the case of near-surface samples with low amounts of Si, reported sample δ^{30}Si values are the mean of at least 3, and up to 11, complete replicate analyses in at least 2 separate analytical sessions. External errors on the seawater data, reported as 2 standard errors of the mean ($2\sigma_{SEM}$), are usually $\pm$0.07‰ or better (see Table 4.2).

In this contribution, the notations Si, [Si] and δ^{30}Si will refer to *dissolved* silicon (i.e. silicic acid), its concentration and isotopic composition respectively.

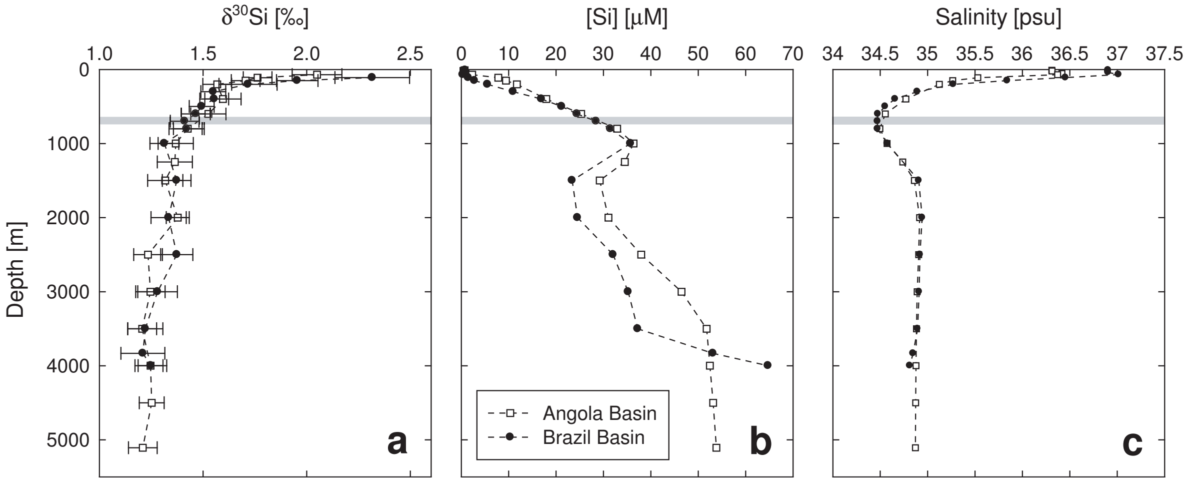

Figure 5.3: Full depth profiles of (*a*) δ^{30}Si, (*b*) Si concentration and (*c*) salinity for two stations from the eastern (Angola Basin, open squares) and western (Brazil Basin, solid squares) Atlantic Ocean. The gray bar in all panels corresponds to the depth of the salinity minimum associated with AAIW.

5.3 Results

Values of δ^{30}Si increase upwards in the water column from +1.2‰ in bottom waters to almost +3‰ in the surface mixed layer (see Table 2 and examples in Fig. 5.3). The δ^{30}Si gradient is strongest within the thermocline, above the salinity minimum associated with Antarctic Intermediate Water (Fig. 5.3c). Figure 5.4 shows the upper ocean distributions of [Si] and δ^{30}Si at two stations (Stas 3 and 13 from expedition KN192-5) in the eastern and western South Atlantic (Angola and Brazil Basins respectively). The depth profiles in Fig. 5.4a and 5.4b show close similarity in both [Si] and δ^{30}Si values up to a depth of $\sim$200 m, above which they diverge. When plotted against potential density σ_θ, however, the [Si] and δ^{30}Si distributions are very similar at both stations (Fig. 5.4d and e).

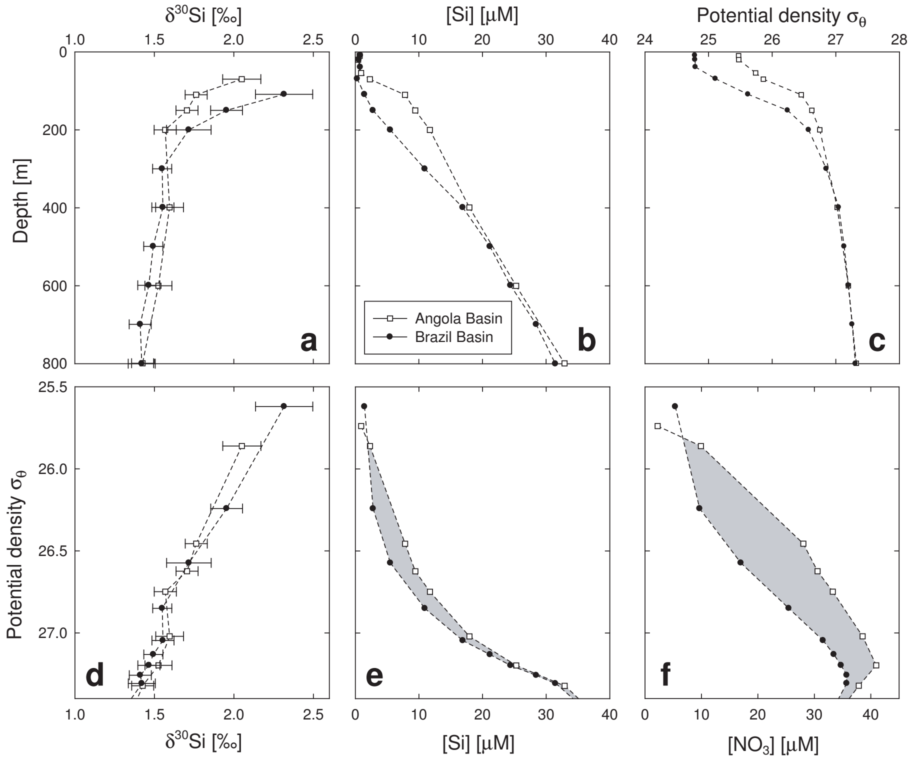

Figure 5.4: Upper ocean profiles above the depth of the salinity minimum (see Fig. 5.3). Depth profiles of (*a*) δ^{30}Si, (*b*) Si concentration and (*c*) potential density are shown in the upper panels, whilst in the lower panels (*d*) δ^{30}Si, (*e*) [Si] and (*f*) [NO$_3$] are plotted against potential density. In panels *e* and *f*, the gray shaded areas emphasize the difference between the strong remineralization signal observed for [NO$_3$] in the Angola Basin, as opposed to a minor [Si] signal.

There is generally a surprisingly strong coherence in the δ^{30}Si systematics throughout the sampled Atlantic thermocline, as illustrated by the relationship between δ^{30}Si and [Si]: values of δ^{30}Si show well-defined relationships with both [Si] and its reciprocal 1/[Si], as shown in Fig. 5.5. The δ^{30}Si–1/[Si] relationship (Fig. 5.5b) exhibits two linear relationships intersecting at a 1/[Si] value (0.09–0.06) corresponding to water samples with σ_θ of 26.8–27.0. In a θ–S diagram (Fig 5.6), it can be seen that almost all samples defining the thermocline (i.e. $\sigma_\theta \leq 27$) δ^{30}Si–1/[Si] relationship are from the Central Waters of the Atlantic thermocline, with samples from all but one station (Sta 11 of expedition ANTXXIII/1) within the South Atlantic Central Water (SACW). Exceptions are three samples from the Bay of Biscay that are denser and Si-poorer than most other samples with similar δ^{30}Si values (Fig. 5.5b). Water-column structure, as evinced by θ–S curves (Fig. 5.6), is considerably different in the Bay of Biscay, reflecting the influence of Mediterranean Overflow Water (MOW).

5.4 Discussion

Unlike the continuous [Si] and δ^{30}Si depth profiles (Fig. 5.3), the Atlantic δ^{30}Si systematics exhibits a surprisingly sharp discontinuity: the Atlantic δ^{30}Si–1/[Si] relationship (Fig. 5.5b) consists of two intersecting linear arrays. In Chapter 4, we show that the steep array in deepwaters ($\sigma_2 \geq$ 36.95) is related to the mixing of Si from northern and southern deepwater sources. Shallower waters do not extend this deepwater array, but scatter closely around a linear relationship with lower slope, extending towards samples in the euphotic zone where Si isotopes are actively fractionated during diatom uptake of Si. Interestingly, the intersection between these two arrays is associated with waters characterized by potential densities of σ_θ = 26.8–27 (colors in Fig. 5.5b) and negative values of Si* around –15 µM (Si* = [Si] - [NO_3]; Table 2 and Supplementary Figure A.10). Thus, potential densities at the sharp discontinuity in the Atlantic δ^{30}Si–1/[Si] relationship correspond to a fundamental oceanographic feature, the base of the main thermocline. Additionally, the negative Si* values are characteristic of Subantarctic Mode Water (SAMW), which ventilates the base of the main thermocline from the south (e.g. Hanawa and Talley, 2001) and has been shown to play a vital role in the replenishment of thermocline nutrients (Sarmiento et al., 2004a; Palter et al., 2010).

These observations indicate that the dichotomy in the Atlantic δ^{30}Si–1/[Si] relationship is brought about by the coherent evolution of δ^{30}Si values of thermocline waters from the pivotal intersection point reflecting SAMW. A simple, coherent δ^{30}Si–1/[Si] relationship applies to the entire latitudinal range of the thermocline sampled in this study, with a clear and continuous gradation in δ^{30}Si values with potential density (Fig. 5.5b) except in the Bay of Biscay, which is influenced by overflows from the Mediterranean Sea. Taken together, these characteristics imply a strong control of physical ocean structure on the δ^{30}Si distribution. Although such a strong physical influence on a nutrient that is cycled through the upper ocean might seem counterintuitive, it is consistent with the nature of dissolved chemical tracers, which record a signal that is integrated over their residence time within the system. This necessitates that we interpret the thermocline δ^{30}Si distribution in the context of the circulation and ventilation of the thermocline – an approach that is necessary to explain the observed δ^{30}Si systematics.

5.4.1 Relevant controls on δ^{30}Si

The fractionation of Si isotopes during the uptake of Si by diatoms in the euphotic zone (De La Rocha et al., 1997) is the *ultimate* source of the δ^{30}Si gradients observed within the ventilated thermocline (and, indeed, the global ocean). However, diatom uptake cannot, of course, be *directly* responsible for any variability in waters outside the near-surface region of active uptake, and thus other processes must transmit the high-δ^{30}Si signal of utilization into the subsurface. Taken at face value, the linear

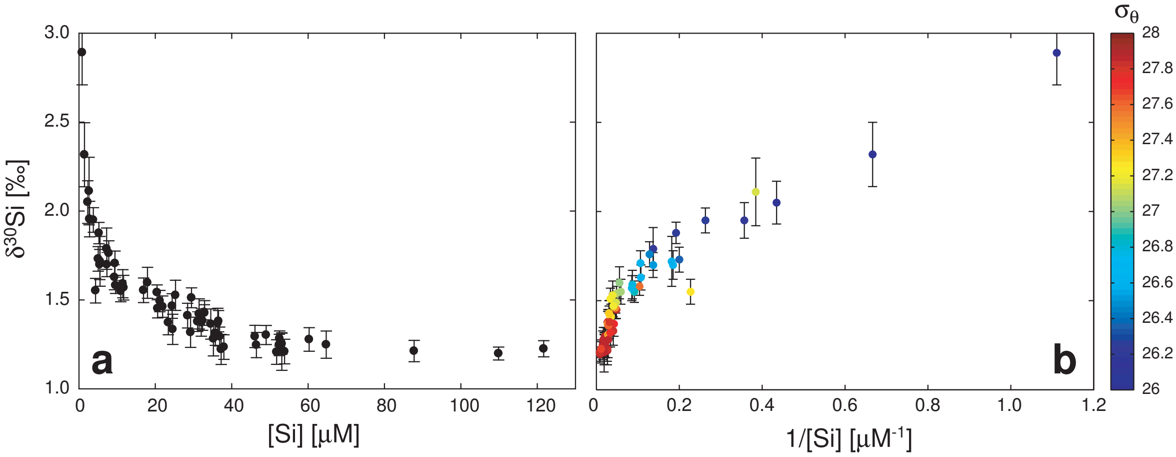

Figure 5.5: Silicon isotope systematics of the Atlantic water column, illustrated by δ^{30}Si–[Si] (panel *a*) and δ^{30}Si–1/[Si] (panel *b*) relationships. In panel *b*, datapoint colors refer to sample potential density σ_θ. Panel *b* clearly shows that the apparently logarithmic δ^{30}Si–[Si] relationship in panel *a* is the result of two intersecting linear δ^{30}Si–1/[Si] arrays. These two arrays intersect at values of σ_θ (26.8–27) corresponding to the base of the main thermocline. The three datapoints whose σ_θ values stand out in the thermocline array are from the Bay of Biscay, which is significantly influenced by overflow waters from the Mediterranean Sea.

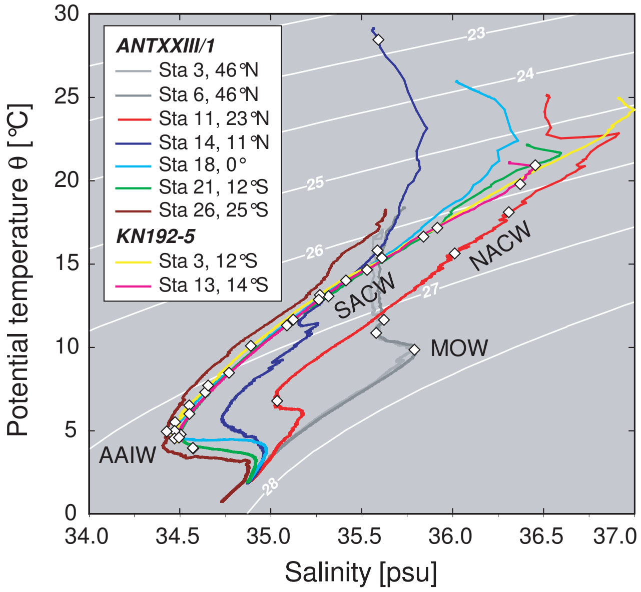

Figure 5.6: A $\theta - S$ plot for all stations shown in Fig. 5.2. Note that most samples discussed here (white diamonds) lie along the linear $\theta - S$ relationship of South Atlantic Central Water (SACW).

δ^{30}Si–1/[Si] relationship defined by thermocline waters (Fig. 5.5b) implies mixing between basal thermocline and near-surface waters (e.g. Albarède, 1996). However, the diapycnal diffusivity of the open ocean thermocline is not sufficiently large (e.g. Toggweiler and Samuels, 1993b; Ledwell et al., 1993; Toole et al., 1994) to be relevant over the lengthscales related to the observed δ^{30}Si–1/[Si] relationship – i.e. $\sim$500 m depth and $\sim$5000 km length. This is illustrated by the thermocline Péclet number that compares vertical diffusive and lateral advective timescales, which has a value of 50 (see Appendix A.3.1). The indicated importance of lateral (strictly, isopycnal) advection is consistent with the clear gradation of δ^{30}Si values with potential density (Fig. 5.5b), a point we shall return to later.

The dissolution of sinking diatom opal is typically implicitly or explicitly assumed to cause δ^{30}Si gradients in the upper mesopelagic ocean (e.g. Cardinal et al., 2005; Beucher et al., 2011). This assumption stems from the intuitive deduction that the inventory of Si contributed by opal dissolution should increase with depth. Since diatom opal generally bears low δ^{30}Si values (e.g. core-top and suspended opal in De La Rocha et al., 1998; Varela et al., 2004; Pichevin et al., 2009), this increasing contribution should result in lower δ^{30}Si values. Additionally, isotope fractionation during opal dissolution (Demarest et al., 2009) bears the potential to further amplify this effect. In other words, this view expands the simple 1D schematic of Fig. 5.1, by taking into account the increasing age of water parcels with depth, which allows them to accumulate more remineralized nutrients. This holds true for the subducted thermocline as well, where estimated ventilation ages increase by a factor of 2–5 (Sabine et al., 2005; Karstensen et al., 2008) over the σ_θ range of the thermocline δ^{30}Si–1/[Si] relationship. However, it is important to note that the degree to which the isotopic signal of opal dissolution is expressed depends not on the *inventory* of remineralized Si, but its *relative* contribution to total Si – i.e. on the proportion of remineralized to preformed Si in the water parcel. Whilst the preformed contribution to total Si is generally low in the thermocline (Sarmiento et al., 2004a), it does increase significantly with depth. Lighter isopycnals ventilated within the subtropical gyre are estimated to have low preformed [Si] (1–3 µM; e.g. Poole and Tomczak, 1999), while the $\sigma_\theta = 27$ isopycnal exhibits a [Si] of around 10 µM near its winter outcrop at $\sim$50°S (Garcia et al., 2010b). This increasing contribution of preformed Si diminishes the potential of opal dissolution to significantly change δ^{30}Si value. In addition, the Si dissolution flux with depth decreases, due a decrease in both the sinking opal flux and water temperature by 20–50% and $\sim$8°C respectively over the 100–400m depth range (Ragueneau et al., 2002; Sarmiento and Gruber, 2006; Sarmiento et al., 2007; Loucaides et al., 2011).

The change in relative importance of ventilation versus remineralization over the depth range of the thermocline can be assessed by scale analysis (e.g. Palter et al., 2005): consider the dimensionless number UC/LJ_{diss}, which is the ratio of the timescales of remineralization and ventilation (where U is lateral velocity, C is a reference (preformed) Si concentration, L is the length scale and J_{diss} is the dissolution rate). Over the depth range of the thermocline, the ventilation timescale L/U increases by a factor of 2–5, whilst the dissolution timescale C/J_{diss} increases by a factor of 3–10 (see Appendix A.3.1). This results in an increase in the value of UC/LJ_{diss} with depth in the thermocline, from $\sim$1 just below the mixed layer to $\sim$10 at the depth of the σ_θ = 27 isopycnal (see Appendix A.3.1). The scale analysis thus indicates that, rather than increasing, the influence of opal dissolution diminishes across the thermocline δ^{30}Si gradient. Thus, opal dissolution cannot be the first-order process responsible for the decrease in δ^{30}Si with depth.

The above analysis has an important implication: if the observed thermocline δ^{30}Si gradient cannot be related to remineralized Si, it must be associated with the *preformed* component of Si, introduced in dissolved form into the subsurface by the physical circulation during water mass subduction. This can be conceptualized by considering that high δ^{30}Si values are a signal of diatom Si uptake at the surface of the ocean. Values of subsurface δ^{30}Si that are higher than the δ^{30}Si value of the source of Si for productivity (ultimately, the deep ocean) must thus document the presence of Si that has been fractionated within the surface ocean, i.e. preformed Si.

The inferred dominant preformed-Si influence on subsurface δ^{30}Si values implies that (a) hydrographic control on the thermocline δ^{30}Si distribution should be relatively strong and (b) δ^{30}Si should be invariant along isopycnals given low diapycnal mixing. These expectations are borne out by the detailed upper ocean δ^{30}Si and [Si] profiles from the eastern and western South Atlantic (Fig. 5.4a and b), which exhibit surprising similarity despite a separation of nearly 3000 km and the proximity of the eastern profile to the Namibian oxygen minimum zone (OMZ). The sections of the [Si] and δ^{30}Si distributions that *do* diverge in the depth profiles (the upper $\sim$200 m) become exactly (δ^{30}Si) or almost ([Si]) identical when plotted against σ_θ (Fig. 5.4d and e), which accounts for differences in the water column structure of the two stations (Fig. 5.4c). The constancy in δ^{30}Si values along isopycnals suggested by Fig. 5.4d is robustly confirmed by the single, simple δ^{30}Si–σ_θ relationship for all thermocline samples (Supp. Fig. A.11).

The similarity observed for [Si] is in marked contrast to the [NO_3] distribution (Fig. 5.4f), which shows an excess of NO_3 associated with the OMZ in the east. The general applicability of this clear contrast is shown by the zonal WOCE section A08 (11°S; Supp. Fig. A.12), which exhibits minimal east-west gradients in [Si] along thermocline isopycnals, contrasting with significant gradients in [NO_3]. This contrasting behavior of [Si] and [NO_3] suggests that the effect of remineralization is considerably less pronounced for Si than for the other macronutrients (compare the size of the gray fields in Fig. 5.4e and f). Such [Si] differences as do exist between the two stations in Fig. 5.4e – presumably due to opal dissolution – do not produce a significant difference in δ^{30}Si values.

These observations thus confirm our inference, drawn initially from simple scale analysis, that the observed vertical gradient in thermocline δ^{30}Si values is related to a δ^{30}Si gradient in the preformed component of Si. In the following, we elucidate how such a gradient may be created in the context of a simple schematic view of thermocline ventilation.

5.4.2 Producing a preformed δ^{30}Si gradient

Figures 5.4d, 5.5b and A.11 show that higher δ^{30}Si values are associated with the lower [Si] of shallower thermocline isopycnals (Fig. 5.4d, e; Supp. Fig. A.11), whilst deeper isopycnals exhibit lower δ^{30}Si values at higher [Si]. The strong isopycnal control on the δ^{30}Si distribution necessitates that we consider how and where the thermocline is ventilated, and how it gains its preformed nutrient inventory.

Figure 5.7 is a simple schematic of thermocline ventilation based on adiabatic thermocline theory (Stommel, 1979; Luyten et al., 1983) and incorporating the mechanisms by which nutrients are supplied to the subtropical gyre (Williams and Follows, 2003). The ventilation of the thermocline isopycnals is achieved in the region of their wintertime surface outcrop, through the subduction of surface waters below the depth of the seasonal thermocline, a process driven by a combination of Ekman pumping and lateral mode water subduction (e.g. Karstensen and Quadfasel, 2002). In the Atlantic, the outcrop region spans the subtropical gyre, with shallower isopycnals being ventilated further north than deeper ones (Fig. 5.7). These shallower isopycnals are associated with a higher preformed δ^{30}Si value, which implies that – analogous to its θ–S distribution (e.g. Iselin, 1939; Poole and Tomczak, 1999) – the vertical δ^{30}Si gradient in the thermocline reflects an isotopic gradient set up at its surface. Following the path of nutrients within the subtropical gyre allows us to suggest how this surface gradient may be produced.

In an oceanic regime where the diapycnal flux of nutrients from the deep ocean is small, the primary means of replenishing thermocline nutrients is by lateral transport across the poleward boundary of the subtropical gyre (Williams and Follows, 2003), the Subtropical Front (STF), where a combination of both wind-driven Ekman transport as well as diffusive and advective eddy fluxes carries Si and other nutrients into the thermocline from the Subantarctic, both at the surface and at depth (Fig. 5.7). Consider any surface ocean volume bounded by two isopycnals and the base of the seasonal thermocline in Fig. 5.7: over the annual cycle, the Si pool supplied to this volume by the geostrophic circulation is (a) partially utilized in the euphotic zone and exported to the seasonal thermocline and deeper, (b) partially subducted into the permanent thermocline at the end of winter, and (c) partially transported further into the gyre within the seasonal thermocline, which shoals equatorward. Thus, Si is cycled numerous times within the seasonal thermocline as it is transported further into the gyre (Williams and Follows, 1998), where the lighter thermocline isopycnals are ventilated. Since a portion of the opal in each surface ocean volume is exported below the seasonal thermocline (Fig. 5.7), there

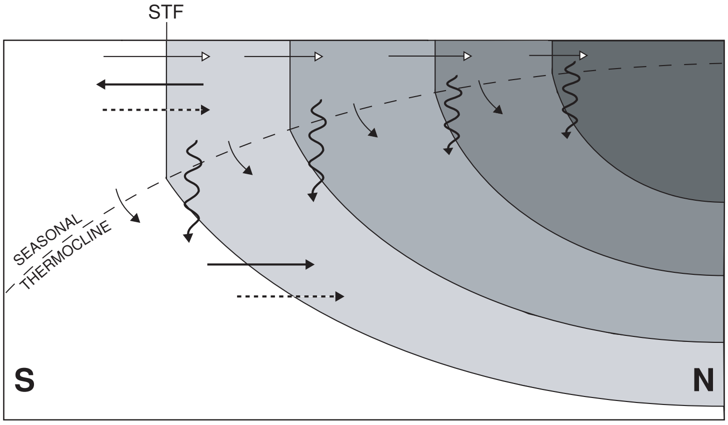

Figure 5.7: Schematic view of the processes transporting Si into and within the ventilated thermocline. White-headed arrows are Ekman and geostrophic transport at the STF and in the gyre interior respectively, solid horizontal arrows are eddy advective ('bolus') fluxes, dotted arrows are eddy diffusive fluxes. Particle export is indicated by downward wavy arrows, whilst the black arrows crossing the seasonal pycnocline represent the annual subduction flux. The shading gradient schematically reflects [Si] and δ^{30}Si, with darker grays corresponding to lower [Si] and higher δ^{30}Si values.

is potential to produce a fractionation signal: since opal preferentially incorporates the lighter isotopes of Si, this series of utilization, remineralization and export events will result in an increase in δ^{30}Si value of the Si available for biological utilization toward the center of the gyre. Thus, a gradient in [Si] and δ^{30}Si values is set up within the seasonal thermocline that is subducted annually into the permanent thermocline (gray shading in Fig. 5.7).

Considering the interaction of biological nutrient utilization within the euphotic zone with the gyre-scale nutrient transport thus provides a mechanism for the development of a preformed δ^{30}Si gradient within the thermocline. The simplicity of the observed δ^{30}Si–1/[Si] relationship may be explained by the fact that the thermocline is ventilated primarily in a few highly dynamic ocean regions such as the Brazil–Malvinas Confluence (Fig. 5.2; Gordon, 1981; Sprintall and Tomczak, 1993; Karstensen and Quadfasel, 2002) that are associated with intense eddy activity (e.g. Legeckis and Gordon, 1982). Thus, the mechanisms of thermocline nutrient transport considered above take place over a background of significant mixing (Gordon, 1981; Piola and Matano, 2001) and mass exchange between the subtropical gyre and the Subantarctic (e.g. McCartney, 1982; Maamaatuaiahutapu et al., 1999; Jullion et al., 2010). The eddy fluxes play an important role in transferring nutrients to the gyre (Williams and Follows, 2003), and the homogenizing effect of the lateral mixing they induce may contribute to the simple δ^{30}Si systematics of the subducting water masses (see Wunsch and Ferrari, 2004). Alternatively, diapycnal mixing in the complex equatorial current system (Stramma and Schott, 1999) may play some role in transferring Si and its associated isotopic signature across isopycnal surfaces, although there does not appear to be significant mixing of high δ^{30}Si signatures into the subsurface in the eastern equatorial Pacific (Beucher et al., 2011).

5.4.3 Open Questions

We have shown that the thermocline δ^{30}Si distribution is strongly coherent both in terms of its isotope systematics (Fig. 5.5) and its isopycnal distribution (Figs. 5.4d, A.11), and that this is related to the dominant influence of preformed Si on the δ^{30}Si distribution. The preformed nutrient inventory of the thermocline is set during thermocline ventilation, and it is thus a surprise that the samples from within the North Atlantic Central Water (n = 2), which is ventilated from the north, show no significant difference in isotope systematics or distribution from the bulk of the samples that are within SACW (Fig. 5.6). On the other hand, the Bay of Biscay shows a distinctly different δ^{30}Si–σ_θ relationship and hosts the few samples that do not conform to the otherwise coherent Atlantic thermocline relationship. The reasons for these similarities and differences are difficult to elucidate given the sparse sampling associated with these two regions.

Additionally, our interpretation of the simple Atlantic δ^{30}Si systematics as essentially a ventilation signal implies that the ventilated thermocline in other ocean basins should show similar systematics; this remains to be shown. Published water column δ^{30}Si studies have thus far focused on high-latitude or equatorial sites (Cardinal et al., 2005; Beucher et al., 2008, 2011) where the thermocline is either not present or significantly altered by the complexity of the equatorial current system, precluding a comparison; data from the ventilated thermocline are limited to a few ($n \leq 5$) points from which no clear systematics can be inferred (Reynolds et al., 2006a). In the light of these questions, it is clear that both large-scale as well as detailed studies of the thermocline δ^{30}Si distribution are required to further our understanding of the δ^{30}Si systematics in the sea.

5.5 Summary and Conclusions

In this contribution, we have presented the first comprehensive δ^{30}Si dataset from the ventilated thermocline. The δ^{30}Si systematics unambiguously documents two features of the Si tracer field that are not otherwise apparent: (a) the Atlantic thermocline is strongly decoupled from the deep ocean in terms of its nutrient cycling, and (b) a significant proportion of the thermocline Si inventory is in fact preformed, as documented by its high δ^{30}Si values that record the signal of diatom Si utilization at the surface. The strong hydrographic control on the δ^{30}Si distribution indicates that it integrates over a number of interacting processes over the residence time of Si within the thermocline, such that water column δ^{30}Si data from the ventilated thermocline cannot be directly used to estimate the isotope effect of diatom Si utilization. Rather, seawater δ^{30}Si values in the upper ocean are a useful tracer of the pathways of Si transport.

The strikingly coherent Atlantic δ^{30}Si–1/[Si] relationship distinguishes between Si cycling within the ventilated thermocline and the deeper ocean, which follow two separate and well-defined linear arrays. The properties of the pivotal intersection between these arrays correspond to the characteristics of SAMW, which provides strong support for the notion that this water mass is a key player in the return of nutrients from the deep sea to the thermocline (Sarmiento et al., 2004a, Chapter 4).

Chapter 6

The South Pacific δ^{30}Si distribution[*]

6.1 Introduction

In the preceding chapters, I have discussed the Atlantic δ^{30}Si distribution both at the basin scale and over the depth range of the thermocline. In both these cases, the data led me to infer that the introduction of high δ^{30}Si values into the subsurface during the ventilation of intermediate and thermocline isopycnals was necessary to explain the observed δ^{30}Si distribution, not only within the thermocline but, ultimately, at the scale of the entire Atlantic Ocean. The inferred importance of the process of subduction in determining the distribution of δ^{30}Si values implies the need for a more detailed understanding of how high δ^{30}Si values, created by biological activity in the surface ocean, can be introduced into the interior. Thus, in this chapter, I focus on a δ^{30}Si dataset from the eastern South Pacific Ocean, which is a key location for the formation of Subantarctic Mode Water and Antarctic Intermediate Water (SAMW and AAIW; McCartney, 1982; Hanawa and Talley, 2001; Aoki et al., 2007; Iudicone et al., 2007; Sallée et al., 2010). This study, which presents the first seawater δ^{30}Si data from the South Pacific, encompasses a latitudinal range from the Antarctic Zone to the tropics. This broad scope allows me to trace the evolution of δ^{30}Si values from the surface Southern Ocean into the ventilated subtropical thermocline.

Thermocline, mode and intermediate waters subducted in the South Pacific Ocean also play an important role in the supply of both oxygen and nutrients to the upwelling zones of the equatorial Pacific (Tsuchiya et al., 1989; Toggweiler et al., 1991; Fine et al., 2001; Dugdale et al., 2002; Karstensen, 2004; Qu et al., 2008; Sallée et al., 2010), a biogeochemically dynamic region that represents the largest oceanic source of CO_2 to the atmosphere (Gruber et al., 2009). The inefficiency of the equa-

---

[*] The data and discussion presented here will be the focus of a future publication in collaboration with the principal investigators of the CLIVAR P18 re-occupation expedition, John L. Bullister and Gregory C. Johnson (National Oceanic and Atmospheric Administration).

Table 6.1: Station locations from which samples presented in this chapter were collected.

Station No.	Station Location	Latitude	Longitude
70	Peru Basin	11° 45' S	130° W
95	Sala y Gómez Ridge	26° 20' S	130° W
114	Southeast Pacific Basin	37° 25' S	130° W
136	Southeast Pacific Basin	50° 15' S	130° W
149	Southeast Pacific Basin	57° 45' S	130° W
158	Southeast Pacific Basin	62° 15' S	130° W

torial Pacific biological pump, manifested by its strong CO_2 outgassing, appears to owe its origin at least partially to the disparity in Si content of South and North Pacific thermocline waters, both of which contribute nutrients to the equatorial Pacific (Dugdale et al., 2002). The Si deficiency of the South Pacific thermocline, produced at high southern latitudes (Sarmiento et al., 2004a), reduces the supply of Si relative to NO_3 in the equatorial Pacific. This reduced Si supply limits the productivity of diatoms that can efficiently export carbon to depth (Dugdale et al., 2002), a condition that is exacerbated by iron limitation (Brzezinski et al., 2008). I will show that the δ^{30}Si distribution in the equatorial thermocline reflects the influence of both sources of Si to, and cycling of Si within, this biogeochemically complex system.

6.2 Sampling and hydrographic description

The samples for which δ^{30}Si data are presented here were collected on expedition 33RO20071215 of R/V *Ronald H. Brown* (15th December 2007 to 23rd February 2008), a re-occupation of the World Ocean Circulation Experiment (WOCE) line P18 undertaken within the Climate Variability and Predictability (CLIVAR) project of the World Climate Research Programme[1]. Samples were collected at six stations along a meridional section at 103° W, from 12° S to 62° S (Fig. 6.1 and Table 6.2). All samples were filtered onboard using 0.2 µm GFF filters and acidified with 1% v/v distilled 6 M HCl in the laboratory at least 12 hr before sample processing. Sample processing and analytical methods are described in detail in Chapter 2.

In the following, the general hydrography of line P18 will first be briefly described in order to introduce the water mass structure and circulation of the region (Section 6.2.1). This allows a discussion of the hydrography of the six δ^{30}Si stations in the regional context (Section 6.2.2).

---

[1] `http://www.clivar.org/` and `http://www.wcrp-climate.org/`

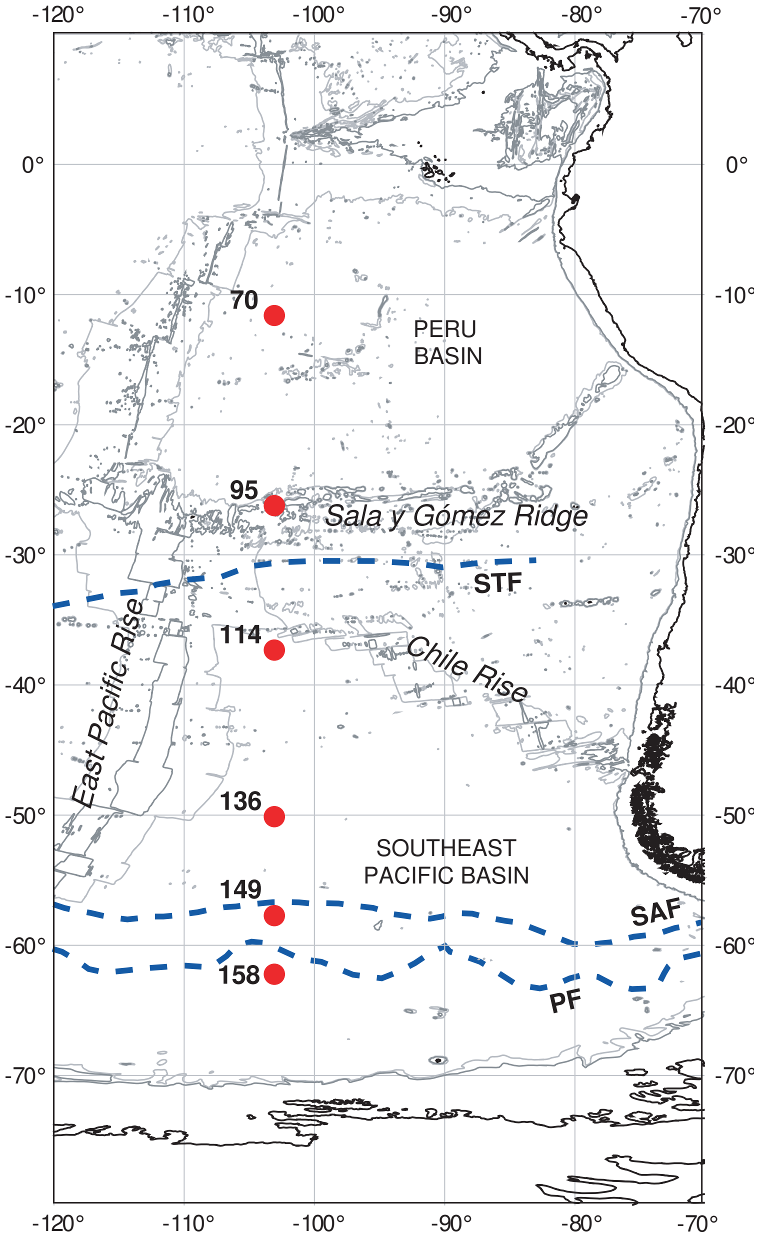
-120°
-110°
-100°
-90°
-80°
-70°
0°
-10°
-20°
-30°
-40°
-50°
-60°
-70°
70
PERU
BASIN
95
Sala y Gómez Ridge
STF
114
Chile Rise
East Pacific Rise
136
SOUTHEAST
PACIFIC BASIN
149
SAF
158
PF

Figure 6.1: Map of the eastern South Pacific Ocean showing locations of stations from which samples were collected. Dark and light grey lines represent the 3000 m and 3500 m isobaths respectively. The dashed blue lines mark the location of the Subtropical Front (STF), Subantarctic Front (SAF) and Polar Front (PF) following Orsi et al. (1995).

6.2.1 South Pacific hydrography

Line P18 traverses the western margin of three deep ocean basins (Fig. 6.1): the Southeast Pacific Basin, the Chile Basin, and the Peru Basin, which are separated from each other by Chile Rise (35° S at 103° W) and Sala y Gómez Ridge (26–27° S). The deep Pacific Ocean displays little variability in the conservative parameters potential temperature θ and salinity S, since it only possesses one source of deep water, Circumpolar Deep Water (CDW) from the Southern Ocean (e.g. Schmitz, 1996a). The main salinity feature at depth (Fig. 6.2) is a muted maximum in the far south, deepening from about 1200 m at 70° S to the bottom at ∼45° S. This is a highly diluted North Atlantic Deep Water signal in the Upper Circumpolar Deep Water (Warren, 1973; Tsuchiya and Talley, 1998; Tomczak and Godfrey, 2003). The potential temperature distribution shows the cold Circumpolar Deep Water extending northwards along the bottom up to Chile Rise, whilst bottom waters in the Chile and southern Peru Basins are warmer. Oxygen concentrations, [O_2], follow the cold tongue of CDW to Chile Rise. Above this lies a mild mid-depth [O_2] minimum (Fig. 6.3) that has been associated with return flow from the North Pacific (Reid, 1986; Tsuchiya and Talley, 1998). The basins to the north of Chile Rise are generally less well-oxygenated at depth; in the Peru Basin, [O_2] decreases in two steps that are both associated with increases in Si concentration, [Si] (Fig. 6.3). The low [O_2] and high [Si] in the northern Peru Basin are related to the westward flow of deepwaters of North Pacific origin that enter the Peru Basin at its northeastern margin (Reid, 1986, 1997).

In contrast to the deep ocean, the upper ∼1 km of the South Pacific water column shows rich water mass structure, reflected most clearly in the salinity distribution (Fig. 6.2). The most striking feature is the tongue of low salinity (34.2–34.3 psu) that extends from the sea surface at high latitudes to 20° S, associated with the spreading of AAIW and SAMW (Tsuchiya and Talley, 1996, 1998) that are formed by deep winter convection in the subantarctic South Pacific (Hanawa and Talley, 2001; Sloyan et al., 2010). Subantarctic Mode Water can be identified as a pronounced potential vorticity minimum within the salinity minimum (not shown). The high [O_2] (Fig. 6.3) of SAMW and AAIW highlight the importance of these waters for the ventilation of the subtropical subsurface at thermocline and intermediate depths. The northern end of the pronounced salinity minimum at 20° S is related to the anticyclonic subtropical circulation, which advects AAIW and SAMW westwards at this latitude. The salinity minimum persists to the north at slightly higher salinity (∼34.55), tracing AAIW that has entered the zonal equatorial circulation further west (Tsuchiya, 1991; Tsuchiya and Talley, 1996, 1998).

Another major feature of the salinity distribution is the bowl of high-salinity water that extends from the Subtropical Front to about 10° S at the surface (and further north within the subsurface), with a maximum depth of ∼300 m. The potential vorticity distribution (not shown) allows the distinction of

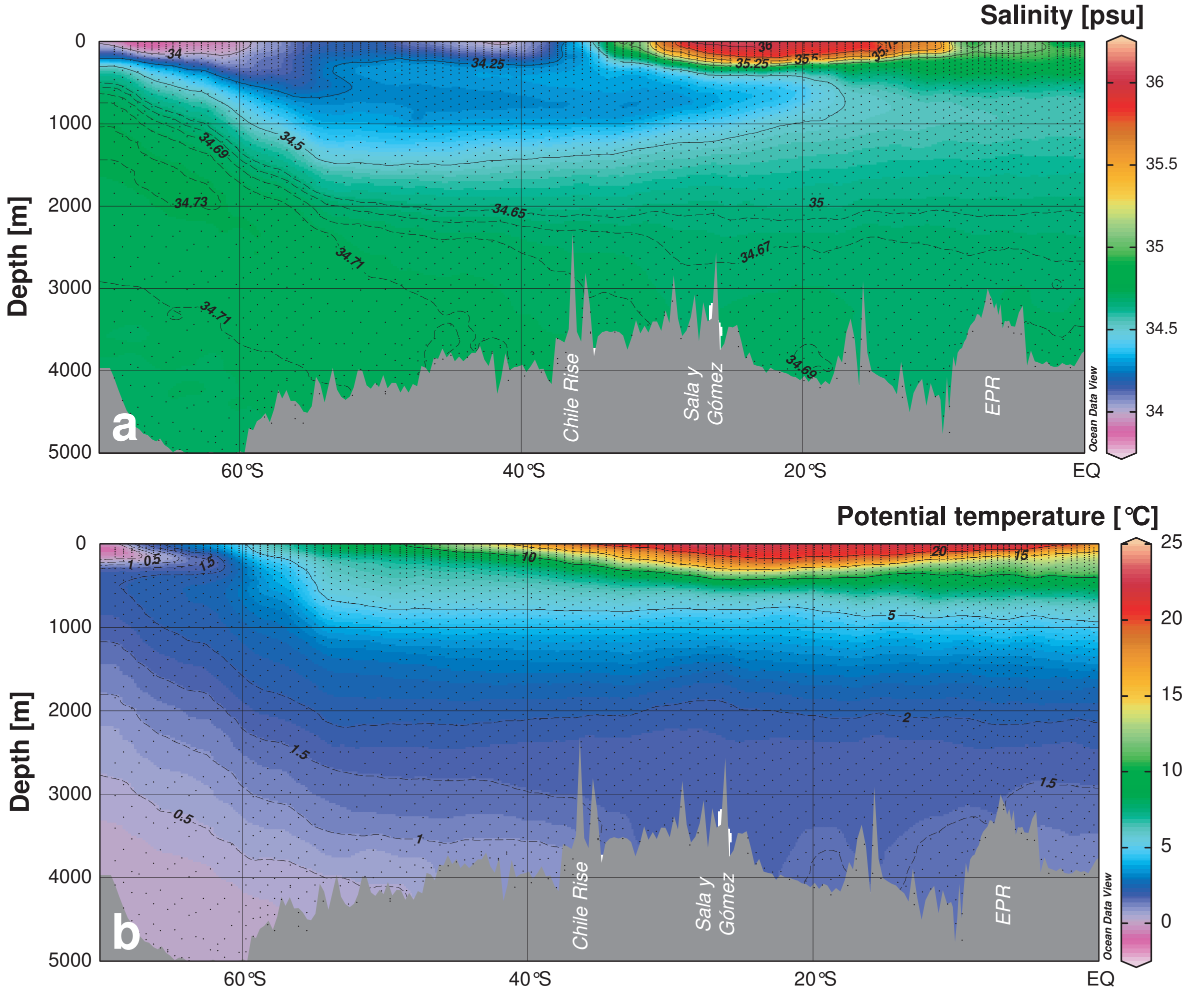

Figure 6.2: South Pacific (*a*) salinity and (*b*) potential temperature distributions along line P18. Note the difference in contour interval between the upper ocean (solid) and deep ocean (dashed) contours. See text for description of the main features. EPR is the East Pacific Rise. Data are from the CLIVAR & Carbon Hydrographic Data Office (`http://cchdo.ucsd.edu/`).

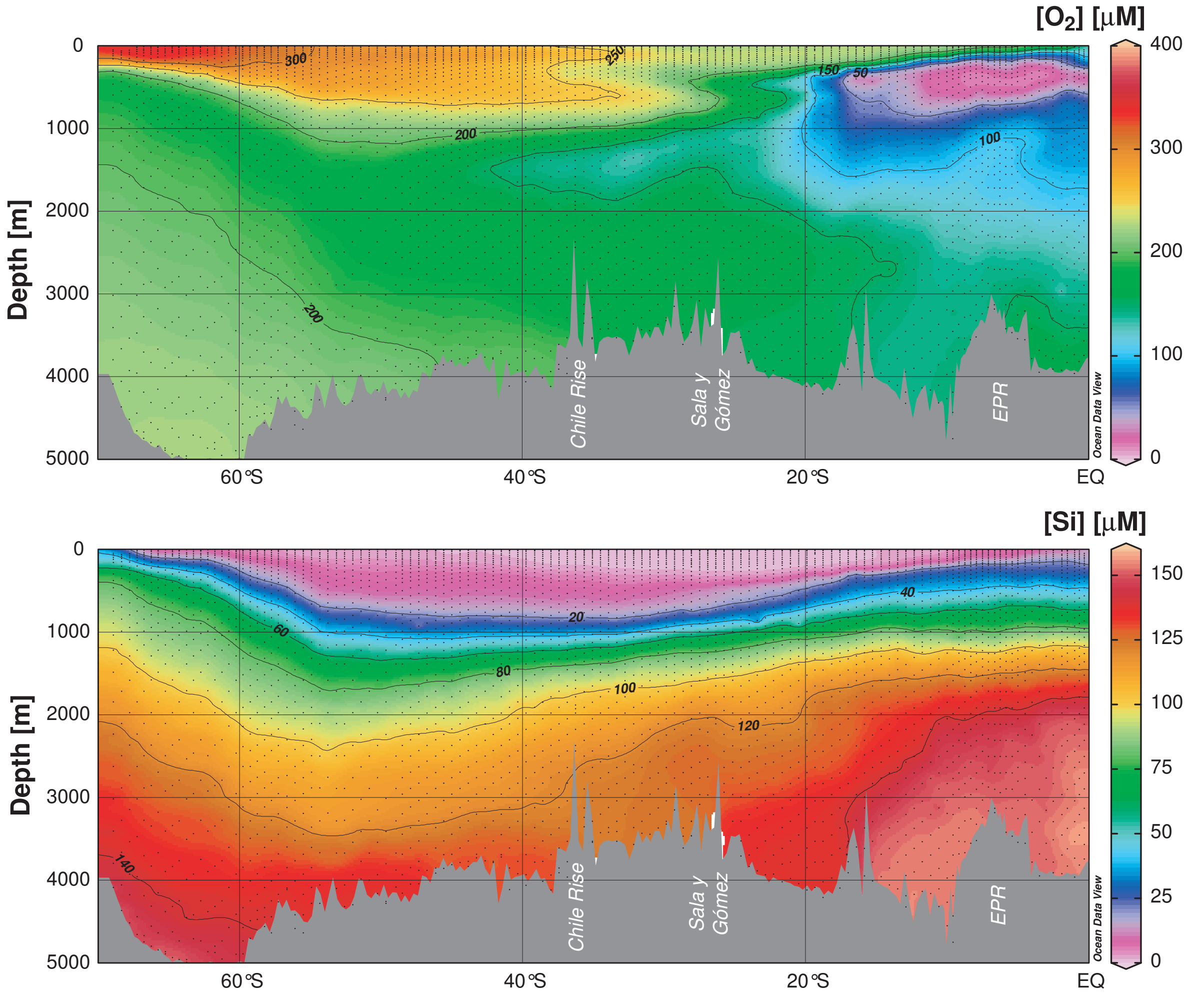

Figure 6.3: South Pacific (*a*) oxygen and (*b*) Si distributions along line P18. See text for description of the main features. EPR is the East Pacific Rise. Data are from the CLIVAR & Carbon Hydrographic Data Office (`http://cchdo.ucsd.edu/`).

South Pacific Eastern Subtropical Mode Water (SPESTMW) centred around 150m depth (σ_θ = 25.3) from the salinity maximum of Subtropical Water (STW) above it (Tsuchiya and Talley, 1996; Johnson and McPhaden, 1999; Hanawa and Talley, 2001; O'Connor et al., 2002; Wong and Johnson, 2003; Qu et al., 2008). The SPESTMW, which forms equatorward of the subtropical front (Wong and Johnson, 2003), plays an important role in ventilating mid-thermocline isopycnals (Karstensen et al., 2008; Qu et al., 2008); it is highly nutrient-depleted, with Si concentrations below 1 µM over its entire depth and lateral extent (Fig. 6.3).

North of 20° S, the water column below SPESTMW and STW is dominated by more uniformly saline waters of the equatorial regime. These waters host the South Pacific oxygen minimum zone (OMZ), with [O_2] <30 µM within the most intense portion of the OMZ centred at 400 m water depth and 6° S (Fig. 6.3). A minor oxygen minimum extends further south to about 27° S at $\sim$400 m, associated with a weak halostad. A similar feature observed at 88° W has been suggested to record influence from waters of the Peru–Chile Undercurrent (Tsuchiya and Talley, 1998), although it is questionable whether the influence of these waters can be expected to be observed as far offshore as line P18.

6.2.2 Hydrography at δ^{30}Si stations

The stations from which samples for analysis of δ^{30}Si were collected are presented in a θ–S diagram in Fig. 6.4. As is to be expected from the general description above, the θ–S relationships of all stations are very similar at depth, with minor variability associated with the strength of the UCDW salinity maximum. Station 158 at 62° S shows the near-surface temperature minimum typical of the water column south of the Antarctic Polar Front (Whitworth and Nowlin, 1987; Pollard et al., 2002). Salinity decreases monotonically towards the surface at Sta 158, as it does just south of the Subantarctic Front at Sta 149 (58° S), except for some minor interleaving. Stations further north all exhibit the deep salinity minimum of AAIW, while both Subantarctic stations Sta 136 (50° S) and Sta 114 (37.5° S) additionally show a salinity maximum above this, at potential densities of σ_θ = 26.95. At shallower depths, salinities decrease towards the surface at both these stations. Station 114 appears as a transitional station in terms of its upper water column structure, with salinity decreasing towards the surface (as at the stations further south), while temperature rises strongly (as at the stations further north). This apparently transitional character is possibly related to the presence of Shallow Salinity Minimum Water at these latitudes (Karstensen, 2004). Station 114 also exhibits strong interleaving of salty, warm water with fresher, cooler waters in the upper 400 m of the water column ($\sigma_\theta \leq 26.9$).

Station 95 at 26° S is situated north of the Subtropical Front (Fig. 6.1), a fact that is clearly reflected in its θ–S relationship: above the AAIW salinity minimum, salinity increases more strongly than further south, exhibiting a mildly low-oxygen (<150 µM) halostad at σ_θ = 26.4–26.8 (400–500 m) that has a very sharp upper transition to the highly saline SPESTMW and STW at σ_θ = 26.38 (360 m). At Sta 70 (12° S), the θ–S relationship is markedly different from those at all other stations. The AAIW salinity minimum is shifted to higher salinities, reflecting the presence of the equatorial variety of AAIW, with only 25% of the oxygen concentration of AAIW at Sta 95 (Fig. 6.3). A halostad at σ_θ = 26.1–26.62 (170–250 m) is associated with the lowest [O$_2$] observed at any of the six stations (< 10 µM). Above this, the high-salinity signature of STW is apparent as a subsurface S maximum around σ_θ = 25.2 (100 m).

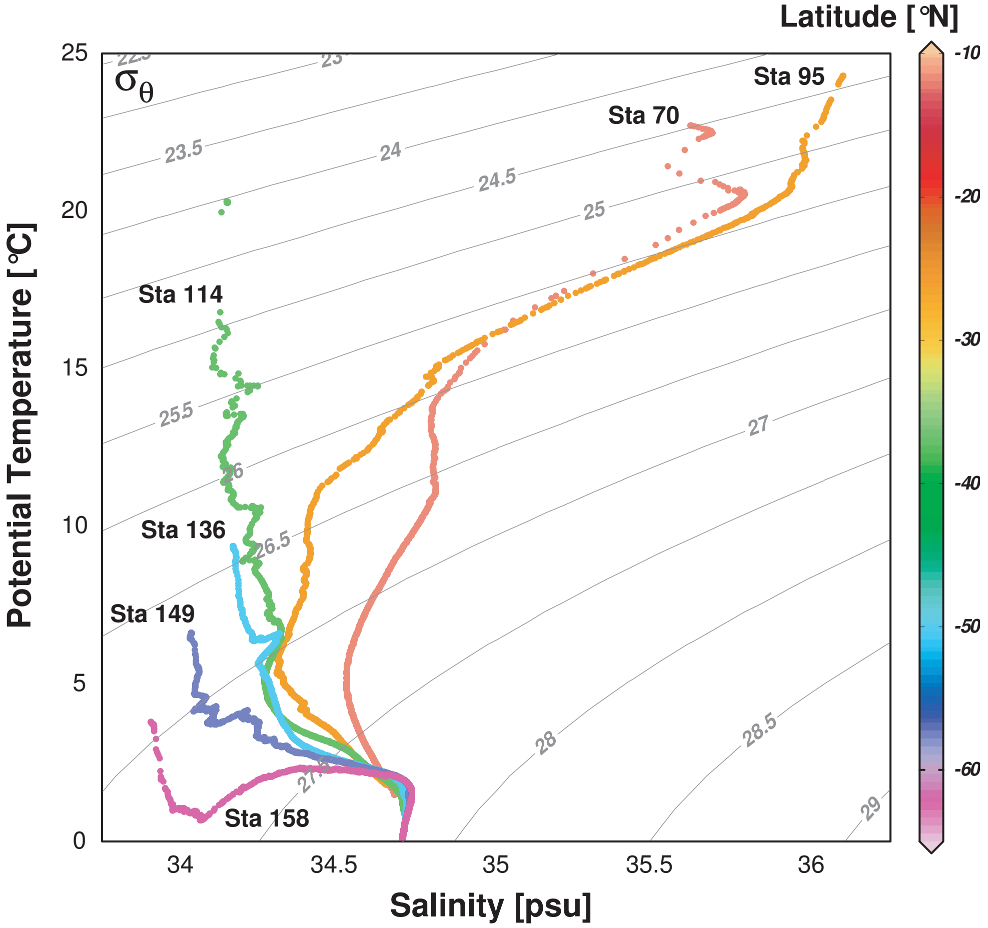

Figure 6.4: Potential temperature–salinity diagram for stations from which samples were analysed for δ^{30}Si (see Fig. 6.1 for station locations). Data are from the CLIVAR & Carbon Hydrographic Data Office (`http://cchdo.ucsd.edu/`).

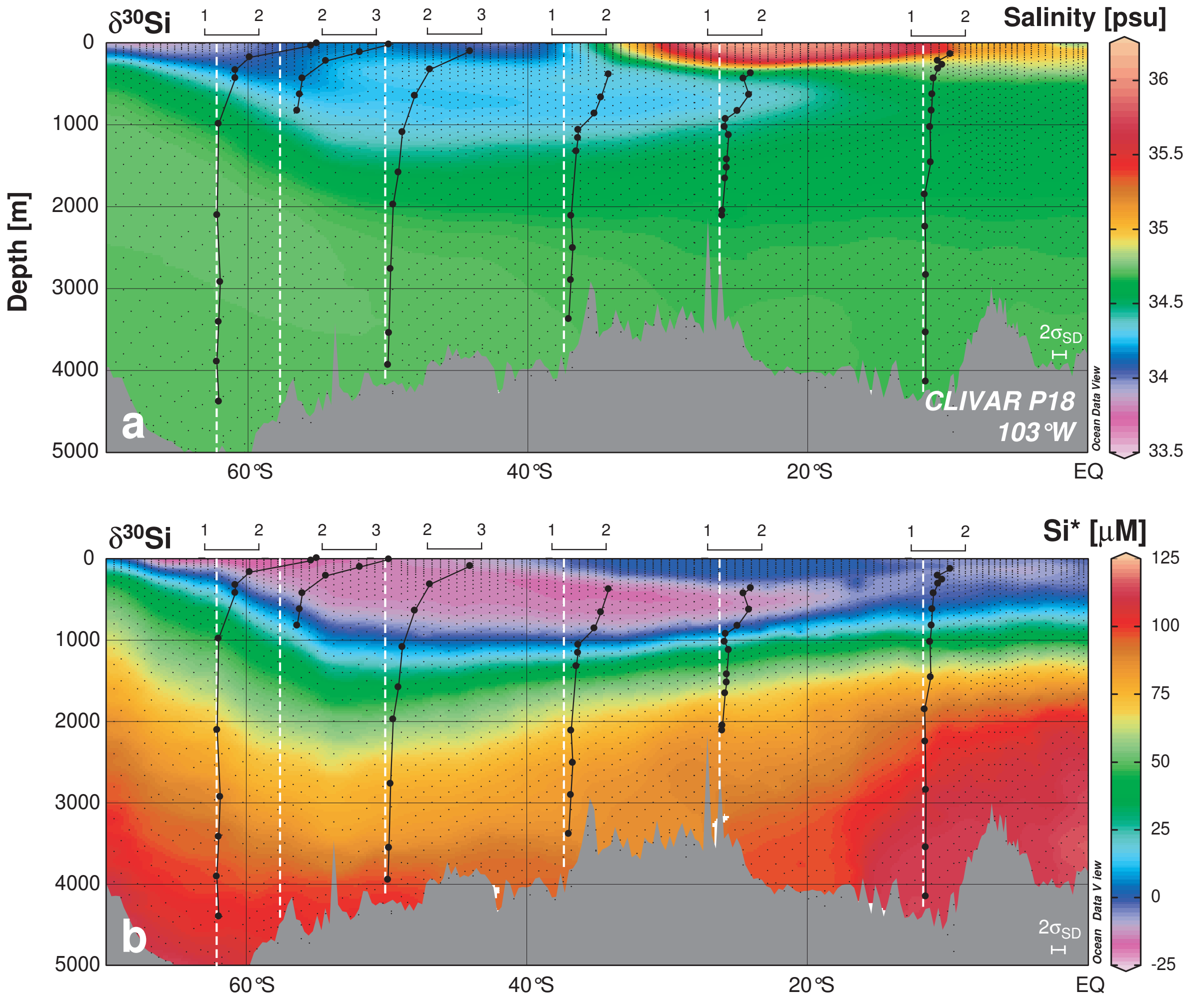

Figure 6.5: Depth profiles of δ^{30}Si overlain on colour maps of (a) salinity and (b) Si* = Si – NO_3. The white line in each profile marks the sampling position as well as a δ^{30}Si value of +1.22‰, corresponding to CDW (Chapter 4).

6.3 Results

Depth profiles of δ^{30}Si values are displayed over colour maps of salinity and Si* (defined as [Si] – [NO_3]) in Fig. 6.5 and tabulated in Table 6.2. The extremely low [Si] (0.5–1.5 µM) in the uppermost water column 37.5° S, 26° S and 12° S precluded analysis of these samples, given collected sample volumes of 50–100 ml.

Values of δ^{30}Si generally increase upwards through the water column, with the highest values (up to +3.2‰) found within the surface mixed layer. At depth, the Southern Ocean is exceptionally homogeneous, with an average δ^{30}Si value of +1.25±0.05‰ ($2\sigma_{SD}$, n = 6) at water depths $\geq$ 1000 m (equivalent to neutral density $\gamma^n \geq 27.93$ or potential density $\sigma_\theta \geq 27.70$)[2]. Deepwaters at stations further north show similarly low δ^{30}Si values: the average δ^{30}Si value for all samples outside the Southern Ocean below the salinity minimum of AAIW ($\geq$1400 m, $\gamma^n \geq 27.77$, $\sigma_\theta \geq 27.56$) is +1.32±0.11‰ ($2\sigma_{SD}$, n = 20). Over the same density range as the deep Southern Ocean ($\gamma^n \geq 27.93$) the average δ^{30}Si value is +1.30±0.08‰ ($2\sigma_{SD}$, n = 13). A Monte Carlo t-test indicates a probability of only 7% that these values are significantly different at the 95% level (see Appendix A.4.1), emphasising the high degree of homogeneity in deepwater δ^{30}Si values. Visually, the Chile Basin appears as an exception, with the entire deep water column exhibiting a slightly higher δ^{30}Si value than in the Southern Ocean (Fig. 6.5), but the Monte Carlo approach indicates only a 25% probability that this difference is significant.

In general, seawater δ^{30}Si values show the strongest vertical gradients within the uppermost 1000 m of the water column, although the depth extent of these gradients varies strongly with latitude (Fig. 6.5) and, on visual inspection, appears to follow the salinity minimum associated with the spreading of AAIW. The strong deepening of the gradient can be quantitatively illustrated by considering the depth at which seawater δ^{30}Si values nominally exceed +1.6‰: this surface deepens from 175 m at 62° S to a maximum of 858 m at 37.5° S before shoaling northwards, reaching $\sim$150 m at 12° S[3]. Figure 6.6 compares the depth of this surface to two surfaces that follow the deepening and spreading of AAIW north of 50° S (Tsuchiya and Talley, 1998; Sarmiento et al., 2004a): the $\gamma^n = 27.25$ surface and the deepest surface with negative values of the tracer Si*. Figure 6.6 shows a clear similarity between the latitudinal depth changes of these two surfaces with the depth of elevated δ^{30}Si values[4]. This similarity implies a strong isopycnal component of the δ^{30}Si distribution, confirming the visual impression given by Fig. 6.5. Considering the significant variation in the depths of isopycnal surfaces across the latitudinal range of this study, a direct comparison of δ^{30}Si depth profiles cannot be made.

---

[2] Here and in the following, I refer to neutral density γ^n (Jackett and McDougall, 1997) since this allows a better comparison of seawater density over large depth ranges. Values of potential density σ_θ are included for the reader's reference, since these values are likely to be more familiar.

[3] The same pattern is produced by considering any other elevated δ^{30}Si value, e.g. +1.5‰.

[4] The high subsurface δ^{30}Si values are similarly associated with high oxygen concentrations (Fig. 6.3).

A more appropriate and systematic view is provided by Figs. 6.7a & b, which plots δ^{30}Si values and [Si] against neutral density γ^n. The density profiles of δ^{30}Si emphasise the coherence in the δ^{30}Si distribution along isopycnals. Profiles in the deeper water column ($\gamma^n \geq 27.7$) show that δ^{30}Si values do not change significantly at depth (Fig. 6.7c), even though [Si] increases northwards along isopycnals by as much as 63% (Fig. 6.7d). In the upper water column, however, both marked differences as well as clear structure are seen in the δ^{30}Si distribution. The summer and winter mixed layers (stars in Fig. 6.7) of the polar stations (62° and 58° S) show high δ^{30}Si values (+1.8‰ to +3.2‰) at relatively high densities (up to γ^n = 27.5) that outcrop at these high latitudes. In the subsurface water column below the depth of the winter mixed layer, all stations from 62° S to 37.5° S exhibit very similar δ^{30}Si–γ^n relationships, increasing to δ^{30}Si values of around +1.8‰ at $\gamma^n \approx 27.15$ (σ_θ = 27.0). A completely different δ^{30}Si–γ^n relationship is seen at 12° S, where δ^{30}Si values remain constant around a value of +1.4‰ up to densities as low as γ^n = 26.6. The only non-monotonic δ^{30}Si–γ^n relationship is observed at 26° S, which remains similar to the more southerly stations up to $\gamma^n \approx 27.15$, after which it appears to follow the relationship defined by the water column at 12° S.

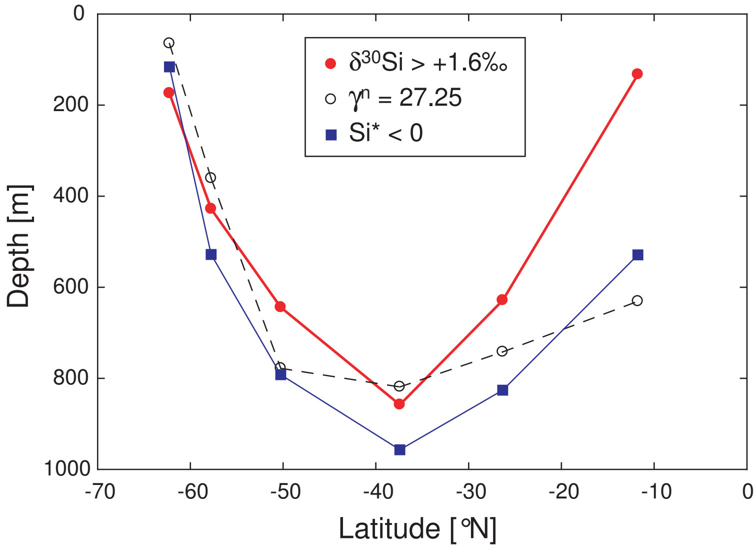

Figure 6.6: A comparison of the deepest depth of elevated δ^{30}Si values ($>$ +1.6‰) with the depths of two surfaces that follow the spreading of AAIW northwards, showing the strong similarity in evolution with latitude. Note that both the Si* $<$ 0 and δ^{30}Si $>$ +1.6‰ surface shoal more strongly than the isopycnal γ^n = 27.25 surface in the equatorial Pacific Ocean, documenting an additional control on δ^{30}Si here, as discussed in Section 6.4.2.

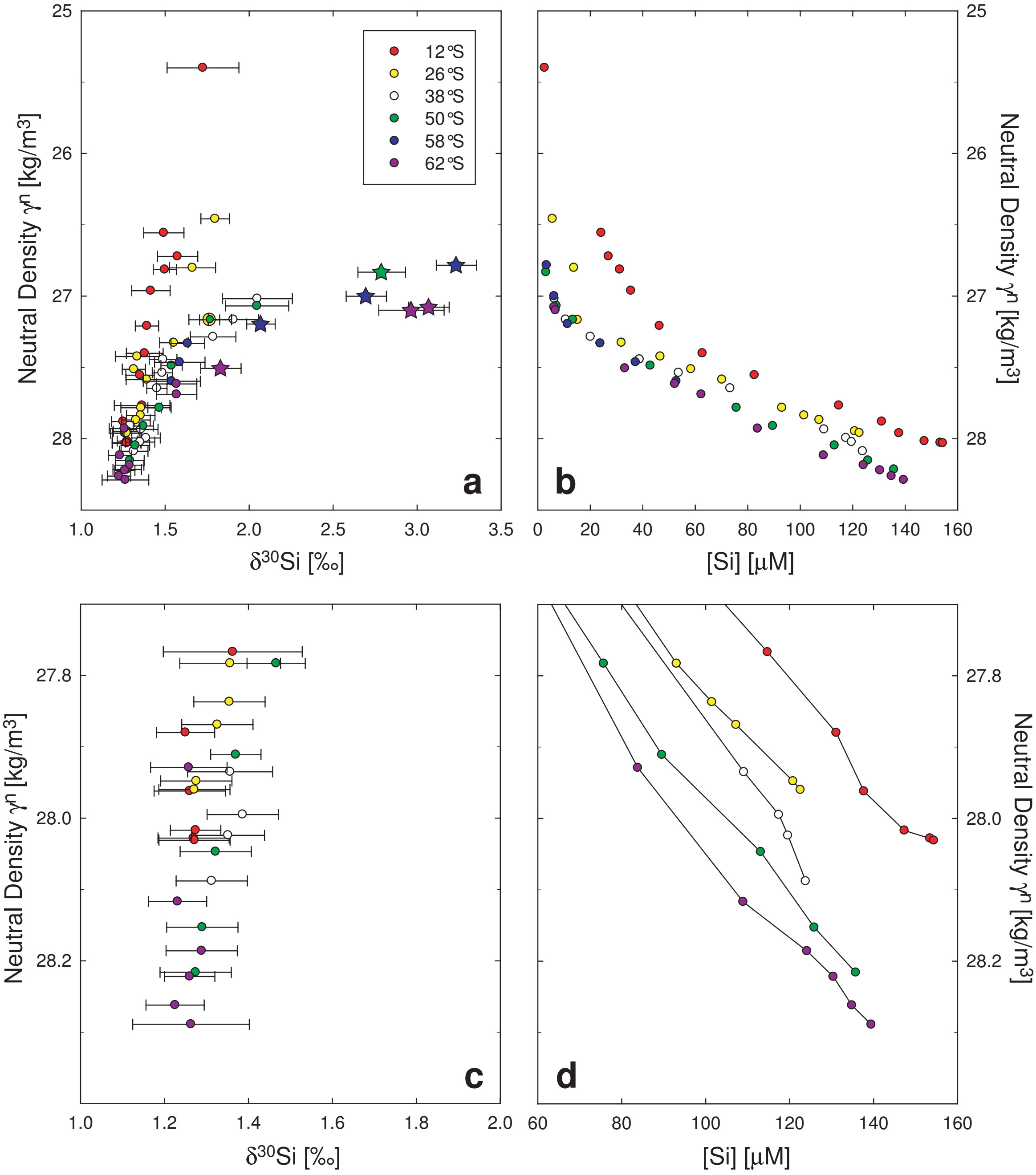

Figure 6.7: Density profiles of δ^{30}Si values (*a, c*) and [Si] (*b,d*) over the entire sampled water column (upper panels) and below γ^n = 27.7. Note the different *x*-axis scales in the upper and lower panels.

6.4 Discussion

The latitudinal range covered by the samples in this study, from high polar latitudes to the tropics, provides a rare glimpse into the evolution of seawater δ^{30}Si values, and thus the cycling and transport of Si, in a region of the ocean that is particularly important for providing nutrients and oxygen to the low-latitude thermocline (McCartney, 1982; Hanawa and Talley, 2001; Karstensen et al., 2008; Palter et al., 2010; Sloyan et al., 2010). In the following, I will first discuss the handful of δ^{30}Si values from the surface summer and winter mixed layers, as a prelude to following their introduction into the subsurface, where I am able to document a coherent water mass control on the δ^{30}Si distribution within the realm of the Pacific subtropical circulation (Section 6.4.1). The distribution of δ^{30}Si values in the equatorial Pacific thermocline differs from the distribution seen in the subtropics, a feature that documents a change in the dominant source of Si in the thermocline and/or the accumulation of remineralised Si in the eastern equatorial Pacific (Section 6.4.2). Finally, I briefly discuss the homogeneous δ^{30}Si values observed in the deep Pacific, and identify key questions related to the sources of Si to the deep Pacific that will require more detailed study in the future (Section 6.4.3).

6.4.1 Introduction of high δ^{30}Si values into the subsurface

Values of δ^{30}Si are high in the surface mixed layers of the Antarctic and Polar Frontal Zone stations at 62° S and 58° S, as well as in the nutricline just below the base of the mixed layer at 58° S and at the Subantarctic station at 50° S. These elevated δ^{30}Si values are the direct result of Si isotope fractionation during uptake of Si by diatoms; satellite-based estimates[5] indicate that the highest chlorophyll *a* concentrations were attained about 6–8 weeks before the *Ronald H. Brown* arrived at high latitudes in late summer (February 2008). The extremely high values of up to +3.2‰ confirm previous observations that diatom Si isotope fractionation in the surface Southern Ocean produces highly elevated δ^{30}Si values at relatively high [Si] of 3–6 µM[6]. Thus, the late summer mixed layers at high latitudes represent a considerable inventory of high-δ^{30}Si silicic acid, such that they have the potential to influence seawater δ^{30}Si values when mixed with other water masses by physical processes. Below, I show that this influence is clearly visible, and trace the introduction of the surface nutrient utilisation signal into the ocean interior over a number of steps.

Deep winter convection: At high latitudes, strong cooling of surface water in winter leads to destabilisation of the water column and convection to depths of 100–>400 m (e.g. Dong et al., 2008), forming a thick winter mixed layer with uniform properties. Analysis of the δ^{30}Si sytematics of the

---

[5] MODIS Aqua data. See Supplementary Figure A.13.

[6] Mixed layer data from this study are compared with surface Southern Ocean data from other sectors in Supp. Fig. A.14.

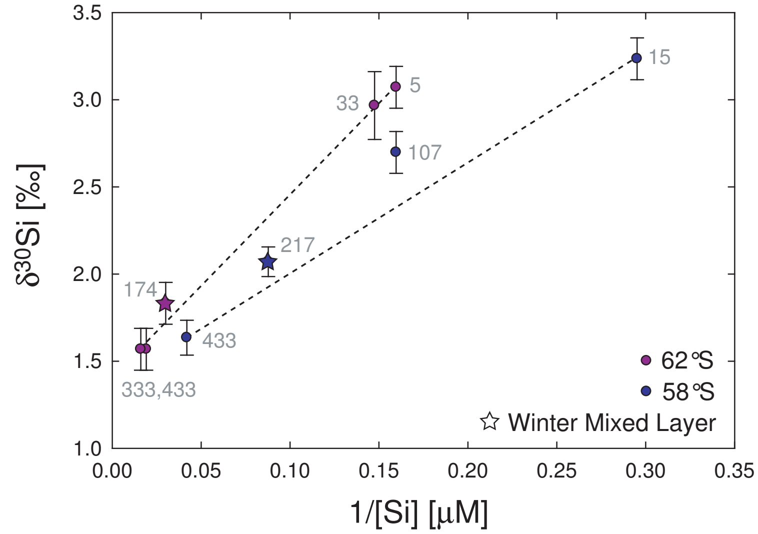

Figure 6.8: A mixing diagram for samples in the near-surface polar ocean. Stars represent the winter mixed layer identified by the temperature minimum (62° S) or potential vorticity minimum (58° S). Dotted lines are drawn between the shallowest and deepest samples (depths indicated by grey numbers, in metres) to guide the eye; note that the winter mixed layer at 58° S appears to be more consistent with mixing between the base of the mixed layer and the deeper water column, which highlights that the real system is more spatially complex than assumed in this simple view.

near-surface water column at the polar stations shows that the high δ^{30}Si values produced in the surface during summer are communicated to the winter mixed layer[7] during deep winter convection: the mixing diagram in Fig. 6.8 shows that the winter mixed layers lie on a mixing line between the summer mixed layer and the deeper water column. Since the Si-depleted surface waters mix with Si-replete subsurface waters during convection, the δ^{30}Si signal of utilisation is strongly attenuated at this step, from values over +3‰ to values around +2‰, but the influence of the high-δ^{30}Si signal is still clearly expressed, as similarly observed by Fripiat (2010), who identified numerous ‘mixing interfaces’ in the Indian sector of the Southern Ocean.

Viewed in terms of annual mass balance, the high δ^{30}Si value of the winter mixed layer implies that a significant portion of the opal produced in the surface ocean is exported past the depth of deepest convection, and that this opal has a low δ^{30}Si value. Thus, the effects of a strongly expressed isotope effect of Si utilisation, efficient particulate export, and buoyancy-driven mixing combine over the annual cycle to fractionate Si isotopes between the deeper Southern Ocean and the annually accessible surface. This is the first step in the production of a high δ^{30}Si value in the ocean interior, as I discuss below.

Formation of Mode and Intermediate Waters: The winter convection that leads to deep mixed layers in the Subantarctic Zone is the first step in the formation of SAMW, of which southeast Pacific

---

[7] Winter mixed layers were identified by the temperature minimum at 62° S and a potential vorticity minimum at 58° S.

AAIW is the densest type (McCartney, 1977; Hanawa and Talley, 2001)[8]. These water masses are introduced into the interior thermocline by the combined effects of lateral induction, Ekman pumping, and mesoscale eddy-induced advection (Karstensen and Quadfasel, 2002; Sallée et al., 2010). When they subduct, the water masses introduce the properties of the Subantarctic winter mixed layer, such as high concentrations of oxygen and anthropogenic chlorofluorocarbons (CFCs) and negative Si* values (Sarmiento et al., 2004a), into the permanent thermocline (Stommel, 1979). This same process also necessarily subducts the high δ^{30}Si values of the winter mixed layer into the ocean interior. As the δ^{30}Si–γ^n relationship documents (Fig. 6.7), these high values are not destroyed by mixing downstream, but rather conserved exceptionally well along the flow path of SAMW and AAIW within the thermocline interior. It can be seen that for all samples within the SAMW–AAIW density range of γ^n = 27.15–27.3, the δ^{30}Si values of all stations south of 12° S are essentially identical to each other (and to the winter mixed layer at 58° S, although this is most likely fortuitous); the same feature is illustrated in a less quantitative but more visually striking manner in Fig. 6.5, where the high δ^{30}Si values are seen to follow the tongue of low salinity and negative Si* that corresponds to SAMW/AAIW. The close correspondence of the presence of these well-ventilated waters with high δ^{30}Si values in the subsurface is further illustrated by the correlation between high δ^{30}Si values and significant concentrations of anthropogenic CFC-11 in subsurface waters, as shown in Fig. 6.9.

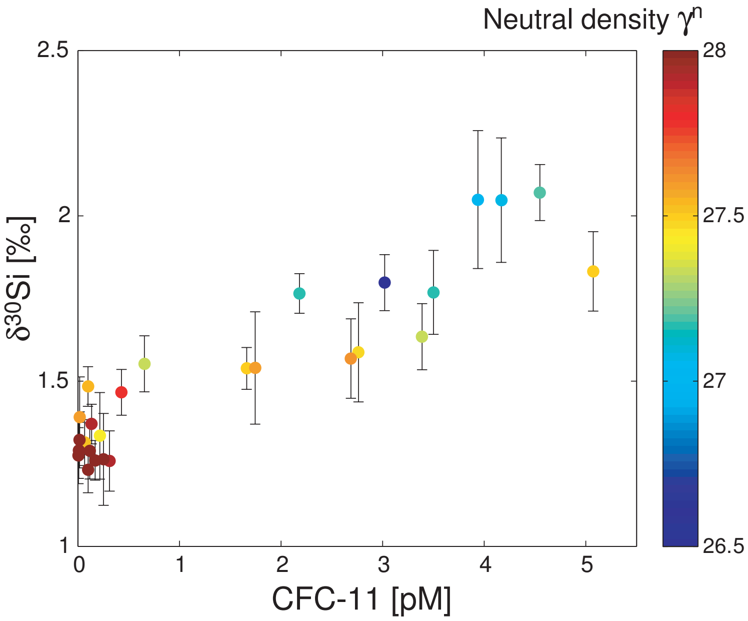

Figure 6.9: CFC-11 concentrations plotted against δ^{30}Si values for samples below the depth of the mixed layer. The poorly-ventilated equatorial Pacific station is excluded. Datapoint colour corresponds to neutral density.

---

[8] Winter (July–September) outcrops of the γ^n = 27.15 − 27.3 isopycnals corresponding to the density range of SAMW and AAIW are located at 56°–61° S at this longitude (Antonov et al., 2010; Locarnini et al., 2010)

The analysis of this unique dataset spanning both high southern latitudes and the subtropical thermocline thus allows the analysis of the development and introduction of high δ^{30}Si values into the upper ocean interior by intermediate and mode waters of Southern Ocean origin. I have shown that the high δ^{30}Si values of SAMW and AAIW derive from the properties of the high-latitude mixed layer, which possess high δ^{30}Si values due to the balance between efficient opal export and deep winter convection. The good conservation of these high values as the waters transit equatorwards indicates that either the Si inventory of the SAMW and AAIW remains dominantly preformed (i.e. introduced in dissolved form during subduction), or that the δ^{30}Si value of sinking opal that dissolves in them is not sufficiently to have a significant influence on their isotope compositions. The close similarity of [Si] along isopycnal surfaces for all stations south of the equatorial regime at the density level of SAMW and AAIW (Fig. 6.7b) indicates that, as in the waters of the Atlantic thermocline (Chapter 5), the preformed component is indeed dominant. This picture changes dramatically in the equatorial regime north of 20° S, and it is to this section of the dataset that I now turn.

6.4.2 Low δ^{30}Si in the equatorial Pacific

The δ^{30}Si distribution at 12° S is completely different from that at the more southerly stations, with uniformly low values throughout the upper water column. It is apparent that the high δ^{30}Si signature of SAMW and AAIW, which is strongly conserved further south, has been lost in the equatorial Pacific. In the following, I attempt to identify the origin of this difference, which requires consideration of the circulation and nature of biogeochemical cycling in the equatorial Pacific Ocean.

As noted in Section 6.2.1, θ–S relationships (Fig. 6.4) and geographical tracer distributions (Figs. 6.2 and 6.3) show that the thermocline water column at 12° S is very different from that within the gyre: it is more saline, poorer in oxygen and richer in nutrients. These features are the result of a number of processes. Thermocline waters of the subtropical gyre transit to the equatorial regime via a northward western boundary undercurrent in the western Pacific. The downward mixing of upper, more saline waters in the undercurrent is the most likely cause of the salinity increase observed (Tsuchiya and Talley, 1996), since AAIW already exhibits the typical salinity and density of its equatorial type (S = 34.5, γ^n = 27.45) when it reaches the western equatorial Pacific (Tsuchiya, 1991). Within the equatorial system, conservative parameters show little zonal variability below the surface. In stark contrast to this, biogeochemical tracers such as oxygen and nitrate show strong zonal gradients along ispycnals, with the eastern Pacific being nitrate-richer and oxygen-poorer than the west (Fig. 6.10a,b); indeed, the eastern Pacific hosts the ocean's most extensive oxygen minimum zones (OMZs). The oxygen depletion and nitrate enrichment are the result of a combination of sluggish ventilation, strongly zonal flow, and the remineralisation of organic matter that leads to a high oxygen demand (e.g. Karstensen et al., 2008). These processes lead to the build-up of a large pool of regenerated nutrients in the eastern subsurface (e.g. Toggweiler and Carson, 1995).

Interestingly, Si is an exception to the general rule of strong zonal concentration gradients (Fig. 6.10c): Si concentrations primarily show a strong meridional gradient, with no zonal component along the equator, while a mild zonal gradient is associated with the Peruvian coastal upwelling centred at about 10° S. These two gradients reflect two different processes that control the Si distribution in the equatorial Pacific thermocline. The meridional gradient is the result of the very marked difference in the Si content of thermocline waters of South and North Pacific origin. This disparity is displayed in the distribution of the tracer Si*, which increases from negative values in the south (representing a Si deficit) to highly positive values in the north (Fig. 6.10d; Sarmiento et al., 2004a). At the depth level of the Equatorial Undercurrent that is fed by both northern and southern sources (Tsuchiya et al., 1989; Toggweiler et al., 1991), Dugdale et al. (2002) have shown that, although northern and southern waters contribute equally to equatorial waters in terms of volume flux, their disparate Si content results in waters of North Pacific origin contributing disproportionately to the Si budget, supplying 70% of Si in the EUC. This lateral influence of the Si-rich North Pacific is reflected in the meridional Si* and [Si] gradient across the equatorial Pacific Ocean.

However, in addition to this meridional gradient, there is also a zonal [Si] gradient south of the equator, associated with the Peruvian coastal upwelling. This gradient can be viewed as the result of an additional enrichment of Si on isopycnals towards the east, over and above the enrichment caused by the incorporation of a North Pacific Si-rich component. Such an enrichment is analogous to the accumulation of regenerated nitrate documented by the model of Toggweiler and Carson (1995), suggesting that there is a significant contribution of remineralised Si at the eastern margin of the equatorial Pacific thermocline, which may find its surface expression in the tongue of high surface [Si] (6–8 µM) extending westwards from the Peruvian coast (Garcia et al., 2010b).

Thus, the >100% increase in [Si] (from 21 µM to 46 µM) at SAMW densities ($\gamma^n \approx 27.15$) between 26° S and 12° S can be viewed as the combined result of lateral input of Si from the North Pacific, and the accumulation of remineralised Si within the shadow zone of the eastern equatorial Pacific thermocline. A simple isotope mass balance calculation indicates that to explain the observed decrease in δ^{30}Si values at the density level of SAMW (from +1.76‰ to +1.38‰) between 26° S and 12° S, these two processes would need to add Si with an isotopic composition of +1.2‰, a value that is not abnormal for either seawater or diatom opal. An estimate of the value for the North Pacific source is hampered by the paucity of data. However, at 24° N 170° E, Reynolds et al. (2006a) reported δ^{30}Si values of +1.31‰ and +1.32‰ at depths that bracket the γ^n = 27.15 surface (600 m and 900 m), indicating that the input of North Pacific Si would be expected to lower δ^{30}Si values in the equatorial Pacific thermocline. The dissolution of opal produced in the Peruvian coastal upwelling may also add

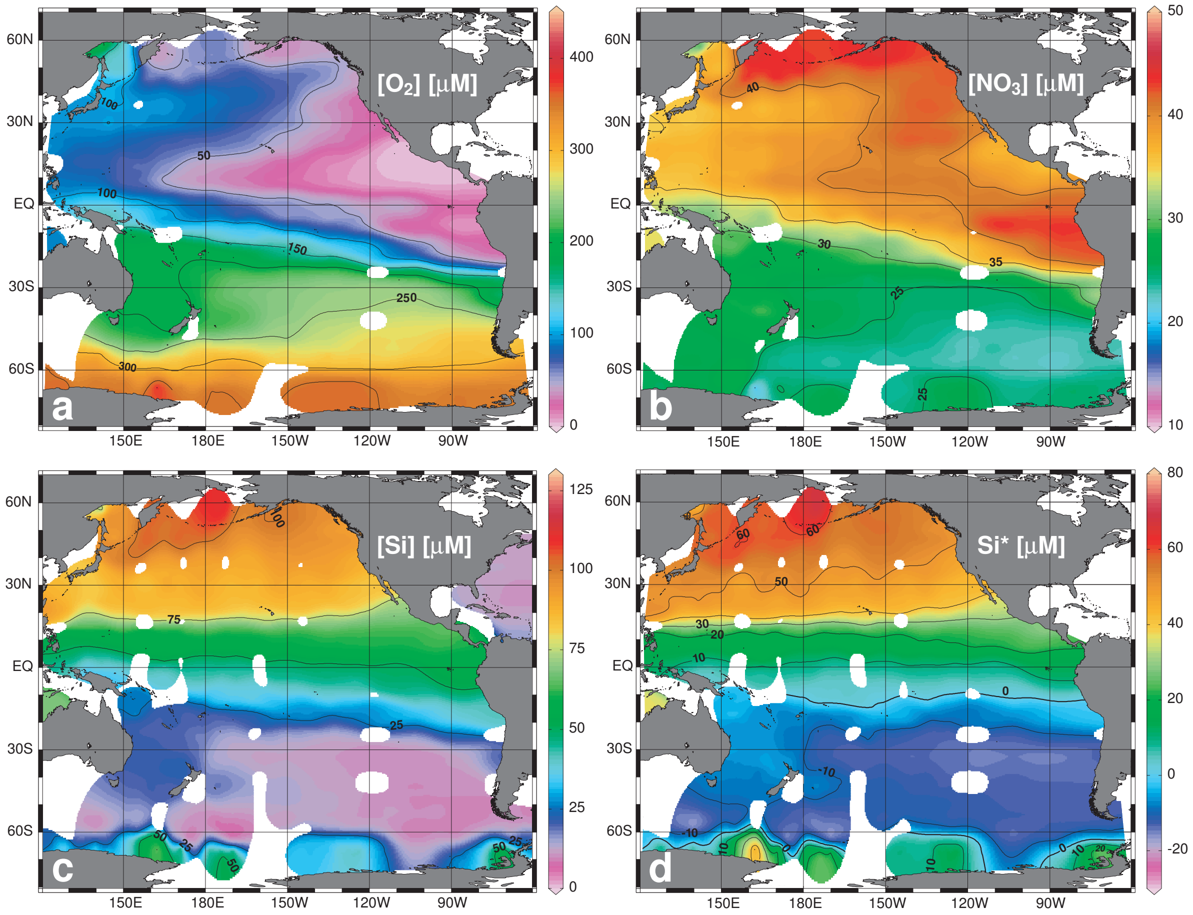
[O$_2$] [μM]
a
60N
30N
EQ
30S
60S
150E
180E
150W
120W
90W
400
300
200
100
0
50
100
150
250
300
[NO$_3$] [μM]
b
50
40
30
20
10
35
25
[Si] [μM]
c
125
100
75
50
25
0
Si* [μM]
d
80
60
40
20
0
-20
-10
10

Figure 6.10: Concentrations of biogeochemical tracers along the γ^n = 27.15 surface that corresponds to SAMW in the South Pacific Ocean. Data are from the eWOCE database (Schlitzer, 2000), plotted using Ocean Data View (Schlitzer, 2009). Note that values of Si* in the eastern Pacific Ocean are affected by denitrification in the suboxic water column.

Si with a low δ^{30}Si value to the thermocline, by a similar mechanism to that we have seen at work in another upwelling region, the Southern Ocean. In the Peruvian upwelling, Si utilisation is below 100%, as documented by elevated [Si] at the surface (Garcia et al., 2010b). As a result, opal exported from the surface will tend to add a low δ^{30}Si value to the subsurface when it dissolves. Thus, the possibility exists for subsurface waters to accumulate a pool of Si with lower δ^{30}Si values during their long residence in the shadow zone of the equatorial thermocline.

In the light of these considerations, it becomes apparent that the observed differences in the δ^{30}Si distribution in the subtropical and equatorial Pacific thermocline are due to the fact that (a) the equatorial Pacific is one of the few ocean regions where the thermocline Si inventory is not dominantly supplied by waters of Southern Ocean origin (Dugdale et al., 2002; Sarmiento et al., 2004a) and/or that (b) the remineralised component of Si appears to be higher in the southeast equatorial region, associated with the Peruvian coastal upwelling. In other words, the subsurface δ^{30}Si distribution traces the cycling of Si within the upper ocean, but records the combination of a preformed signal and a remineralised signal that is integrated over the entire circulation history of the water mass in which the dissolved Si pool is transported, and must be interpreted as such. Although the conflation of source and cycling signals in the equatorial Pacific means that the effect of dissolution cannot be robustly separated from the signal of Si addition from the North Pacific, it appears that the sluggish circulation of the eastern equatorial Pacific, which contains some of the most poorly-ventilated waters of the global ocean (Karstensen et al., 2008; Garcia et al., 2010a) allows such a remineralisation signal to be recorded, whilst within well-ventilated thermocline waters, the δ^{30}Si signal is dominated by the preformed component of Si introduced into the thermocline by SAMW and AAIW.

6.4.3 The deep Pacific δ^{30}Si distribution

Unlike the rich structure observed in the upper ocean, the deepwaters analysed in this study exhibit remarkable homogeneity in δ^{30}Si values. In the Southern Ocean, δ^{30}Si values average +1.25±0.05‰ over the entire deep water column. This value is indistinguishable from the δ^{30}Si value of +1.21±0.06‰ reported in Chapter 4 for CDW from Drake Passage, and from that of 1.22±0.12‰ reported by Cardinal et al. (2005) for the deep Southern Ocean south of Australia (~140° E). It thus appears that the δ^{30}Si value of Circumpolar Deep Water is zonally homogeneous at the sub-0.1‰ level at densities higher than $\gamma^n \approx 27.7$, despite a significant [Si] gradient within these waters. I confirmed this strong zonal homogeneity by analysing six Southern Ocean deepwaters from 2040 m – 5120 m at 44° S 30° E (i.e. south of Africa), which similarly exhibit an average δ^{30}Si value of 1.26±0.13‰(Table 6.2). Additionally, the statistical tests detailed in Section 6.3 indicate that one cannot attribute significance to the small nominal δ^{30}Si variations observed further north in the deep South Pacific. Thus, to first order certainly, δ^{30}Si values are homogeneous in the deep southern and equatorial Pacific Ocean. The degree of δ^{30}Si homogeneity is illustrated by Fig. 6.7c, which shows no significant δ^{30}Si differences for deepwaters with $\gamma^n > 27.7$ – including those from the northern Peru Basin (12°S) whose properties suggest a North Pacific origin – whilst δ^{30}Si values in less dense waters begin to increase (Fig. 6.7a). Although uncertainties regarding the deep Pacific δ^{30}Si distribution (discussed below) make firm conclusions difficult, I would argue that this marked constancy may reflect a fundamental property of the oceanic δ^{30}Si distribution. The density level below which no significant δ^{30}Si variation occurs corresponds closely to the density that separates the upper and lower cells of the overturning circulation in the inverse model of Lumpkin and Speer (2007, γ^n = 27.6); i.e. the two "loops" of Toggweiler et al.'s (2006) schematic alluded to earlier in this thesis (Fig. 4.5). This separation reflects the fact that the only source of deepwaters to the Pacific is CDW from the deep Southern Ocean, the lower limb of the MOC[9]. If the δ^{30}Si values of these deepwaters remain constant over their multicentennial sojourn in the deep Pacific (Matsumoto, 2007), the implication is that the accumulation of Si from the dissolution of sinking diatom opal produces no significant δ^{30}Si signal in the deep Pacific Ocean. This would, in turn, indicate that the production of significant deepwater δ^{30}Si variation requires the presence of a δ^{30}Si signal in the preformed component, analogous to the case for both SAMW/AAIW (Section 6.4.1) and North Atlantic Deep Water (Chapter 4). However, as I detail below, there are a number of inconsistencies in the deep Pacific δ^{30}Si distribution that need to be resolved before this conclusion can be robustly made.

Beucher et al. (2008) and Beucher et al. (2011) have analysed δ^{30}Si in waters of the equatorial Pacific (4° N–3° S) and documented average deepwater[10] δ^{30}Si values +1.32±0.11‰ (n = 6) and +1.39±0.07‰ (n = 6) at 110° W and 140° W respectively. These values are very similar to the average deep South Pacific δ^{30}Si value of +1.30±0.08‰ reported here. Beucher et al. (2008), however, attributed significance to the fact that their average deep equatorial Pacific δ^{30}Si value is nominally higher than that of CDW reported by De La Rocha et al. (2000) and Cardinal et al. (2005). In the light of the high δ^{30}Si values they observed in the extremely Si-enriched waters of the Cascadia Basin (adjacent to the North American coast at 47° N), they hypothesised that the higher values observed at the equator might result from mixing of the low δ^{30}Si value of CDW with a more positive δ^{30}Si signature in the plume of high [Si] the emanates from the northeast Pacific at mid-depth. I test this hypothesis in Fig. 6.11, which is a mixing diagram that compares the Cascadia Basin δ^{30}Si data of Beucher et al. (2008) to all data from the deep southern and equatorial Pacific Ocean (this study;

---

[9] Whilst a North Atlantic signal is resolvable in some properties of CDW, such as S, the low [Si] of NADW means that it plays a completely negligible role for δ^{30}Si, as documented by the homogeneity in deep Southern Ocean δ^{30}Si values, even within the freshly imported NADW salinity maximum at 30° E south of Africa (Table 6.2).

[10] Beucher et al. (2008) use a criterion of $\geq$2000 m water depth, which is essentially equivalent to my criterion of $\gamma^n \geq$ 27.93 outside the Southern Ocean.

Beucher et al., 2008, 2011) with [Si] equal to or higher than that of the deep inflow of CDW into the Pacific Ocean (120 µM; e.g. Warren, 1973). These data are compared to the Cascadia Basin data of Beucher et al. (2008). Figure 6.11 shows that although waters of the Cascadia Basin are clearly both Si-richer and higher in δ^{30}Si than the deep Southern Ocean, waters at intermediate latitudes show no systematic relationship between δ^{30}Si values and [Si] that would be expected from mixing (such as seen in Chapter 4, Fig. 4.3). Any variability is clearly at the limit of analytical resolution, especially considering that offsets on the order of ±0.1‰ between laboratories are possible (Reynolds et al., 2007). The lack of clear variation from the equator southward indicates the necessity of a more systematic study of the δ^{30}Si distribution in the northeast Pacific, which hosts the core of the high-Si plume, before Beucher et al.'s (2008) inference of an influence of Cascadia Basin waters on the deep Pacific δ^{30}Si distribution can be robustly confirmed or excluded.

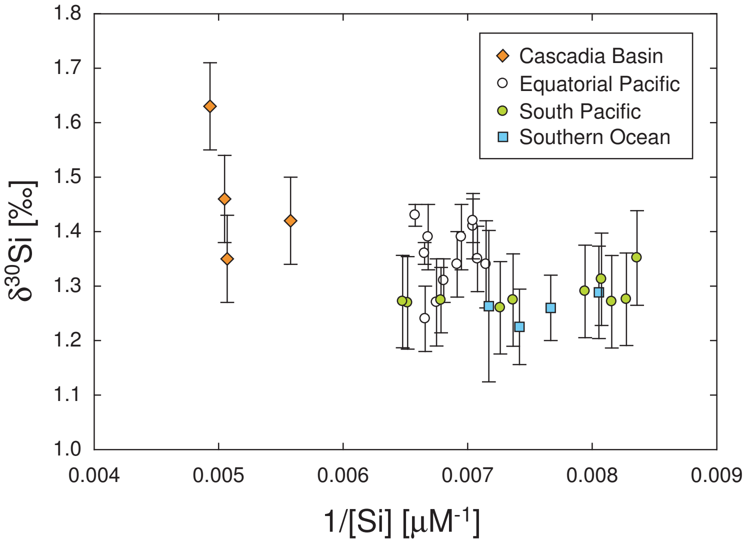

Figure 6.11: A mixing diagram showing deepwaters from the Pacific sector of the Southern Ocean to the Cascadia Basin in the North Pacific (47° N). All deepwater ($\gamma^n \geq 27.93$) samples with [Si] ≥ 120 µM (i.e., the [Si] of the deep CDW inflow into the South Pacific) are included. Cascadia Basin and Equatorial Pacific data are from Beucher et al. (2008, 2011).

The need for such independent confirmation is highlighted by the fact that *low* δ^{30}Si values of approximately +0.8‰ were documented by De La Rocha et al. (2000) and Reynolds et al. (2006a) in the deep northwest Pacific (25°–45° N, 150°–170° W). These low δ^{30}Si values are difficult to reconcile with the values of around +1.3‰ observed in deepwaters of North Pacific origin in this study and by Beucher et al. (2008, Fig. 6.11). The pioneering analyses of De La Rocha et al. (2000) do, however, show variations of as much as ±0.5‰ below 2000 m at a single North Pacific station, as well as values as low as +0.8‰ at 300 m water depth at 24° N. Considering the bandwidth of seawater δ^{30}Si variation documented by the literature published since that first study, these features do cast some doubt on the accuracy of these data. The data of Reynolds et al. (2006a), on the other hand, do not appear anomalous. However, producing the δ^{30}Si values of +0.86‰ to +1.05‰ observed by them in CDW at 24° N requires the addition of Si with a δ^{30}Si value of +0.1‰ to -0.8‰ as CDW flows north from the western South Pacific. Such low values, which are unlikely to be associated with diatom opal or seawater Si, would seem to indicate that the deep North Pacific δ^{30}Si distribution might be affected by hydrothermal input of Si (δ^{30}Si ≈ -0.3‰; De La Rocha et al., 2000) or some as yet undocumented process. Furthermore, considering that the Si-rich deepwaters in the equatorial and southern Pacific, which should represent the return flow from the North Pacific Ocean, exhibit δ^{30}Si values that are higher than those observed further north, it appears that if low δ^{30}Si values exist in the northwestern Pacific, they are contained there by the cyclonic circulation of the region (Reid, 1997). The above discussion, with its many uncertainties, clearly indicates that a systematic regional-scale study of the North Pacific is required, especially including the high-Si plume that emanates from the northeastern Pacific. In the absence of this, it is not possible to come to firm conclusions regarding the large-scale Pacific δ^{30}Si distribution and what features of the oceanic Si cycle it records. This is unfortunate, since a more robust handle on the Pacific δ^{30}Si distribution would allow us to make firm statements regarding the controls on the ocean's global-scale δ^{30}Si distribution. Nonetheless, the low δ^{30}Si variability I observe at densities associated with the lower cell of the meridional overturning circulation, including high-[Si] waters returning from the North Pacific Ocean, suggests that the δ^{30}Si values of deepwaters are not strongly altered by opal dissolution along their deep circulation path; i.e. that large variations in deepwater δ^{30}Si signatures requires the introduction of a preformed δ^{30}Si signal, as in the Atlantic Ocean (Chapter 4). This conclusion must, however, remain tentative until the North Pacific δ^{30}Si distribution is better constrained.

6.5 Conclusions

In this chapter, I have presented new δ^{30}Si data from the eastern South Pacific and the Pacific sector of the Southern Ocean, a region that plays an important role in the ventilation of the mid- and low-latitude thermocline. By analysing the evolution of the δ^{30}Si distribution from the Antarctic Zone into the ventilated thermocline, I was able to trace the incorporation of high δ^{30}Si values into AAIW and SAMW, as I had previously inferred (Chapter 4), and their export to the thermocline interior. Here, the δ^{30}Si distribution documents the dominant influence of the spreading of AAIW and SAMW in determining the mesopelagic δ^{30}Si distribution, tracing the important contribution of the preformed component to the Si inventory of the thermocline. The data also reveal that the high δ^{30}Si signature of AAIW/SAMW is not conserved in the equatorial Pacific. This marked change in the thermocline and intermediate δ^{30}Si distribution appears to record two phenomena: a switch in the dominant source of thermocline Si from the Southern Ocean to the North Pacific (Dugdale et al., 2002; Sarmiento et al., 2004a), and the accumulation of remineralised Si in the shadow zone of the eastern equatorial Pacific. The strong difference in thermocline δ^{30}Si values thus shows that seawater δ^{30}Si values trace Si cycling within the ocean, but that the signal it records must be interpreted in the context of water mass history.

The low variability of δ^{30}Si values in deep South Pacific waters denser than γ^n = 27.7, which circulate within the lower limb of the meridional overturning circulation (Fig. 1.1; Lumpkin and Speer, 2007), suggests that the dissolution of opal is able to produce only a small change in deepwater δ^{30}Si values. However, the certainty of such a conclusion is undermined by uncertainties that still exist regarding the deep Pacific δ^{30}Si distribution, especially in the North Pacific. A detailed study of the meridional and/or zonal δ^{30}Si distribution in the North Pacific, including its high-Si plume, is needed before robust conclusions can be drawn.

Table 6.2: Hydographic, nutrient and Si isotope data for all samples from CLIVAR line P18 re-occupation. *n* denotes number of complete replicates. Also included are 6 datapoints from the deep Southern Ocean south of Africa, collected on the CLIVAR re-occupation of WOCE line I06S (expedition 33RR20080204).

Station	**Latitude**	**Depth**	σ_θ	θ	S	**[O_2]**	**[Si]**	**[NO_3]**	**[PO_4]**	**Si***	**δ^{30}Si**	**$2\sigma_{SEM}$**[a]	*n*
		m	**kg/m^3**	**°C**	**psu**	**µM**	**µM**	**µM**	**µM**	**µM**	‰	external	
CLIVAR P18 re-occupation, 103°W:													
70	11°45' S	5	24.559	22.717	35.714	227.0	1.4	6.7	0.7	-5.2	-		
		33	24.624	22.453	35.700	226.4	1.5	6.8	0.7	-5.2	-		
		83	25.175	20.638	35.764	219.3	2.1	4.2	0.9	-2.2	-		
		133	25.382	19.036	35.483	186.4	2.7	7.4	2.6	-4.7	1.73	0.21	1
		182	26.226	13.080	34.804	8.7	19.1	25.1	2.6	-6.1	-		
		215	26.496	11.685	34.803	14.2	24.2	29.7	2.5	-5.4	1.49	0.12	1
		265	26.652	10.783	34.790	-	27.0	33.4	2.6	-6.4	1.57	0.12	1
		314	26.737	10.152	34.758	20.9	31.3	35.6	2.8	-4.3	1.50	0.07	3
		430	26.872	8.957	34.676	23.4	35.5	38.8	3.0	-3.3	1.42	0.11	2
		625	27.088	6.959	34.572	27.5	46.4	43.8	3.1	2.7	1.39	0.07	3
		824	27.254	5.399	34.527	49.0	62.8	44.8	3.1	18.0	1.38	0.11	3
		1024	27.39	4.280	34.539	74.4	82.6	43.3	3.0	39.3	1.35	0.08	2
		1172	27.458	3.762	34.557	85.7	94.0	42.4	2.9	51.6	-		
		1454	27.564	2.957	34.593	97.6	114.8	41.4	2.8	73.4	1.36	0.17	1
		1848	27.655	2.269	34.632	118.1	131.1	39.7	2.7	91.5	1.25	0.07	3
		2241	27.713	1.831	34.661	135.8	137.7	38.4	2.6	99.3	1.26	0.08	2
		2831	27.748	1.565	34.680	141.8	147.4	38.1	2.6	109.2	1.27	0.06	4
		3533	27.753	1.497	34.679	141.1	153.4	38.2	2.6	115.2	1.27	0.08	2
		3776	27.754	1.489	34.680	141.3	154.2	38.2	2.6	115.9	-		
		4132	27.755	1.484	34.681	141.1	154.4	38.2	0.1	116.1	1.27	0.08	2
95	26°20' S	6	24.4	24.293	36.116	217.4	0.7	0.2	0.1	0.5	-		
		46	25.026	21.742	35.966	232.4	0.7	0.2	0.1	0.5	-		
		105	25.315	20.554	35.918	235.0	0.7	0.2	0.2	0.5	-		

table continues on next page

Station	**Latitude**	**Depth** m	σ_θ kg/m^3	θ °C	S psu	[O_2] µM	[Si] µM	[NO_3] µM	[PO_4] µM	Si* µM	δ^{30}Si ‰	2σ_{SEM}^{a} external	*n*
		206	25.556	18.276	35.458	233.9	0.7	0.5	1.3	0.2	-		
		366	26.392	10.706	34.440	188.2	5.6	17.8	2.1	-12.1	1.80	0.08	2
		430	26.713	8.581	34.398	136.2	13.9	27.8	2.0	-14.0	1.66	0.14	2
		629	27.03	5.841	34.313	210.1	15.2	29.7	2.1	-14.5	1.76	0.06	4
		727	27.09	5.332	34.310	197.0	21.4	31.9	2.4	-10.6	-		
		826	27.167	4.89	34.343	171.6	31.9	35.0	2.6	-3.1	1.55	0.08	2
		924	27.257	4.442	34.393	144.5	46.7	37.8	2.6	8.9	1.33	0.13	2
		1022	27.336	3.905	34.422	140.8	58.5	38.5	2.7	19.9	1.31	0.07	3
		1122	27.403	3.608	34.468	134.6	70.3	39.0	2.7	31.2	1.39	0.12	3
		1223	27.456	3.322	34.500	134.9	78.5	39.0	2.6	39.5	-		
		1321	27.529	2.908	34.543	143.0	88.1	38.2	2.6	49.8	-		
		1418	27.571	2.663	34.568	149.4	93.1	37.8	2.5	55.3	1.36	0.12	1
		1518	27.616	2.396	34.596	154.0	101.5	37.3	2.5	64.2	1.35	0.08	2
		1650	27.641	2.207	34.608	156.8	107.3	36.9	2.5	70.4	1.33	0.08	2
		1849	27.686	1.969	34.640	159.7	116.5	36.7	2.5	79.9			
		2044	27.702	1.850	34.649	160.4	120.9	36.6	2.5	84.3	1.28	0.08	2
		2105	27.711	1.810	34.656	160.3	122.6	36.6	0.4	86.0	1.27	0.08	2
114	37° 25' S	9	24.044	20.267	34.150	237.4	0.1	4.6	0.6	-4.5	-		
		116	25.84	12.414	34.136	271.8	0.6	7.6	1.0	-7.0	-		
		191	26.29	10.361	34.230	249.5	1.3	14.2	1.5	-12.8	-		
		379	26.904	6.822	34.316	252.3	6.4	22.9	1.7	-16.5	2.05	0.21	2
		660	27.024	5.680	34.280	254.4	10.7	25.7	2.0	-15.0	1.91	0.15	5
		858	27.124	4.768	34.271	228.0	20.1	29.9	2.4	-9.8	1.79	0.14	1
		1057	27.263	3.872	34.326	191.6	38.8	34.3	2.5	4.5	1.49	0.08	4
		1156	27.35	3.486	34.387	167.0	53.7	36.6	2.7	17.2	1.48	0.06	4
		1319	27.45	3.156	34.473	139.9	73.4	38.5	2.7	34.8	1.45	0.06	4
		1516	27.538	2.807	34.543	134.9	90.4	38.6	2.5	51.8	-		
		2106	27.695	1.955	34.650	163.6	109.1	35.9	2.5	73.3	1.36	0.10	4
		2499	27.744	1.680	34.686	193.0	117.5	35.4	2.4	82.1	1.39	0.08	2
		2891	27.757	1.567	34.691	173.8	119.6	35.1	2.4	84.5	1.35	0.09	2
		3365	27.79	1.250	34.704	185.6	123.8	34.5	1.2	89.3	1.31	0.08	2
136	50° 15' S	5	26.406	9.385	34.170	290.2	1.7	16.7	1.4	-15.0	-		
		99	26.736	7.345	34.194	299.9	3.2	17.8	1.5	-14.6	2.79	0.14	1
		322	26.948	6.402	34.300	281.3	7.2	21.8	1.8	-14.6	2.05	0.19	2
		644	27.022	5.530	34.255	256.1	13.5	26.0	2.2	-12.5	1.77	0.13	2
		940	27.21	4.230	34.305	216.3	32.2	31.7	2.3	0.4	-		
		1087	27.302	3.576	34.338	206.8	42.9	33.5	2.5	9.5	1.54	0.06	4
		1579	27.565	2.489	34.543	176.1	75.7	35.7	2.4	40.1	1.47	0.07	3
		1972	27.684	2.161	34.657	174.7	89.6	34.7	2.4	54.9	1.37	0.06	4
		2366	27.745	1.827	34.701	178.7	102.2	34.3	2.4	67.8	-		
		2757	27.775	1.513	34.708	182.1	113.2	34.3	2.4	78.8	1.32	0.08	2
		3538	27.821	0.921	34.714	198.8	125.9	34.0	2.4	91.9	1.29	0.08	2
		3928	27.842	0.538	34.711	209.5	135.8	34.1	1.5	101.7	1.27	0.08	2
149	57° 45' S	15	26.721	6.551	34.038	309.2	3.4	21.0	1.5	-17.7	3.23	0.12	1
		58	26.735	6.459	34.039	308.7	3.4	20.9	1.6	-17.6	-		
		107	26.893	5.392	34.070	309.5	6.3	22.2	1.8	-15.9	2.70	0.12	1
		215	27.039	4.328	34.104	300.0	11.4	25.6	2.1	-14.2	2.07	0.08	2
		428	27.155	4.046	34.213	248.4	23.8	30.0	2.3	-6.2	1.63	0.10	2

table continues on next page

Station	**Latitude**	**Depth**	σ_θ	θ	S	**[O$_2$]**	**[Si]**	**[NO$_3$]**	**[PO$_4$]**	**Si***	**δ^{30}Si**	**2σ_{SEM}**[a]	n
		m	**kg/m^3**	**°C**	**psu**	**μM**	**μM**	**μM**	**μM**	**μM**	‰	external	
		624	27.271	3.271	34.262	228.5	37.3	32.8	2.4	4.5	1.59	0.15	2
		824	27.391	2.846	34.363	204.2	52.8	34.7	2.5	18.1	1.54	0.17	1
		1054	27.511	2.586	34.485	183.4	67.8	35.7	1.7	32.2	-		
158	62° 15' S	4	26.938	3.807	33.910	328.5	6.3	25.1	1.7	-18.8	3.07	0.12	1
		32	26.956	3.698	33.918	329.3	6.8	25.2	2.2	-18.4	2.97	0.19	1
		174	27.287	0.901	34.048	313.7	33.3	31.2	2.4	2.1	1.83	0.12	1
		330	27.396	2.094	34.290	227.6	52.3	34.7	2.5	17.6	1.57	0.12	1
		428	27.467	2.327	34.403	198.8	62.4	35.8	2.4	26.6	1.57	0.12	1
		987	27.698	2.097	34.668	182.0	83.9	34.1	2.3	49.7	1.26	0.09	4
		1382	27.764	1.816	34.722	191.8	91.4	32.8	2.3	58.6	-		
		2102	27.814	1.209	34.729	202.2	108.9	33.0	2.3	76.0	1.23	0.07	3
		2494	27.824	0.963	34.721	205.8	116.6	33.2	2.3	83.4	-		
		2918	27.833	0.721	34.714	210.0	124.2	33.5	2.3	90.7	1.29	0.08	2
		3405	27.843	0.475	34.707	214.1	130.4	33.6	2.3	96.8	1.26	0.06	4
		3891	27.854	0.233	34.704	219.1	134.9	33.8	2.3	101.0	1.23	0.07	3
		4378	27.863	0.089	34.704	221.7	139.5	33.8	2.4	105.7	1.26	0.14	1
		4863	27.864	0.026	34.702	222.7	143.5	33.9	0.0	109.6	-		
Indo-Atlantic Sector of the Southern Ocean, 30° E (CLIVAR I06S re-occupation):													
33	43° 30' S	2041	27.775	2.45	34.801	213.1	60.9	28.1	1.9	32.8	1.38	0.12	1
		2602	27.821	2.09	34.821	224.7	65.2	27.2	1.9	38.0	1.18	0.14	1
		3202	27.839	1.53	34.789	222.1	83.9	28.8	2.0	55.0	1.27	0.12	1
		3799	27.840	0.84	34.731	219.0	108.6	31.5	2.2	77.1	1.25	0.12	1
		4400	27.840	0.34	34.693	220.3	125.8	33.1	2.3	92.7	1.26	0.12	1
		5125	27.846	-0.15	34.669	231.2	134.5	33.6	2.3	100.9	1.25	0.12	1

---

[a] where n = 1, errors are external 2σ_{SD}.

Chapter 7

Concluding remarks

7.1 Summary

In this thesis, I have presented a seawater δ^{30}Si dataset that spans a broad geographic range within the Atlantic and South Pacific Oceans. These data present a coherent view of the oceanic δ^{30}Si distribution, and provide strong evidence for an oceanic Si cycle that is strongly dominated by the interaction between the physical circulation and biological activity in the Southern Ocean.

The deep Atlantic Ocean displays a highly coherent δ^{30}Si distribution at the basin scale, exhibiting a surprisingly large and systematic meridional gradient in deepwater δ^{30}Si values, as well as small but resolvable vertical gradients within the deep water column. In Chapter 4, I was able to show that these gradients are the result of the quasi-conservative mixing of Si from the two sources of deepwater to the Atlantic Ocean: high δ^{30}Si values are associated with the Si-poor watermasses that combine to form NADW, whilst low δ^{30}Si values are transported into the abyssal Atlantic by Si-rich AABW from the Southern Ocean. The quasi-conservativity of Si documented by the deep δ^{30}Si distribution indicates that the dissolution of sinking opal in the Atlantic Ocean contributes insignificantly to the Si inventory of the deep watermasses.

Furthermore, I argued that the high δ^{30}Si value exported from the North Atlantic in NADW must reflect the supply of Si with a high δ^{30}Si value to the North Atlantic via the upper return path of the meridional overturning circulation (MOC). This implies that the high δ^{30}Si value of NADW ultimately owes its existence to diatom Si utilisation at high *southern* latitudes, which fractionates Si isotopes between the shallow (AAIW/SAMW) and deep (AABW) waters exported from the Southern Ocean, i.e. between the upper and lower limbs of the MOC.

The Atlantic silicon isotope sytematics also document a sharp discontinuity in the δ^{30}Si distribution at the transition to the ventilated thermocline, documenting that the thermocline is strongly decoupled from the deep ocean in terms of its Si cycling (Chapter 5). The properties of the water column at this sharp transition correspond to those of SAMW, indicating that this watermass plays a key role in the supply of Si to the ventilated thermocline. Building upon arguments developed from the fundamental considerations introduced in Chapter 3, I argue that the vertical δ^{30}Si gradient, which extends to significant depth within the thermocline, must be created by the physical transport of Si from the surface ocean into the interior during ventilation of thermocline isopycnals. This mechanism implies that a significant proportion of the subsurface Si inventory is preformed, rather than being added by the dissolution of sinking opal, an inference that is supported by the strong hydrographic control on the thermocline δ^{30}Si distribution.

In Chapter 6, I presented a δ^{30}Si dataset from the southeast Pacific Ocean, extending from the Antarctic Zone of the Southern Ocean to the equatorial Pacific. This wide latitudinal span allowed me to trace the incorporation of high δ^{30}Si values into SAMW and AAIW, and their export to the thermocline interior. The data reveals that high δ^{30}Si values created in the surface Southern Ocean by diatom Si utilisation are partially preserved in the winter mixed layer following deep convection, such that they can be introduced into the interior thermocline during the subduction of SAMW and AAIW. These watermasses conserve their δ^{30}Si signature as they transit the subtropical gyre, as documented by the strong isopycnal control on the δ^{30}Si distribution. In the equatorial Pacific Ocean, the high δ^{30}Si values subducted at SAMW and AAIW densities are absent, a feature that most likely documents a combination of the introduction of North Pacific Si into the equatorial thermocline, as well as the accumulation of remineralised Si within the poorly-ventilated waters of the eastern equatorial Pacific Ocean.

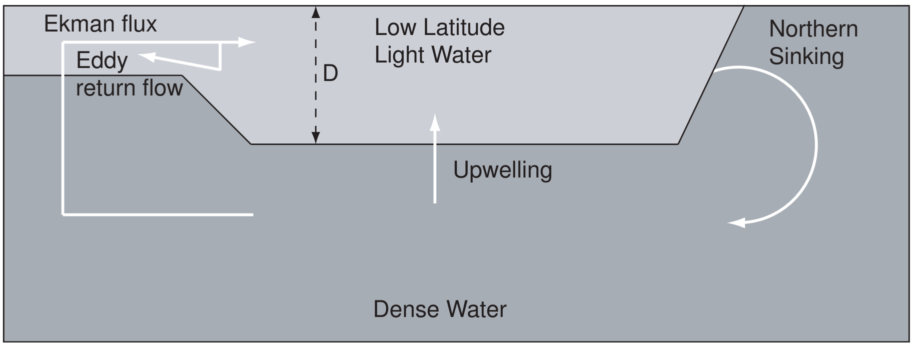

Figure 7.1: A representation of the key features of the analytical model of Gnanadesikan (1999b). The depth of the oceanic pycnocline *D* may be maintained by balancing the northern sinking of waters either by upwelling through the pycnocline at low latitudes, or by wind-driven upwelling at high southern latitudes.

7.2 Synthesis

This thesis has documented that the oceanic δ^{30}Si distribution exhibits clear structure at the large scale, which is brought about by the transport of δ^{30}Si signatures by watermasses that play a key role in the meridional overturning circulation. Specifically, the data show that the low-latitude thermocline bears the high-δ^{30}Si signature of SAMW and AAIW at all locations where the Si* distribution indicates that they dominate the Si inventory of the thermocline. This coherent picture allows me to come full circle and address the questions regarding the pathways of large-scale ocean nutrient transport posed at the beginning of this thesis.

As summarised in the schematic diagram of Fig. 7.1, nutrients may be supplied to the thermocline from the deep ocean either through the upwelling of deepwaters at low latitudes (Stommel and Arons, 1960), or by a lateral supply of waters that have been exposed to biological activity in the surface Southern Ocean (Toggweiler and Samuels, 1993a). A dominance of the latter pathway would predict that the nutrient properties of waters in the thermocline reflect such a biological signal from the surface Southern Ocean. This is precisely what the thermocline δ^{30}Si distribution documents, both in the Atlantic as well as in the Pacific Oceans: rather than the low δ^{30}Si value that would be expected to be supplied by the upwelling of deepwaters, the upper ocean exhibits elevated δ^{30}Si values – tracing Si that has been fractionated by biological activity in the surface ocean – that extend to density levels ventilated from the south by SAMW and AAIW.

In principle, the propagation of a high δ^{30}Si signal to the base of the thermocline and below could also be produced by a high diapycnal diffusivity, which in turn would suggest strong, diffusely-distributed upwelling. However, I would argue that the oceanic δ^{30}Si distribution provides strong evidence against this. The data presented here have shown that surface δ^{30}Si signatures in the mixed layer are elevated to similar values of around +3‰ at both high and low latitudes. Since the higher Si content of the high-latitude mixed layer provides it with greater leverage during mixing with the subsurface, large diapycnal mixing in the Stommel and Arons (1960) paradigm would be expected to result in a deeper vertical δ^{30}Si gradient at high latitudes. As we have seen, the exact opposite is the case (e.g. Fig. 6.5). Rather, the data presented here document a strong isopycnal control on the upper ocean's δ^{30}Si distribution, both over large distances as well as when isopycnal surfaces deepen by over half a kilometre, strengthening the evidence for a small value of diapycnal diffusivity in the thermocline.

The insights provided by the upper ocean δ^{30}Si distribution are complemented by observations of δ^{30}Si in the deep sea. The transequatorial coherence of the deep Atlantic δ^{30}Si distribution documents quasi-conservative behaviour of Si at depth. This quasi-conservativity indicates that the dissolution of opal contributes negligibly to the Si content of Atlantic deepwaters, in contrast to the expected behaviour if significant upwelling of deepwaters were to occur at low latitudes. Furthermore,

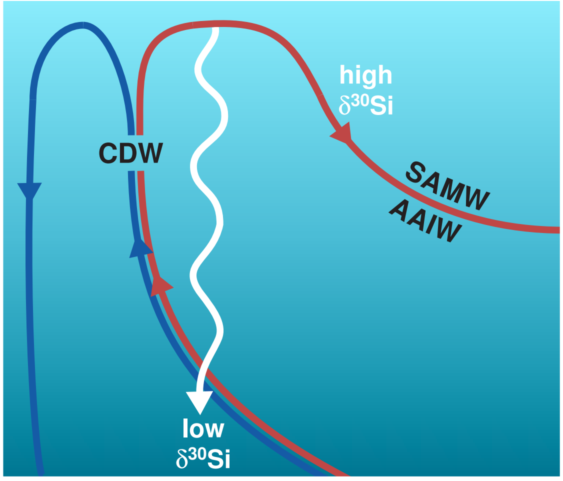

Figure 7.2: A cartoon representing the mechanism by which the Southern Ocean produces large-scale subsurface δ^{30}Si variation in the ocean. Silicon taken up from upper (red) limb of the overturning circulation is exported to depth as opal (white arrow), some of which sinks past the density level that separates the upper and lower (blue) limbs of the overturning circulation. This incomplete mass transfer is associated with a fractionation of Si isotopes between the two limbs of the overturning circulation. Figure based on schematics by Sarmiento et al. (2004a) and Toggweiler et al. (2006).

the fact that the high-δ^{30}Si signature of the Southern Ocean watermasses SAMW and AAIW is imparted to NADW implies minimal entrainment of deeper waters during their northward passage to the North Atlantic.

In summary, the view of oceanic nutrient transport provided by the δ^{30}Si distribution is one in which the Southern Ocean plays a vital role in supplying the nutrients that support primary productivity in the surface ocean. The δ^{30}Si distribution implies that large-scale subsurface δ^{30}Si variability in the ocean ultimately has its origin in the surface ocean at high southern latitudes. The ability of the Southern Ocean to create large isotopic signals is the combined result of the unique configuration of its circulation and the efficiency with which the heavily silicified diatoms of the Southern Ocean export opal to depth (Figure 7.2). In the Southern Ocean, the upward heaving of Si-rich waters in a highly seasonal and dynamic setting supports a strongly diatom-dominated ecosystem. Diatoms take up Si from the upwelled deepwaters that are transported northwards in the upper limb of the overturning circulation, producing a residual high δ^{30}Si signature in the near-surface high-latitude ocean that documents the export of low-δ^{30}Si opal. This export flux partially sinks to depths where its dissolution contributes to the lower limb of the overturning circulation, effectively leading to a fractionation of Si isotopes between the two limbs of the MOC. The high δ^{30}Si, low [Si] signal produced by diatoms in the surface waters of the upper MOC limb persists in the deep winter mixed layers of the region, which are eventually subducted as SAMW and AAIW and transported equatorwards. The upper ocean δ^{30}Si distribution traces this high-latitude δ^{30}Si signal through the low-latitude thermocline, with a strong hydrographic control that indicates that preformed Si represents a large proportion of the Si inventory. Together, these observations imply that the low Si content of the ocean's thermocline does not primarily document a generally slow dissolution of opal (Broecker and Peng, 1982), but is rather a distal signal of its efficient export past the base of the winter mixed layer in the Southern Ocean (Sarmiento et al., 2004a, 2007).

Appendix A

Supplementary Information

A.1 Appendix to Chapter 3

A.1.1 Closed system isotope fractionation with periodic back-reaction

The model simulates isotope fractionation during the transfer of an element from a reactant pool to a product pool:

$$R \xrightarrow{k_i} P$$

This is implemented by tracing the concentrations of two isotopes ('light' and 'heavy') of the element in the two pools: R_{light} and R_{heavy} in the reactant pool, and P_{light} and P_{heavy} in the product pool. Isotope fractionation during the reaction is modelled by allowing the two isotopes to react at different (first-order) rates, k_{light} and k_{heavy}, with the relationship:

$$k_{heavy} = \alpha \cdot k_{light}$$

where α is the fractionation factor associated with the reaction (α is a unitless number close to 1, while the isotope effect ε is defined as $(\alpha - 1) \times 1000$ and has units of permil). The backward reaction,

$$P \xrightarrow{k_d} R$$

proceeds at the same rate, k_d, for both isotopes, such that this reaction is not associated with an isotopic fractionation. This can be formulated as a set of ordinary differential equations (ODEs):

$$\frac{d}{dt}\begin{bmatrix} R_{light} \\ P_{light} \\ R_{heavy} \\ P_{heavy} \end{bmatrix} = \begin{bmatrix} -k_{light} & k_d & 0 & 0 \\ k_{light} & -k_d & 0 & 0 \\ 0 & 0 & -k_{heavy} & k_d \\ 0 & 0 & k_{heavy} & -k_d \end{bmatrix} \times \begin{bmatrix} R_{light} \\ P_{light} \\ R_{heavy} \\ P_{heavy} \end{bmatrix}$$

For $k_d = 0$, the solution of this system produces an evolution of the isotopic composition of the reactant pool (R_{heavy}/R_{light}, or the corresponding δ-value) according to the Rayleigh equation (solid black curve in Fig. 3.1). If $k_d > 0$, the system evolves to a stable equilibrium with finite R and P pools (some point on the dashed line in Fig. 3.1). The periodic back-reaction model presented in the manuscript was solved numerically with the condition:

$$k_d = \begin{cases} 0, & \text{if } \sin(a \cdot t) > 0 \\ b, & \text{if } \sin(a \cdot t) < 0 \end{cases}$$

where t is time, a is an arbitrary constant and b is the value of parameter k_d as defined in the model.

A.1.2 Two-box model of utilisation and mixing

The model consists of a "surface" box in which the dissolved reactant is converted (at first-order rate k_i, i = light or heavy) into an exported product, and a "deep" box in which the product is completely remineralised to the reactant. The two boxes are connected by an exchange volume flux, Q_{ex}. As in Section A.1.1, both the light and heavy isotopes of the element are traced by the model. Indeed, the two models are mathematically essentially identical, as the system of ODEs indicates:

$$\frac{d}{dt}\begin{bmatrix} M_{surf}^{light} \\ M_{deep}^{light} \\ M_{surf}^{heavy} \\ M_{deep}^{heavy} \end{bmatrix} = \begin{bmatrix} -\left(\frac{Q_{ex}}{V_{surf}} + k_{light}\right) & \frac{Q_{ex}}{V_{deep}} & 0 & 0 \\ \left(\frac{Q_{ex}}{V_{surf}} + k_{light}\right) & -\frac{Q_{ex}}{V_{deep}} & 0 & 0 \\ 0 & 0 & -\left(\frac{Q_{ex}}{V_{surf}} + k_{heavy}\right) & \frac{Q_{ex}}{V_{deep}} \\ 0 & 0 & \left(\frac{Q_{ex}}{V_{surf}} + k_{heavy}\right) & \frac{Q_{ex}}{V_{deep}} \end{bmatrix} \times \begin{bmatrix} M_{surf}^{light} \\ M_{deep}^{light} \\ M_{surf}^{heavy} \\ M_{deep}^{heavy} \end{bmatrix}$$

where M_j^i is the mass of the isotope i in the box j, V_j is the volume of the box j and k_{light} and k_{heavy} are as defined in Section A.1.1.

For a model with initially homogeneous concentration $C_{surf} = M_{surf}/V_{surf} = M_{deep}/V_{deep} = C_{deep}$ and $Q_{ex} = 0$ (i.e. isolated surface box), the surface box evolves according to the Rayleigh equation as illustrated by the solid line in Fig. 3.2. If the uptake reaction is subsequently stopped (i.e. $k_{light} = k_{heavy} = 0$) and the two reservoirs allowed to mix (i.e. $Q_{ex} \neq 0$), the surface box evolves along a binary mixing curve as represented by the dashed lines in Fig. 3.2. For a given amount of mixing with the deep box, the degree to which the isotope composition of the reactant in the surface box deviates from Rayleigh behaviour depends on the degree to which the reactant was depleted in the surface box prior to mixing, as illustrated in the figure.

A.1.3 Advection–diffusion–reaction model

Model description: Essentially, this model embeds the non-dimensional isotope fractionation model ("chemistry/biology") of Section A.1.1 into a spatial framework ("physics"). This spatial framework is a simplified representation of ocean advection and mixing as a one-dimensional advective–diffusive transport, such that the concentration of the dissolved reactant at any (Eulerian) point in the model varies with time as:

$$\frac{\partial R_i}{\partial t} = -w\frac{\partial R_i}{\partial z} + \frac{\partial}{\partial z}\left(\kappa_z\frac{\partial R_i}{\partial z}\right) - k_i(z)R_i + k_d P_i$$

where z is depth (positive downwards), R_i is the concentration of the isotope i (light or heavy) in the dissolved (reactant) pool and $k_i(z)$ is the depth-dependent reaction rate associated with its uptake by biology (see Section A.1.1). Advective velocity (up-/downwelling) is given by w, while κ_z is the depth-variable vertical turbulent diffusivity. The corresponding equation for the particulate product is:

$$\frac{\partial P_i}{\partial t} = -w_s\frac{\partial P_i}{\partial z} + k_i(z)R_i - k_d P_i$$

where P_i is the concentration of the isotope i in the particulate (product) pool and w_s is the settling velocity of the particles. The depth-dependency of the uptake rate is simplified as:

$$k_i = \begin{cases} b, & \text{if } z \leq MLD \\ 0, & \text{if } z > MLD \end{cases}$$

such that uptake is constant in the mixed layer and zero in the water column below. Non-zero minimal mixed-layer reactant concentrations can be explicitly prescribed in the model by replacing the term $k_i(z)R_i$ by the term $k_i(z)(R_i - R_i^{crit})$, where R_i^{crit} is the concentration of the isotope i at which uptake in the mixed layer ceases.

Boundary conditions: The model is solved numerically for steady-state using a boundary-value problem solver (the `bvp4c` routine in MATLAB ver. R2008b). The concentration and isotope composition of the reactant at the lower boundary are prescribed, while the mixed layer is free to evolve to a steady state; the upper boundary condition is simply a zero first derivative of concentration and isotope composition. The product pool requires only one boundary condition, which is that the particle flux through the top boundary is zero. The particle flux through the bottom boundary is not prescribed, but in the steady state solution is such that model mass and isotopic balance is maintained.

A.1.4 Influence of remineralisation on subsurface isotopic gradients

We invoke simple mass-balance considerations to show that remineralisation cannot be the driver of isotopic gradients observed in the near-surface water column (see also Chapter 5). Consider the case of an element for which the lighter isotope is preferentially incorporated by biology during uptake. The euphotic zone thus tends towards 'heavier' (i.e., enriched in the heavy isotope) isotopic compositions as the degree of elemental drawdown in the euphotic zone increases. The particulate matter formed at any point of time is 'lighter' (i.e. depleted in the heavy isotope) than the euphotic zone by an amount that is dictated by the isotopic fractionation factor associated with uptake. If the uptake is considered to be irreversible in the euphotic zone, the dissolved and particulate pools in the euphotic zone will evolve according to either the Rayleigh equation (if the euphotic zone is strongly isolated from the underlying water column) or will evolve to an equilibrium between supply and export (if the dissolved pool is continually replenished by the physical circulation). In the case of equilibrium behaviour, no particulates can be produced with isotopic composition that are isotopically heavier than the isotopic composition of the subsurface source, and in this case it is evident that remineralisation of any particulate export cannot lead to a gradient towards isotopically heavier compositions in the subsurface. If the isolation of the euphotic zone is sufficiently strong that Rayleigh-type behaviour results, the dissolved pool may evolve to such extreme isotopic compositions that the particulate matter produced by uptake is indeed isotopically heavier than the source. This occurs when more than 63% of the initial dissolved pool has been utilised. It is important to note, however, that these extreme isotopic compositions are the result of the closed mass balance implicit to the Rayleigh model. Thus, the export of isotopically heavy particulate matter from the euphotic zone is necessarily preceded by the export of isotopically light particulate matter. Thus, while it is in theory possible for this isotopically extreme particulate matter to impart some heavy isotopic signature to the subsurface water column, this would require that isotopically light particulate matter produced at low degrees of drawdown not remineralise in the subsurface, while the isotopically heavy particulate matter produced at high degrees of drawdown in the surface does. Such a fortuitous constellation cannot be invoked to explain the near-surface isotopic gradients towards the 'residual' signal of utilisation in the euphotic zone that are essentially a universal feature of the near-surface ocean for numerous biogeochemically cycled elements.

A.2 Appendix to Chapter 4

A.2.1 Complete [Si] and δ^{30}Si depth profiles

Depth profiles for all stations included in Chapter 4 are shown below, arranged into four groups (Figs. A.1, A.2, A.3 and A.4).

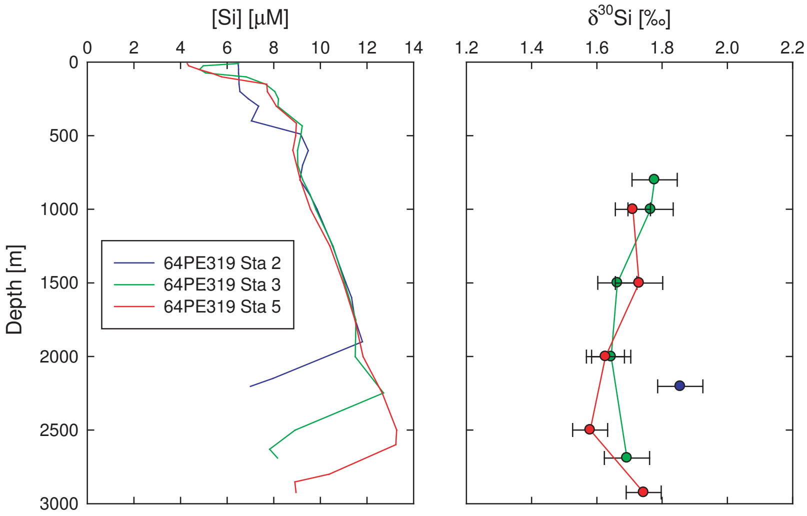

Figure A.1: High northern latitude Atlantic stations (expedition 64PE319).

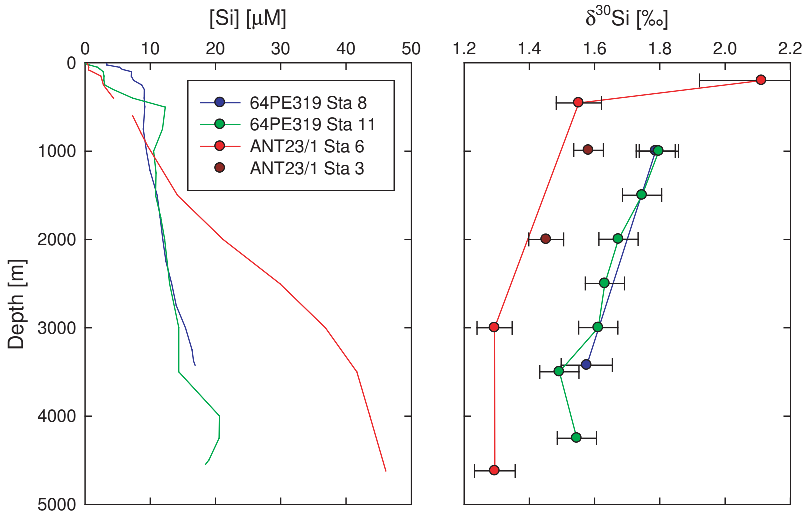

Figure A.2: Labrador Sea and temperate eastern (ANT XXIII/1) and western (64PE319) Atlantic stations.

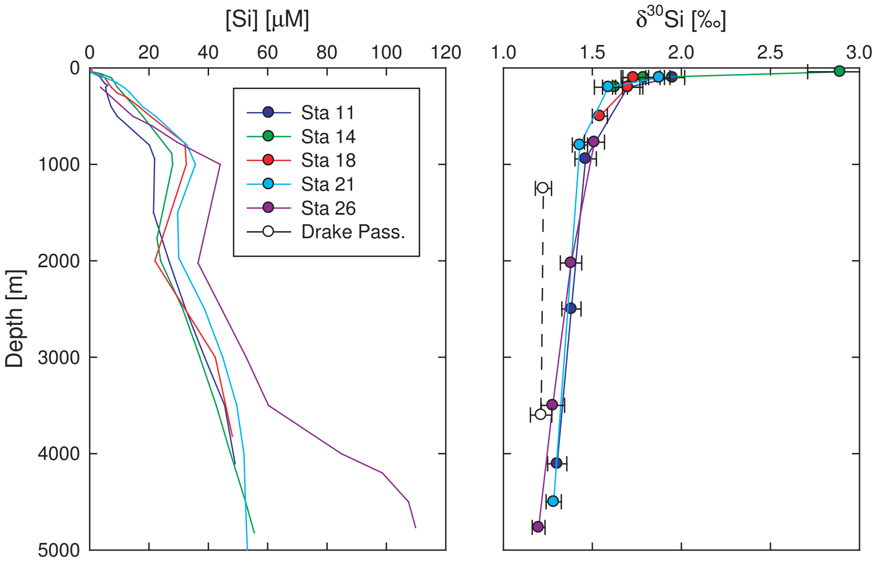

Figure A.3: Eastern Atlantic stations from expedition ANTXXIII/1, with Drake Passage profile for comparison (note different δ^{30}Si scale from previous figures).

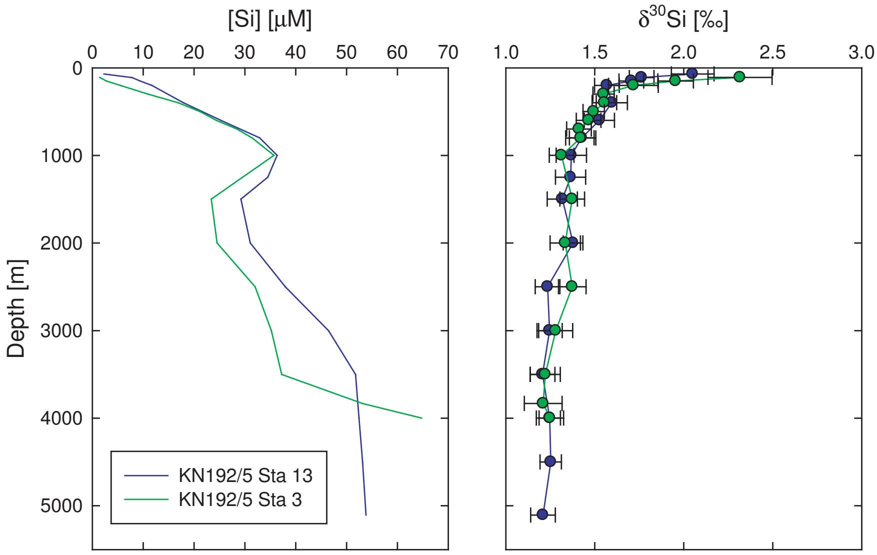

Figure A.4: Eastern (Sta 13) and western (Sta 3) South Atlantic stations (expedition KN192-5).

A.2.2 Endmember contribution calculations & PO_4^* correction

Endmember contributions: Calculations of f_{NA} were carried out for samples with $\sigma_2 \geq 36.95$ ($\sim$2000 m) following Gruber (1998) by first computing the value of the quasi-conservative tracer PO_4^* for each sample:

$$PO_4^* = PO_4 + \frac{O_2}{170} - 1.95 \text{ [µmol/kg]}$$

Note that this PO_4^* definition incorporates the revised Redfield $r_{P:O}$ ratio of Anderson and Sarmiento (1994), as implemented by Gruber (1998) and Sarmiento et al. (2007). We then utilized the endmember PO_4^* concentrations defined by Gruber (1998) to calculate f_{NA} as:

$$f_{NA} = \frac{PO^*_{4,SO} - PO^*_{4,sample}}{PO^*_{4,SO} - PO^*_{4,NA}}$$

Calculation of PO_4^* for samples from cruise ANT-XXIII/1 was not possible using in situ data, due to the strong drift in the oxygen sensor (Rutgers van der Loeff , ed.). We were thus obliged to draw [O_2] data from the nearest gridpoint of World Ocean Atlas (WOA09; Garcia et al., 2010a). For consistency, we also used WOA09 phosphate data for these calculations (Garcia et al., 2010b). Calculations for samples from KN192-05 and 64PE319 utilized cruise CTD (O_2) and bottle (PO_4) data. The amplitude of systematic errors resulting from the use of WOA09 data is difficult to assess, but the similarity of PO_4^* values at 4500m depth for ANT-XXIII/1 Sta 21 (PO_4^* = 0.98 µmol/kg) and KN192-05 station 13 (PO_4^* = 0.94 µmol/kg), which are within 2° of each other in the Angola Basin, seems to indicate the these are small, <0.05 in f_{NA}, which translates to a difference of 0.005‰–0.05‰ in $\delta^{30}Si_{mix}$ values, being at the lower end of this range for the South Atlantic.

We additionally found that PO_4^* data from cruise 64PE319 were systematically shifted to lower values than those at the closest stations from the TTO-NAS program, which was the basis for the analysis of Gruber (1998). Although this difference is generally only $\sim$0.05 µmol/kg, the calculation of $\delta^{30}Si_{mix}$ values is highly sensitive to small PO_4^* variations in close proximity to the low-Si North Atlantic endmember; furthermore, the offset is such that most samples have an apparent PO_4^* value lower than that of the North Atlantic endmember value of 0.76 µmol/kg as defined by Gruber (1998), leading to physically meaningless results. The differences in PO_4^* appear to derive from a discrepancy in measured oxygen concentrations between the two expeditions. It is currently unclear whether this inconsistency is due to analytical biases between the two expeditions or a true change in oxygenation of the northern North Atlantic over the last three decades; regardless of its cause, however, this discrepancy introduces a systematic error into the $\delta^{30}Si_{mix}$ values calculated for the 64PE319 samples. Thus, as detailed below, we corrected the 64PE319 PO_4^* values to establish consistency with the TTO-NAS dataset (and thus the endmember definitions of Gruber (1998)). Samples that possessed

PO_4^* values below that of the North Atlantic endmember after this correction were arbitrarily corrected to a value of 0.76 µmol/kg to enable a rough estimation of $\delta^{30}Si_{mix}$; these samples are highlighted in Fig. 4.4 and Table 4.2.

Silicon concentrations of the endmembers were estimated from the PO_4^*–[Si] relationship using the eWOCE database (Schlitzer, 2000). The estimated values of 10.7±2.1 µM for $[Si]_{NA}$ and 122.6±4.9 µM for $[Si]_{SA}$ are very similar to the concentrations observed in the northern North Atlantic (ISOW) and Southern Ocean (CDW) samples, respectively. These samples were used to characterize the endmember $\delta^{30}Si$ values (+1.7‰ and +1.2‰ respectively; see Table 4.2).

Errors associated with the calculation of $\delta^{30}Si_{mix}$ values were estimated by Monte Carlo simulation using 10^4 datasets perturbed by a normally-distributed random variable with variance equal to the uncertainty on endmember values. Average uncertainty on $\delta^{30}Si_{mix}$ associated with the endmember [Si] concentration uncertainty is ±0.02‰, while that related to endmember $\delta^{30}Si$ values is ±0.06‰. The uncertainty on $\delta^{30}Si_{mix}$ values considering both these sources of random error is ±0.07‰ ($2\sigma_{SD}$).

PO_4^* correction: The North Atlantic data basis for Gruber's (1998) analysis stems from the Transient Tracers in the Ocean (TTO) program (Brewer et al., 1986). Since we calculated PO_4^* values for 64PE319 samples that were more extreme (i.e. lower) than the North Atlantic endmember value of 0.76 µmol/kg stipulated by Gruber (1998), we attempted to make a direct data comparison. TTO-NAS stations were selected from the eWOCE database (Schlitzer, 2000) based on their geographical proximity to 64PE319 stations (Table A.1).

Table A.1: Locations of TTO stations used for comparison to 64PE319 stations.

TTO-NAS Station	Coordinates	64PE319 Station	Coordinates
Sta 171 *14 August 1981*	63.7°N 33°W	Sta 2 *2 May 2010*	64°N 34.3°W
Sta 179 *26 August 1981*	59.3°N 40°W	Sta 5	60.4°N 37.9°W
Sta 203 *09 September 1981*	56°N 46°W	Sta 8	54°N 45.8°W
Sta 226 *26 September 1981*	46.7°N 40°W	Sta 11 *11 May 2010*	47.8°N 39.4°W

Comparison of T–S curves (Fig. A.5) and potential density profiles (Fig. A.6) shows that the water mass structure at these stations, although not identical, is very similar, especially for the water masses below 2000 m with which we are concerned.

When comparing PO_4^* profiles, however, discrepancies become clearly apparent. Figures A.7 and A.8 display these discrepancies in depth as well as potential density profiles. Especially in the plots against potential density in Fig. A.8, the similarity in the structure of the profiles, especially above σ_θ = 27.75 (i.e. ∼2000 m), is striking, as is the offset of around 0.05 µmol/kg. It appears that this difference in PO_4^* stems from an offset in the measured oxygen concentrations between the two expeditions (not

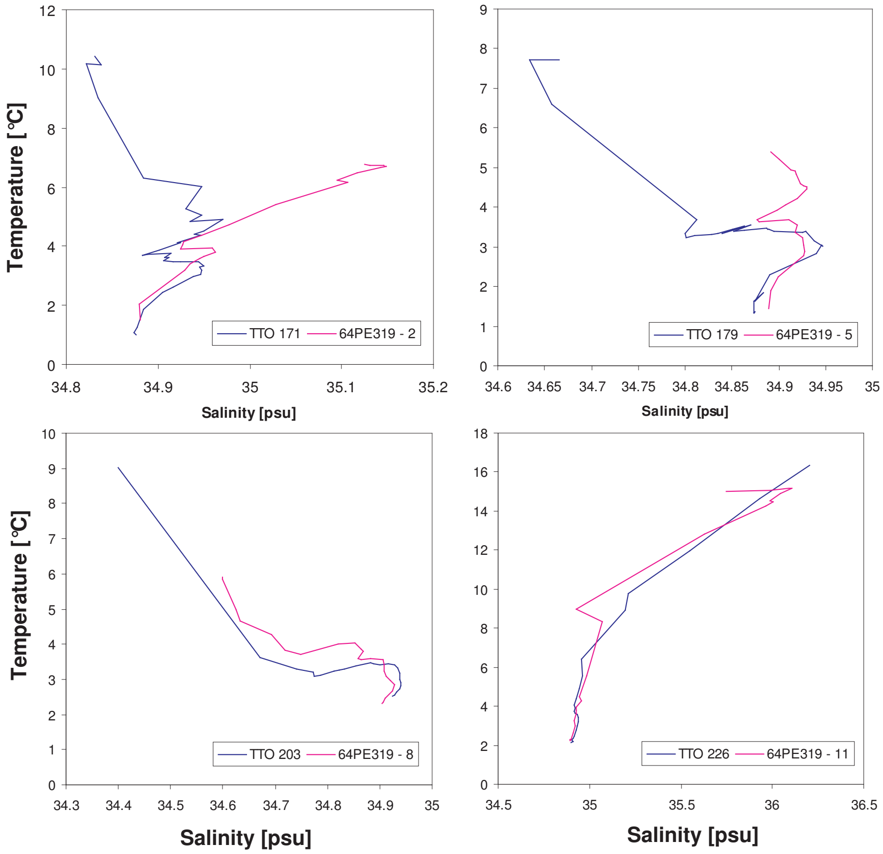

Figure A.5: Temperature–salinity comparisons of the TTO-NAS and 64PE319 stations used to correct PO_4^* values.

shown). Whether this is an analytical reproducibility issue or reflects real changes in the North Atlantic is unclear; the largest discrepancies of $\sim$0.1 µmol/kg are observed at the northernmost station.

In order to create a consistent data framework in which to perform the unmixing analysis of Gruber (1998), we attempt to apply the simplest possible correction to the data to establish consistency with the TTO dataset. Based on the average observed offset, the simplest correction is to add 0.05 µmol/kg to the PO_4^* values calculated for the 64PE319 samples. This correction is sufficient to increase all but three PO_4^* values above the value of 0.76 µmol/kg defined for the North Atlantic endmember by Gruber (1998), and results in corrected PO_4^* profiles that match the TTO data very well, as shown in Fig. A.9. We thus do not apply any further correction to the data. The two PO_4^* values that lie below 0.76 µmol/kg are arbitrarily increased to this value to obtain a rough handle on their mixing-predicted values, but since this “correction” has no robust justification, the points thus modified for the endmember contribution calculation are highlighted in Chapter 4.

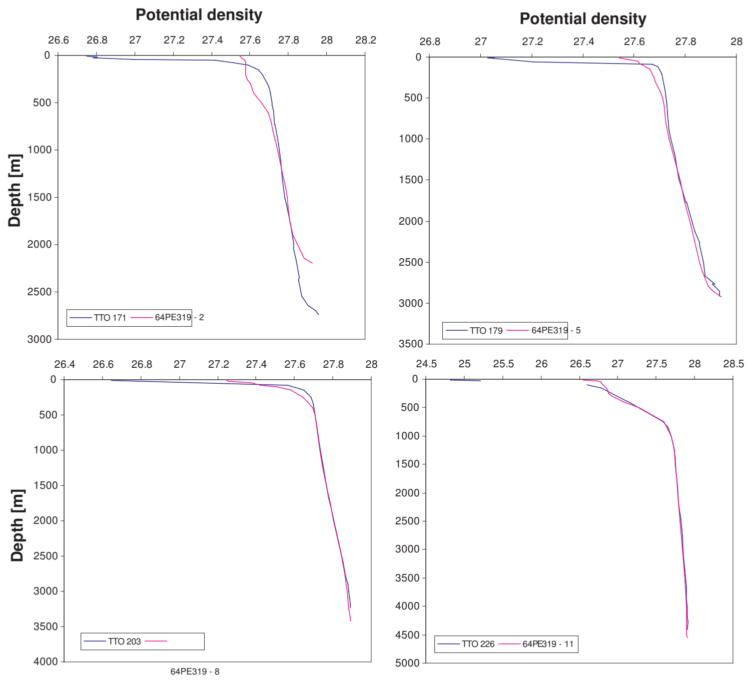

Figure A.6: Comparison of potential density (σ_θ) profiles for the TTO-NAS and 64PE319 stations.

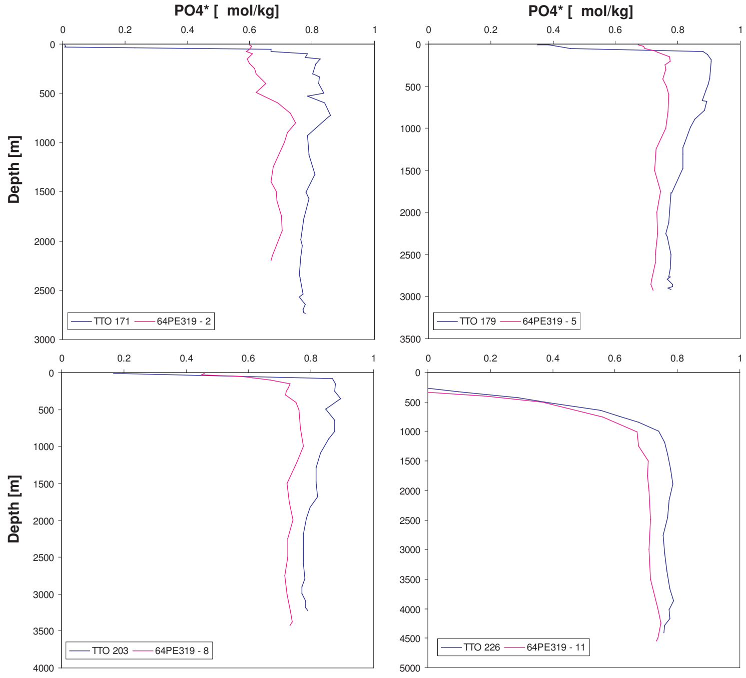

Figure A.7: Comparison of depth profiles of PO_4^* from TTO-NAS and 64PE319 stations.

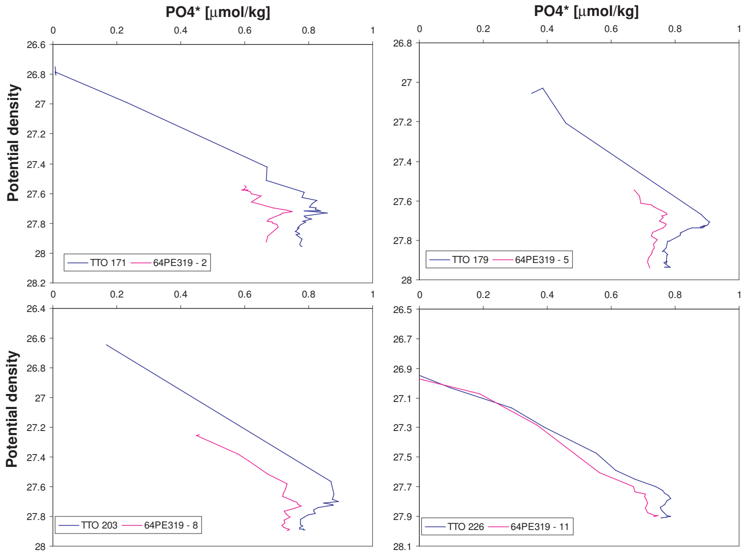

Figure A.8: Comparison of PO₄∗–potential density relationships between TTO-NAS and 64PE319 stations.

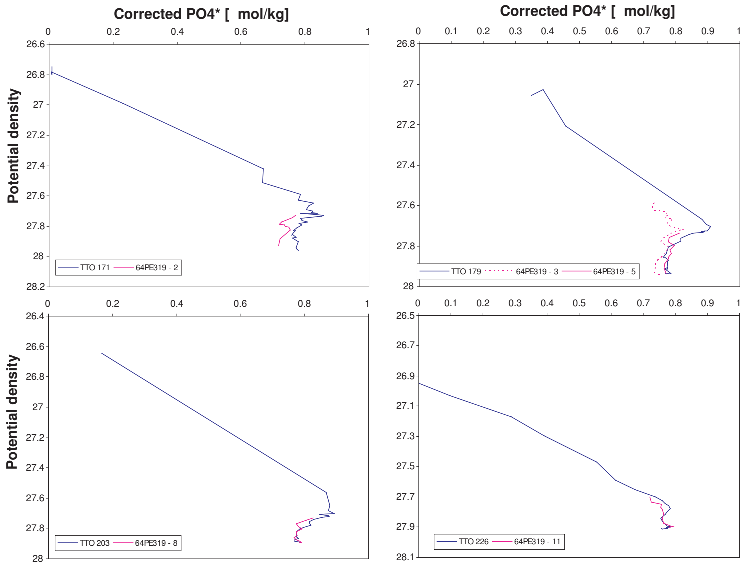

Figure A.9: PO_4^* values for samples corrected by addition of 0.05 µmol/kg to calculated values for 64PE319 samples ($\geq$2000 m water depth), in comparison to TTO data. Note that PO_4^* values from Sta 2, from which the raw data show the strongest offset to TTO data, continue to exhibit a discrepancy to TTO data even after correction, while the other stations show good consistency. 64PE319 Sta 3 is also shown in upper right panel for comparison, although no TTO-NAS station is sufficiently close to it to provide good control.

A.2.3 Box model

The 8-box model of the ocean applied in this study draws on the architecture of the 7-box model of Toggweiler (1999) and its adaptation to the Si cycle by Reynolds (2009). We separate the “Atlantic” box a of Toggweiler (1999) into two boxes, a “North Atlantic” box and a “deep low-latitude” box, in order to more clearly separate the two δ^{30}Si endmembers that are the focus of our analysis, the subpolar North Atlantic and the deep Southern Ocean. This has the added advantage of removing the confounding effect of low-latitude remineralisation on box *a* of Toggweiler’s (1999) model. Since the ocean is modeled as a closed system, the entire particulate flux exported from surface ocean boxes dissolves in the underlying deep boxes. The model is solved numerically in MATLAB using the stiff ordinary differential equation solver `ode15s`. Low numerical error tolerances ensure accurate mass conservation (relative mass deviation $\sim 1 \times 10^{-14}$). Initial conditions are an homogeneous ocean in Si concentration and isotope concentration, corresponding to a global oceanic Si inventory of 97 Pmol (Tréguer et al., 1995)and a oceanic mean δ^{30}Si value of +1.2‰(Reynolds, 2009). The model reaches steady state for concentration and isotopic composition within $\sim$1500 model years; solution requires $\sim$2 sec of CPU time as documented by MATLAB’s `profile` function.

Unlike the model of Reynolds (2009), our model traces two isotopes of Si, “^{30}Si” and “^{28}Si”. Values of δ^{30}Si are calculated using the standard δ-definition, and isotope fractionation during Si-uptake in the surface ocean is modeled by applying different first-order rates to this reaction for the two isotopes, such that:

$$k_{30} = \alpha \cdot k_{28}$$

where k_i is the first-order reaction rate associated with the isotope ^{i}Si and α is the fractionation factor associated with the reaction (α = 0.9989; De La Rocha et al., 1997). For simplicity, isotopic fractionation during opal dissolution is not included in the model.

Parameters used in the model, and the source of their numerical values, are given in Table A.2. Modeled total particulate export across the base of the surface boxes (250 m at high latitudes, 100 m at low latitudes; Toggweiler, 1999) is 85 Tmol Si yr^{-1}, corresponding to 0.24 mol Si m^{-2} yr^{-1}, with the Southern Ocean (Polar and Subantarctic) contributing 46% of this flux. These values are consistent with numerous estimates (e.g. Nelson et al., 1995; Dunne et al., 2007; Sarmiento et al., 2007).

Table A.2: Parameters of the 8-box model used in Chapter 4.

Parameter	Value	Unit	Reference
Volume			
Whole ocean	1292	10^{15} m^3	Toggweiler (1999); Levitus (1982)
Surface North Atlantic	8.7	10^{15} m^3	Toggweiler (1999)
Surface low-latitude	26.2	10^{15} m^3	Toggweiler (1999)
Surface Subantarctic	8.7	10^{15} m^3	Toggweiler (1999)
Surface Polar Southern Ocean	4.4	10^{15} m^3	Toggweiler (1999)
Intermediate water	297	10^{15} m^3	Toggweiler (1999)
Deep North Atlantic	100	10^{15} m^3	modified from Toggweiler (1999)
Deep low-latitude	201	10^{15} m^3	modified from Toggweiler (1999)
Deep "Southern" Ocean	646	10^{15} m^3	Toggweiler (1999)
Water fluxes			
Overturning flux	20	Sv	Toggweiler (1999)
Southern Ocean exchange flux (deepsurface)	60	Sv	modern solution, Toggweiler (1999)
Low-latitude exchange flux (intermediatesurface)	40	Sv	Toggweiler (1999)
Productivity rates			
Surface low-latitude	1.5	yr^{-1}	constraint: low-latitude [Si] $\sim$1 µM
Other surface boxes	0.04	yr^{-1}	Reynolds (2009)
Fraction of LL productivity dissolving in intermediate box *f*	0.36	-	Reynolds (2009)

A.3 Appendix to Chapter 5

A.3.1 Scale analysis

To assess the relevance of vertical diffusive processes relative to lateral advection, the relevant Péclet number $Pe = UD^2/\kappa_v L$ can be utilized. Here U is lateral (isopycnal) velocity, L is the lateral length scale, κ_v is the vertical (diapycnal) diffusivity and D is the vertical length scale. For the relevant length scales of D = 500 m (approximate depth of the $\sigma_\theta = 27$ isopycnal) and L = 5000 km (distance from Subtropical Front to equator), we obtain a Pe value of 50 for a diapycnal diffusivity of 10^{-5}m^2/s (e.g. Ledwell et al., 1998) and horizontal velocities of 1 cm/s (e.g. Tomczak and Godfrey, 2003).

The timescales of ventilation versus dissolution in the thermocline can be compared using the non-dimensional number UC/LJ_{diss} (parameters explained in main text, Section 5.4.1). Estimates of ventilation timescales for the density range σ_θ = 25–27 indicate that L/U increases by a factor of 2–5 (Sabine et al., 2005; Karstensen et al., 2008), approximately from 5 to 20 years. The concentration of preformed Si increases by a factor of 3–10 over this same density range, from 1–3 µM to $\sim$10 µM. Opal export fluxes in the Atlantic are estimated at 0.04–0.12 mol/m^2/yr (Ragueneau et al., 2002); how this flux changes with depth is uncertain (Ragueneau et al., 2002; Sarmiento et al., 2007), but we can use the approximation of Sarmiento and Gruber (2006):

$$\phi^{Opal}(z) = P^{Opal} \cdot p_e \cdot z_0^{0.858} \cdot z^{-0.448}$$

(where z_0 = 100m, z is depth, p_e is the export fraction, and $Prod^{Opal}$ is the production of opal in the euphotic zone) to estimate that the flux at 400 m water depth (the approximate depth of the

σ_θ = 27 isopycnal) is ~50% lower than at 100 m. The depth derivative of the above equation gives the dissolution flux, such that, assuming an opal export flux of 0.1 mol/m^2/yr, we can calculate values of J_{diss} of 0.4 mmol/m^3/yr at 100 m and 0.06 mmol/m^3/yr at 400 m depth. With these values, we arrive at a dissolution timescale C/J_{diss} of 5 yr at 100 m and 200 yr at 400 m. This results in the fact that the timescale ratio UC/LJ_{diss} increases from values of ~1 near the base of the mixed layer to a value of 10 at σ_θ = 27, indicating the decreasing influence of dissolution compared to the ventilation supply of the preformed component.

A.3.2 Supplementary figures

Supplementary figures to chapter 5 are provided below (Figs. A.10, A.11 and A.12).

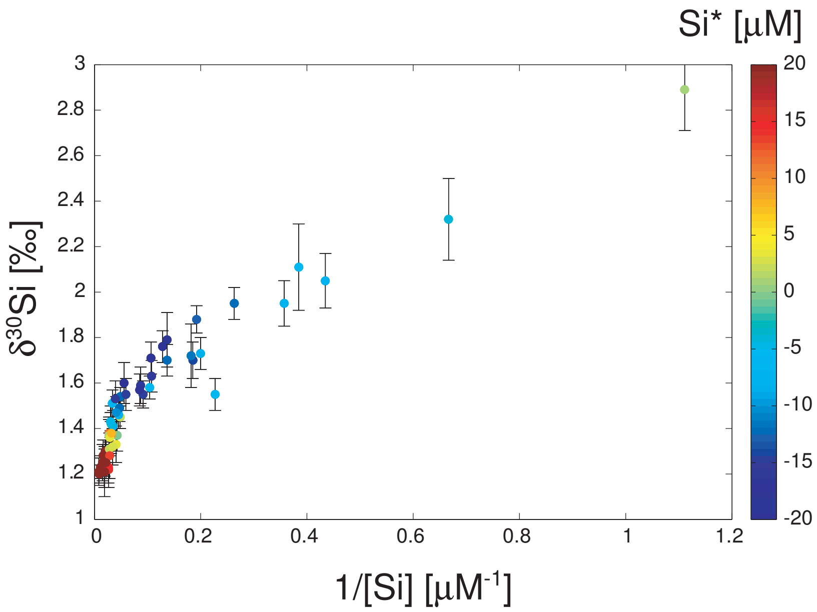

Figure A.10: As in Fig 5.5, but with symbols colored according to their Si* values. The SAMW signature of low Si* values is apparent at the intersection between the two linear δ^{30}Si–1/[Si] sections.

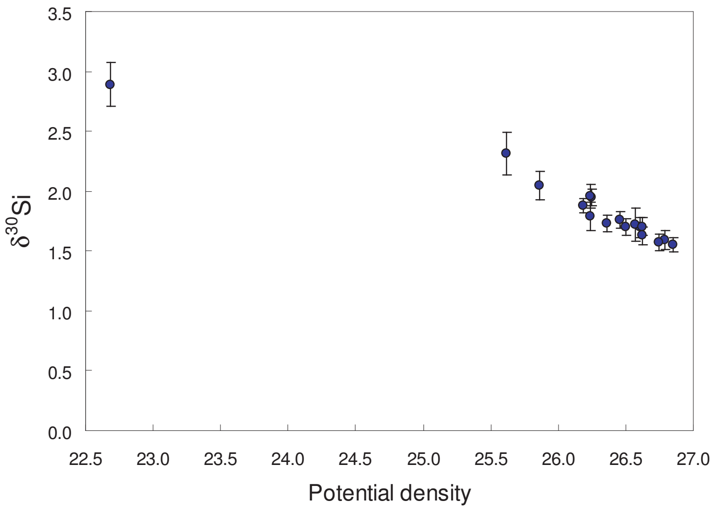

Figure A.11: Relationship between δ^{30}Si and potential density σ_θ for all samples with $\sigma_\theta \leq 27$, displaying the coherent isopycnal structure of thermocline δ^{30}Si. Only the upper-leftmost point is within the mixed layer where θ and S are non-conservative.

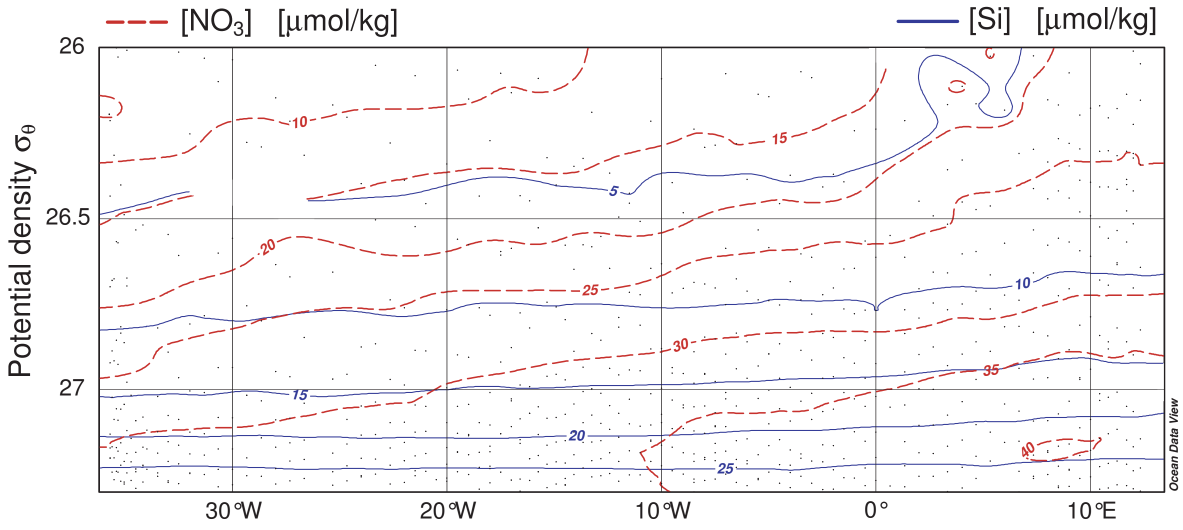

Figure A.12: Isopycnal distribution of nitrate (dashed lines) and Si (solid lines) across the South Atlantic thermocline (11°S, WOCE A08). The upward slope of the nitrate isopleths towards the east documents the increasing contribution of remineralized nitrate; these sloping nitrate isopleths cut across Si isopleths that remain essentially horizontal across the Atlantic except in the least dense portion of the thermocline (see also Fig. 5.4). Data are from the eWOCE database (Schlitzer, 2000).

A.4 Appendix to Chapter 6

A.4.1 Monte Carlo *t*-test

A Monte Carlo method was adopted to compare deepwater δ^{30}Si values in the South Pacific, since variability is small compared to the analytical uncertainty on the data. All δ^{30}Si datapoints from two datasets being compared were perturbed 10^4 times by a normally-distributed random variable with a variance corresponding to the analytical uncertainty on the datapoints. After each perturbation, a two-sided unequal variance *t*-test (Welch's *t*-test) was performed on these dataset pairs and the *p*-value corresponding to the test statistic recorded. The probabilities reported in Chapter 6 refer to the relative proportion of *p*-values that were smaller than α = 0.05.

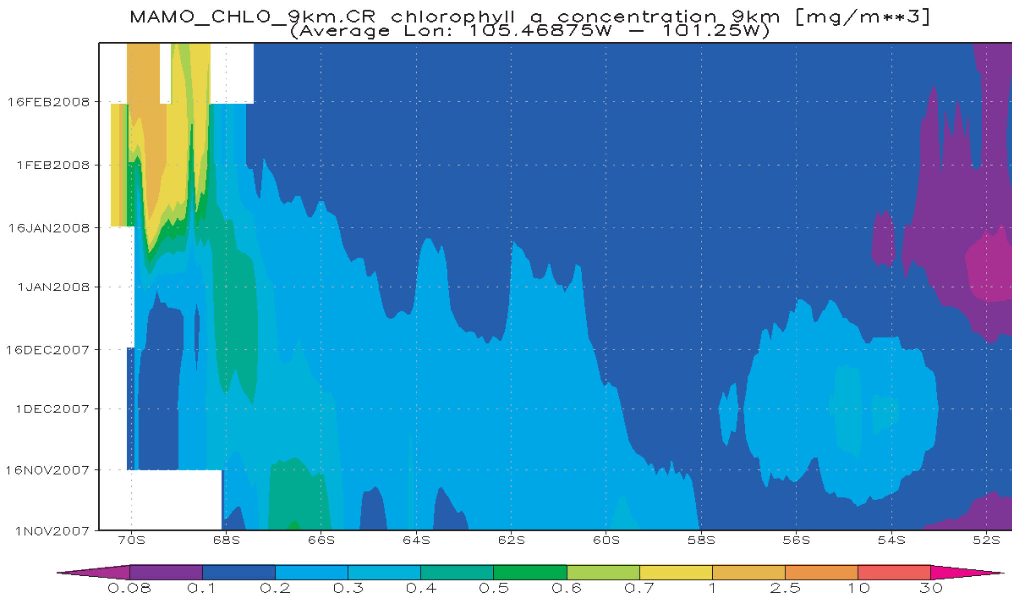

Figure A.13: A Hovmöller (latitude–time) plot of chlorophyll *a* concentrations (mg/m^3; colourbar) in the Subantarctic and Antarctic Zones at ~103° W, from November 2007 to February 2008. The expedition 33RO20071215 of R/V *Ronald H. Brown* reached these high latitudes in February 2008. From satellite data (MODIS Aqua), accessed using the Giovanni online data system (`http://reason.gsfc.nasa.gov/Giovanni/`), developed and maintained by the NASA Goddard Earth Sciences (GES) Data and Information Services Center (DISC).

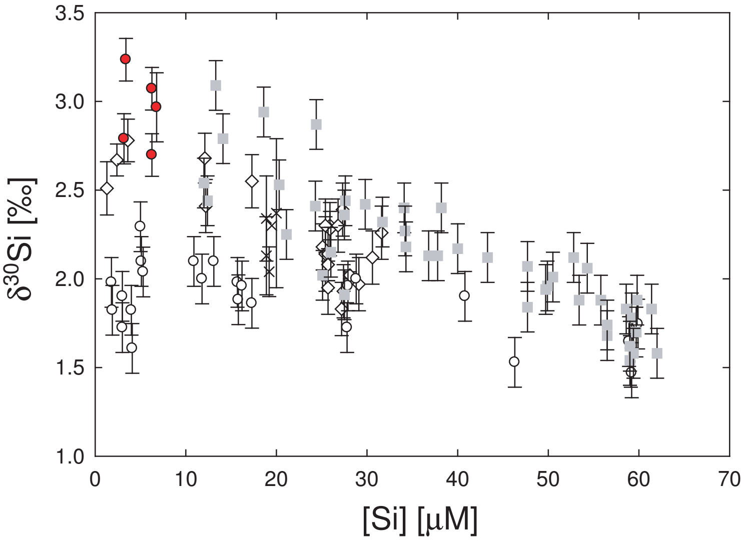

Figure A.14: A comparison of the surface Southern Ocean δ^{30}Si data from 62° S 103° W (red circles) with published data (grey squares: Varela et al. (2004), open circles: Cardinal et al. (2005), crosses: Cavagna et al. (2011), open diamonds: Fripiat et al. (2011). My data is consistent with the high values seen by most authors; the reason for the comparatively low values observed by Cardinal et al. (2005) is not known.

References

Albarède, F. (1996). *Introduction to Geochemical Modeling*. Cambridge University Press, Cambridge.

Albarède, F. and B. L. Beard (2004). Analytical methods for non-traditional isotopes. In: C. M. Johnson, B. L. Beard and F. Albarède (eds.) *Geochemistry of non-traditional stable isotopes*, volume 55 of *Reviews in Mineralogy and Geochemistry*. Mineralogical Society of America, Washington DC.

Alldredge, A. L. and C. C. Gotschalk (1989). Direct observations of the mass flocculation of diatom blooms: characteristics, settling velocities and formation of diatom aggregates. *Deep Sea Research* **36**: 159–171.

Altabet, M. A. (2001). Nitrogen isotopic evidence for micronutrient control of fractional NO_3-utilization in the equatorial Pacific. *Limnology and Oceanography* **46**: 368–380.

Altabet, M. A. and R. François (1994). Sedimentary nitrogen isotopic ratio as a recorder for surface ocean nitrate utilization. *Global Biogeochemical Cycles* **8**: 103–116.

Altabet, M. A., C. Pilskaln, R. Thunell, C. Pride, D. Sigman, F. Chavez and R. Francois (1999). The nitrogen isotope biogeochemistry of sinking particles from the margin of the Eastern North Pacific. *Deep Sea Research Part I: Oceanographic Research Papers* **46**: 655–679.

Anderson, L. A. and J. L. Sarmiento (1994). Redfield ratios of remineralization determined by nutrient data analysis. *Global Biogeochemical Cycles* **8**: 65–80.

Antonov, J. I., D. Seidov, T. P. Boyer, R. A. Locarnini, A. Mishonov and H. E. Garcia (2010). *World Ocean Atlas 2009, Volume 2: Salinity*. NOAA Atlas NESDIS 69. U.S. Government Printing Office, Washington DC.

Aoki, S., M. Hariyama, H. Mitsudera, H. Sasaki and Y. Sasai (2007). Formation regions of Subantarctic Mode Water detected by OFES and Argo profiling floats. *Geophysical Research Letters* **34**.

Armbrust, E. V. (2009). The life of diatoms in the world's oceans. *Nature* **459**: 185–192.

Armytage, R. M. G., R. B. Georg, P. S. Savage, H. M. Williams and A. N. Halliday (2011). Silicon isotopes in meteorites and planetary core formation. *Geochimica et Cosmochimica Acta* **75**: 3662–3676.

Basile-Doelsch, I., J. D. Meunier and C. Parron (2005). Another continental pool in the terrestrial silicon cycle. *Nature* **433**: 399–402.

Bermin, J., D. Vance, C. Archer and P. Statham (2006). The determination of the isotopic composition of Cu and Zn in seawater. *Chemical Geology* **226**: 280–297.

Beucher, C. P., M. A. Brzezinski and X. Crosta (2007). Silicic acid dynamics in the glacial sub-Antarctic: Implications for the silicic acid leakage hypothesis. *Global Biogeochemical Cycles* **21**: doi:10.1029/2006GB002746.

Beucher, C. P., M. A. Brzezinski and J. L. Jones (2008). Sources and biological fractionation of Silicon isotopes in the Eastern Equatorial Pacific. *Geochimica et Cosmochimica Acta* **72**: 3063–3073.

Beucher, C. P., M. A. Brzezinski and J. L. Jones (2011). Mechanisms controlling silicon isotope distribution in the Eastern Equatorial Pacific. *Geochimica et Cosmochimica Acta* **75**: 4286–4294.

Bigeleisen, J. (1949a). The relative velocities of isotopic molecules. *Journal of Chemical Physics* **17**: 675–678.

Bigeleisen, J. (1949b). The validity of the use of tracers to follow chemical reactions. *Science* **110**: 14–16.

Bigeleisen, J. (1955). Statistical mechanics of isotopic systems with small quantum corrections. I. General considerations and the rule of the geometric mean. *Journal of Chemical Physics* **23**: 2264–2267.

Bigeleisen, J. and M. G. Mayer (1947). Calculation of equilibrium constants for isotopic exchange reactions. *Journal of Chemical Physics* **15**: 261–267.

Boyd, P. W. and M. J. Ellwood (2010). The biogeochemical cycle of iron in the ocean. *Nature Geoscience* **3**: 675–682.

Brambilla, E., L. D. Talley and P. E. Robbins (2008). Subpolar Mode Water in the northeastern Atlantic: 2. Origin and transformation. *Journal of Geophysical Research – Oceans* **113**: C04026.

Brewer, P. G., A. Bradshaw and R. Williams (1986). Measurements of total carbon dioxide and alkalinity in the North Atlantic ocean in 1981. In: J. Trabalka and D. Reichle (eds.) *The Changing Carbon Cycle, A Global Analysis*, 358–381. Springer Verlag, New York.

Broecker, W. S. (1974). "NO", a conservative water-mass tracer. *Earth and Planetary Science Letters* **23**: 100–107.

Broecker, W. S. (1979). A revised estimate for the radiocarbon age of North Atlantic Deep Water. *Journal of Geophysical Research – Oceans* **84**: 3218–3226.

Broecker, W. S. (1987). The biggest chill. *Natural History Magazine* **97**: 74–82.

Broecker, W. S. (1991). The great ocean conveyor. *Oceanography* **4**: 79–89.

Broecker, W. S. and T. H. Peng (1982). *Tracers In The Sea*. Eldigio Press/Lamont-Doherty Geological Observatory, Palisades, NY.

Broecker, W. S. and T. Takahashi (1980). Hydrography of the central Atlantic – III: The North Atlantic deep-water complex. *Deep Sea Research Part A – Oceanographic Research Papers* **27**: 591–613.

Broecker, W. S., T. Takahashi and M. Stuiver (1980). Hydrography of the central Atlantic – II: Waters beneath the Two-Degree Discontinuity. *Deep Sea Research Part A – Oceanographic Research Papers* **27**: 397–419.

Broecker, W. S., T. Takahashi and T. Takahashi (1985). Sources and flow patterns of deep-ocean waters as deduced from potential temperature, salinity, and initial phosphate concentration. *Journal of Geophysical Research – Oceans* **90**: 6925–6939.

Broecker, W. S., S. Blanton, W. M. Smethie and G. Ostlund (1991). Radiocarbon decay and oxygen utilization in the deep Atlantic Ocean. *Global Biogeochemical Cycles* **5**: 87–117.

Brzezinski, M. A. (1985). The Si:C:N ratio of marine diatoms: Interspecific variability and the effect of some environmental variables. *Journal of Phycology* **21**: 347–357.

Brzezinski, M. A., C. J. Pride, V. M. Franck, D. M. Sigman, J. L. Sarmiento, K. Matsumoto, N. Gruber, G. H. Rau and K. H. Coale (2002). A switch from $Si(OH)_4$ to NO_3^- depletion in the glacial Southern Ocean. *Geophysical Research Letters* **29**: doi: 10.1029/2001GL014349.

Brzezinski, M. A., M. L. Dickson, D. M. Nelson and R. Sambrotto (2003). Ratios of Si, C and N uptake by microplankton in the Southern Ocean. *Deep-Sea Research Part II – Topical Studies in Oceanography* **50**: 619–633.

Brzezinski, M. A., J. L. Jones, C. P. Beucher, M. S. Demarest and H. L. Berg (2006). Automated determination of silicon isotope natural abundance by the acid decomposition of cesium hexafluosilicate. *Analytical Chemistry* **78**: 6109–6114.

Brzezinski, M. A., C. Dumousseaud, J. W. Krause, C. I. Measures and D. M. Nelson (2008). Iron and silicic acid concentrations together regulate Si uptake in the equatorial Pacific Ocean. *Limnology and Oceanography* **53**: 875–889.

Buchanan, D. L., A. Nakao and G. Edwards (1953). Carbon isotope effects in biological systems. *Science* **117**: 541–545.

Buesseler, K. O. (1998). The decoupling of production and particulate export in the surface ocean. *Global Biogeochemical Cycles* **12**: 297–310.

Cardinal, D., L. Y. Alleman, J. de Jong, K. Ziegler and L. André (2003). Isotopic composition of silicon measured by multicollector plasma source mass spectrometry in dry plasma mode. *Journal of Analytical Atomic Spectrometry* **18**: 213–218.

Cardinal, D., L. Y. Alleman, F. Dehairs, N. Savoye, T. W. Trull and L. Andre (2005). Relevance of silicon isotopes to Si-nutrient utilization and Si-source assessment in Antarctic waters. *Global Biogeochemical Cycles* **19**: doi: 10.1029/2004GB002364.

Cavagna, A.-J., F. Fripiat, F. Dehairs, D. A. Wolf-Gladrow, B. Cisewski, N. Savoye, L. André and D. Cardinal (2011). Silicon uptake and supply during a Southern Ocean iron fertilization experiment (EIFEX) tracked by Si isotopes. *Limnology and Oceanography* **56**: 147–160.

Cermeño, P., S. Dutkiewicz, R. P. Harris, M. Follows, O. Schofield and P. G. Falkowski (2008). The role of nutricline depth in regulating the ocean carbon cycle. *Proceedings of the National Academy of Sciences* **105**: 20344–20349.

Chisholm, S. W. and F. M. M. Morel (1991). Special Issue: What controls phytoplankton production in nutrient-rich areas of the open sea? *Limnology and Oceanography* **36**: 1507–1970.

Claquin, P., V. Martin-Jézéquel, J. C. Kromkamp, M. J. W. Veldhuis and G. W. Kraay (2002). Uncoupling of silicon compared to carbon and nitrogen metabolism, and the role of the cell cycle, in continuous cultures of *Thalassiosira pseudonana* (Bacillariophyceae) under light, nitrogen and phosphorus control. *Journal of Phycology* **38**: 922–930.

Criss, R. E. (1999). *Principles of Stable Isotope Distribution*. Oxford University Press, Oxford.

Crosta, X., C. Beucher, K. Pahnke and M. A. Brzezinski (2007). Silicic acid leakage from the Southern Ocean: Opposing effects of nutrient uptake and oceanic circulation. *Geophysical Research Letters* **34**: doi: 10.1029/2006GL029083.

De La Rocha, C. L. (2002). Measurement of silicon stable isotope natural abundances via multicollector inductively coupled plasma mass spectrometry (MC-ICP-MS). *Geochemistry Geophysics Geosystems* **3**: 10.1029/2002GC000310.

De La Rocha, C. L. (2003). Silicon isotope fractionation by marine sponges and the reconstruction of the silicon isotope composition of ancient deep water. *Geology* **31**: 423–426.

De La Rocha, C. L., M. A. Brzezinski and M. J. DeNiro (1997). Fractionation of silicon isotopes by marine diatoms during biogenic silica formation. *Geochimica et Cosmochimica Acta* **61**: 5051–5056.

De La Rocha, C. L., M. A. Brzezinski, M. J. DeNiro and A. Shemesh (1998). Silicon-isotope composition of diatoms as an indicator of past oceanic change. *Nature* **395**: 680–683.

De La Rocha, C. L., M. A. Brzezinski and M. J. DeNiro (2000). A first look at the distribution of the stable isotopes of silicon in natural waters. *Geochimica et Cosmochimica Acta* **64**: 2467–2477.

Del Amo, Y. and M. A. Brzezinski (1999). The chemical form of dissolved Si taken up by marine diatoms. *Journal of Phycology* **35**: 1162–1170.

Demarest, M. S., M. A. Brzezinski and C. P. Beucher (2009). Fractionation of silicon isotopes during biogenic silica dissolution. *Geochimica et Cosmochimica Acta* **73**: 5572–5583.

DeMaster, D. J. (2002). The accumulation and cycling of biogenic silica in the Southern Ocean: revisiting the marine silica budget. *Deep Sea Research Part II: Topical Studies in Oceanography* **49**: 3155–3167.

DeMaster, D. J. (2009). Marine silica cycle. In: J. H. Steele, K. K. Turekian and S. A. Thorpe (eds.) *Encyclopedia of Ocean Sciences*, 678–685. Academic Press, Oxford, 2nd edition.

Dickson, R. R. and J. Brown (1994). The production of North Atlantic Deep Water: Sources, rates, and pathways. *Journal of Geophysical Research – Oceans* **99**: 12319–12341.

DiFiore, P. J., D. M. Sigman, T. W. Trull, M. J. Lourey, K. Karsh, G. Cane and R. Ho (2006). Nitrogen isotope constraints on subantarctic biogeochemistry. *Journal of Geophysical Research – Oceans* **111**: doi: 10.1029/2005jc003216.

Ding, T., S. Jiang, D. Wan, Y. Li, H. Song, Z. Liu and X. Yao (1996). *Silicon isotope geochemistry*. Geological Publishing House, Beijing.

Ding, T., D. Wan, C. Wang and F. Zhang (2004). Silicon isotope compositions of dissolved silicon and suspended matter in the Yangtze River, China. *Geochimica et Cosmochimica Acta* **68**: 205–216.

Dong, S., J. Sprintall, S. T. Gille and L. Talley (2008). Southern Ocean mixed-layer depth from Argo float profiles. *Journal of Geophysical Research – Oceans* **113**: doi: 10.1029/2006jc004051.

Douthitt, C. B. (1982). The geochemistry of the stable isotopes of silicon. *Geochimica et Cosmochimica Acta* **46**: 1449–1458.

Dugdale, R. C. and F. P. Wilkerson (1998). Silicate regulation of new production in the equatorial Pacific upwelling. *Nature* **391**: 270–273.

Dugdale, R. C. and F. P. Wilkerson (2001). Sources and fates of silicon in the ocean: the role of diatoms in the climate and glacial cycles. *Scientia Marina* **65 Suppl. 2**: 141–152.

Dugdale, R. C., F. P. Wilkerson and H. J. Minas (1995). The role of a silicate pump in driving new production. *Deep Sea Research Part I: Oceanographic Research Papers* **42**: 697–719.

Dugdale, R. C., A. G. Wischmeyer, F. P. Wilkerson, R. T. Barber, F. Chai, M. S. Jiang and T. H. Peng (2002). Meridional asymmetry of source nutrients to the equatorial Pacific upwelling ecosystem and its potential impact on ocean-atmosphere CO2 flux; a data and modeling approach. *Deep Sea Research Part II: Topical Studies in Oceanography* **49**: 2513–2531.

Dunne, J. P., R. A. Armstrong, A. Gnanadesikan and J. L. Sarmiento (2005). Empirical and mechanistic models for the particle export ratio. *Global Biogeochemical Cycles* **19**: doi:10.1029/2004GB002390. GB4026.

Dunne, J. P., J. L. Sarmiento and A. Gnanadesikan (2007). A synthesis of global particle export from the surface ocean and cycling through the ocean interior and on the seafloor. *Global Biogeochemical Cycles* **21**. GB4006.

Dutay, J. C., J. L. Bullister, S. C. Doney, J. C. Orr, R. Najjar, K. Caldeira, J. M. Campin, H. Drange, M. Follows, Y. Gao, N. Gruber, M. W. Hecht, A. Ishida, F. Joos, K. Lindsay, G. Madec, E. Maier-Reimer, J. C. Marshall, R. J. Matear, P. Monfray, A. Mouchet, G. K. Plattner, J. Sarmiento, R. Schlitzer, R. Slater, I. J. Totterdell, M. F. Weirig, Y. Yamanaka and A. Yool (2002). Evaluation of ocean model ventilation with CFC-11: comparison of 13 global ocean models. *Ocean Modelling* **4**: 89–120.

Dutkiewicz, S., M. J. Follows and J. G. Bragg (2009). Modeling the coupling of ocean ecology and biogeochemistry. *Global Biogeochemical Cycles* **23**: doi: 10.1029/2008gb003405.

Egge, J. K. and D. L. Asknes (1992). Silicate as a regulating nutrient in phytoplankton competition. *Marine Ecology – Progress Series* **83**: 281–289.

Elderfield, H. and R. E. M. Rickaby (2000). Oceanic Cd/P ratio and nutrient utilization in the glacial Southern Ocean. *Nature* **405**: 305–310.

Eldevik, T., J. E. O. Nilsen, D. Iovino, K. Anders Olsson, A. B. Sando and H. Drange (2009). Observed sources and variability of Nordic seas overflow. *Nature Geoscience* **2**: 406–410.

Engström, E., I. Rodushkin, D. C. Baxter and B. Öhlander (2006). Chromatographic purification for the determination of dissolved silicon isotopic compositions in natural waters by high-resolution multicollector inductively coupled plasma mass spectrometry. *Analytical Chemistry* **78**: 250–257.

Epstein, S. and H. P. J. Taylor (1970). ^{18}O/^{16}O, ^{30}Si/^{28}Si, D/H and ^{13}C/^{12}C studies on lunar rocks and minerals. *Science* **167**: 533–535.

Falkowski, P. G., R. T. Barber and V. Smetacek (1998). Biogeochemical controls and feedbacks on ocean primary production. *Science* **281**: 200–206.

Falkowski, P. G., E. A. Laws, R. T. Barber and J. W. Murray (2003). Phytoplankton and their role in primary, new and export production. In: M. J. R. Fasham (ed.) *Ocean Biogeochemistry: The Role of the Ocean Carbon Cycle in Global Change*. Springer, Berlin.

Fine, R. A., J. L. Reid and H. G. Östlund (1981). Circulation of tritium in the Pacific Ocean. *Journal of Physical Oceanography* **11**: 3–14.

Fine, R. A., K. A. Maillet, K. F. Sullivan and D. Willey (2001). Circulation and ventilation flux of the Pacific Ocean. *Journal of Geophysical Research – Oceans* **106**: 22159–22178.

Fitoussi, C., B. Bourdon, T. Kleine, F. Oberli and B. C. Reynolds (2009). Si isotope systematics of meteorites and terrestrial peridotites: implications for Mg/Si fractionation in the solar nebula and for Si in the Earth's core. *Earth and Planetary Science Letters* **287**: 77–85.

Follows, M. J., S. Dutkiewicz, S. Grant and S. W. Chisholm (2007). Emergent biogeography of microbial communities in a model ocean. *Science* **315**: 1843–1846.

Foster, T. D. and E. C. Carmack (1976). Frontal zone mixing and Antarctic Bottom Water formation in the southern Weddell Sea. *Deep Sea Research and Oceanographic Abstracts* **23**: 301–317.

Fripiat, F. (2010). *Isotopic approaches of the silicon cycle: the Southern Ocean case study*. Ph.D. thesis, Université Libre de Bruxelles.

Fripiat, F., A.-J. Cavagna, N. Savoye, F. Dehairs, L. André and D. Cardinal (2011). Isotopic constraints on the Si-biogeochemical cycle of the Antarctic Zone in the Kerguelen area (KEOPS). *Marine Chemistry* **123**: 11–22.

Galbraith, E., M. Kienast, S. L. Jaccard, T. Pedersen, B. G. Brunelle, D. M. Sigman and T. Kiefer (2008). Consistent relationship between global climate and surface nitrate utilization in the western subarctic Pacific throughout the last 500 ka. *Paleoceanography* **23**: doi:10.1029/2007PA001518.

Ganachaud, A. and C. Wunsch (2000). Improved estimates of global ocean circulation, heat transport and mixing from hydrographic data. *Nature* **408**: 453–457.

Garcia, H. E., R. A. Locarnini, T. P. Boyer and J. I. Antonov (2010a). *World Ocean Atlas 2009, Volume 3: Dissolved Oxygen, Apparant Oxygen Utilization, and Oxygen Saturation*. NOAA Atlas NESDIS 70. U.S. Government Printing Office, Washington DC.

Garcia, H. E., R. A. Locarnini, T. P. Boyer and J. I. Antonov (2010b). *World Ocean Atlas 2009, Volume 4: Nutrients (phosphate, nitrate, silicate)*. NOAA Atlas NESDIS 71. U.S. Government Printing Office, Washington DC.

Gent, P. R. and J. C. McWilliams (1990). Isopycnal mixing in ocean circulation models. *Journal of Physical Oceanography* **20**: 150–155.

Georg, R., B. Reynolds, M. Frank and A. Halliday (2006a). Mechanisms controlling the silicon isotopic compositions of river waters. *Earth and Planetary Science Letters* **249**: 290–306.

Georg, R., B. Reynolds, M. Frank and A. Halliday (2006b). New sample preparation techniques for the determination of Si isotopic compositions using MC-ICPMS. *Chemical Geology* **235**: 95–104.

Georg, R. B., A. N. Halliday, E. A. Schauble and B. C. Reynolds (2007). Silicon in the Earth's core. *Nature* **447**: 1102–1106.

Georg, R. B., C. Zhu, B. C. Reynolds and A. N. Halliday (2009). Stable silicon isotopes of groundwaters, feldspars, and clay coatings in the Navajo Sandstone aquifer, Black Mesa, Arizona, USA. *Geochimica et Cosmochimica Acta* **73**: 2229–2241.

Gerya, T. (2010). *Introduction to Numerical Geodynamic Modelling*. Cambridge University Press, Cambridge.

Gnanadesikan, A. (1999a). A global model of silicon cycling: Sensitivity to eddy parametrization and dissolution. *Global Biogeochemical Cycles* **13**: 199–220.

Gnanadesikan, A. (1999b). A simple predictive model for the structure of the oceanic pycnocline. *Science* **283**: 2077–2079.

Gnanadesikan, A. and J. R. Toggweiler (1999). Constraints placed by silicon cycling on vertical exchange in general circulation models. *Geophysical Research Letters* **26**: 1865–1868.

Gnanadesikan, A., R. D. Slater, N. Gruber and J. L. Sarmiento (2002). Oceanic vertical exchange and new production: a comparison between models and observations. *Deep Sea Research Part II: Topical Studies in Oceanography* **49**: 363–401.

Gnanadesikan, A., J. Dunne, R. Key, K. Matsumoto, J. L. Sarmiento, R. Slater and P. S. Swathi (2004). Oceanic ventilation and biogeochemical cycling: Understanding the physical mechanisms that produce realistic distributions of tracers and productivity. *Global Biogeochemical Cycles* **18**: doi:10.1029/2003GB002097.

Goldman, J. G. (1988). Spatial and temporal discontinuities of biological processes in pelagic surface waters. In: B. J. Rothschild (ed.) *Toward a Theory of Biological–Physical Interactions in the World Ocean*, 273–296. Kluwer Acadamic Publishing, Dordrecht.

Gordon, A. L. (1981). South Atlantic thermocline ventilation. *Deep Sea Research Part A. Oceanographic Research Papers* **28**: 1239–1264.

Gordon, A. L. (1991). The role of thermohaline circulation in global climate change. In: *Lamont-Doherty Geological Observatory 1990 1991 Report*, 44–51. Lamont-Doherty Geological Observatory of Columbia University, Palisades, New York.

Gruber, N. (1998). Anthropogenic CO_2 in the Atlantic Ocean. *Global Biogeochemical Cycles* **12**: 165–191.

Gruber, N. and J. L. Sarmiento (2002). Large-scale biogeochemical-physical interactions in elemental cycles. In: A. R. Robinson, J. J. McCarthy and B. J. Rothschild (eds.) *Biological-Physical Interactions in the Sea*, volume 12 of *The Sea: Ideas and Observations on Progress in the Study of the Seas*, 337–399. John Wiley & Sons, New York.

Gruber, N., M. Gloor, S. E. Mikaloff Fletcher, S. C. Doney, S. Dutkiewicz, M. J. Follows, M. Gerber, A. R. Jacobson, F. Joos, K. Lindsay, D. Menemenlis, A. Mouchet, S. A. Müller, J. L. Sarmiento and T. Takahashi (2009). Oceanic sources, sinks, and transport of atmospheric CO_2. *Global Biogeochemical Cycles* **23**: doi: 10.1029/2008gb003349.

Hanawa, K. and L. D. Talley (2001). Mode waters. In: G. Siedler, J. A. Church and J. Gould (eds.) *Ocean circulation and climate – observing and modelling the global ocean*, volume Volume 77 of *International Geophysics*, 373–386. Academic Press, San Diego.

Hansen, B. and S. Østerhus (2000). North Atlantic–Nordic Seas exchanges. *Progress in Oceanography* **45**: 109–208.

Holfort, J. and G. Siedler (2001). The meridional oceanic transports of heat and nutrients in the South Atlantic. *Journal of Physical Oceanography* **31**: 5–29.

Holloway, G. (1986). Estimation of oceanic eddy transports from satellite altimetry. *Nature* **323**: 243–244.

Huhn, O., H. H. Hellmer, M. Rhein, C. Rodehacke, W. Roether, M. P. Schodlok and M. Schröder (2008). Evidence of deep- and bottom-water formation in the western Weddell Sea. *Deep Sea Research Part II: Topical Studies in Oceanography* **55**: 1098–1116.

Iler, R. K. (1979). *Chemistry of Silica: Solubility, Polymerization, Colloid and Surface Properties and Biochemistry*. John Wiley & Sons, Inc., New York.

Isachsen, P. E., C. Mauritzen and H. Svendsen (2007). Dense water formation in the Nordic Seas diagnosed from sea surface buoyancy fluxes. *Deep Sea Research Part I: Oceanographic Research Papers* **54**: 22–41.

Iselin, C. O. (1939). The influence of vertical and lateral turbulence on the characteristics of the waters at mid-depths. *Transactions of the American Geophysical Union* **20**: 414–417.

Ito, T. and M. J. Follows (2005). Preformed phosphate, soft tissue pump and atmospheric CO_2. *Journal of Marine Research* **63**: 813–839.

Iudicone, D., K. B. Rodgers, R. Schopp and G. Madec (2007). An exchange window for the injection of Antarctic Intermediate Water into the South Pacific. *Journal of Physical Oceanography* **37**: 31–49.

Jackett, D. R. and T. J. McDougall (1997). A neutral density variable for the world's oceans. *Journal of Physical Oceanography* **27**: 237–263.

Jeandel, C., Y. Godderis, B. Peucker-Ehrenbrink, F. Lacan and T. Arsouze (2009). Impact of the boundary processes on Si, Ca and Mg inputs to the ocean. *Geochimica et Cosmochimica Acta* **73**: A588.

Jenkins, W. J. (1998). Studying subtropical thermocline ventilation and circulation using tritium and ^{3}He. *Journal of Geophysical Research – Oceans* **103**: 15817–15831.

Jenkins, W. J. and S. C. Doney (2003). The subtropical nutrient spiral. *Global Biogeochemical Cycles* **17**: doi:10.1029/2003GB002085.

Jin, X., N. Gruber, J. P. Dunne, J. L. Sarmiento and R. A. Armstrong (2006). Diagnosing the contribution of phytoplankton functional groups to the production and export of particulate organic carbon, $CaCO_3$, and opal from global nutrient and alkalinity distributions. *Global Biogeochemical Cycles* **20**: doi: 10.1029/2005GB002532.

John, S. G., R. W. Geis, M. A. Saito and E. A. Boyle (2007). Zinc isotope fractionation during high-affinity and low-affinity zinc transport by the marine diatom *Thalassiosira oceanica*. *Limnology and Oceanography* **52**: 2710–2714.

Johnson, G. C. and M. J. McPhaden (1999). Interior pycnocline flow from the subtropical to the equatorial Pacific Ocean. *Journal of Physical Oceanography* **29**: 3073–3089.

Jullion, L., K. J. Heywood, A. C. Naveira Garabato and D. P. Stevens (2010). Circulation and Water Mass Modification in the Brazil–Malvinas Confluence. *Journal of Physical Oceanography* **40**: 845–864.

Karl, D. M. and G. Tien (1992). MAGIC: A sensitive and precise method for measuring dissolved phosphorus in aquatic environments. *Limnology and Oceanography* **37**: 105–116.

Karstensen, J. (2004). Formation of the South Pacific Shallow Salinity Minimum: A Southern Ocean Pathway to the Tropical Pacific. *Journal of Physical Oceanography* **34**: 2398–2412.

Karstensen, J. and D. Quadfasel (2002). Formation of southern hemisphere thermocline waters: water mass conversion and subduction. *Journal of Physical Oceanography* **32**: 3020–3038.

Karstensen, J., L. Stramma and M. Visbeck (2008). Oxygen minimum zones in the eastern tropical Atlantic and Pacific oceans. *Progress in Oceanography* **77**: 331–350.

Kawase, M. and J. L. Sarmiento (1985). Nutrients in the Atlantic thermocline. *Journal of Geophysical Research – Oceans* **90**: 8961–8979.

Kawase, M. and J. L. Sarmiento (1986). Circulation and nutrients in middepth Atlantic waters. *Journal of Geophysical Research – Oceans* **91**.

Kendall, C. and D. H. Doctor (2003). Stable isotope applications in hydrologic studies. In: H. D. Holland and K. K. Turekian (eds.) *Treatise on Geochemistry*, volume 5, 319–364. Elsevier Ltd., Amsterdam.

Knapp, A. N., P. J. DiFiore, C. Deutsch, D. M. Sigman and F. Lipschultz (2008). Nitrate isotopic composition between Bermuda and Puerto Rico: implications for N_2 fixation in the Atlantic Ocean. *Global Biogeochemical Cycles* **22**: doi:10.1029/2007GB003107.

Kohfeld, K. E., C. Le Quéré, S. P. Harrison and R. F. Anderson (2005). Role of marine biology in glacial-interglacial CO_2 cycles. *Science* **308**: 74–78.

Kuhlbrodt, T., A. Griesel, M. Montoya, A. Levermann, M. Hofmann and S. Rahmstorf (2007). On the driving processes of the Atlantic meridional overturning circulation. *Reviews of Geophysics* **45**: RG2001, doi: 10.1029/2004rg000166.

Lacan, F., A. Radic, C. Jeandel, F. Poitrasson, G. Sarthou, C. Pradoux and R. Freydier (2008). Measurement of the isotopic composition of dissolved iron in the open ocean. *Geophysical Research Letters* **35**: doi: 10.1029/2008gl035841.

Larqué, L., K. Maamaatuaiahutapu and V. Garçon (1997). On the intermediate and deep water flows in the South Atlantic Ocean. *Journal of Geophysical Research – Oceans* **102**: 12425–12440.

Law, C. S., A. P. Martin, M. I. Liddicoat, A. J. Watson, K. J. Richards and E. M. S. Woodward (2001). A Lagrangian SF_6 tracer study of an anticyclonic eddy in the North Atlantic: patch evolution, vertical mixing and nutrient supply to the mixed layer. *Deep Sea Research Part II: Topical Studies in Oceanography* **48**: 705–724.

Ledwell, J. R., A. J. Watson and C. S. Law (1993). Evidence for slow mixing across the pycnocline from an open-ocean tracer-release experiment. *Nature* **364**: 701–703. 10.1038/364701a0 10.1038/364701a0.

Ledwell, J. R., A. J. Watson and C. S. Law (1998). Mixing of a tracer in the pycnocline. *Journal of Geophysical Research – Oceans* **103**: 21,49921,529.

Legeckis, R. and A. L. Gordon (1982). Satellite observations of the Brazil and Falkland currents – 1975 1976 and 1978. *Deep Sea Research Part A. Oceanographic Research Papers* **29**: 375–401.

Levitus, S. (1982). Climatological Atlas of the World Ocean. Technical report, NOAA/ERL GFDL Professional Paper.

Levitus, S., M. E. Conkright, J. L. Reid, R. G. Najjar and A. Mantyla (1993). Distribution of nitrate, phosphate and silicate in the world oceans. *Progress in Oceanography* **31**: 245–273.

Locarnini, R. A., A. Mishonov, J. I. Antonov, T. P. Boyer and H. E. Garcia (2010). *World Ocean Atlas 2009, Volume 1: Temperature*. NOAA Atlas NESDIS 68. U.S. Government Printing Office, Washington DC.

Loucaides, S., P. Van Cappellen, V. Roubeix, B. Moriceau and O. Ragueneau (2011). Controls on the recycling and preservation of biogenic silica from biomineralization to burial. *Silicon* doi: 10.1007/s12633–011–9092–9.

Lumpkin, R. and K. Speer (2003). Large-scale vertical and horizontal circulation in the North Atlantic Ocean. *Journal of Physical Oceanography* **33**: 1902–1920.

Lumpkin, R. and K. Speer (2007). Global ocean meridional overturning. *Journal of Physical Oceanography* **37**: 2550–2562.

Luyten, J. R., J. Pedlosky and H. Stommel (1983). The ventilated thermocline. *Journal of Physical Oceanography* **13**: 292–309.

Maamaatuaiahutapu, K., C. Provost, C. Andrié and X. Vigan (1999). Origin and ages of mode waters in the Brazil-Malvinas Confluence region during austral winter 1994. *Journal of Geophysical Research – Oceans* **104**: 21051–21061.

Maier-Reimer, E., U. Mikolajewicz and K. Hasselmann (1993). Mean circulation of the Hamburg LSG OGCM and Its sensitivity to the thermohaline surface forcing. *Journal of Physical Oceanography* **23**: 731–757.

Mantyla, A. W. and J. L. Reid (1983). Abyssal characteristics of the world ocean waters. *Deep Sea Research Part A. Oceanographic Research Papers* **30**: 805–833.

Marchetti, A. and N. Cassar (2009). Diatom elemental and morphological changes in response to iron limitation: a brief review with potential paleoceanographic applications. *Geobiology* **7**: 419–431.

Marchetti, A. and P. J. Harrison (2007). Coupled changes in the cell morphology and elemental (C, N, and Si) composition of the pennate diatom *Pseudo-nitzschia* due to iron deficiency. *Limnology and Oceanography* **52**: 2270–2284.

Margalef, R. (1978). Life-forms of phytoplankton as survival alternatives in an unstable environment. *Oceanologica Acta* **1**: 493–509.

Marinov, I., A. Gnanadesikan, J. R. Toggweiler and J. L. Sarmiento (2006). The Southern Ocean biogeochemical divide. *Nature* **441**: 964–967.

Marshall, D. (1997). Subduction of water masses in an eddying ocean. *Journal of Marine Research* **55**: 201–222.

Martin, J. H. (1990). Glacial–interglacial CO_2 change: the iron hypothesis. *Paleoceanography* **5**: 1–13.

Martin-Jézéquel, V., M. Hildebrand and M. A. Brzezinski (2000). Silicon metabolism in diatoms: implications for growth. *Journal of Phycology* **36**: 821–840.

Matsumoto, K. (2007). Radiocarbon-based circulation age of the world oceans. *Journal of Geophysical Research – Oceans* **112**: doi:10.1029/2007JC004095.

Matsumoto, K., J. L. Sarmiento and M. A. Brzezinski (2002). Silicic acid leakage from the Southern Ocean: A possible explanation for glacial atmospheric pCO_2. *Global Biogeochemical Cycles* **16**: doi: 10.1029/2001GB001442. 1031.

Mauritzen, C. (1996a). Production of dense overflow waters feeding the North Atlantic across the Greenland-Scotland Ridge. Part 1: Evidence for a revised circulation scheme. *Deep Sea Research Part I: Oceanographic Research Papers* **43**: 769–806.

Mauritzen, C. (1996b). Production of dense overflow waters feeding the North Atlantic across the Greenland-Scotland Ridge. Part 2: An inverse model. *Deep Sea Research Part I: Oceanographic Research Papers* **43**: 807–835.

McCartney, M. S. (1977). Subantarctic Mode Water. In: M. Angel (ed.) *A Voyage of Discovery, Supplement to Deep-Sea Research Vol. 24*, 103–119. Pergamon Press, Oxford.

McCartney, M. S. (1982). The subtropical recirculation of Mode Waters. *Journal of Marine Research* **40 (Suppl.)**: 427–464.

McCartney, M. S. and C. Mauritzen (2001). On the origin of the warm inflow to the Nordic Seas. *Progress in Oceanography* **51**: 125–214.

McCartney, M. S. and L. D. Talley (1982). The Subpolar Mode Water of the North Atlantic Ocean. *Journal of Physical Oceanography* **12**: 1169–1188.

Measures, C. I., W. M. Landing, M. T. Brown and C. S. Buck (2008). High-resolution Al and Fe data from the Atlantic Ocean CLIVAR-CO_2 Repeat Hydrography A16N transect: Extensive linkages between atmospheric dust and upper ocean geochemistry. *Global Biogeochemical Cycles* **22**: GB1005.

Milligan, A. J., D. E. Varela, M. A. Brzezinski and F. M. M. Morel (2004). Dynamics of silicon metabolism and silicon isotopic discrimination in a marine diatom as a function of pCO_2. *Limnology and Oceanography* **49**: 322–329.

Miyake, Y. and E. Wada (1967). The abundance ratio of $^{15}N/^{14}N$ in marine environments. *Records of Oceanographic Works in Japan* **9**: 37–53.

Moore, C. M., M. M. Mills, E. P. Achterberg, R. J. Geider, J. LaRoche, M. I. Lucas, E. L. McDonagh, X. Pan, A. J. Poulton, M. J. A. Rijkenberg, D. J. Suggett, S. J. Ussher and E. M. S. Woodward (2009). Large-scale distribution of Atlantic nitrogen fixation controlled by iron availability. *Nature Geoscience* **2**: 867–871.

Munk, W. and C. Wunsch (1998). Abyssal recipes II: energetics of tidal and wind mixing. *Deep Sea Research Part I: Oceanographic Research Papers* **45**: 1977–2010.

Najjar, R. G., X. Jin, F. Louanchi, O. Aumont, K. Caldeira, S. C. Doney, J. C. Dutay, M. Follows, N. Gruber, F. Joos, K. Lindsay, E. Maier-Reimer, R. J. Matear, K. Matsumoto, P. Monfray, A. Mouchet, J. C. Orr, G. K. Plattner, J. L. Sarmiento, R. Schlitzer, R. D. Slater, M. F. Weirig, Y. Yamanaka and A. Yool (2007). Impact of circulation on export production, dissolved organic matter, and dissolved oxygen in the ocean: Results from Phase II of the Ocean Carbon-cycle Model Intercomparison Project (OCMIP-2). *Global Biogeochemical Cycles* **21**: doi: 10.1029/2006gb002857.

Naveira Garabato, A. C., K. L. Polzin, B. A. King, K. J. Heywood and M. Visbeck (2004). Widespread intense turbulent mixing in the Southern Ocean. *Science* **303**: 210–213.

Nelson, D. M., P. Tréguer, M. A. Brzezinski, A. Leynaert and B. Quéguiner (1995). Production and dissolution of biogenic silica in the ocean – Revised global estimates, comparison with regional data and relationship to biogenic sedimentation. *Global Biogeochemical Cycles* **9**: 359–372.

O'Connor, B. M., R. A. Fine, K. A. Maillet and D. B. Olson (2002). Formation rates of subtropical underwater in the Pacific Ocean. *Deep Sea Research Part I: Oceanographic Research Papers* **49**: 1571–1590.

Olbers, D. and M. Wenzel (1989). Determining diffusivities from hydrographic data by inverse methods with applications to the Circumpolar Current. In: D. Anderson and J. Willebrand (eds.) *Oceanic Circulation Models: Combining Data and Dynamics*, 95–139. Kluwer Academic Publishers, Dordrecht.

Opfergelt, S., B. Delvaux, L. André and D. Cardinal (2008). Plant silicon isotopic signature might reflect soil weathering degree. *Biogeochemistry* **91**: 163–175.

Orsi, A. H., T. Whitworth and W. D. Nowlin (1995). On the meridional extent and fronts of the Antarctic Circumpolar Current. *Deep Sea Research Part I: Oceanographic Research Papers* **42**: 641–673.

Orsi, A. H., G. C. Johnson and J. L. Bullister (1999). Circulation, mixing, and production of Antarctic Bottom Water. *Progress in Oceanography* **43**: 55–109.

Palter, J. B. and M. S. Lozier (2008). On the source of Gulf Stream nutrients. *Journal of Geophysical Research – Oceans* **113**: doi: 0.1029/2007jc004611.

Palter, J. B., M. S. Lozier and R. T. Barber (2005). The effect of advection on the nutrient reservoir in the North Atlantic subtropical gyre. *Nature* **437**: 687–692.

Palter, J. B., J. L. Sarmiento, A. Gnanadesikan, J. Simeon and R. D. Slater (2010). Fueling export production: nutrient return pathways from the deep ocean and their dependence on the meridional overturning circulation. *Biogeosciences* **7**: 3549–3568.

Peterson, R. G. and L. Stramma (1991). Upper-level circulation in the South Atlantic Ocean. *Progress in Oceanography* **26**: 1–73.

Pichevin, L., B. C. Reynolds, R. S. Ganeshram, I. Cacho, L. Pena, K. Keefe and R. M. Ellam (2009). Enhanced carbon pump inferred from relaxation of nutrient limitation in the glacial ocean. *Nature* **459**: 1114–1117.

Piola, A. R. and R. P. Matano (2001). Brazil and Falklands (Malvinas) Currents. In: J. H. Steele, K. K. Turekian and S. Thorpe (eds.) *Encyclopedia of Ocean Sciences*, 422–430. Academic Press, Oxford.

Pollard, R. T., M. I. Lucas and J. F. Read (2002). Physical controls on biogeochemical zonation in the Southern Ocean. *Deep Sea Research Part II: Topical Studies in Oceanography* **49**: 3289–3305.

Polzin, K. L., J. M. Toole and R. W. Schmitt (1995). Finescale parameterizations of turbulent dissipation. *Journal of Physical Oceanography* **25**: 306–328.

Polzin, K. L., J. M. Toole, J. R. Ledwell and R. W. Schmitt (1997). Spatial variability of turbulent mixing in the abyssal ocean. *Science* **276**: 93–96.

Pondaven, P., M. Gallinari, S. Chollet, E. Bucciarelli, G. Sarthou, S. Schultes and F. Jean (2007). Grazing-induced changes in cell wall silicification in a marine diatom. *Protist* **158**: 21–28.

Poole, R. and M. Tomczak (1999). Optimum multiparameter analysis of the water mass structure in the Atlantic Ocean thermocline. *Deep Sea Research Part I: Oceanographic Research Papers* **46**: 1895–1921.

Qu, T., S. Gao, I. Fukumori, R. A. Fine and E. J. Lindstrom (2008). Subduction of South Pacific waters. *Geophysical Research Letters* **35**: L02610.

Ragueneau, O., P. Tréguer, A. Leynaert, R. F. Anderson, M. A. Brzezinski, D. J. DeMaster, R. C. Dugdale, J. Dymond, G. Fischer, R. Francois, C. Heinze, E. Maier-Reimer, V. Martin-Jézéquel, D. M. Nelson and B. Quéguiner (2000). A review of the Si cycle in the modern ocean: recent progress and missing gaps in the application of biogenic opal as a paleoproductivity proxy. *Global and Planetary Change* **26**: 317–365.

Ragueneau, O., N. Dittert, P. Pondaven, P. Treguer and L. Corrin (2002). Si/C decoupling in the world ocean: is the Southern Ocean different? *Deep-Sea Research Part II – Topical Studies in Oceanography* **49**: 3127–3154.

Ragueneau, O., S. Schultes, K. D. Bidle, P. Claquin and B. La Moriceau (2006). Si and C interactions in the world ocean: Importance of ecological processes and implications for the role of diatoms in the biological pump. *Global Biogeochemical Cycles* **20**: doi:10.1029/2006GB002688.

Ragueneau, O., A. Regaudie-de Gioux, B. Moriceau, M. Gallinari, A. Vangriesheim, F. Baurand and A. Khripounoff (2009). A benthic Si mass balance on the Congo margin: Origin of the 4000 m DSi anomaly and implications for the transfer of Si from land to ocean. *Deep Sea Research Part II: Topical Studies in Oceanography* **56**: 2197–2207.

Raven, J. A. (1983). The transport and function of silicon in plants. *Biological Reviews* **58**: 179–207.

Rayleigh (1902). On the distillation of binary mixtures. *The Philosphical Magazine* **4**: 521–537.

Reid, J. L. (1986). On the total geostrophic circulation of the South Pacific Ocean: Flow patterns, tracers and transports. *Progress in Oceanography* **16**: 1–61.

Reid, J. L. (1989). On the total geostrophic circulation of the South Atlantic Ocean: Flow patterns, tracers, and transports. *Progress In Oceanography* **23**: 149–244.

Reid, J. L. (1994). On the total geostrophic circulation of the North Atlantic Ocean: Flow patterns, tracers, and transports. *Progress in Oceanography* **33**: 1–92.

Reid, J. L. (1997). On the total geostrophic circulation of the Pacific Ocean: flow patterns, tracers, and transports. *Progress in Oceanography* **39**: 263–352.

Reynolds, B. C. (2009). Modeling the modern marine δ^{30}Si distribution. *Global Biogeochemical Cycles* **23**: doi:10.1029/2008GB003266.

Reynolds, B. C. (2011). Silicon isotopes as tracers of terrestrial processes. In: M. Baskaran (ed.) *Handbook of Environmental Isotope Geochemistry*, Advances in Isotope Geochemistry, 87–104. Springer, Berlin, Heidelberg.

Reynolds, B. C., M. Frank and A. N. Halliday (2006a). Silicon isotope fractionation during nutrient utilization in the North Pacific. *Earth and Planetary Science Letters* **244**: 431–443.

Reynolds, B. C., R. B. Georg, F. Oberli, U. Wiechert and A. N. Halliday (2006b). Re-assessment of silicon isotope reference materials using high-resolution multi-collector ICP-MS. *Journal of Analytical Atomic Spectrometry* **21**: 266–269.

Reynolds, B. C., J. Aggarwal, L. André, D. Baxter, C. Beucher, M. A. Brzezinski, E. Engström, R. B. Georg, M. Land, M. J. Leng, S. Opfergelt, I. Rodushkin, H. J. Sloane, S. H. J. M. van den Boorn, P. Z. Vroon and D. Cardinal (2007). An inter-laboratory comparison of Si isotope reference materials. *Journal of Analytical Atomic Spectrometry* **22**: 561–568.

Reynolds, J. H. and J. Verhoogen (1953). Natural variations in the isotopic composition of silicon. *Geochimica et Cosmochimica Acta* **3**: 224–234.

Rickli, J., M. Frank and A. N. Halliday (2009). The hafnium–neodymium isotopic composition of Atlantic seawater. *Earth and Planetary Science Letters* **280**: 118–127.

Rintoul, S. R. and C. Wunsch (1991). Mass, heat, oxygen and nutrient fluxes and budgets in the North Atlantic Ocean. *Deep Sea Research* **38, Suppl. 1**: S355–S377.

Ripperger, S., M. Rehkämper, D. Porcelli and A. N. Halliday (2007). Cadmium isotope fractionation in seawater – A signature of biological activity. *Earth and Planetary Science Letters* **261**: 670–684.

Robinson, A. and H. Stommel (1959). The oceanic thermocline and the associated thermohaline circulation. *Tellus* **11**: 295–308.

Rooth, C. G. and G. Östlund (1972). Penetration of tritium into the Atlantic thermocline. *Deep Sea Research and Oceanographic Abstracts* **19**: 481–492.

Rosman, K. J. R. and P. D. P. Taylor (1998). Isotopic compositions of the elements 1997. *Pure and Applied Chemistry* **70**: 217–235.

Rutgers van der Loeff (ed.), M. (2007). *The expeditions ANT-XXIII/1 of the Research Vessel Polarstern in 2005*, volume 556 of *Reports on Polar and Marine Research*. Alfred Wegner Institute for Polar and Marine Research, Bremerhaven.

Sabine, C. L., R. Key, A. Kozyr, R. A. Feely, R. Wanninkhof, F. J. Millero, T. H. Peng, J. L. Bullister and K. Lee (2005). Global Ocean Data Analysis Project (GLODAP): results and data. Technical Report ORNL/CDIAC-145, NDP-083, Carbon Dioxide Information Analysis Center, Oak Ridge National Laboratory, U. S. Dept. of Energy.

Sallée, J.-B., K. Speer, S. Rintoul and S. Wijffels (2010). Southern Ocean thermocline ventilation. *Journal of Physical Oceanography* **40**: 509–529.

Sarmiento, J. L. and N. Gruber (2006). *Ocean Biogeochemical Dynamics*. Princeton University Press, Princeton.

Sarmiento, J. L. and J. R. Toggweiler (1984). A new model for the role of the oceans in determining atmospheric pCO_2. *Nature* **308**: 621–624.

Sarmiento, J. L., N. Gruber, M. A. Brzezinski and J. P. Dunne (2004a). High-latitude controls of thermocline nutrients and low latitude biological productivity. *Nature* **427**: 56–60.

Sarmiento, J. L., R. Slater, R. Barber, L. Bopp, S. C. Doney, A. C. Hirst, J. Kleypas, R. Matear, U. Mikolajewicz, P. Monfray, V. Soldatov, S. A. Spall and R. Stouffer (2004b). Response of ocean ecosystems to climate warming. *Global Biogeochemical Cycles* **18**: doi: 10.1029/2003gb002134. Times Cited: 162.

Sarmiento, J. L., J. Simeon, A. Gnanadesikan, N. Gruber, R. M. Key and R. Schlitzer (2007). Deep ocean biogeochemistry of silicic acid and nitrate. *Global Biogeochemical Cycles* **21**: doi:10.1029/2006GB002720.

Savage, P. S., R. B. Georg, R. M. G. Armytage, H. M. Williams and A. N. Halliday (2010). Silicon isotope homogeneity in the mantle. *Earth and Planetary Science Letters* **295**: 139–146.

Schlitzer, R. (2000). Electronic atlas of WOCE hydrographic and tracer data now available. *Eos Transactions AGU* **81**: 45.

Schlitzer, R. (2009). Ocean Data View, http://odv.awi.de.

Schmittner, A., N. M. Urban, K. Keller and D. Matthews (2009). Using tracer observations to reduce the uncertainty of ocean diapycnal mixing and climate–carbon cycle projections. *Global Biogeochemical Cycles* **23**: doi: 10.1029/2008gb003421.

Schmitz, W. J. (1995). On the interbasin-scale thermohaline circulation. *Reviews of Geophysics* **33**: 151–173.

Schmitz, W. J. (1996a). The Pacific and Indian Oceans/A Global Update. Technical report, Woods Hole Oceanographic Institution.

Schmitz, W. J. (1996b). Some Global Features/North Atlantic Circulation. Technical report, Woods Hole Oceanographic Institution.

Schmitz, W. J. and M. S. McCartney (1993). On the North Atlantic circulation. *Reviews of Geophysics* **31**: 29–49.

SCORWorkingGroup (2007). GEOTRACES – An international study of the global marine biogeochemical cycles of trace elements and their isotopes. *Chemie der Erde – Geochemistry* **67**: 85–131.

Sigman, D. M., M. A. Altabet, D. C. McCorkle, R. Francois and G. Fischer (1999). The δ^{15}N of nitrate in the Southern Ocean: Consumption of nitrate in surface waters. *Global Biogeochemical Cycles* **13**: 1149–1166.

Sigman, D. M., M. A. Altabet, D. C. McCorkle, R. Francois and G. Fischer (2000). The δ^{15}N of nitrate in the Southern Ocean: Nitrogen cycling and circulation in the ocean interior. *Journal of Geophysical Research-Oceans* **105**: 19599–19614.

Sigman, D. M., P. J. DiFiore, M. P. Hain, C. Deutsch, Y. Wang, D. M. Karl, A. N. Knapp, M. F. Lehmann and S. Pantoja (2009a). The dual isotopes of deep nitrogen as a constraint on the cycle and budget of oceanic fixed nitrogen. *Deep-Sea Research Part I – Oceanographic Research Papers* **56**: 1419–1439.

Sigman, D. M., K. L. Karsh and K. L. Casciotti (2009b). Nitrogen isotopes in the ocean. In: J. H. Steele, K. K. Turekian and S. A. Thorpe (eds.) *Encyclopedia of Ocean Sciences*, 40–54. Academic Press, Oxford, 2nd edition.

Sigman, D. M., M. P. Hain and G. H. Haug (2010). The polar ocean and glacial cycles in atmospheric CO_2 concentration. *Nature* **466**: 47–55.

Sloyan, B. M. and S. R. Rintoul (2001a). Circulation, renewal, and modification of Antarctic Mode and Intermediate Water. *Journal of Physical Oceanography* **31**: 1005–1030.

Sloyan, B. M. and S. R. Rintoul (2001b). The Southern Ocean limb of the global deep overturning circulation. *Journal of Physical Oceanography* **31**: 143–173.

Sloyan, B. M., L. D. Talley, T. K. Chereskin, R. Fine and J. Holte (2010). Antarctic Intermediate Water and Subantarctic Mode Water Formation in the Southeast Pacific: The Role of Turbulent Mixing. *Journal of Physical Oceanography* **40**: 1558–1574.

Smetacek, V. (1985). Role of sinking in diatom life-history cycles: ecological, evolutionary and geological significance. *Marine Biology* **84**: 239–251.

Smetacek, V. (1999). Diatoms and the ocean carbon cycle. *Protist* **150**: 25–32.

Smetacek, V., P. Assmy and J. Henjes (2004). The role of grazing in structuring Southern Ocean pelagic ecosystems and biogeochemical cycles. *Antarctic Science* **16**: 541–558.

Sprintall, J. and M. Tomczak (1993). On the formation of central water and thermocline ventilation in the southern hemisphere. *Deep Sea Research Part I: Oceanographic Research Papers* **40**: 827–848.

Stommel, H. (1958). The abyssal circulation. *Deep Sea Research* **5**: 80–82.

Stommel, H. (1979). Determination of water mass properties of water pumped down from the Ekman layer to the geostrophic flow below. *Proceedings of the National Academy of Sciences of the United States of America* **76**: 3051–3055.

Stommel, H. and A. B. Arons (1960). On the abyssal circulation of the world ocean – II. An idealized model of the circulation pattern and amplitude in oceanic basins. *Deep Sea Research* **6**: 217–233.

Stramma, L. and M. England (1999). On the water masses and mean circulation of the South Atlantic Ocean. *Journal of Geophysical Research – Oceans* **104**: 20863–20883.

Stramma, L. and F. Schott (1999). The mean flow field of the tropical Atlantic Ocean. *Deep Sea Research Part II – Topical Studies in Oceanography* **46**: 279–303.

Stramma, L., H. S. John, K. T. Karl and A. T. Steve (2001). Current systems in the Atlantic Ocean. In: *Encyclopedia of Ocean Sciences*, 589–598. Academic Press, Oxford.

Strickland, J. and T. Parsons (1968). *A Practical Handbook of Seawater Analysis*, volume 167 of *Bulletin of the Fisheries Research Board of Canada*. Fisheries Research Board of Canada.

Stumm, W. and J. J. Morgan (1981). *Aquatic Chemistry*. John Wiley & Sons, Inc., New York, 2nd edition.

Takeda, S. (1998). Influence of iron availability on nutrient consumption ratio of diatoms in oceanic waters. *Nature* **393**: 774–777.

Talley, L. D. (2008). Freshwater transport estimates and the global overturning circulation: Shallow, deep and throughflow components. *Progress in Oceanography* **78**: 257–303.

Talley, L. D., J. L. Reid and P. E. Robbins (2003). Data-based meridional overturning streamfunctions for the global ocean. *Journal of Climate* **16**: 3213–3226.

Thomson, C. W. (1878). *The voyage of the Challenger: The Atlantic*. Harper and Brothers, New York.

Tipper, E. T., P. Louvat, F. Capmas, A. Galy and J. Gaillardet (2008). Accuracy of stable Mg and Ca isotope data obtained by MC-ICP-MS using the standard addition method. *Chemical Geology* **257**: 65–75.

Toggweiler, J. R. (1999). Variation of atmospheric CO_2 by ventilation of the ocean's deepest water. *Paleoceanography* **14**: 571–588.

Toggweiler, J. R. and S. Carson (1995). What are upwelling systems contributing to the ocean's carbon and nutrient budgets? In: C. Summerhayes, K.-C. Emeis, M. V. Angel, R. L. Smith and B. Zeitzschel (eds.) *Upwelling in the Ocean: Modern Processes and Ancient Records*, 337–360. John Wiley & Sons, Chichester.

Toggweiler, J. R. and B. Samuels (1993a). Is the magnitude of the deep outflow from the Atlantic Ocean actually governed by Southern Hemisphere winds? In: M. Heimann (ed.) *The Global Carbon Cycle*, volume 15 of *NATO ASI Series. Series I, Global environmental change*, 303–331. Springer, Berlin.

Toggweiler, J. R. and B. Samuels (1993b). New radiocarbon constraints on the upwelling of abyssal water to the ocean's surface. In: M. Heimann (ed.) *The Global Carbon Cycle*, volume 15 of *NATO ASI Series. Series I, Global environmental change*, 333–366. Springer, Berlin.

Toggweiler, J. R. and B. Samuels (1995). Effect of Drake Passage on the global thermohaline circulation. *Deep Sea Research Part I: Oceanographic Research Papers* **42**: 477–500.

Toggweiler, J. R. and B. Samuels (1998). On the ocean's large-scale circulation near the limit of no vertical mixing. *Journal of Physical Oceanography* **28**: 1832–1852.

Toggweiler, J. R., K. Dixon and W. S. Broecker (1991). The Peru upwelling and the ventilation of the South Pacific thermocline. *Journal of Geophysical Research – Oceans* **96**: 20467–20497.

Toggweiler, J. R., J. L. Russell and S. R. Carson (2006). Midlatitude westerlies, atmospheric CO_2, and climate change during the Ice Ages. *Paleoceanography* **21**: 10.1029/2005PA001154.

Tomczak, M. and J. S. Godfrey (2003). *Regional Oceanography: An Introduction*. Daya Publishing House, Delhi.

Toole, J. M., K. L. Polzin and R. W. Schmitt (1994). Estimates of diapycnal mixing in the abyssal ocean. *Science* **264**: 1120–1123.

Tozzi, S., O. M. Schofield and P. Falkowski (2004). Historical climate change and ocean turbulence as selective agents for two key phytoplankton functional groups. *Marine Ecology – Progress Series* **274**: 123–132.

Tréguer, P., D. M. Nelson, A. J. van Bennekom, D. J. Demaster, A. Leynaert and B. Queguiner (1995). The silica balance in the world ocean – a reestimate. *Science* **268**: 375–379.

Tsuchiya, M. (1989). Circulation of the Antarctic Intermediate Water in the North Atlantic Ocean. *Journal of Marine Research* **47**: 747–755.

Tsuchiya, M. (1991). Flow path of Antarctic Intermediate Water in the western equatorial South Pacific Ocean. *Deep Sea Research Part A – Oceanographic Research Papers* **38**: S273–S279.

Tsuchiya, M. and L. Talley (1996). Water-property distributions along an eastern Pacific hydrographic section at 135W. *Journal of Marine Research* **54**: 541–564.

Tsuchiya, M. and L. D. Talley (1998). A Pacific hydrographic section at 88°W: Water-property distribution. *Journal of Geophysical Research – Oceans* **103**: 12899–12918.

Tsuchiya, M., R. Lukas, R. A. Fine, E. Firing and E. Lindstrom (1989). Source waters of the Pacific Equatorial Undercurrent. *Progress in Oceanography* **23**: 101–147.

Tsuchiya, M., L. D. Talley and M. S. McCartney (1992). An eastern Atlantic section from Iceland southward across the equator. *Deep Sea Research Part A. Oceanographic Research Papers* **39**: 1885–1917.

Tsuchiya, M., L. D. Talley and M. S. McCartney (1994). Water-mass distributions in the western South Atlantic: A section from South Georgia Island (54°S) northward across the equator. *Journal of Marine Research* **52**: 55–81.

Urey, H. C. (1947). The thermodynamic properties of isotopic substances. *Journal of the Chemical Society* 562–581.

van Bennekom, A. J. and G. W. Berger (1984). Hydrography and silica budget of the Angola Basin. *Netherlands Journal of Sea Research* **17**: 149–200.

Van den Boorn, S. H. J. M., P. Z. Vroon, C. C. van Belle, B. van der Wagt, J. Schwieters and M. J. van Bergen (2006). Determination of silicon isotope ratios in silicate materials by high-resolution MC-ICP-MS using a sodium hydroxide sample digestion method. *Journal of Analytical Atomic Spectrometry* **21**: 734–742.

van den Boorn, S. H. J. M., P. Z. Vroon and M. J. van Bergen (2009). Sulfur-induced offsets in MC-ICP-MS silicon-isotope measurements. *Journal of Analytical Atomic Spectrometry* **24**: 1111–1114.

Varela, D. E., C. J. Pride and M. A. Brzezinski (2004). Biological fractionation of silicon isotopes in Southern Ocean surface waters. *Global Biogeochemical Cycles* **18**: doi: 10.1029/2003GB002140.

Volk, T. and M. I. Hoffert (1985). Ocean carbon pumps: analysis of relative strengths and efficiencies in ocean-driven atmsopheric CO_2 changes. In: E. T. Sundquist and W. S. Broecker (eds.) *The Carbon Cycle and Atmospheric* CO_2*: Natural Variations Archean to Present*. American Geophysical Union, Washington, D.C.

Ward, B. B. (2008). Nitrification in marine systems. In: D. G. Capone, D. A. Bronk, M. R. Mulholland and E. J. Carpenter (eds.) *Nitrogen in the Marine Environment*, 199–261. Academic Press, San Diego.

Warren, B. (1981). Deep circulation of the World Ocean. In: B. Warren and C. Wunsch (eds.) *Evolution of Physical Oceanography*, 6–41. MIT Press, Cambridge MA.

Warren, B. and K. Speer (1991). Deep circulation in the eastern South Atlantic Ocean. *Deep Sea Research* **38**: S281–S322.

Warren, B. A. (1973). Transpacific hydrographic sections at lats. 43°S and 28°S: the SCORPIO expedition–II. deep water. *Deep Sea Research and Oceanographic Abstracts* **20**: 9–38.

Weiss, R. F., H. Östlund and H. Craig (1979). Geochemical studies of the Weddell Sea. *Deep Sea Research* **26**: 1093–1120.

Welander, P. (1959). An advective model of the ocean thermocline. *Tellus* **11**: 309–318.

Whitworth, I., T. and J. Nowlin, W. D. (1987). Water masses and currents of the Southern Ocean at the Greenwich Meridian. *Journal of Geophysical Research – Oceans* **92**: 6462–6476.

Wille, M., J. Sutton, M. J. Ellwood, M. Sambridge, W. Maher, S. Eggins and M. Kelly (2010). Silicon isotopic fractionation in marine sponges: A new model for understanding silicon isotopic variations in sponges. *Earth and Planetary Science Letters* **292**: 281–289.

Williams, R. G. and M. J. Follows (1998). The Ekman transfer of nutrients and maintenance of new production in the North Atlantic. *Deep-Sea Research Part I – Oceanographic Research Papers* **45**: 461–489.

Williams, R. G. and M. J. Follows (2003). Physical transport of nutrients and the maintenance of biological production. In: M. J. R. Fasham (ed.) *Ocean Biogeochemistry: a synthesis of the Joint Global Flux Study (JGOFS)*, Global Change: The IGBP series. Springer, Berlin.

Williams, R. G., V. Roussenov and M. J. Follows (2006). Nutrient streams and their induction into the mixed layer. *Global Biogeochemical Cycles* **20**: doi: 10.1029/2005gb002586.

Wischmeyer, A. G., C. L. De La Rocha, E. Maier-Reimer and D. A. Wolf-Gladrow (2003). Control mechanisms for the oceanic distribution of silicon isotopes. *Global Biogeochemical Cycles* **17**: doi:10.1029/2002GB002022.

Wong, A. P. S. and G. C. Johnson (2003). South Pacific Eastern Subtropical Mode Water. *Journal of Physical Oceanography* **33**: 1493–1509.

Worthington, L. V. (1977). The case for near-zero production of Antarctic Bottom Water. *Geochimica et Cosmochimica Acta* **41**: 1001–1006.

Wüst, G. (1935). Schichtung und Zirkulation des Atlantischen Ozeans: Die Stratosphäre. In: *Wissenschaftliche Ergebnisse der Deutschen Atlantischen Expedition 'Meteor' 1925–1927*, volume 6. Berlin.

Wunsch, C. and R. Ferrari (2004). Vertical mixing, energy and the general circulation of the oceans. *Annual Review of Fluid Mechanics* **36**: 281–314.

York, D. (1968). Least Squares fitting of a straight line with correlated errors. *Earth and Planetary Science Letters* **5**: 320–324.

Young, E. D., A. Galy and H. Nagahara (2002). Kinetic and equilibrium mass-dependent isotope fractionation laws in nature and their geochemical and cosmochemical significance. *Geochimica et Cosmochimica Acta* **66**: 1095–1104.

Zambardi, T. and F. Poitrasson (2011). Precise determination of silicon isotopes in silicate rock reference materials by MC-ICP-MS. *Geostandards and Geoanalytical Research* **35**: 89–99.

Acknowledgements

Scarily enough, I've now spent 9 years at ETH, for more than 5 of which I've been associated with the Isotope Geochemistry group. Naturally, there are many people to thank. Ben, first of all, for your infinite patience with my rambling, your indulgence of my – generally premature – excitement at something unexpected in the data, and for allowing me to spend a lot of time reading and playing around with MATLAB, and not very much writing. I appreciate both your scientific and analytical guidance and the incredible amount of scientific freedom you've allowed me in the last four years. I'm grateful to Bernard for first allowing me to undertake an ambitious stable isotope project during my Diplomarbeit, and, both then and during my Ph.D., providing acute analyses of how to improve the robustness of my science. A big thank-you is also due to Niki, who over the years has spent a good deal of time discussing the data with me from an oceanographic perspective. John Rudge is gratefully thanked for helping me get started with MATLAB, and for writing a very useful short note on the statistics of standard error calculations. Also, starting out as a geologist in an oceanography Ph.D. is hard, which is why I'm grateful for Jörg's patience and help in getting my bearings in the Atlantic.

Mass spectrometers, and especially my beloved *Nu1700*, are temperamental beasts. Which is why everyone in the isotope geochemistry group counts themselves lucky that – until the end of this year at least – we have an analytical guardian angel in the form of Felix. Thanks a million for your tireless committment. If there were any justice in the world, your six-month-long spike-searching odyssey would have earned you a medal. The same goes for Colin and your brave resistance to the ever-increasing seismic terror – don't worry, it'll all be over soon!

Further analytical gratitude is owed to Heiri, Urs, Andreas, Donat and Marie-Thérèse, to my companionable labmate Caroline, to Ruth for her ICP-OES measurements of anion concentrations, and to the efforts of Silvio Canonica and Jacqueline Traber (EAWAG) to undertake UV-irradiation tests on my seawater samples.

But the last four years have – thankfully – not just been about silicon. I've been lucky enough to find a group of friends in Zurich that will make leaving this city rather hard. Jonas, thanks for asking, in the summer of 2003, whether I wanted to revise Bouguer anomalies. Christoph, you made the excellent – albeit uninformed – decision of moving into Hardstrasse, and it's been great sharing a flat, innumerable bowls of pasta as well as food for thought with you the last three years (Jeff and Anne – thanks for reminding us that there's more to life than isotopes!). Janne – thanks for being a great officemate and friend. Marion and Jess, thanks for Friday Beer and all the brilliant parties! Steffi, even though you didn't speak to me for the first seven years, you've made up for it in the last year and a half. Jörg & Eli, why did you guys leave Zurich? Flo, thanks for not playing tennis in the office during those last few weeks; much appreciated. Uli, thanks for the company in the office over the last weekends! Olivier, thanks for sharing your good taste in food, beer and music (do I still have your CDs?). I'm proud to have been chosen to be Antoine's official scatterchron-calculator. Peter, your foot-tapping soundtrack to the end of my Ph.D. will stay with me for life. Thomas, thanks for all your brilliant air-keyboard solos. Magali, your 10pm visits during my pre-submission rush were very welcome. And then of course there's everone that contributes to the lively social life of the department: Jean-Pierre, Teo, Matt, Pietro, Pinar, Dave, Gabriel, Diana, Kerry, Asia, Cris, Jean-Diego (ha!), Gaudenz, Stefanie, Ulrike, Alice, Julie, Julia, Anja, Marietta, Saka, Daniela, Alejo, Santanu and many others – thanks to all of you. Also, congratulations are due to the brave one-time cricketers – Michael, Dave, Mark and Alistair – and to the serial tennisers (?) – Remco, Tamara, Mark (again!) and Esther.

Away from the ETH, I've enjoyed evenings of cooking with Joëlle, arancini and possibly the best cocktails on Earth with Nicole & Dony, theatre, films, hiking, and pastis(!) with Annika, the initiation of my brunch-addiction with Piotr & Natalie, and almost-five-lake hikes with Michael & Domenika. Thanks!

Adri, your decision to get off the train at Hardbrücke on that day in August 2002 was obviously prescient. Thanks for helping me get started here, big brother. Nicole, thanks for always making me feel at home, in Basel, Luzern and Emmen. Sam, Julia and Göttikind Alina, you're all a complete delight!

Nats, I don't know how we're going to manage (perhaps) actually living on the same continent, but it'll be fun, I think.

Parentals, what can I say. Thank you for everything.

Corinne: .

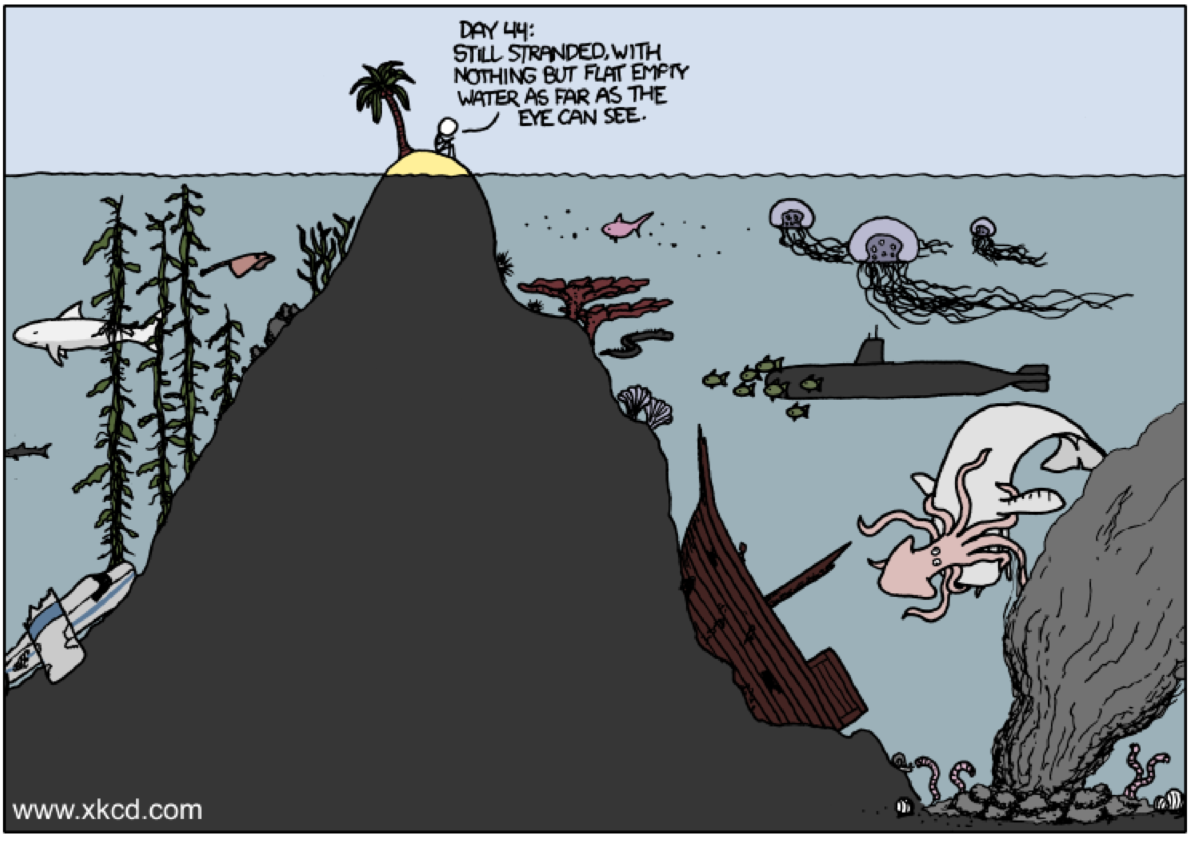
DAY 44:
STILL STRANDED, WITH NOTHING BUT FLAT EMPTY WATER AS FAR AS THE EYE CAN SEE.
www.xkcd.com

CURRICULUM VITÆ

Name	Gregory Friedrich de Souza
Date of birth	30.04.1981
Place of birth	Mumbai, India
Nationalities	Swiss, Indian (Overseas Citizen)

Degrees

2007	M.Sc., ETH Zurich, Switzerland (Grade 5.8) Thesis title: “^{87}Sr/^{86}Sr and $\delta^{88/86}$Sr in the forefield of the Damma Glacier, Switzerland” Supervisors: Dr. B. C. Reynolds, Prof. B. Bourdon
2001	B.Sc., University of Mumbai, India (First class)

Education

2007 – 2011	Doctoral programme in the Department of Earth Sciences ETH Zurich, Switzerland
2002 – 2007	Graduate studies in Earth Sciences, Geochemistry & Isotope Geology major ETH Zurich, Switzerland
1998 – 2001	Undergraduate studies, Geology major St. Xavier’s College, University of Mumbai, India
1996 – 1998	Junior College, natural sciences St. Xavier’s College, Mumbai, India
1986 – 1996	Primary and secondary school St. Stanislaus’ High School, Mumbai, India